Tuning the Properties of Ceramic Solid Electrolytes for Lithium Batteries



Stefanie Zekoll

St Cross College

Department of Materials

University of Oxford

A thesis submitted for the degree of

Doctor of Philosophy

Trinity 2018

Declaration of Originality

I, Stefanie Zekoll, certify that the work presented in this thesis is the result of my own work and has not been submitted to the University of Oxford or any other institution for any degree, diploma or other qualification. Any collaborations on this work or work performed by others included in this thesis has been clearly referenced and acknowledged. The work for this thesis, which is approximately 39,850 words in length, has been carried out within the Department of Materials at the University of Oxford from January 2015 to September 2018 under the supervision of Prof. Peter G. Bruce.

Acknowledgments

I would first like to express my sincere gratitude to my supervisor Prof. Peter Bruce for giving me the opportunity to join his research group and work on the very cutting-edge of battery research in such a thriving and stimulating environment. I would like to thank him for his guidance, support and expertise throughout this project.

Special thanks go to Dr. Jitti Kasemchainan, for his invaluable help and guidance from the very beginning to the very end of this project. Thank you for sharing your immense battery knowledge with me and for all the insightful advice and fruitful discussions we have had along the way.

I would also like to thank past members of the Bruce group, Dr. Felix Richter and Dr. Ola Hekselman for their guidance and support during the first half of this project, Dr. Cassian Marriner-Edwards for his help with designing the 3D microarchitectures and templates, and Dr. Christian Kuss for contributing very useful finite element modelling data towards this project.

I would also like to acknowledge my collaborators Dr. Job Thijssen and Dr. Robert Wallace (University of Edinburgh) for valuable scientific discussions and their contribution of micro-computed tomography scans and bijel samples. I would also like to thank Prof. David Armstrong and Dr. Bo-Shiuan Li (Department of Materials, University of Oxford) for letting me use their mechanical testing equipment and for their expertise and continuous help with the measurements. A further thank goes to Dr. Kalin Dragnevski and Dr. Marzena Tkaczyk (Department of Engineering, University of Oxford) for the performance of in-situ compression tests and optical depth profiling on

my samples and Dr. Philip Holdway (Oxford Materials Characterisation Service, University of Oxford) for his help with XPS measurements.

Additional thanks go to Prof. Clare Grey, Dr. Lauren Marbella and Steffen Emge (Department of Chemistry, University of Cambridge) for an enjoyable collaboration during the second half of my project. I am grateful for their time performing ^{7}Li NMR and ^{7}Li MRI measurements on my cells and for the many valuable scientific discussions that followed.

Finally, I would like to thank the remainder of the Bruce group for all the entertaining lunch breaks, coffee breaks and social gatherings, which have made my time in Oxford especially enjoyable.

Abstract

The potential of all-solid-state batteries with lithium metal anodes to be safer, more energy dense and better performing energy storage devices than current lithium ion batteries has led to a major drive in developing solid electrolytes that combine high ionic conductivity with suitable interfacial and mechanical properties. This work analyses the electrochemical and mechanical properties of two ceramic solid electrolytes, $Li_{1.4}Al_{0.4}Ge_{1.6}(PO_4)_3$ (LAGP) and $Li_{6.5}La_3Zr_{1.5}Ta_{0.5}O_{12}$ (LLZTO), and their interfacial behaviour with a lithium metal anode. A novel synthetic route to a 3D hybrid solid electrolyte with tuneable properties and a new approach to diagnose cell failure in all-solid-state batteries are presented.

A hybrid electrolyte with 3D bicontinuous ordered ceramic and polymer microchannels was successfully synthesised using 3D printing. While the ceramic solid electrolyte channels enable high ionic conduction pathways, the presence of non-conductive polymer channels provides the hybrid with structural stability and resilience to fracture. Full control of the hybrid's parameters such as the choice of ceramic electrolyte, polymer, microarchitecture and ceramic-to-polymer ratio was demonstrated. The LAGP-epoxy hybrid electrolyte with a gyroid microarchitecture achieved the highest ionic conductivity of 1.6×10^{-4} $S \cdot cm^{-1}$, which is only lowered by the volume of non-conductive polymer present and the channel tortuosity. The favourable combination of the epoxy polymer's fracture strength and the 'easy-to-fill' gyroid channels, improved the hybrid's electrochemical and mechanical performance compared to a LAGP pellet. The variation of the ceramic electrolyte and the microarchitecture influence the hybrid's electrochemical properties, while the polymer volume fraction provides a suitable 3D backbone to increase the hybrid's mechanical stability and cycle life. Despite the sintering challenges of LLZTO, a possible synthetic route to generate LLZTO-epoxy hybrid electrolytes was also demonstrated.

Additionally, inhibiting lithium dendrite growth in LLZTO and other solid electrolytes is another vital challenge. Hence, this work also presents a new method to diagnose dendrite growth by combining galvanostatic cycling with *ex-situ* magnetic resonance imaging. This approach allowed the identification of lithium dendrites in short-circuit cells and monitoring of their location in 3D space at different stages of cycling.

List of Publications

1. Stefanie Zekoll, Cassian Marriner-Edwards, A. K. Ola Hekselman, Jitti Kasemchainan, Christian Kuss, David E. J. Armstrong, Dongyu Cai, Robert J. Wallace, Felix H. Richter, Job Thijssen and Peter G. Bruce. Hybrid electrolytes with 3D bicontinuous ordered ceramic and polymer microchannels for all-solid state batteries. *Energy Environmental Science*. **11**, 185-201 (2018).

2. Lauren E. Marbella, Stefanie Zekoll, Jitti Kasemchainan, Steffen P. Emge, Peter G. Bruce and Clare P. Grey. ^{7}Li NMR Chemical Shift Imaging To Detect Microstructural Growth of Lithium in All-Solid-State Batteries. *Chemistry of Materials.* 31, 8, 2762-2769 (2019).

List of Abbreviations

1D	-	one-dimensional
2D	-	two-dimensional
3D	-	three-dimensional
AC	-	alternating current
AES	-	Auger electron spectroscopy
Al	-	aluminium
Ar	-	argon
Au	-	gold
Ba	-	barium
Bijel	-	bicontinuous interfacially-jammed emulsion gel
BMS	-	bulk magnetic susceptibility
Br	-	bromine
BSE	-	backscattering electrons
C	-	carbon
C	-	capacitor
CA	-	citric acid monohydrate
Ca	-	calcium
CAD	-	computer-aided design
Cd	-	cadmium
Cl	-	chlorine
CPE	-	constant phase element
Cr	-	chromium
CSA	-	chemical shift anisotropy
CSI	-	chemical shift imaging
CT	-	x-ray computed tomography
Cu	-	copper
DiLL	-	dip-in laser lithography
DLW	-	direct laser writing
EDX	-	energy dispersive x-ray spectroscopy
EG	-	ethylene glycol
EIS	-	electrochemical impedance spectroscopy
EV	-	electric vehicle
FAST	-	field-assisted sintering technology
FID	-	free induction decay
Ga	-	gallium
Ga	-	gallium
Ge	-	germanium
GPEs	-	gel polymer electrolytes
Hf	-	hafnium
HFP	-	hexafluoropropylene

I	-	iodine
j	-	current density
KSA	-	Knight shift anisotropy
La	-	lanthanum
LAGP	-	$Li_{1+x}Al_xGe_{2-x}(PO_4)_3$
LATP	-	$Li_{1.4}Al_{0.4}Ti_{1.6}(PO_4)_3$
LCO	-	$LiCoO_2$
Li	-	lithium
LiPON	-	lithium phosphorus oxynitride
LISICON	-	lithium ion super ionic conductor
LLTO	-	$Li_{3x}La_{(2/3)-x}TiO_3$
LLZO	-	$Li_7La_3Zr_2O_{12}$
LLZTO	-	$Li_{6.5}La_3Zr_{1.5}Ta_{0.5}O_{12}$
LSTZ	-	$Li_{3/8}Sr_{7/16}Ta_{3/4}Zr_{1/4}O_3$
LTP	-	$LiTi_2(PO_4)_3$
MAS NMR	-	Magic angle spinning NMR
MCI	-	mixed electronic and ionic conducting interphase
Mg	-	magnesium
micro-CT	-	x-ray micro-computed tomography
MRI	-	magnetic resonance imaging
N	-	nitrogen
Na	-	sodium
NASICON	-	sodium ion super ionic conductor
Nb	-	niobium
NCA	-	$LiNiCoAlO_2$
Ni	-	nickel
NMC	-	$LiNiMnCoO_2$
NMR	-	nuclear magnetic resonance
O	-	oxygen
OCV	-	open circuit voltage
P	-	phosphorus
PECS	-	precision etching coating system
PEO	-	polyethylene oxide
PMMA	-	polymethylmethacrylate
PP	-	polypropylene
PVDF	-	poly(vinylidene fluoride)
PXRD	-	powder x-ray diffraction
Q	-	capacity
R	-	resistor
RF	-	radio frequency
RT	-	room temperature
S	-	sulfur

Sb	-	antimony
Sc	-	scandium
SE	-	secondary electrons
SEI	-	solid electrolyte interphase
SEM	-	scanning electron microscopy
Si	-	silicon
SiC	-	silicon carbide
SPEs	-	solid polymer electrolytes
SPS	-	spark plasma sintering
Te	-	tellurium
T_g	-	glass transition temperature
Ti	-	titanium
UHV	-	ultra-high vacuum
UV	-	ultraviolet
Voxel	-	volume pixel
W	-	tungsten
XPS	-	x-ray photoelectron spectroscopy
Y	-	yttrium
Zn	-	zinc
Zr	-	zirconium

Table of Contents

Declaration of Originality ...…… i

Acknowledgements ……..……... iii

Abstract ...……...…….....v

List of Publications ...…….…..….....vii

List of Abbreviations …….....ix

Table of Contents …..……..…….xiii

Chapter 1: Introduction

1.1. Introduction……...…….....1

1.2. The rechargeable Li-ion battery……....2

1.2.1. How does a Li-ion battery work?.....2

1.2.2. What are the challenges facing current Li-ion batteries?.....5

1.3. The all-solid-state Li battery.....7

1.3.1. Advantages of an all-solid-state Li battery.....7

1.3.2. Types of solid electrolytes.....9

1.3.2.1. Ceramic electrolytes.....10

1.3.2.2. Polymer electrolytes.....17

1.3.2.3. Composite solid electrolytes.....19

1.3.3. Challenges facing all-solid-state Li batteries.....20

1.3.3.1. The chemical stability of the solid electrolyte with Li metal.....20

1.3.3.2. Interfacial resistances at the electrode-electrolyte interface.....23

1.3.3.3. The Li dendrite problem.....24

1.3.3.4. Mechanical properties of solid electrolytes.....27

1.4. Aim of this work.....29

1.5. References.....30

Chapter 2: Experimental Techniques

2.1. Synthesis Techniques.....39

2.1.1. 3D Printing.....39

2.1.2. Sol-Gel Synthesis.....40

2.2. Characterisation Techniques.....41

2.2.1. Powder X-ray Diffraction.....41

2.2.2. Scanning Electron Microscopy.....44

2.2.3. Electron Dispersive X-ray Spectroscopy.....46

2.2.4. X-ray Photoelectron Spectroscopy.....47

2.2.5. X-ray Micro-computed Tomography.....48

2.2.6. Solid-state Nuclear Magnetic Resonance.....49

2.2.7. Magnetic Resonance ^{7}Li Chemical Shift Imaging.....52

2.3. Electrochemical Techniques.....53

2.3.1. Alternating Current Electrochemical Impedance Spectroscopy.....53

2.3.2. Galvanostatic Cycling…….....59

2.4. Mechanical Testing Techniques.....60

2.4.1. Compression testing…….....60

2.4.2. Four-point bending…….....62

2.4.3. Nanoindentation…….....64

2.5. References…….....66

Chapter 3: Electrochemical and Mechanical Analysis of the Interfacial and Bulk Properties of $Li_{1.4}Al_{0.4}Ge_{1.6}(PO_4)_3$ as Solid Electrolyte

3.1. Aim.....69

3.2. Introduction.....69

3.3. Experimental Methods.....70

3.3.1. Synthesis of $Li_{1.4}Al_{0.4}Ge_{1.6}(PO_4)_3$.....70

3.3.2. Microstructural analysis.....71

3.3.2.1. SEM and EDX.....71

3.3.2.2. PXRD.....72

3.3.2.3. XPS….....72

3.3.3. Electrochemical analysis.....72

3.3.3.1. EIS.....72

3.3.3.2. Galvanostatic cycling.....73

3.3.4. Mechanical analysis.....74

3.3.4.1. Compression testing.....74

3.3.4.2. Four-point bending.....74

3.3.4.3. Nanoindentation….....75

3.4. Results and Discussion.....75

3.4.1. Synthesis and characterisation of LAGP.....75

3.4.2. Impedance measurements with Au blocking electrodes.....78

3.4.3. Impedance measurements with Li metal electrodes.....79

3.4.4. Effect of surface polishing on the impedance.....81

3.4.5. Characterisation of the reactivity of LAGP with Li metal.....84

3.4.6. Reactivity of LAGP with Li metal over time.....86

3.4.7. Galvanostatic cycling with Li metal electrodes.....90

3.4.8. Analysis of the mechanical properties of LAGP.....96

3.5. Conclusions.....99

3.6. References.....100

Chapter 4: Synthesis and Characterisation of a 3D Ordered Hybrid Electrolyte using $Li_{1.4}Al_{0.4}Ge_{1.6}(PO_4)_3$ and an Epoxy Polymer

4.1. Aim.....103

4.2. Introduction.....103

4.3. Experimental Methods.....104

4.3.1. Synthesis of the 3D structured LAGP-epoxy hybrid electrolyte.....104

4.3.1.1. Design of the gyroid microarchitecture and template.....104

4.3.1.2. 3D Printing of the gyroid template.....106

4.3.1.3. Synthesis of the LAGP ceramic electrolyte.....106

4.3.1.4. Synthesis of the structured LAGP scaffold.....106

4.3.1.5. Epoxy polymer filling of the structured LAGP scaffold.....107

4.3.2. Microstructural analysis.....107

4.3.2.1. SEM and EDX.....107

4.3.2.2. PXRD.....108

4.3.2.3. X-ray micro-CT.....108

4.3.3. Electrochemical analysis.....108

4.3.3.1. EIS.....108

4.3.3.2. Galvanostatic cycling.....109

4.3.4. Mechanical analysis.....109

4.3.4.1. Compression testing.....109

4.3.4.2. Four-point bending.....109

4.4. Results and Discussion.....109

4.4.1. Synthesis of the 3D LAGP-epoxy hybrid electrolyte.....109

4.4.1.1. Design and fabrication of the 3D printed gyroid template.....111

4.4.1.2. Filling procedure of the 3D printed gyroid template.....112

4.4.2. Characterisation of the 3D LAGP-epoxy hybrid electrolyte.....115

4.4.3. Impedance measurements with Au blocking electrodes.....118

4.4.4. Effect of solvent on the filling procedure.....120

4.4.5. Impedance measurements with Li metal electrodes.....123

4.4.6. Galvanostatic cycling with Li metal electrodes.....125

4.4.7. Analysis of the mechanical properties of the hybrid.....135

4.5. Conclusions.....139

4.6. References.....140

Chapter 5: Tuning the Properties of the 3D Ordered Hybrid Electrolyte

5.1. Aim.....143

5.2. Introduction.....143

5.3. Experimental Methods.....144

5.3.1. Synthesis of the 3D ordered hybrid electrolyte.....144

5.3.1.1. Design and fabrication of the 3D printed templates.....144

5.3.1.2. Design of the four microarchitectures.....144

5.3.1.3. Synthesis of the 3D ordered LAGP-polymer electrolyte.....146

5.3.1.4. Synthesis of the 3D ordered LLZTO-polymer electrolyte.....146

5.3.2. Microstructural analysis.....147

5.3.2.1. SEM and EDX.....147

5.3.2.2. X-ray micro-CT.....147

5.3.3. Electrochemical analysis.....148

5.3.3.1. EIS.....148

5.3.3.2. Galvanostatic cycling.....148

5.3.4. Mechanical analysis.....149

5.3.4.1. *In-situ* SEM compression testing.....149

5.3.4.2. Compression testing.....149

5.3.4.3. Four-point bending.....149

5.4. Results and Discussion.....150

5.4.1. Choice and design of the four microarchitectures.....150

5.4.2. Synthesis of the 3D ordered LAGP-polymer electrolyte.....151

5.4.3. Effect of microarchitecture and type of polymer on the ionic conductivity.....157

5.4.4. Effect of microarchitecture and type of polymer on the cycling performance with Li metal electrodes.....161

5.4.5. Synthesis of the 3D ordered LAGP-epoxy electrolytes with different ceramic-to-polymer ratios.....163

5.4.6. Effect of the ceramic-to-polymer ratio on the ionic conductivity.....165

5.4.7. Effect of the ceramic-to-polymer ratio on the cycling performance with Li metal electrodes.....167

5.4.8. Mechanical properties of the 3D ordered LAGP-polymer electrolytes.....168

5.4.9. Synthesis of a 3D gyroid LLZTO-epoxy electrolyte.....172

5.4.10. Electrochemical properties of the 3D gyroid LLZTO-epoxy electrolyte.....178

5.4.11. Mechanical properties of the 3D gyroid LLZTO-epoxy electrolyte.....179

5.5. Conclusions.....180

5.6. References.....183

Chapter 6: Electrochemical and Microstructural Analysis of the Interfacial and Bulk Properties of $Li_{6.5}La_3Zr_{1.5}Ta_{0.5}O_{12}$ as Solid Electrolyte

6.1. Aim.....185

6.2. Introduction.....185

6.3. Experimental Methods.....186

6.3.1. Synthesis of $Li_{6.5}La_3Zr_{1.5}Ta_{0.5}O_{12}$.....186

6.3.2. Microstructural analysis.....188

6.3.2.1. SEM and EDX.....188

6.3.2.2. PXRD.....188

6.3.2.3. ^{7}Li NMR and ^{7}Li MRI.....189

6.3.3. Electrochemical analysis.....190

6.3.3.1. EIS.....190

6.3.3.2. Galvanostatic cycling.....190

6.4. Results and Discussion.....190

6.4.1. Synthesis and characterisation of LLZTO.....190

6.4.2. Impedance measurements with Au blocking electrodes.....194

6.4.3. Effect of sintering temperature on LLZTO.....195

6.4.4. Effect of sintering time on LLZTO.....197

6.4.5. Impedance measurements with Li metal electrodes.....200

6.4.6. Galvanostatic cycling with Li metal electrodes.....202

6.4.7. Li dendrite imaging in LLZTO by SEM and EDX.....206

6.4.8. Li dendrite imaging in LLZTO by ^{7}Li CSI.....207

6.5. Conclusions.....211

6.6. References.....214

Chapter 7: Conclusions and Outlook.....217

Appendices.....223

Chapter 1: Introduction

1.1. Introduction

With the world's population expected to reach ten billion by the end of this century,[1] the need for affordable and sustainable energy is crucial to ensure and satisfy ever-growing demand. Significant research into both renewable energy technologies and sustainable energy storage systems is needed. Rechargeable lithium (Li)-ion batteries have proven to be one of the most promising energy storage systems for portable electronics, electric vehicles (EV) and large-scale grid applications.[2,3,4] Since their commercialisation by Sony in 1991,[5] rechargeable Li-ion batteries have surpassed many other battery systems due to their high energy densities (120-150 $Wh \cdot kg^{-1}$), high average cell voltages (3.6 V) and versatile usage (Figure 1.1).[3]

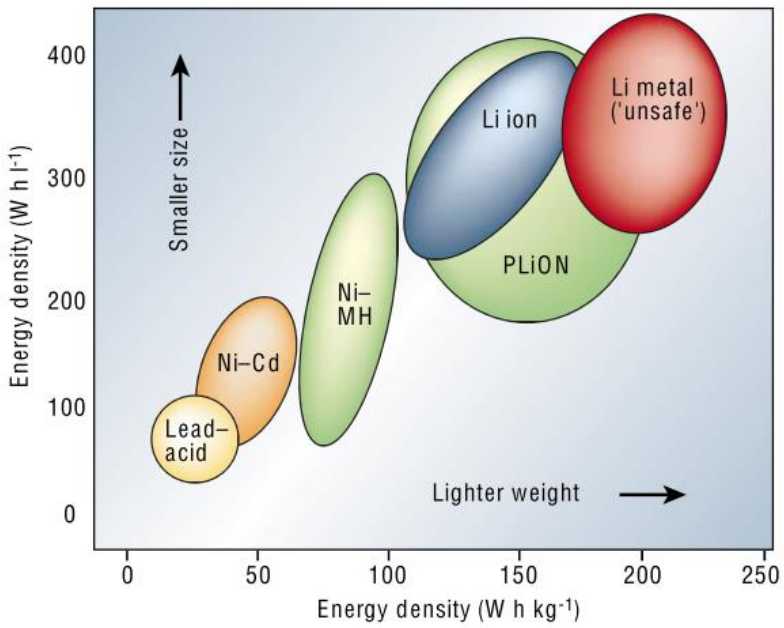


Figure 1.1. Gravimetric and volumetric energy density of the Li-ion battery compared to other battery systems. [3]

Nevertheless, continued research into novel electrode and electrolyte materials is needed to further improve the cost, efficiency and safety of current Li-ion batteries. Novel solid electrolyte materials, which could replace flammable liquid electrolytes, are hoped to enhance battery safety and durability, while simultaneously allowing for further versatility in cell assembly and battery design.

This Chapter aims to serve as an introduction to the work performed in this thesis and summarises the recent advances made in the field of solid electrolytes and the challenges these face when implemented in an all-solid-state Li battery. Firstly, a general introduction into the operation of a Li-ion battery and its remaining challenges is given. The concept of an all-solid-state Li battery is then proposed and its advantages over current liquid electrolyte Li-ion battery systems are demonstrated. The main section of this Chapter focuses on the properties of several solid electrolyte materials investigated so far and their challenges when assembled in a cell with a Li metal electrode. Finally, an insight into the specific aims of this work is given.

1.2. The rechargeable Li-ion battery

1.2.1. How does a Li-ion battery work?

Li-ion batteries are divided into two categories: primary (non-rechargeable) and secondary (rechargeable) Li-ion batteries. While non-rechargeable batteries are still more commonly implemented as disposable batteries, rechargeable Li-ion batteries have gained in importance due to their increased use in both portable electronic devices and the transportation industry.[6]

A conventional rechargeable Li-ion battery cell consists of three key components: the cathode (positive electrode), the anode (negative electrode) and the electrolyte, which

separates the electrode materials. Alternating charge and discharge processes, also known as intercalation and de-intercalation processes, occur within the electrochemical cell when in operation. During discharge, Li^+ ions migrate from the anode through the electrolyte medium to the cathode, where the cations are accommodated within organised layers or appropriate tunnels provided by the cathode material's structure. In order to maintain charge neutrality within both electrodes, one electron (e^-) per Li^+ ion is simultaneously released to an external circuit, which powers an attached device. The opposite insertion reaction occurs upon charging. Li^+ ions from the cathode are re-intercalated into the anode material, which at the same time regains electrons with the help of an applied current (Figure 1.2).[7]

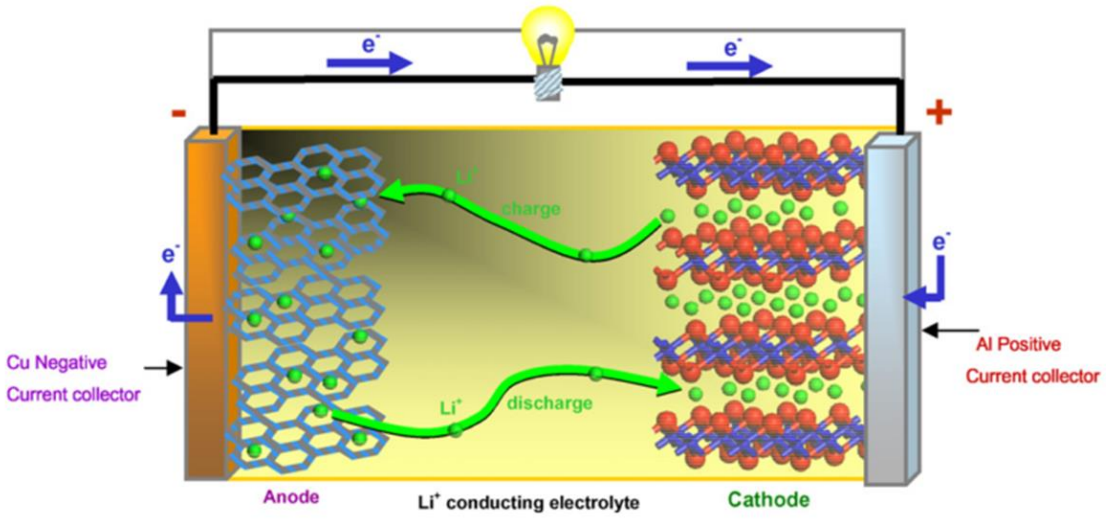


Figure 1.2. Schematic representation of a rechargeable Li-ion battery cell.[8]

Graphite is the most common anode material used in commercial Li-ion batteries due its high surface area, low manufacturing costs and favourable structural properties to intercalate Li^+ ions into its layers.[9] Materials such as silicon (Si)[10] and titanium oxides,[11] however, are currently being investigated as potential future alternatives. Layered lithium transition metal oxides such as $LiCoO_2$ (LCO), but also $LiNiCoAlO_2$ (NCA) and

$LiNiMnCoO_2$ (NMC) are one of the most efficient cathode materials used so far. This is mainly due to their high specific capacities (155 $Ah \cdot kg^{-1}$, 180 $Ah \cdot kg^{-1}$ and 160 $Ah \cdot kg^{-1}$ for LCO, NCA and NMC, respectively) and cell voltages (3.9 V, 3.7 V and 3.8 V for LCO, NCA and NMC, respectively).[12] The toxicity and cost of cobalt in LCO has also led to significant research moving toward safer and more environmentally friendly cathode materials. Olivine-type or spinel-type materials such as $LiFePO_4$ and $LiMnPO_4$ have shown to be promising alternatives.[12]

The capacity (in $Ah \cdot kg^{-1}$ or $Ah \cdot L^{-1}$) is determined as the amount of charge per unit weight or unit volume that can be extracted from the battery cell upon discharge at a specific current over time. The higher the capacity of the electrode materials, the more Li^+ ions can be accommodated into and extracted out of both electrode structures. The theoretical capacity (in $mAh \cdot g^{-1}$) of an electrode material is given by:

$$Q = \frac{nF}{3600\ M_W} \tag{1.1}$$

where n is the number of charge carriers, F is the Faraday constant and M_w is the molecular weight of the active electrode material. For some electrode materials, not all of the Li can be extracted out of the structure during charge, which leads to a lower practical capacity. This is the case for LCO where only half of the available Li can be extracted from its lattice. Hence, its practical capacity is much lower than its calculated theoretical capacity (274 $Ah \cdot kg^{-1}$). The cell voltage is defined as the difference between the chemical potential of the Li in the cell's anode (μ_a) and cathode (μ_c) as follow:

$$V = \frac{\mu_a - \mu_c}{nF} \tag{1.2}$$

Similarly to the capacity, the higher the cell voltage, the more energy per unit charge is available to transport electrons through the circuit.[13] Both of these cell characteristics are

linked to the energy density, the amount of energy that can be stored in a battery (in $Wh \cdot kg^{-1}$ or $Wh \cdot L^{-1}$), which is defined as the product of the capacity that can be reversibly transferred between both electrodes and the cell voltage. Increasing the cell voltage and/or capacity, increases the energy density of the battery, which ultimately leads to a battery with an improved cell performance. The longer a battery can maintain its practical capacity, i.e. extract and store Li^+ ions over many charge and discharge processes whilst operating within a stable voltage window, the higher its efficiency. The coulombic efficiency, which is defined as the ratio between the discharge capacity and the charge capacity in the same cycle, gives an indication of the cycle life of a battery. The loss of Li due to the consumption of Li by parasitic reactions, the degradation of electrode materials and increases in internal resistances in the cell are all aging processes that promote capacity loss, which needs to be limited to maintain the battery's lifetime.

1.2.2. What are the challenges facing current Li-ion batteries?

Over the last two decades, Li-ion batteries have been the most attractive and popular battery systems. The development of suitable electrode materials enables Li-ion batteries to achieve energy densities twice as high as previous nickel-cadmium (Ni-Cd) battery systems. With an average cell voltage of up to 3.6 V compared to only 1.2 V in alkaline battery systems,[3] Li-ion batteries also benefit from a very successful reversible insertion process between both cathode and anode materials.

Nevertheless, several challenges remain for Li-ion batteries so that they may be fully utilised in EVs, microelectronics and medical devices. One of these challenges is the Li-ion battery's safety. Even though liquid electrolytes have shown excellent electrochemical and interfacial properties for Li-ion transport, the presence of highly flammable and toxic solvents does not guarantee safe functioning of the battery cell over

time.[14] Liquid electrolytes are prone to undergo chemical reactions at the electrode-electrolyte interface at high operating voltages and temperatures. This leads to decomposition reactions and, ultimately, to the formation of unwanted by-products such as LiF, Li_2O, Li_2CO_3 and solvent-specific alkyl carbonates.[15,16] These are known to aggregate and form a so-called solid electrolyte interphase (SEI) layer at the electrode-electrolyte boundary. While a small SEI build-up is beneficial to the cell by acting as a protective layer between the negative electrode and the electrolyte medium, long-term SEI growth gradually blocks the active material's surface. This effectively inhibits Li-ion intercalation, causes short-circuits, and can ultimately lead to hazards such as leakages, explosions and fires.[17]

While a continuous increase in the energy density of Li-ion batteries has been achieved over the past few years by the discovery of new higher capacity cathode materials, concerns exist that this growth might soon stagnate unless a change in the anode material is implemented. The specific capacity of graphite is limited to 372 $mAh \cdot g^{-1}$, which if replaced by Li-Si alloy anodes could unlock specific capacities of over 3000 $mAh \cdot g^{-1}$.[12] Unfortunately, the reactivity of the liquid electrolyte with Li and the increased volume expansions obtained in Si anodes remain on-going drawbacks. Additionally, the versatile usage of Li-ion batteries requires unique battery performances and sizes for each application. While microelectronics and medical devices rely on the development of Li-ion batteries on the millimetre and micrometre scale,[18] EVs and large scale grid applications desire much larger, but also lighter, high energy density Li-ion batteries with enhanced cell capacities.[19] The need for additional packaging materials to guarantee the safety in current Li-ion batteries increases the weight and volume of the overall battery. This makes the fabrication of Li-ion micro-batteries, but also the improvement of energy density and battery performance, particularly challenging. Hence, research focuses on

finding suitable materials to further facilitate the varied applications of Li-ion batteries. Employing improved active electrode and electrolyte materials, whilst reducing the amount of non-active cell components, has the potential to significantly reduce the cost of current Li-ion batteries; a vital criterion for the future of EVs in the automotive market.[12] Hence, continuous research into alternative materials and new concepts to further improve performance, safety and sustainability, is needed.

1.3. The all-solid-state Li battery

1.3.1. Advantages of an all-solid-state Li battery

The use of liquid electrolytes in current Li-ion batteries has raised significant safety and durability concerns. Therefore, research into solvent-free solid electrolytes that could replace current liquid systems has become one of the key efforts today. The replacement of the liquid electrolyte with an equally efficient non-flammable solid electrolyte would drastically improve the safety of the battery and eliminate unwanted side reactions, leakages and explosion risks.[20]

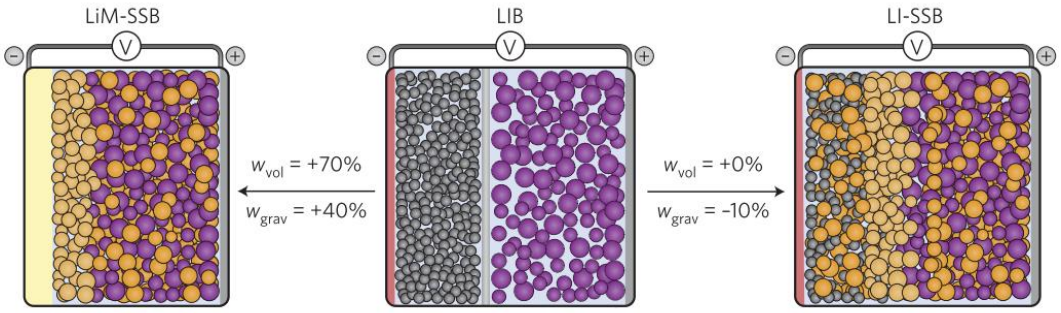


Figure 1.3. Illustration of the difference between a conventional Li-ion battery (middle) and an all-solid state battery with a graphite anode (right) and with a Li metal anode (left).[21]

However, as shown in Figure 1.3, substituting the liquid electrolyte with a solid electrolyte alone is not sufficient to outperform current Li-ion technologies. The true

benefit of all-solid-state batteries, next to the utilisation of a safe electrolyte, is their ability to potentially unlock the use of Li metal as the anode, which would allow for an increase in specific energy density of 70 %.[21]

Thus far, graphite has been the anode of choice in current Li-ion batteries due to its high specific capacity (372 $mAh \cdot g^{-1}$) and good compatibility with current liquid electrolytes. In contrast, a Li metal anode has a specific capacity of 3860 $mAh \cdot g^{-1}$. Unfortunately, liquid electrolytes are highly reactive towards Li metal.[22,23] This is observed by the formation of so-called Li dendrites at the electrode-electrolyte interfaces, which are responsible for accelerated cell degradation, short-circuits and, ultimately, cell failure.[24] The use of a solid electrolyte, which forms a stable interface with Li metal, would resolve this issue. The solid electrolyte acts as both an ionic conductor and physical separator between both electrodes and prevents the formation of Li dendrites growing from the electrode interface into the electrolyte, inhibiting short-circuit during operation.[25,26] Hence, all-solid-state batteries have the ability to simplify the current Li-ion cell by reducing the use of inactive components and additional safety packaging material,[20] thereby increasing the battery's energy density and lifetime.[27]

Despite these advantages, the achievement of an all-solid-state lithium battery is still a work in progress. While liquid electrolytes display ionic conductivity values of 10^{-2} $S \cdot cm^{-1}$ and higher, not all solid electrolytes achieve values close to that range.[28] This is a shortcoming for the overall performance of a battery. Numerous solid electrolytes are very rigid and brittle,[29] which results in poor interfacial contact between the electrode and the electrolyte and premature cell failures at higher current densities.[30,31] Consequently, the mechanical and interfacial properties of solid electrolytes and their high manufacturing costs can be considered as the main challenges to be tackled in order for all-solid-state batteries to reach their full potential.

1.3.2. Types of solid electrolytes

Solid electrolytes are classified into two categories: inorganic (ceramic) and organic (polymer) electrolytes. An ideal solid electrolyte is required to:

- Be a good Li-ion conductor (with ionic conductivity values of $> 10^{-4}$ $S \cdot cm^{-1}$ at room temperature (RT)).
- Have a Li^+ transference number (the fraction of current carried by a specific ion in the electrolyte) close to unity.
- Have a negligible electronic conductivity ($< 10^{-10}$ $S \cdot cm^{-1}$).
- Be chemically and electrochemically stable with the cathode material of choice.
- Achieve a good contact at the electrode-electrolyte interface.
- Be stable in air and moisture.
- Be stable against Li metal.
- Have suitable mechanical properties to avoid Li dendrite formation and fracture upon cell volume changes.

While most polymer electrolytes exhibit mechanical and interfacial properties that make them soft and elastic enough to accommodate potential volume changes or stresses in a cell, ceramic Li-ion conductors struggle to achieve good contacts at the electrode-electrolyte interface[32] and fracture easily due to their brittleness.[29] Alternatively, ceramic electrolytes can attain much higher ionic conductivities than any reported solid polymer electrolyte so far.[33] Hence, finding an ideal solid electrolyte represents a significant challenge. An overview of the different types of solid electrolytes that have been investigated so far, is given in Figure 1.4. Their specific advantages and disadvantages are described in the following sections of this Chapter.

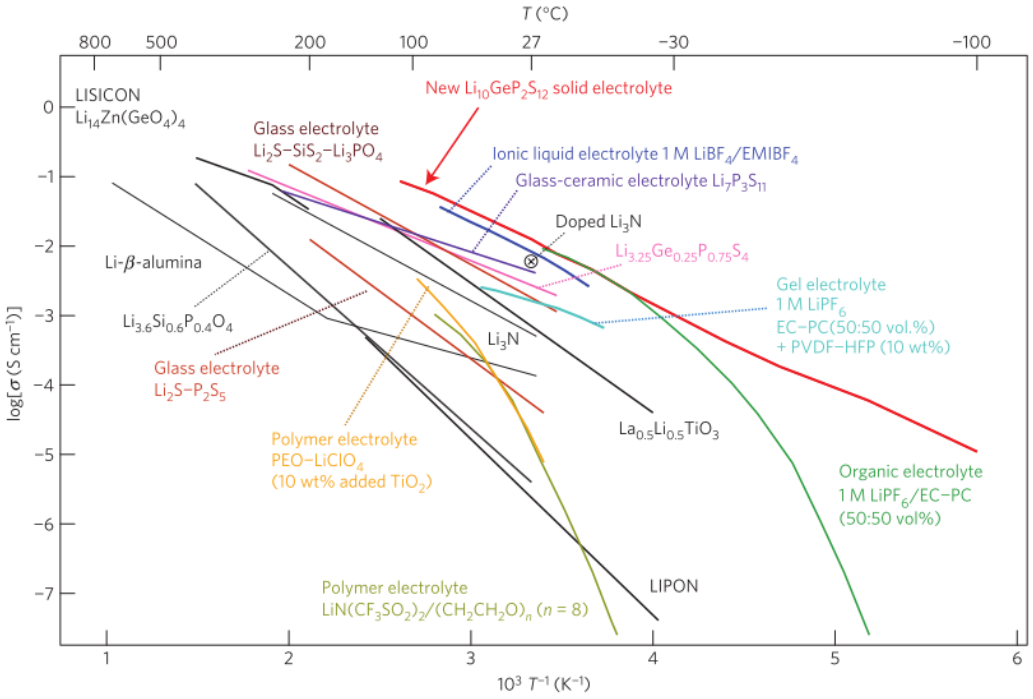


Figure 1.4. Comparison between the Arrhenius plots of different types of solid electrolytes and the currently used organic electrolyte (in green).[33]

1.3.2.1. Ceramic electrolytes

NASICON Li-ion conductors

NASICON-type Li-ion conductors are the Li analogues of the sodium (Na)-ion super ionic conductors (NASICON). The repeating unit within the material's crystal structure is described by the general formula $LiM^{IV}_2(PO_4)_3$, where M^{IV} = titanium (Ti), zirconium (Zr), germanium (Ge) or hafnium (Hf). NASICON-type Li-ion conductors consist of MO_6 octahedra linked to PO_4 tetrahedra to form a three-dimensional (3D) network with interstitial channels suitable for fast Li-ion transport.[34] Figure 1.5 illustrates the crystal structure of $LiGe_2(PO_4)_3$, a typical NASICON-type Li-ion conductor.

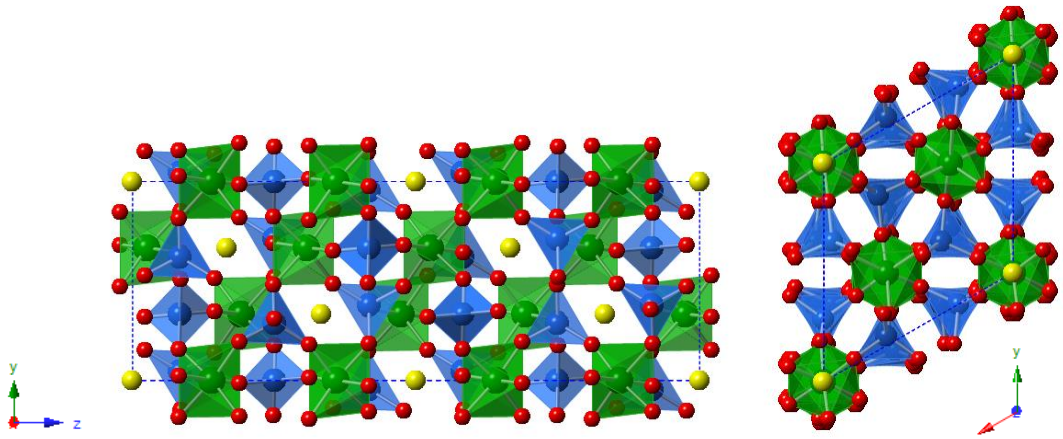


Figure 1.5. Crystallographic representation of $LiGe_2(PO_4)_3$, a NASICON-type Li-ion conductor (crystallographic data obtained from [35]).

$Li_{1+x}M_xTi_{2-x}(PO_4)_3$, where M = aluminium (Al), scandium (Sc) or chromium (Cr), has shown the most promising bulk electrochemical properties of all, with ionic conductivities reaching up to 10^{-3} S·cm^{-1} at RT.[36,37] Unfortunately, Ti^{4+} is easily reduced to Ti^{3+} in contact with Li metal, which complicates its use as future solid electrolyte material.[38] Doping $LiTi_2(PO_4)_3$ (LTP) with trivalent metals such as Al and Cr, improves the electrochemical stability and increases the ionic conductivity from 2 x 10^{-6} S·cm^{-1} to 7 x 10^{-4} S·cm^{-1} at RT.[36] Simultaneous Al^{3+} and Si^{4+} doping to give $Li_{1.7}Al_{0.3}Ti_{1.7}Si_{0.4}P_{2.6}O_{12}$ further increases the total ionic conductivity up to 2.4 x 10^{-3} S·cm^{-1} at RT, as has been reported by Yi *et al*.[37] The substitution of Ti with Ge has also shown promising results. High ionic conductivity values in the order of 10^{-4} S·cm^{-1} have been reported for the glass-ceramic $Li_{1+x}Al_xGe_{2-x}(PO_4)_3$ (LAGP).[39,40,41] Crystallised from a precursor glass, glass-ceramics benefit from having lower grain boundary resistances than pure crystalline ceramics due to the presence of a favourable amorphous phase between grains.[42] LAGP has an increased stability in both air and water compared to other NASICON-type Li-ion conductors.[43] Nevertheless, stability issues

remain when in contact with Li metal due to similar reducing issues with Ge as has been seen with Ti. Recent investigations into alternative sintering methods such as spark plasma sintering (SPS), also known as field-assisted sintering technology (FAST),[44] have shown increased pellet densities and conductivity values for LATP and LAGP type Li-ion conductors.[45] Instead of conventionally sintering $Li_{1.4}Al_{0.4}Ti_{1.6}(PO_4)_3$ (LATP) at 850 °C for 5 hours, similar or improved results at a reduced sintering temperature of 650 °C for only 5 minutes were achieved using FAST, leading to a theoretical density of 100 % for LATP with a total ionic conductivity of 1.12×10^{-3} S cm^{-1} at RT.[46]

LISICON Li-ion conductors

Li-ion super ionic conductors (LISICON)-type solid electrolytes were, along with NASICON-type Li-ion conductors, one of the first reported types of solid electrolyte material. A typical Li-ion conductor, which adopts the LISICON structure, is $Li_{14}ZnGe_4O_{16}$. First reported by Hong in 1978,[47] $Li_{14}ZnGe_4O_{16}$ forms a 3D framework with suitable mobile sites for Li-ion diffusion. Although the material can achieve high ionic conductivities at elevated temperatures, only low ionic conductivities in the range of 10^{-7} $S \cdot cm^{-1}$ have been achieved at RT.[48] $Li_{14}ZnGe_4O_{16}$ is also highly reactive with Li metal and atmospheric CO_2, leading to a steady decrease of the material's electrochemical performance over time.[49]

Perovskite-type Li-ion conductors

The discovery of $Li_{3x}La_{(2/3)-x}TiO_3$ (LLTO),[50] which crystallises into a perovskite-type ABO_3 arrangement, has revealed a completely new class of Li-ion conducting materials. The advantages of LLTO include a large electrochemical stability window (>8 V vs. Li^+/Li), and stability in air, water and both high and low temperatures.[50] Depending on the Li content in the composition, LLTO either adopts an orthorhombic ($0.03 \leq x < 0.1$) or a tetragonal symmetry ($0.1 \leq x < 0.167$). The Li-rich tetragonal

arrangement has the advantage of having Li-ion conducting pathways in all three dimensions, which explains the higher ionic conductivity obtained in these compositions compared to Li-poor compositions, which only allow two-dimensional (2D) Li-ion conduction to take place.[50,51] Figure 1.6 displays the crystal structure of the perovskite-type ABO_3 arrangement in LLTO.

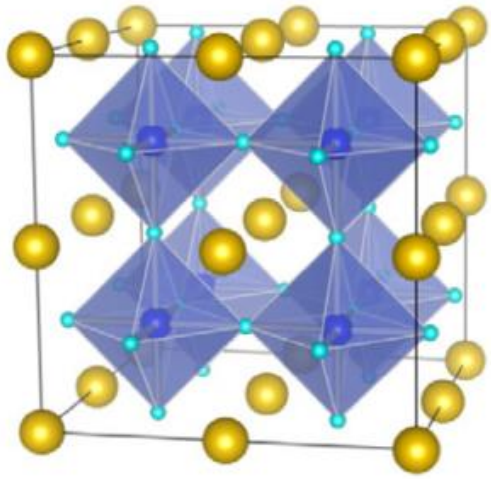


Figure 1.6. Crystallographic representation of the ABO_3 arrangement in an ordered perovskite-structure oxide. A sites, which can be occupied by Li ions, lanthanum (La) ions or a vacancy, are labelled as yellow spheres; B-site ions (here Ti ions; dark blue spheres) form BO_6 octahedra with oxygen (O) atoms (light blue spheres). [52]

Although LLTO shows high bulk conductivities in the range of 10^{-3} $S \cdot cm^{-1}$, its grain boundary conductivity may only attain values of up to 10^{-5} $S \cdot cm^{-1}$. This, together with its instability against Li metal (due to the reduction of Ti^{4+} to Ti^{3+}) are its two main downsides. Several attempts to increase the grain boundary conductivity have been made. The addition of an amorphous layer of silica between the LLTO grains[53] or the introduction of $Li_7La_3Zr_2O_{12}$ (LLZO) powder into the LLTO lattice[54] both decrease the grain boundary resistance within LLTO, and increase its total ionic conductivity up to

1 x 10^{-4} S·cm^{-1} at RT. Al doping[55] and niobium (Nb) doping[56] also increases its ionic conductivity. Recent investigations into moisture-free synthesis methods showed promising results in decreasing the grain boundary resistance and raising the conductivity of LLTO even further.[57] The synthesis of a perovskite-type material with the chemical formula $Li_{3/8}Sr_{7/16}Ta_{3/4}Zr_{1/4}O_3$ (LSTZ) showed enhanced stability against Li metal compared to other perovskite-type LLTO systems. This is due to the favourable replacement of Ti by Zr at the B-sites, and La by Sr at the A-sites within the perovskite ABO_3 arrangement. Partial substitution of the $SrZrO_3$ arrangement by Li and Ta ions has also been carried out. Using a powder-bed sintering method to prevent any Li loss or the formation of impurity phases, enabled an improvement of the grain to grain contact and achievement of a relatively high total ionic conductivity of 2.7 x 10^{-4} S·cm^{-1} at RT.[58]

Garnet-type Li-ion conductors

Garnet-type materials with the general formula $Li_5La_3M_2O_{12}$ (M = tantalum (Ta), Nb, Zr), count towards one of the most promising oxide Li-ion conducting materials. Since being first reported by Thangadurai and Weppner in 2003 for their favourable Li-ion conducting properties,[59] garnet-type materials have been the subject of considerable investigation into their potential use as solid electrolytes in all-solid-state Li batteries. Garnet-type materials exhibit a high electrochemical voltage window (up to 5 V vs. Li^+/Li [60]), total ionic conductivities of up to 10^{-4} S·cm^{-1} and, most importantly, excellent stability when in contact with Li metal.[61] $Li_7La_3Zr_2O_{12}$ (LLZO) is the most reported and successful non-doped garnet-type composition.[62] Here, LaO_8 dodecahedrons are connected to ZrO_6 octahedrons to form a 3D framework with 3D interconnecting channels suitable for Li-ion transport (Figure 1.7). Depending on the synthesis conditions, LLZO can either crystallise as a cubic or tetragonal phase. Electrochemical impedance spectroscopy (EIS) shows that higher ionic conductivities are achieved within

LLZO's cubic arrangement than within its tetragonal arrangement (~10^{-4} S·cm^{-1} vs. ~10^{-6} S·cm^{-1} at RT). However, this requires the ceramic material to be sintered at temperatures above 1200 °C instead of only ~980 °C.[62,63] The stabilisation of the cubic phase at RT is achieved by doping, with Al, gallium (Ga) and Ta being the most successful doping agents so far. The substitution of Li^{+} and Zr^{4+} by larger ions expands the lattice and enables a more efficient Li-ion conduction process to occur throughout the 3D framework.[64,65,66] With a total ionic conductivity value of 1 x 10^{-3} S·cm^{-1} at RT, Ta-doped $Li_{6.4}La_3Zr_{1.4}Ta_{0.6}O_{12}$ displays one of the highest total ionic conductivity values for a garnet-type Li-ion conductor reported thus far.[60]

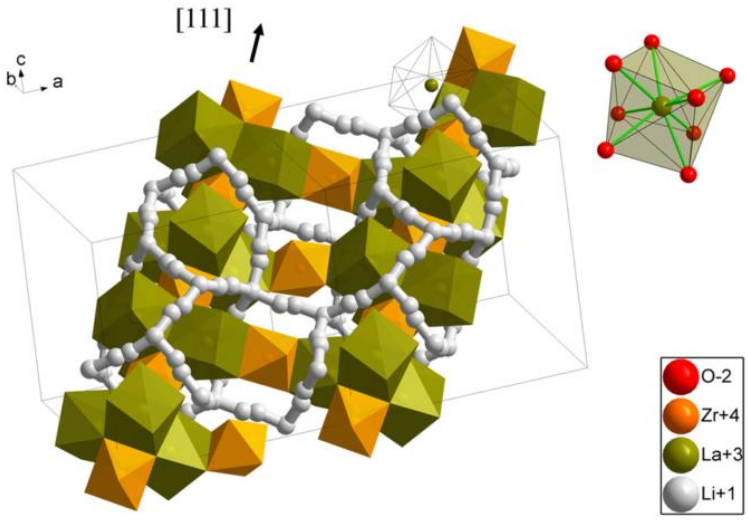


Figure 1.7. Representation of the cubic phase crystal structure of LLZO.[67]

Thio-LISICON Li-ion conductors

Recent work in trying to improve the conductivity and stability of oxide-based LISICON-type materials has led to the discovery of their sulphur-based analogues, also

known as ‘thio-LISICON’ Li-ion conductors. This newer category of solid electrolytes, first introduced by Kanno *et al.* in 2001,[68] show remarkable electrochemical properties, with total ionic conductivity values above 10^{-4} S·cm^{-1} at RT. $Li_{10}GeP_2S_{12}$ was the first Li-ion conducting solid electrolyte material to display better Li-ion conduction than current liquid electrolytes; achieving a total ionic conductivity value of 1.2 x 10^{-2} S·cm^{-1} at RT.[33] (Figure 1.8)

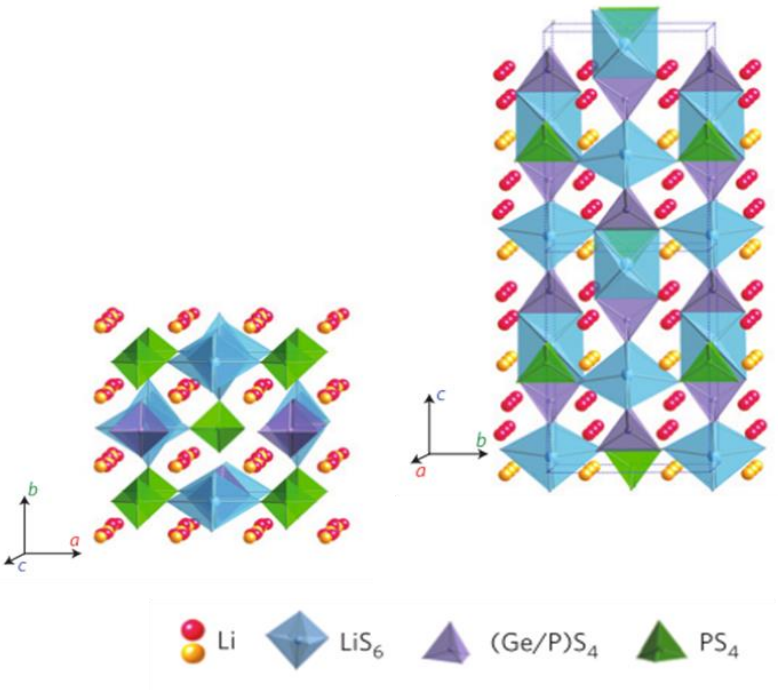


Figure 1.8. Crystal structure of $Li_{10}GeP_2S_{12}$ showing the Li-ion diffusion pathways along the a- and c-axis (adapted from Kamaya et al. [69]).

Soon after, Seino *et al.* reported a glass-ceramic with the chemical composition $70Li_2S{\cdot}30P_2S_5$, which exhibits an even higher ionic conductivity of 1.7 x 10^{-2} S·cm^{-1} at RT.[70] The so far highest reported Li-ion conducting sulphide electrolyte is $Li_{9.54}Si_{1.74}P_{1.44}S_{11.7}Cl_{0.3}$ with an ionic conductivity of 2.5 x 10^{-2} S·cm^{-1} at RT.[71] The advantage of sulphur (S)-based versus O-based 3D framework materials is mainly the size of the corresponding anion. As the ionic radius of a sulphide ion (S^{2-}) is greater than

an oxide ion (O^{2-}), larger pathways for Li-ion conduction can be formed, which lower the activation energy of ion migration. S^{2-} ions also benefit from being more polarizable than O^{2-} ions, which results in a weaker interaction between the Li^+ ions and the remaining 3D framework, thus enabling faster conduction through the crystal lattice.[68]

Thio-LISICON-type materials are mechanically softer (more formable) than their oxide analogues and are more easily processed at RT with their electrode counterpart to achieve better contact at the electrode-electrolyte interface.[72] However, their instability in air and moisture, instabilities with Li metal and high-voltage cathodes as well as their brittleness remain major shortcomings.[73]

1.3.2.2. Polymer electrolytes

Polyethylene oxide (PEO)-based polymer materials, reported by Wright *et al*. were one of the first polymer complexes to be considered as electrolytes in electrochemical devices.[74] Since then, increased amounts of research into several other Li-salt polymer complexes have been undertaken.[75] Polymer electrolytes are divided into two categories: solid polymer electrolytes (SPEs) and gel polymer electrolytes (GPEs)

SPEs are crystalline or amorphous polymer complexes formed by the solvation of a Li salt in a solid polymer chain.[18] Most commonly, PEO is used as the polymer host due to its ability to dissolve various Li salts within its chains.[18,76] Common Li salts used in SPEs include LiI, $LiCF_3SO_3$ and $LiPF_6$.[77] While it was long thought that only polymer electrolytes in the amorphous phase (above the glass transition temperature, T_g) have the ability to conduct Li^+ ions, Bruce *et al.* have proven that purely crystalline polymer electrolytes can also display Li-ion conductive properties via ion-hopping mechanisms, compared to segmental chain motions.[77,78] (Figure 1.9).

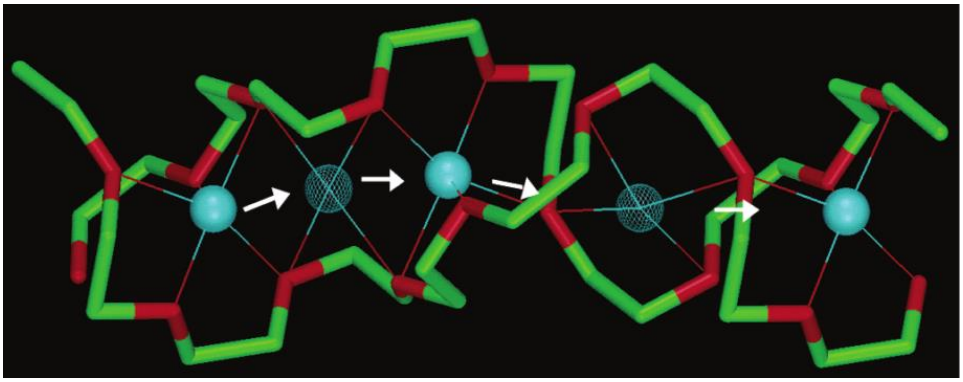


Figure 1.9. Li^+ ion migration through the crystalline polymer electrolyte $PEO_6{\cdot}LiPF_6$. Li^+ cations are displayed as blue spheres, while the PEO chains are represented by carbon (C)(green) and O (red) sticks. Thin lines show the coordination of Li^+ to O atoms within the tunnel.[78]

Overall, SPEs benefit from several advantages over other types of electrolyte system such as increased safety (due to the absence of any liquid), increased flexibility, potential chemical stability against Li metal, and overall enhanced mechanical stability.[75,18,79] Nevertheless, ionic conductivity values obtained in SPEs (10^{-8} - 10^{-4} $S{\cdot}cm^{-1}$ at RT) remain low.[79] Several methods to enhance the conductivity have been conducted, these include increasing the number of chain ends,[80] aliovalent and isovalent doping,[76,81] lowering the molecular weight[78] or even introducing plasticisers[82] to increase the amorphous content within the polymer complex.

GPEs are slightly different to SPEs as they are composed of an organic liquid electrolyte solution incorporated within a polymer matrix.[83] This gives rise to a so-called polymer gel, where Li-ion conduction occurs in a similar manner to liquid electrolyte systems. Although these achieve ionic conductivities in the range of 10^{-3} $S{\cdot}cm^{-1}$, issues such as undesired chemical side reactions, leakages and cell degradations, as seen in pure liquid electrolytes, remain present.[18] Polymer hosts within GPE include PEO,[84,85]

poly(vinylidene fluoride) (PVDF),[86] polymethylmethacrylate (PMMA),[87] and a combination of PVDF with hexafluoropropylene (PVDF-HFP).[88] A good affinity between the polymer matrix and the liquid component is essential to ensure maximum absorbance without any loss of the polymer's structural integrity. Another challenge with GPEs is the achievement of a high Li^+ transference number. While in solid electrolytes a transference number of unity is easily achieved, liquid electrolytes often contain, along with Li^+, other charge carriers such as the anions associated with the Li salt or the solvent. Thus, typical Li^+ transference numbers in these type of systems can be as low as 0.3.[89] Increasing the transference number counts as one of the main challenges to be solved.[90,89]

1.3.2.3. Composite solid electrolytes

The complementarity seen between polymer and ceramic electrolytes, specifically regarding their mechanical and electrochemical properties, has led to significant research in trying to combine both polymer and ceramic electrolytes into one composite material.[6]

The addition of inorganic fillers such as α-alumina[91], silica[92] or LLZO particles[93] to solid polymer electrolytes has shown to increase the overall ionic conductivity, mechanical stability and chemical stability with Li metal. The synthesis of electrospun LLZO nanofibers into a PEO matrix has recently shown to provide continuous, non-interruptive, high ionically conductive pathways.[94] Additionally, aligning these ceramic nanowires, as shown by the work of Liu *et al.* with LLTO, along the Li-ion conduction flow drastically increases the ionic conductivity compared to randomly dispersed LLTO particles.[95] The same idea was shown by aligning LATP nanoparticles by an ice templating method.[96] The ionic conduction of Li-ions is certainly more favourable within the better conducting electrolyte (ceramic phase) due to the relatively high resistance at the polymer-ceramic interface. To avoid high resistances between both electrolytes, a one-particle thick

flexible electrolyte membrane composed of $Li_{1.6}Al_{0.5}Ti_{0.95}Ta_{0.5}(PO_4)_3$ particles dispersed in a cyclo-olefin polymer matrix has also been reported.[97]

1.3.3. Challenges facing all-solid-state Li batteries

While the challenge of attaining high ionic conductivities in solid electrolytes has recently been unlocked by the synthesis of several classes of sulphide materials[69–71], many more hurdles on the road to commercialisation are only just being discovered. So far, most research has focused on the solid electrolytes alone with minimal research yet being done on full all-solid-state cells. The most vital challenge is finding a solid electrolyte that is compatible with both a Li metal anode and a high-voltage cathode. This requires three components that are stable with each other, show low interfacial resistances at their respective solid-solid interfaces, retain fast Li-ion conduction across all three layers and can operate at the required currents and capacities for a substantial amount of time without showing any signs of material degradation, capacity losses or cell failures. The following sections summarise the most crucial problems currently being tackled by the solid-state battery community with regards to the solid electrolyte-Li metal interface. Note that, similar, if not more problematic challenges are found at the electrolyte-cathode interface, which are not discussed in this Chapter.

1.3.3.1. The chemical stability of the solid electrolyte with Li metal

The reactivity of several solid electrolytes with Li metal has been extensively studied by Janek and co-workers over the past years using photoelectron spectroscopy within a sputter chamber. Their results have led to the conclusion that there are three types of possible interfaces[98] that can form between the solid electrolyte and Li: a thermodynamically stable interface (Figure 1.10-a), a reactive interface that either leads to the formation of a growing mixed electronic and ionic conducting (MCI) interphase

layer (Figure 1.10-b) or the formation of an interphase layer that is only ionically and not electronically conductive, which eventually stabilises as a thin interphase layer, similar to the SEI formation in liquid electrolytes (Figure 1.10-c).

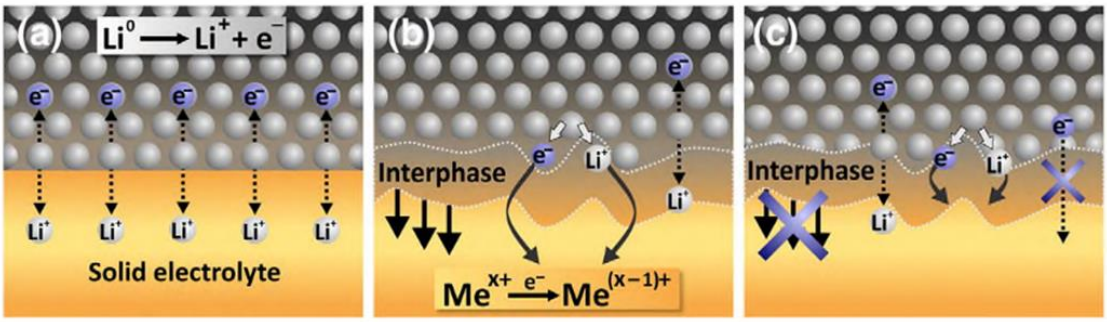


Figure 1.10. Schematic of the three possible interfaces that can occur between the solid electrolyte and Li metal upon contact: (a) non-reactive and thermodynamically stable interface, (b) reactive interface leading to the formation of a mixed electronic and ionic conducting (MCI) (growing) interphase and (c) reactive interface leading to the formation of a metastable (non-growing) SEI.[98]

Due to the reactivity of Li, the cases where an interphase layer between the solid electrolyte and the Li is formed are the most probable. The formation of an ever-growing interphase is the least desirable case and has mainly been observed with solid electrolytes that are composed of elements that become easily reduced by Li such as Ti or Ge in $Li_{1.6}Al_{0.5}Ti_{0.95}Ta_{0.5}(PO_4)_3$ (LATTP),[38] LAGP[38] or LLTO[98] (Figure 1.10-b). Lithium phosphorus oxynitride (LiPON), one of the few commercialised thin film solid electrolytes, is known to react with Li, but forms a stable interphase layer such as an SEI as described in Figure 1.10-c composed of mainly Li_2O, Li_3P and Li_3N.[99]

Regarding the sulphide electrolytes $Li_7P_3S_{11}$, Li_6PS_5X (with X = chlorine (Cl), bromine (Br) and iodine (I)) and $Li_{10}GeP_2S_{12}$, all react with Li by forming an SEI layer.[100,101,102] While the thickness of the SEI in $Li_7P_3S_{11}$ and Li_6PS_5X remains small, a rapidly growing

SEI is observed in $Li_{10}GeP_2S_{12}$ due to the strongly reducing properties of Ge in the presence of Li.

The chemical and electrochemical instability of many solid electrolytes with Li metal was also proven experimentally and by first principle calculations by the calculation of their respective electrochemical windows versus Li (Figure 1.11).[103,104]

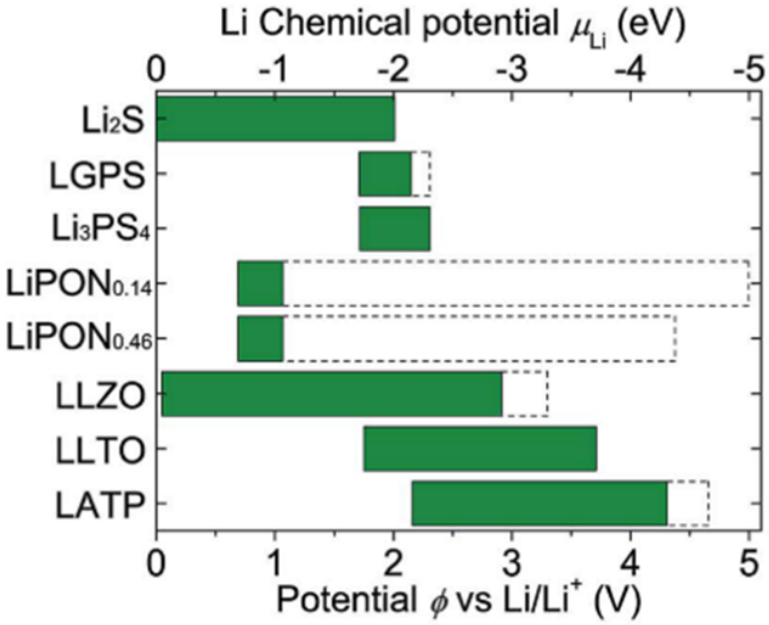


Figure 1.11. Electrochemical windows of several solid electrolytes against Li metal (adapted from Zhu et al.[103]*).*

From the promising solid electrolytes discussed previously in this Chapter, LLZO shows the lowest reduction potential versus Li of 0.05 V. Hence, this further supports LLZO's stability against Li metal. LLZO could be one of the few solid electrolytes that falls into the rare 'type a' category of possible solid electrolyte-Li interfaces (Figure 1.10-a). Nevertheless, as long as the resistance of the SEI remains small enough, the outcome described in Figure 1.10-c can be considered as the most sought after. The formed SEI layer can provide an improved degree of wetting at the electrode-electrolyte interface, while remaining thin enough to not impede the overall resistance of the cell with time.

1.3.3.2. Interfacial resistances at the electrode-electrolyte interface

Due to the solid-solid nature of all interfaces in an all-solid-state battery, wetting properties play a significant role in achieving good interfacial contacts between electrode and electrolyte materials needed for long-lasting cells. The degree of wetting has an immediate effect on the interfacial resistances, which are directly related to the maximum current density at which all-solid-state cells can effectively be cycled.[31]

Large interfacial resistances have specifically been observed for cells using LLZO as the solid electrolyte. The surface of LLZO pellets readily reacts with air to form a thin nanometre layer of Li_2CO_3 that significantly adds to the interfacial resistance between LLZO and Li metal.[105] Hence, the preparation of a clean surface is vital to improve the electrode-electrolyte contact (Figure 1.12).

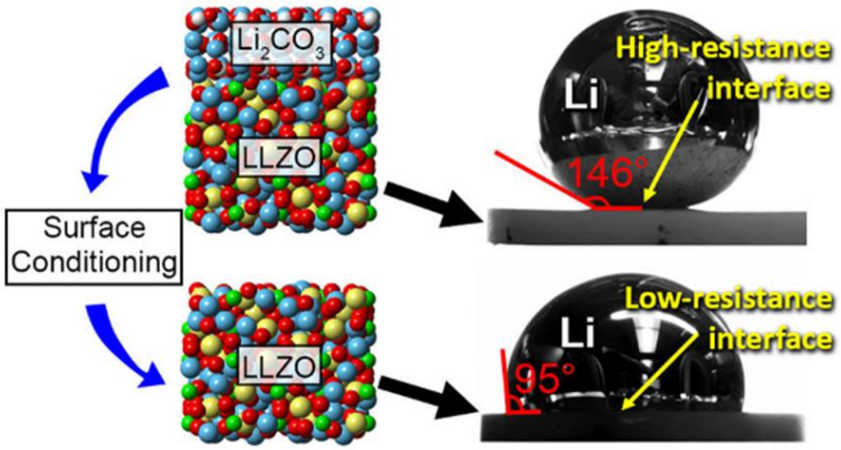


Figure 1.12. Improvement of the wetting properties of LLZO with molten Li by heating the surface to remove any undesired species.[106]

For LLZO, this was successfully achieved by polishing the LLZO pellets in argon (Ar), which led to a reduction of the interfacial resistance from 960 $\Omega \cdot cm^2$ to 109 $\Omega \cdot cm^2$. Improvements in the wettability of the Li-LLZO interface have also been attained by depositing thin nanometre layers of Al (75 $\Omega \cdot cm^2$)[107], gold (Au) (117 $\Omega \cdot cm^2$)[108] and Ge

(115 $\Omega \cdot cm^2$)[109], all of which are known to favourably alloy with Li. The addition of a Au buffer layer was also reported to improve the Li dissolution and deposition at the interface between Li_2S-P_2S_5 electrolytes and Li.[110] Recently however, an even lower reduction of the interfacial resistance for the LLZO electrolyte down to 2 $\Omega \cdot cm^2$ was achieved by heating the pellet's surface up to 500 ºC prior to cell assembly.[106] This approach drastically reduced the contact angle of LLZO with molten Li metal and increased the current density at which the cell could comfortably be cycled.

1.3.3.3. The Li dendrite problem

While finding a chemically stable solid electrolyte with a low interfacial resistance upon contact with Li metal is an essential requirement, the smooth cycling of such an electrolyte within an all-solid-state cell is still not ensured. Most solid electrolytes, especially the ones that show an increased stability with Li and which do not form a MCI interphase layer, such as LLZO, have shown to short-circuit imminently as soon as higher current densities are applied.[111] The origin of this short-circuit behaviour has been attributed to the formation of Li dendrites, which grow through the solid electrolyte from one Li electrode to the other.

It was believed that solid electrolytes, compared to liquid electrolytes, could impede the formation and growth of dendritic Li through the cell by acting as a physical separator between the Li metal and the opposing electrode. A model proposed by Monroe and Newman in 2005 suggested that as long as the solid electrolyte possesses a shear modulus twice the value of Li (i.e. 4.2 GPa[112]), the formation of dendrites is suppressed.[113] However, many observations have shown that Li deposits form readily along the grain boundaries and in voids of solid electrolytes leading to cell failure, whether this is in Li_2S-P_2S_5 [114], LLZO[115] or Li_3PS_4[116] solid electrolytes (Figure 1.13). Note that while the

shear modulus of the sulphides lie at the borderline of the Monroe-Newman model (7.1 GPa for the Li_2S-P_2S_5 glass),[29] a shear modulus for LLZO of 60 GPa was measured,[117] which would fit the mechanical property requirements for Li dendrite prevention.

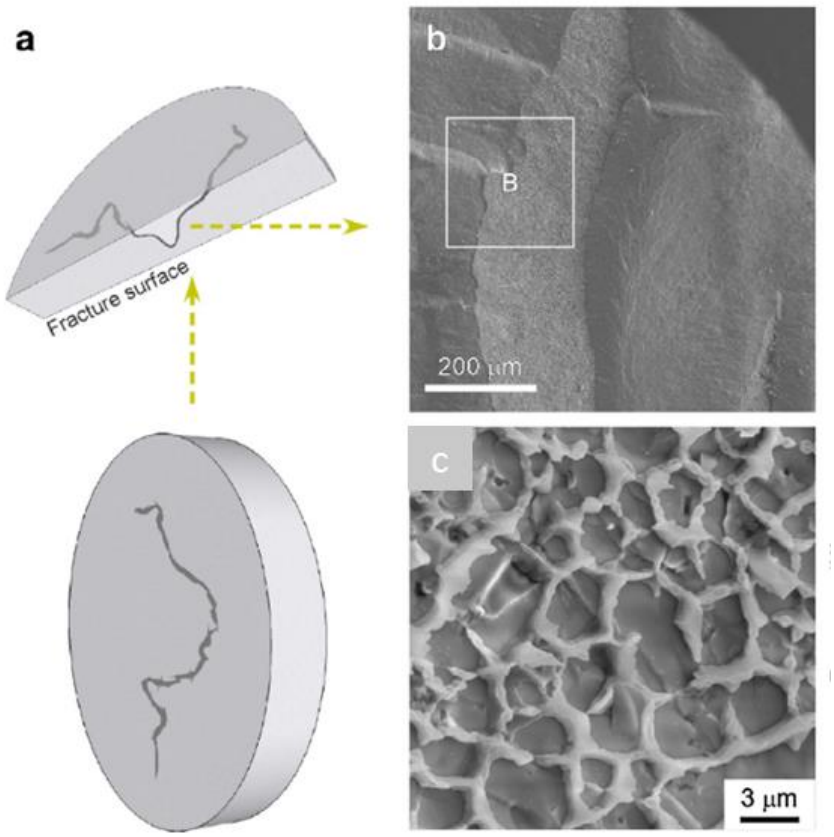


Figure 1.13. SEM images of the web-like structure of Li dendrites observed in a fractured LLZO pellet after short-circuit due to cycling: (a) schematic representation of the Li dendrite through the pellet, (b) SEM image of pellet cross-section and (c) magnified SEM image of the web-like dendrite structures (Figure adapted from Cheng et al.[118]*).*

The mechanism by which Li dendrites form and grow through solid electrolytes is still not fully understood. Similarly, what parameters and conditions trigger them in the first place remain unknown. Studies by Porz *et al.* recently suggested that Li dendrite

penetration occurs through pre-existing flaws at the surface of the solid electrolyte.[116] Their electrochemical model proposes that the failure observed in brittle solid electrolytes occurs by a Griffith-like mechanism. The flaws or cracks become filled with plated Li. Once a specific critical current density is reached, high enough mechanical stresses are exerted onto the filled flaws for them to propagate. Hence, it is so far believed that surface morphologies and defects of solid electrolytes, are, next to grain boundaries, significant factors affecting Li dendrite propagation.

One of the main challenges in understanding Li dendrites is the difficulty of imaging and characterising their presence in all-solid-state cells. The analysis of short-circuited cells by scanning electron microscopy (SEM) or optical microscopy only shows information of either the surface or a randomly chosen cross-section of the cell. Additionally, a Li dendrite that is causing short-circuit can be as thin as a few nanometres, which can be extremely difficult to image, even with the best microscopes. The low electron density of Li makes its characterisation by energy dispersive X-ray spectroscopy (EDX) near to impossible.[118,119] Recently, a technique combining SEM, EDX and Auger electron spectroscopy (AES) showed some promising results in being able to image and characterise Li dendrites between LLZO grains (Figure 1.14).[118] X-ray tomography yet struggles with distinguishing dendritic Li features from void space due to their similarly low X-ray attenuation, but has shown success in providing information of failure mechanisms through the tracking of cracks and porosity through the solid electrolyte.[120] Hence, it is yet extremely difficult to obtain a 3D representation of their growth through a solid-state cell.

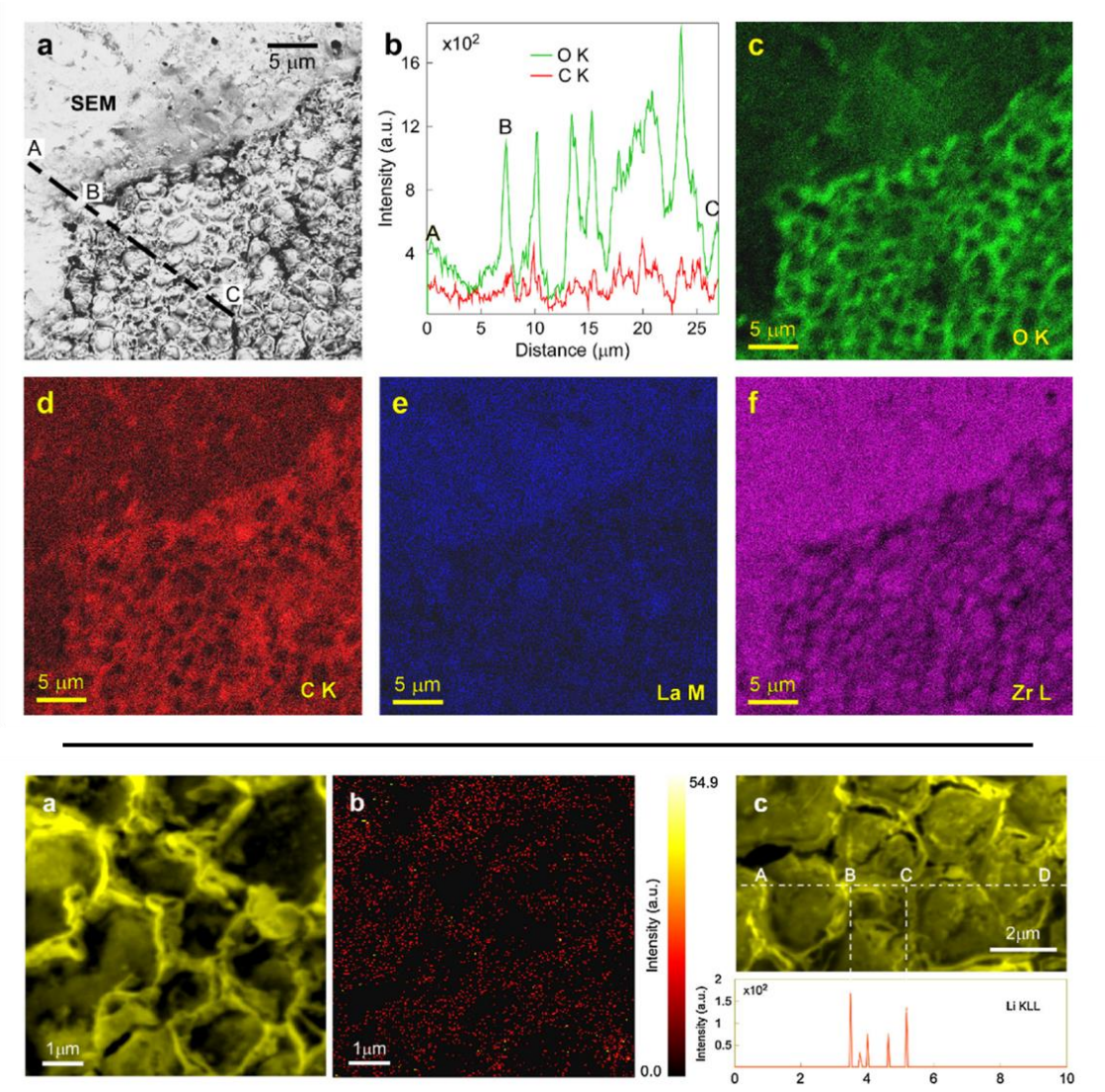


Figure 1.14. EDX (top panel) and AES (bottom panel) images of Li dendrites surrounding LLZO grains in a web-like fashion (Adapted from Cheng et al.[118]*).*

1.3.3.4. Mechanical properties of solid electrolytes

As ceramic solid electrolytes need to act as a physical barrier between electrodes, withstand the penetration of Li dendrites, but also accommodate potential electrode volume changes during cycling, their mechanical properties are vital to fit all of the requirements above. Recently, significant effort has been made to characterise the mechanical properties of promising solid electrolytes and understand which properties are essential to ensure long-term cycling in an all-solid-state battery. Several properties

that have been discussed in literature so far are the elastic properties (Young's modulus), the plastic properties (hardness) and the fracture properties (fracture toughness) using several techniques such as resonant ultrasound spectroscopy,[121] nano and micro indentation,[122,123] acoustic impulse excitation[117] and single edge notch bending.[124]

Measuring the Young's modulus and shear modulus gives an indication of the stiffness of the solid electrolyte. The Young's modulus of several oxide solid electrolytes such as LLZO, LLTO and LATP were measured to be ~150 GPa, ~200 GPa and ~115 GPa, respectively.[121,123,124] The shear modulus of LLZO was calculated as ~ 60 GPa.[117] Much lower values were obtained for the Young's modulus of sulphide solid electrolytes, such as for the Li_2S-P_2S_5 glasses (18-25 GPa),[125] which also showed to exhibit a shear modulus of 7.1 GPa.[29] If the Monroe-Newman model[113] is true, sulphides are close to not rigid enough to withstand dendrites due to their low shear moduli. Nevertheless, the shear modulus of LLZO is much higher than the minimum shear modulus required, but short-circuits due to Li dendrites still occur.[126] It is yet unclear whether the chemical difference of LLZO grain boundaries compared to LLZO grains results in radical differences in their mechanical properties that could allow for lower shear moduli and Li dendrites to penetrate through.[127] Other properties such as the hardness (the resistance to deformation), and the fracture toughness (the resistance to fracture once a crack has been formed) have also been considered. For the oxide ceramic electrolytes this resulted in hardness values of around ~ 6-10 GPa and fracture toughness values of ~ 1-2 $MPa \cdot m^{-2}$, confirming their dominantly covalent bonding and their brittle nature.[121–124] The hardness and fracture toughness of sulphide electrolytes lies around ~2 GPa and ~0.2 $MPa \cdot m^{-2}$, resulting in an even more brittle behaviour compared to their oxide equivalent.[29]

1.4. Aim of this work

As reported in this Chapter, the challenges facing all-solid-state lithium batteries are multiple and significant tuning of the properties of existing solid electrolytes is still needed to be able to meet the requirements of an ideal solid electrolyte.

In the first instance, this work aims to provide a thorough analysis of the most air-stable ceramic electrolyte LAGP, mainly its interfacial properties with Li metal, its mechanical properties, and to understand which of these properties affect its cycling performance and eventual failure in a symmetrical Li cell.

In a second instance, a new synthetic route to a solid electrolyte with tuneable mechanical properties that can retain its favourable ionic conductivity is presented. This is shown by the development of a 3D ordered bicontinuous hybrid electrolyte composed of ceramic electrolyte channels for Li-ion conduction and non-conductive polymer channels that provide a structured 3D backbone to mitigate the ceramic material's brittle properties. The synthesis of the hybrid is initially demonstrated by the use of a 3D printed template with a gyroid microarchitecture, LAGP as the ceramic electrolyte and an epoxy polymer. Its electrochemical and mechanical performance are compared to a LAGP pellet of equivalent size and shape.

Subsequently, the flexibility of the 3D ordered hybrid electrolyte in terms of the choice of the ceramic and polymer material, the 3D template microarchitecture and the ceramic-to-polymer ratio is demonstrated. How each of these tuneable parameters affects the performance of the hybrid is analysed.

Finally, the synthetic challenges regarding the LLZO solid electrolyte and the difficulty to image and characterise Li dendrites within a symmetrical Li | LLZO | Li cell are being discussed. A novel approach in combining electrochemical measurements with ^{7}Li

chemical shift imaging to understand the progression of Li dendrites and diagnose cell failure in all-solid-state battery cells is proposed.

1.5. References

1. Gerland, P. *et al.* World population stabilization unlikely this century. *Science (80-.).* **346,** 234–237 (2014).
2. Larcher, D. & Tarascon, J. Towards greener and more sustainable batteries for electrical energy storage. *Nat. Chem.* **7,** 19–29 (2014).
3. Tarascon, J. & Armand, M. Issues and challenges facing rechargeable lithium batteries. *Nature* **414,** 359–367 (2001).
4. Armand, M. & Tarascon, J. Building better batteries. *Nature* **451,** 652–657 (2008).
5. Kotobuki, M. & Koishi, M. Preparation of Li1.5Al0.5Ti1.5(PO4)3 solid electrolyte via a sol–gel route using various Al sources. *Ceram. Int.* **39,** 4645–4649 (2013).
6. Wang, Y. & Zhong, W.-H. Development of Electrolytes towards Achieving Safe and High-Performance Energy-Storage Devices: A Review. *ChemElectroChem* **2,** 22–36 (2015).
7. Sideris, P. J. & Greenbaum, S. G. *Batteries for Sustainability*. (Springer, New York, 2013).
8. Patil, A. *et al.* Issue and challenges facing rechargeable thin film lithium batteries. *Mater. Res. Bull.* **43,** 1913–1942 (2008).
9. Goriparti, S. *et al.* Review on recent progress of nanostructured anode materials for Li-ion batteries. *J. Power Sources* **257,** 421–443 (2014).
10. Nitta, N. & Yushin, G. High-Capacity Anode Materials for Lithium-Ion Batteries: Choice of Elements and Structures for Active Particles. *Part. Part. Syst. Charact.* **31,** 317–336 (2014).
11. Hong, Z. & Wei, M. Layered titanate nanostructures and their derivatives as negative electrode materials for lithium-ion batteries. *J. Mater. Chem. A* **1,** 4403 (2013).
12. Blomgren, G. E. The Development and Future of Lithium Ion Batteries. *J. Electrochem. Soc.* **164,** A5019–A5025 (2017).
13. Kraytsberg, A. & Ein-Eli, Y. Higher, Stronger, Better… A Review of 5 Volt Cathode Materials for Advanced Lithium-Ion Batteries. *Adv. Energy Mater.* **2,** 922–939 (2012).
14. Wen, J., Yu, Y. & Chen, C. A Review on Lithium-Ion Batteries Safety Issues: Existing Problems and Possible Solutions. *Mater. Express* **2,** 197–212 (2012).
15. Xu, K. Nonaqueous Liquid Electrolytes for Lithium-Based Rechargeable

Batteries Nonaqueous Liquid Electrolytes for Lithium-Based Rechargeable Batteries. *Chem. Rev.* **104,** 4303–4418 (2004).

16. Masquelier, C. Solid electrolytes: Lithium ions on the fast track. *Nat. Mater.* **10,** 649–650 (2011).

17. Pinson, M. B. & Bazant, M. Z. Theory of SEI Formation in Rechargeable Batteries: Capacity Fade, Accelerated Aging and Lifetime Prediction. *J. Electrochem. Soc.* **160,** A243–A250 (2013).

18. Wang, Y. *et al.* Lithium and lithium ion batteries for applications in microelectronic devices: A review. *J. Power Sources* **286,** 330–345 (2015).

19. Manzetti, S. & Mariasiu, F. Electric vehicle battery technologies: From present state to future systems. *Renew. Sustain. Energy Rev.* **51,** 1004–1012 (2015).

20. Knauth, P., Marseille, M., Masquelier, C. & Amiens, L. *All Solid State Batteries : Are They a Viable Option ?* (2012).

21. Janek, J. & Zeier, W. G. A solid future for battery development. *Nat. Energy* **1,** 16141 (2016).

22. Chen, J. Recent Progress in Advanced Materials for Lithium Ion Batteries. *Materials (Basel).* **6,** 156–183 (2013).

23. Park, M. S. *et al.* A highly reversible lithium metal anode. *Sci. Rep.* **4,** 3815 (2014).

24. Lu, Y., Tu, Z. & Archer, L. A. Stable lithium electrodeposition in liquid and nanoporous solid electrolytes. *Nat. Mater.* **13,** 961–969 (2014).

25. Khurana, R., Schaefer, J. L., Archer, L. A. & Coates, G. W. Suppression of lithium dendrite growth using cross-linked polyethylene/poly(ethylene oxide) electrolytes: A new approach for practical lithium-metal polymer batteries. *J. Am. Chem. Soc.* **136,** 7395–7402 (2014).

26. Kim, S.-H., Choi, K.-H., Cho, S.-J., Kil, E.-H. & Lee, S.-Y. Mechanically compliant and lithium dendrite growth-suppressing composite polymer electrolytes for flexible lithium-ion batteries. *J. Mater. Chem. A* **1,** 4949 (2013).

27. Oudenhoven, J. F. M., Baggetto, L. & Notten, P. H. L. All-solid-state lithium-ion microbatteries: A review of various three-dimensional concepts. *Adv. Energy Mater.* **1,** 10–33 (2011).

28. Wang, Y. *et al.* Design principles for solid-state lithium superionic conductors. *Nat. Mater.* **14,** 1026–1031 (2015).

29. McGrogan, F. P. *et al.* Compliant Yet Brittle Mechanical Behavior of Li2S-P2S5 Lithium-Ion-Conducting Solid Electrolyte. *Adv. Energy Mater.* **7,** 1602011 (2017).

30. Han, X. *et al.* Negating interfacial impedance in garnet-based solid-state Li metal batteries. *Nat. Mater.* **1,** (2016).

31. Sharafi, A., Meyer, H. M., Nanda, J., Wolfenstine, J. & Sakamoto, J. Characterizing the Li–Li7La3Zr2O12 interface stability and kinetics as a function of temperature and current density. *J. Power Sources* **302,** 135–139

(2016).

32. Yamada, H., Oga, Y., Saruwatari, I. & Moriguchi, I. Local Structure and Ionic Conduction at Interfaces of Electrode and Solid Electrolytes. *J. Electrochem. Soc.* **159,** A380 (2012).

33. Kamaya, N. *et al.* A lithium superionic conductor. *Nat. Mater.* **10,** 682–686 (2011).

34. Masquelier, C. & Croguennec, L. Polyanionic (phosphates, silicates, sulfates) frameworks as electrode materials for rechargeable Li (or Na) batteries. *Chem. Rev.* **113,** 6552–91 (2013).

35. Alami, M. *et al.* Structure and thermal expansion of LiGe2(PO4)3. *Journal of Solid State Chemistry* **90,** 185–193 (1991).

36. Aono, H. Ionic Conductivity of Solid Electrolytes Based on Lithium Titanium Phosphate. *J. Electrochem. Soc.* **137,** 1023 (1990).

37. Yi, E. *et al.* Materials that can replace liquid electrolytes in Li batteries: Superionic conductivities in Li1.7Al0.3Ti1.7Si 0.4P2.6O12. Processing combustion synthesized nanopowders to free standing thin films. *J. Power Sources* **269,** 577–588 (2014).

38. Hartmann, P., Leichtweiss, T., Busche, M. R. & Schneider, M. Degradation of NASICON-type materials in contact with lithium metal : Formation of Mixed Conducting Interphases (MCI) on Solid Electrolytes. *J. Phys. Chem. C* **117,** 21064–21074 (2013).

39. Fu, J. Fast Li+ ion conducting glass-ceramics in the system Li2O–Al2O3–GeO2–P2O5. *Solid State Ionics* **104,** 191–194 (1997).

40. Arbi, K., Bucheli, W., Jiménez, R. & Sanz, J. High lithium ion conducting solid electrolytes based on NASICON Li1+xAlxM2−x(PO4)3 materials (M=Ti, Ge and 0≤x≤0.5). *J. Eur. Ceram. Soc.* **35,** 1477–1484 (2015).

41. Kotobuki, M. & Koishi, M. Sol–gel synthesis of Li1.5Al0.5Ge1.5(PO4)3 solid electrolyte. *Ceram. Int.* **5,** 1–6 (2015).

42. Tatsumisago, M., Nagao, M. & Hayashi, A. Recent development of sulfide solid electrolytes and interfacial modification for all-solid-state rechargeable lithium batteries. *J. Asian Ceram. Soc.* **1,** 17–25 (2013).

43. Xu, X., Wen, Z., Wu, X., Yang, X. & Gu, Z. Lithium Ion-Conducting Glass-Ceramics of Li1.5Al0.5Ge1.5(PO4)3-xLi2O (x=0.0-0.20) with Good Electrical and Electrochemical Properties. *J. Am. Ceram. Soc.* **90,** 2802–2806 (2007).

44. Guillon, O. *et al.* Field-assisted sintering technology/spark plasma sintering: Mechanisms, materials, and technology developments. *Adv. Eng. Mater.* **16,** 830–849 (2014).

45. Kali, R. & Mukhopadhyay, A. Spark plasma sintered/synthesized dense and nanostructured materials for solid-state Li-ion batteries: Overview and perspective. *J. Power Sources* **247,** 920–931 (2014).

46. Xu, X., Wen, Z., Yang, X. & Chen, L. Dense nanostructured solid electrolyte

with high Li-ion conductivity by spark plasma sintering technique. *Mater. Res. Bull.* **43,** 2334–2341 (2008).

47. Hong, H. .-P. Crystal structure and ionic conductivity of Li14Zn(GeO4)4 and other new Li+ superionic conductors. *Mater. Res. Bull.* **13,** 117–124 (1978).

48. Alpen, U., Bell, M., Wichelhaus, W., Cheung, K. & Dudley, G. Ionic-Conductivity of Li14Zn(GeO4)4 (LISICON). *Electrochim. Acta* **23,** 1395–1397 (1978).

49. Thangadurai, V. & Weppner, W. Recent progress in solid oxide and lithium ion conducting electrolytes research. *Ionics (Kiel).* **12,** 81–92 (2006).

50. Bohnke, O. The fast lithium-ion conducting oxides Li3xLa2/3 - xTiO3 from fundamentals to application. *Solid State Ionics* **179,** 9–15 (2008).

51. Gao, X. *et al.* Lithium atom and A-site vacancy distributions in lanthanum lithium titanate. *Chem. Mater.* **25,** 1607–1614 (2013).

52. Shimakawa, Y. & Mizumaki, M. Multiple magnetic interactions in A-site-ordered perovskite-structure oxides. *J. Phys. Condens. Matter* **26,** 473203 (2014).

53. Mei, A. *et al.* Role of amorphous boundary layer in enhancing ionic conductivity of lithium-lanthanum-titanate electrolyte. *Electrochim. Acta* **55,** 2958–2963 (2010).

54. Chen, K., Huang, M., Shen, Y., Lin, Y. & Nan, C. W. Enhancing ionic conductivity of Li0.35La0.55TiO3 ceramics by introducing Li7La3Zr2O12. *Electrochim. Acta* **80,** 133–139 (2012).

55. Morata-Orrantia, A., Garcıa-Martin, S. & Alario-Franco, M. A. Optimization of Lithium Conductivity in La / Li Titanates. *Chem. Mater.* **15,** 3991–3995 (2003).

56. Teranishi, T., Yamamoto, M., Hayashi, H. & Kishimoto, A. Lithium ion conductivity of Nd-doped (Li, La)TiO3 ceramics. *Solid State Ionics* **243,** 18–21 (2013).

57. Aguesse, F., López del Amo, J. M., Roddatis, V., Aguadero, A. & Kilner, J. A. Enhancement of the Grain Boundary Conductivity in Ceramic Li 0.34 La 0.55 TiO 3 Electrolytes in a Moisture-free Processing Environment. *Adv. Mater. Interfaces* **1,** 1–9 (2014).

58. Inada, R., Kimura, K., Kusakabe, K., Tojo, T. & Sakurai, Y. Synthesis and lithium-ion conductivity for perovskite-type Li 3/8Sr7/16Ta3/4Zr1/4O3 solid electrolyte by powder-bed sintering. *Solid State Ionics* **261,** 95–99 (2014).

59. Thangadurai, V., Kaack, H. & Weppner, W. J. F. Novel Fast Lithium Ion Conduction in Garnet-Type Li5La3M2O12 (M: Nb, Ta). *ChemInform* **34,** 437–440 (2003).

60. Li, Y., Han, J.-T., Wang, C.-A., Xie, H. & Goodenough, J. B. Optimizing Li+ conductivity in a garnet framework. *J. Mater. Chem.* **22,** 15357 (2012).

61. Thangadurai, V., Narayanan, S. & Pinzaru, D. Garnet-type solid-state fast Li ion conductors for Li batteries: critical review. *Chem. Soc. Rev.* **43,** 4714–27 (2014).

62. Murugan, R., Thangadurai, V. & Weppner, W. Fast lithium ion conduction in garnet-type Li(7)La(3)Zr(2)O(12). *Angew. Chem. Int. Ed. Engl.* **46,** 7778–7781 (2007).

63. Awaka, J., Kijima, N., Hayakawa, H. & Akimoto, J. Synthesis and structure analysis of tetragonal Li7La3Zr2O12 with the garnet-related type structure. *J. Solid State Chem.* **182,** 2046–2052 (2009).

64. Geiger, C. A. *et al.* Crystal chemistry and stability of 'Li 7La 3Zr 2O 12' garnet: A fast lithium-ion conductor. *Inorg. Chem.* **50,** 1089–1097 (2011).

65. Düvel, A., Kuhn, A., Robben, L., Wilkening, M. & Heitjans, P. Mechanosynthesis of Solid Electrolytes: Preparation, Characterization, and Li Ion Transport Properties of Garnet-type Al-doped Li7La3Zr2O12 Crystallizing with Cubic Symmetry. *J. Phys. Chem. C* **116,** 15192–15202 (2012).

66. Allen, J. L., Wolfenstine, J., Rangasamy, E. & Sakamoto, J. Effect of substitution (Ta, Al, Ga) on the conductivity of Li 7La 3Zr 2O 12. *J. Power Sources* **206,** 315–319 (2012).

67. Dumon, A., Huang, M., Shen, Y. & Nan, C.-W. High Li ion conductivity in strontium doped Li7La3Zr2O12 garnet. *Solid State Ionics* **243,** 36–41 (2013).

68. Kanno, R. & Murayama, M. Lithium Ionic Conductor Thio-LISICON: The Li2S-GeS2-P2S5 System. *J. Electrochem. Soc.* **148,** A742 (2001).

69. Kamaya, N. *et al.* A lithium superionic conductor. *Nat. Mater.* **10,** 682–686 (2011).

70. Seino, Y., Ota, T., Takada, K., Hayashi, A. & Tatsumisago, M. A sulphide lithium super ion conductor is superior to liquid ion conductors for use in rechargeable batteries. *Energy Environ. Sci.* **7,** 627–631 (2014).

71. Kato, Y. *et al.* High-power all-solid-state batteries using sulfide superionic conductors. *Nat. Energy* **1,** 16030 (2016).

72. Sakuda, A., Hayashi, A. & Tatsumisago, M. Sulfide solid electrolyte with favorable mechanical property for all-solid-state lithium battery. *Sci. Rep.* **3,** 2261 (2013).

73. Knauth, P. Inorganic solid Li ion conductors: An overview. *Solid State Ionics* **180,** 911–916 (2009).

74. Wright, P. V. Electrical conductivity in ionic complexes of poly(ethylene oxide). *Br. Polym. J.* **7,** 319–327 (1975).

75. Dias, F. B., Plomp, L. & Veldhuis, J. B. J. Trends in polymer electrolytes for secondary lithium batteries. *J. Power Sources* **88,** 169–191 (2000).

76. Christie, A. M., Lilley, S. J., Staunton, E., Andreev, Y. G. & Bruce, P. G. Increasing the conductivity of crystalline polymer electrolytes. *Nature* **433,** 50–53 (2005).

77. Gadjourova, Z., Andreev, Y. G., Tunstall, D. P. & Bruce, P. G. Ionic conductivity in crystalline polymer electrolytes. *Nature* **412,** 520–523 (2001).

78. Stoeva, Z., Martin-Litas, I., Staunton, E., Andreev, Y. G. & Bruce, P. G. Ionic

Conductivity in the Crystalline Polymer Electrolytes PEO6:LiXF6, X= P, As, Sb. *J. Am. Chem. Soc.* **125,** 4619–4626 (2003).

79. Fergus, J. W. Ceramic and polymeric solid electrolytes for lithium-ion batteries. *J. Power Sources* **195,** 4554–4569 (2010).

80. Zhang, C., Staunton, E., Andreev, Y. G. & Bruce, P. G. Doping crystalline polymer electrolytes with glymes. *J. Mater. Chem.* **17,** 3222 (2007).

81. Chuhong, Z., Staunton, E., Andreev, Y. G. & Bruce, P. G. Raising the Conductivity of Crystalline Polymer Electrolytes by Aliovalent Doping. *J. Am. Chem. Soc.* **127,** 18305–18308 (2005).

82. Johan, M. R., Shy, O. H., Ibrahim, S., Mohd Yassin, S. M. & Hui, T. Y. Effects of Al2O3 nanofiller and EC plasticizer on the ionic conductivity enhancement of solid PEO–LiCF3SO3 solid polymer electrolyte. *Solid State Ionics* **196,** 41–47 (2011).

83. Tarascon, J.-M., Gozdz, A. S., Schmutz, C., Shokoohi, F. & Warren, P. C. Performance of Bellcore's plastic rechargeable Li-ion batteries. *Solid State Ionics* **86–88,** 49–54 (1996).

84. Chen, Z., Zhang, L. Z., West, R. & Amine, K. Gel electrolyte for lithium-ion batteries. *Electrochim. Acta* **53,** 3262–3266 (2008).

85. Wang, Y., Li, B., Ji, J., Eyler, A. & Zhong, W. H. A gum-like electrolyte: Safety of a solid, performance of a liquid. *Adv. Energy Mater.* **3,** 1557–1562 (2013).

86. Li, H. *et al.* Gel polymer electrolytes based on active PVDF separator for lithium ion battery. I: Preparation and property of PVDF/poly(dimethylsiloxane) blending membrane. *J. Memb. Sci.* **379,** 397–402 (2011).

87. Sharma, J. P. & Sekhon, S. S. Nanodispersed polymer gel electrolytes: Conductivity modification with the addition of PMMA and fumed silica. *Solid State Ionics* **178,** 439–445 (2007).

88. Park, M. S., Hyun, S. H., Nam, S. C. & Cho, S. B. Performance evaluation of printed LiCoO2 cathodes with PVDF-HFP gel electrolyte for lithium ion microbatteries. *Electrochim. Acta* **53,** 5523–5527 (2008).

89. Zhang, Y. *et al.* A gel single ion polymer electrolyte membrane for lithium-ion batteries with wide-temperature range operability. *RSC Adv.* **4,** 21163 (2014).

90. Huang, L.-Y., Shih, Y.-C., Wang, S.-H., Kuo, P.-L. & Teng, H. Gel electrolytes based on an ether-abundant polymeric framework for high-rate and long-cycle-life lithium ion batteries. *J. Mater. Chem. A* **2,** 10492 (2014).

91. Weston, J. & Steele, B. No Title. *Solid State Ionics* **7,** 75–79 (1982).

92. Shim, J., Kim, D.-G., Kim, H. J., Lee, J. H. & Lee, J.-C. Polymer Composite Electrolytes Having Core–Shell Silica Fillers with Anion-Trapping Boron Moiety in the Shell Layer for All-Solid-State Lithium-Ion Batteries. *ACS Appl. Mater. Interfaces* **7,** 7690–7701 (2015).

93. Choi, J.-H., Lee, C.-H., Yu, J.-H., Doh, C.-H. & Lee, S.-M. Enhancement of ionic conductivity of composite membranes for all-solid-state lithium

rechargeable batteries incorporating tetragonal Li7La3Zr2O12 into a polyethylene oxide matrix. *J. Power Sources* **274,** 458–463 (2015).

94. Fu, K. (Kelvin) *et al.* Flexible, solid-state, ion-conducting membrane with 3D garnet nanofiber networks for lithium batteries. *Proc. Natl. Acad. Sci.* **113,** 7094–7099 (2016).

95. Liu, W. *et al.* Enhancing ionic conductivity in composite polymer electrolytes with well-aligned ceramic nanowires. *Nat. Energy* **2,** 17035 (2017).

96. Zhai, H. *et al.* A Flexible Solid Composite Electrolyte with Vertically Aligned and Connected Ion-Conducting Nanoparticles for Lithium Batteries. *Nano Lett.* **17,** 3182–3187 (2017).

97. Aetukuri, N. B. *et al.* Flexible Ion-Conducting Composite Membranes for Lithium Batteries. *Adv. Energy Mater.* **5,** 1–6 (2015).

98. Wenzel, S., Leichtweiss, T., Krueger, D., Sann, J. & Janek, J. Interphase formation on lithium solid electrolytes — An in situ approach to study interfacial reactions by photoelectron spectroscopy. *Solid State Ionics* **278,** 98–105 (2015).

99. Schwöbel, A., Hausbrand, R. & Jaegermann, W. Interface reactions between LiPON and lithium studied by in-situ X-ray photoemission. *Solid State Ionics* **273,** 51–54 (2015).

100. Wenzel, S. *et al.* Interphase formation and degradation of charge transfer kinetics between a lithium metal anode and highly crystalline Li7P3S11 solid electrolyte. *Solid State Ionics* **286,** 24–33 (2016).

101. Wenzel, S. *et al.* Direct Observation of the Interfacial Instability of the Fast Ionic Conductor Li10GeP2S12 at the Lithium Metal Anode. *Chem. Mater.* **28,** 2400–2407 (2016).

102. Wenzel, S., Sedlmaier, S. J., Dietrich, C., Zeier, W. G. & Janek, J. Interfacial reactivity and interphase growth of argyrodite solid electrolytes at lithium metal electrodes. *Solid State Ionics* **318,** 102–112 (2018).

103. Zhu, Y., He, X. & Mo, Y. First Principles Study on Electrochemical and Chemical Stability of the Solid Electrolyte-Electrode Interfaces in All-Solid-State Li-ion Batteries. *J. Mater. Chem. A* **4,** 1–14 (2015).

104. Richards, W. D., Miara, L. J., Wang, Y., Kim, J. C. & Ceder, G. Interface Stability in Solid-State Batteries. *Chem. Mater.* **28,** 266–273 (2016).

105. Cheng, L. *et al.* The origin of high electrolyte-electrode interfacial resistances in lithium cells containing garnet type solid electrolytes. *Phys. Chem. Chem. Phys.* **16,** 18294–18300 (2014).

106. Sharafi, A. *et al.* Surface Chemistry Mechanism of Ultra-Low Interfacial Resistance in the Solid-State Electrolyte Li7La3Zr2O12. *Chem. Mater.* **29,** 7961–7968 (2017).

107. Fu, K. K. *et al.* Toward garnet electrolyte–based Li metal batteries: An ultrathin, highly effective, artificial solid-state electrolyte/metallic Li interface. *Sci. Adv.* **3,** e1601659 (2017).

108. Tsai, C. L. *et al.* Li7La3Zr2O12 Interface Modification for Li Dendrite Prevention. *ACS Appl. Mater. Interfaces* **8,** 10617–10626 (2016).

109. Luo, W. *et al.* Reducing Interfacial Resistance between Garnet-Structured Solid-State Electrolyte and Li-Metal Anode by a Germanium Layer. *Adv. Mater.* **29,** 1606042 (2017).

110. Kato, A., Hayashi, A. & Tatsumisago, M. Enhancing utilization of lithium metal electrodes in all-solid-state batteries by interface modification with gold thin films. *J. Power Sources* **309,** 27–32 (2016).

111. Wu, B. *et al.* The role of the solid electrolyte interphase layer in preventing Li dendrite growth in solid-state batteries. *Energy Environ. Sci.* **11,** 1803–1810 (2018).

112. Samsonov, G. V. *Handbook of the Physicochemical Properties of the Elements*. (Springer US, 2012).

113. Monroe, C. & Newman, J. The Impact of Elastic Deformation on Deposition Kinetics at Lithium/Polymer Interfaces. *J. Electrochem. Soc.* **152,** A396 (2005).

114. Nagao, M. *et al.* In situ SEM study of a lithium deposition and dissolution mechanism in a bulk-type solid-state cell with a Li2S–P2S5 solid electrolyte. *Phys. Chem. Chem. Phys.* **15,** 18600 (2013).

115. Sudo, R. *et al.* Interface behavior between garnet-type lithium-conducting solid electrolyte and lithium metal. *Solid State Ionics* **262,** 151–154 (2014).

116. Porz, L. *et al.* Mechanism of Lithium Metal Penetration through Inorganic Solid Electrolytes. *Adv. Energy Mater.* **1701003,** 1–12 (2017).

117. Yu, S. *et al.* Elastic Properties of the Solid Electrolyte Li7La3Zr2O12 (LLZO). *Chem. Mater.* **28,** 197–206 (2016).

118. Cheng, E. J., Sharafi, A. & Sakamoto, J. Intergranular Li metal propagation through polycrystalline Li6.25Al0.25La3Zr2O12 ceramic electrolyte. *Electrochim. Acta* **223,** 85–91 (2017).

119. Lang, C. *et al.* Progress in analysing lithium ion battery materials in the SEM. in *European Microscopy Congress 2016: Proceedings* 872–873 (Wiley-VCH Verlag GmbH & Co. KGaA, 2016).

120. Shen, F., Dixit, M. B., Xiao, X. & Hatzell, K. B. Effect of Pore Connectivity on Li Dendrite Propagation within LLZO Electrolytes Observed with Synchrotron X-ray Tomography. *ACS Energy Lett.* **3,** 1056–1061 (2018).

121. Ni, J. E., Case, E. D., Sakamoto, J. S., Rangasamy, E. & Wolfenstine, J. B. Room temperature elastic moduli and Vickers hardness of hot-pressed LLZO cubic garnet. *J. Mater. Sci.* **47,** 7978–7985 (2012).

122. Kim, Y. *et al.* The Effect of Relative Density on the Mechanical Properties of Hot-Pressed Cubic Li7La3Zr2O12. *J. Am. Ceram. Soc.* **99,** 1367–1374 (2016).

123. Cho, Y.-H. *et al.* Mechanical properties of the solid Li-ion conducting electrolyte: Li0.33La0.57TiO3. *J. Mater. Sci.* **47,** 5970–5977 (2012).

124. Jackman, S. D. & Cutler, R. A. Effect of microcracking on ionic conductivity in

LATP. *J. Power Sources* **218,** 65–72 (2012).

125. Sakuda, A., Hayashi, A., Takigawa, Y., Higashi, K. & Tatsumisago, M. Evaluation of elastic modulus of Li2S-P2S5 glassy solid electrolyte by ultrasonic sound velocity measurement and compression test. *J. Ceram. Soc. Japan* **121,** 946–949 (2013).

126. Ren, Y., Shen, Y., Lin, Y. & Nan, C.-W. Direct observation of lithium dendrites inside garnet-type lithium-ion solid electrolyte. *Electrochem. commun.* **57,** 27–30 (2015).

127. Wolfenstine, J., Allen, J. L., Sakamoto, J., Siegel, D. J. & Choe, H. Mechanical behavior of Li-ion-conducting crystalline oxide-based solid electrolytes: a brief review. *Ionics (Kiel).* **24,** 1271–1276 (2018).

Chapter 2: Experimental Techniques

2.1. Synthesis Techniques

2.1.1. 3D Printing

3D printing is an additive manufacturing technique used to create any 3D object of choice with feature sizes from a few millimetres down to the sub-micron range. A computer-aided design (CAD) model of a 3D object is generated and reproduced layer-by-layer in 3D space.[1] The 3D printing performed in this work is based on a stereolithography technology, namely two-photon absorption direct laser writing (DLW) (Figure 2.1).[2]

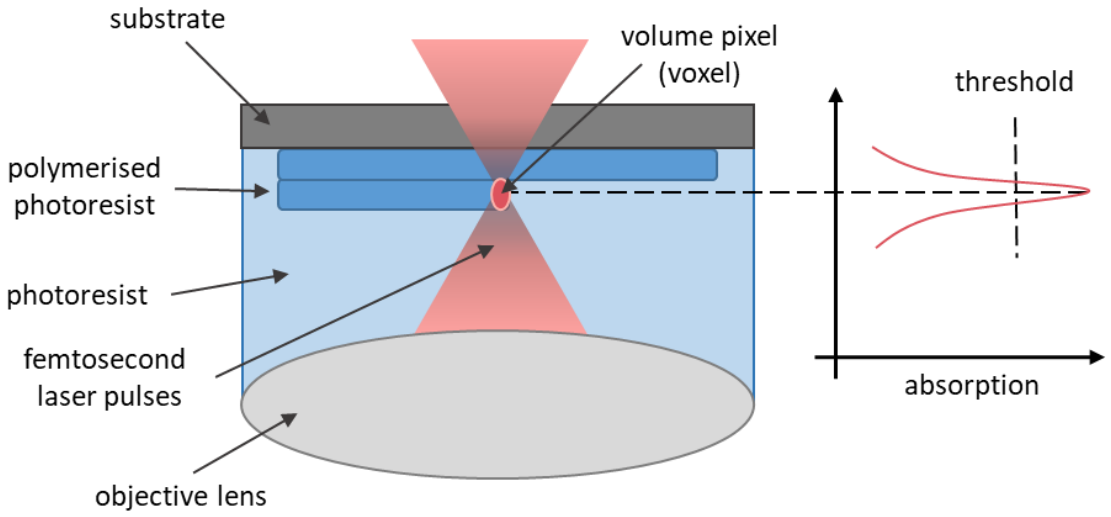


Figure 2.1. Principle of two-photon absorption laser lithography in a 'Dip-in laser lithography' (DiLL) writing configuration (adapted from Nanoscribe, 2014 [3]).

DLW uses a multi-photon photopolymerisation process to solidify matter within a liquid medium. A near-infrared laser with femtosecond laser pulses is focused onto an ultraviolet (UV)-curable photoresist. The intensity generated by the laser focus within a confined volume pixel (voxel) of ellipsoidal shape is high enough to trigger the

probability of non-linear optical absorption processes such as two-photon photopolymerisation to take place. Controlling the path of the laser beam allows for polymerisation to occur at any desired location within the photoresist with a voxel size and ultimate feature size resolution down to the nanometer range.[3]

2.1.2. Sol-Gel Synthesis

Sol-gel synthesis, also called the Pechini method,[4] is a technique used to synthesise multicomponent powders of transition metal oxides from their respective metal salts, a polyhydroxy alcohol (ethylene glycol) and a chelating agent (citric acid). The Pechini method enables the synthesis of high purity and homogenous compositions at low-cost and low temperatures. Metal salts are dissolved in an aqueous solution and gently heated at 80 °C. While the citric acid chelates the metal ions and distributes them homogeneously across the solution, the ethylene glycol polymerises with the metal citrates to form chains of polyesters as shown in Figure 2.2.

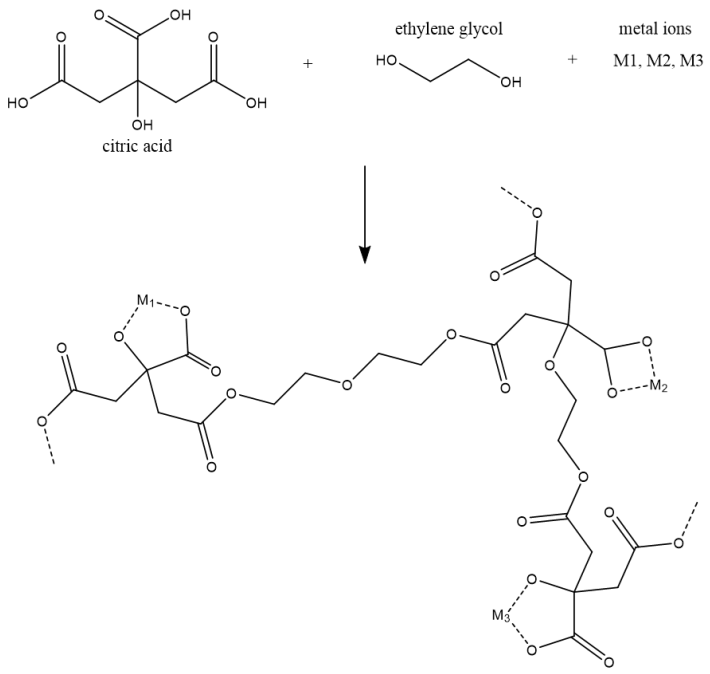


Figure 2.2. Reaction mechanism occurring during a Pechini synthesis (adapted from Sakka, 2005 [4]).

The ratio between the citric acid and the metal ions is vital and affects the even distribution and recombination of metal ions in the aqueous solution. The polymerisation thickens the mixture from an aqueous salt solution to a more viscous gel with time, hence the origin of the name 'sol-gel' synthesis.

2.2. Characterisation Techniques

2.2.1. Powder X-ray Diffraction

Powder x-ray diffraction (PXRD) is a technique used to identify the atomic arrangement such as the crystal structure and the unit cell parameters of a crystalline material. Crystalline secondary phases within a polycrystalline material can also be detected. The interaction of x-rays with the crystalline phase generates a diffraction pattern, which is unique to the material investigated. This exclusive fingerprint gives information on the purity of the material, its degree of crystallinity as well as its grain size.[5]

Solid matter is either present in an amorphous or crystalline state. In the amorphous state, atoms are arranged in a random and disordered manner, similar to a liquid. The atomic arrangement changes constantly and no defined diffraction pattern can be generated. In a crystalline material, atoms are organised in a regular order within the crystal lattice with specific distances apart from each other. The distance between atoms in a crystal lattice are in the range of a few ångströms (10^{-10} m), which corresponds to the wavelength range of x-rays. Hence, x-rays can give information on the arrangement of atoms in a crystal structure.[6]

X-ray light is an electromagnetic wave that is easily scattered in an atom by accelerated electrons. When an x-ray beam with a specific incoming wavelength hits an atom, the atom can scatter the beam at the same wavelength in all directions without the beam

losing any energy. This is called coherent scattering or Thomson scattering.[7] Scattered x-rays from different atoms in the crystal structure interfere with each other either in-phase (constructive interference), where they reinforce each other and show an intense signal or out-of-phase (destructive interference) where their energies cancel each other out and do not show any signal in the diffraction pattern. Bragg's law states that constructive interference can only occur if:

$$n\lambda = 2d_{hkl}\sin(\theta) \tag{2.1}$$

where n is an integer, λ is the wavelength of the incoming x-ray, d_{hkl} is the 'd-spacing' or the distance between two adjacent parallel (hkl) planes in the atomic lattice and θ is the angle of the incoming x-rays. Bragg's law considers that ordered layers of atoms are like reflected planes with a specific distance d_{hkl} between them. Its derivation is best represented by Figure 2.3.

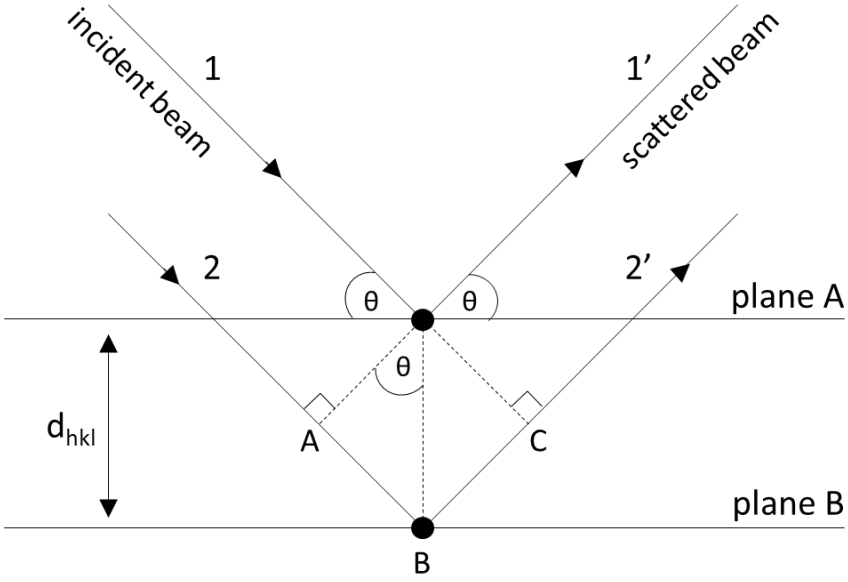


Figure 2.3. Schematic representation of Bragg's law (adapted from West, 2014 [5]).

Only specific angles of incoming x-ray radiation satisfy Bragg's law and will lead to constructive interferences and a peak in the diffraction pattern. Each peak at a specific

angle θ corresponds to a set of parallel planes of atoms in the crystal lattice. Using Bragg's law and the position of the peak in the diffraction pattern, the distance between parallel planes in the crystal structure can be determined, which ultimately gives information on the properties of the unit cell of the material's crystal structure. The intensity of the peak depends on the overall atoms present in the material. The higher the atomic number, the more electrons are present, the better and more intense is the scattering of x-rays. The ability to scatter x-rays is described by the atomic scattering factor f_j and is proportional to the atomic number Z. Materials containing atoms with high atomic number Z will diffract better than ones containing lighter elements. The intensity of a diffracted wave I_{hkl} from a specific (hkl) plane in the lattice is proportional to the square of the structure factor F_{hkl}, which is the sum of the contributions of each atom in the (hkl) plane to the intensity, described by following equation:

$$I_{hkl} \propto |F_{hkl}|^2 \tag{2.2}$$

$$F_{hkl} = \sum_{j=1}^{j=n} f_j \cos 2\pi\left(hx_j + ky_j + lz_j\right) + i \sum_{j=1}^{j=n} f_j \sin 2\pi(hx_j + ky_j + lz_j) \tag{2.3}$$

where, x_j, y_j and z_j are the coordinates of the location of atom j in the unit cell and f_j is the atomic scattering factor of atom j.[5]

A powder x-ray diffractometer is mainly composed of an x-ray source, a sample stage and a detector. An x-ray beam is produced by generating electrons from a tungsten filament, which strike an anode target, and release x-rays with a characteristic wavelength. These x-rays exit the x-ray source by transparent beryllium windows. Monochromators and divergence slits are used to ensure that x-rays of only one specific wavelength and angle exit the source. Additional focussing mirrors and lenses are used to control the x-ray path all the way to the sample holder. From a diffraction measurement, a diffraction pattern of angle 2θ as a function of absolute intensity is

obtained. Each crystalline component in the material shows its own set of diffraction peaks and contributes to the overall diffraction pattern of the material investigated.

2.2.2. Scanning Electron Microscopy

SEM is a microscopy technique used to analyse and image the surface of a specimen at very high magnification down to the nanometre scale. In this work, SEM was used to analyse the microstructure of different solid electrolytes as well as the cross-section of symmetrical Li cells.

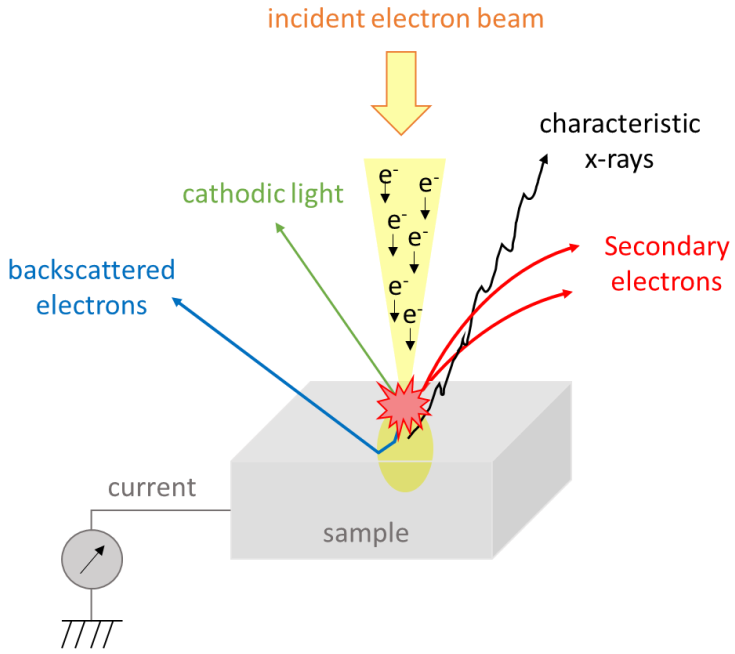


Figure 2.4. SEM signals produced from the sample by the incident electron beam (adapted from Hitachi High-Tech, 2008 [8]).

Electrons are generated from an electron gun and converged into a fine beam by a condenser lens in a column under vacuum (10^{-4}-10^{-6} Pa). Deflection coils control the electron beam in x- and y-direction and scan the surface of the specimen at a specific magnification. The incident electron beam is additionally focused by an objective lens before entering the specimen chamber. Upon contact of the electron beam with the

specimen, several signals are released from the specimen's surface: secondary electrons (SE), backscattering electrons (BSE) and characteristic x-rays (Figure 2.4). Respective detectors capture these signals and convert these into an image.

When an incident electron strikes an atom in the specimen, the electron is either scattered back into vacuum as BSE (reflected back with nearly no loss in energy) or loses some of its initial energy and releases a SE, x-rays and light (cathode luminescence) into vacuum. BSE are the electrons generated from striking the respective atoms present in the specimen. The amount of reflected BSE depends on the composition of the specimen. The higher the mean atomic number or density of the specimen, the larger the count of BSE. Hence, BSE give information on the compositional distribution of the specimen's surface. SE are generated close to the surface of the specimen. The incident electron strikes the specimen and can transfer some of its energy to a free electron, which then has sufficient energy to escape out into vacuum as a SE. In comparison to BSE, SE only have a minimal amount of energy and can only escape if in proximity to the surface. Hence, SE give information on the topographical structure of the specimen.

It is important that the specimen of choice is conductive to avoid an unbalanced charge of the incoming and outgoing electrons during imaging. This can cause a so-called 'charge-up' phenomenon, which is observed by a distorted or an uneven bright electron image.[8] This typical phenomenon can be avoided by reducing the accelerating voltage, the irradiating current or coating the specimen with a conductive metal. A high-quality vacuum within the instrument and moisture-free specimen further avoid any contamination and improve the irradiation process of the specimen. Beam damage can also occur if the specimen readily heats up and undergoes thermal or chemical changes when irradiated by the electron beam. The precautions mentioned above can help to avoid damage of the sample upon prolonged beam exposure.

2.2.3. Electron Dispersive X-ray Spectroscopy

EDX is performed in conjunction with SEM. An x-ray detector captures emitted x-rays when a finely converged electron beam is focused onto a specimen of choice in a vacuum chamber. An incident electron strikes an electron within the specimen's atomic orbital. While the incoming electron is inelastically scattered back into vacuum, the electron within the orbital gains some energy and is ejected out of the orbital. This results in a vacant shell, which is immediately refilled by an electron from an outer shell to account for the charge loss within the atom. The transition from a full to a partially vacant shell generates x-rays that are characteristic to the element present in the specimen. Figure 2.5 illustrates this process. The energy difference between the two orbitals is unique and is precisely associated to the elemental composition of the specimen.

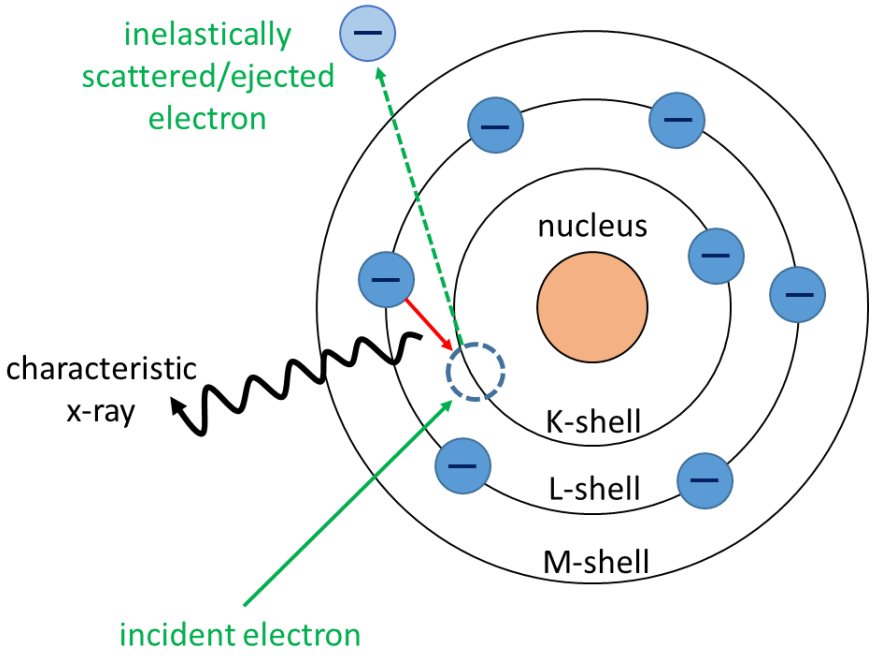


Figure 2.5. Principles of EDX (adapted from Hitachi High-Tech, 2008 [8]).

2.2.4. X-ray Photoelectron Spectroscopy

X-ray photoelectron spectroscopy (XPS) is a surface analysis technique used to quantitatively measure the elemental composition of the initial first 10 nm of the surface of any given material. The technique is based on the photoelectric effect.[9] An x-ray beam is used to irradiate the top first atomic layers of the material's surface. Depending on the energy of the x-ray beam, enough energy can be absorbed by a core electron for it to be ejected as photoelectron from the atomic vacuum. The amount of ejected photoelectrons and their respective kinetic energies are then measured by an energy analyser (Figure 2.6).

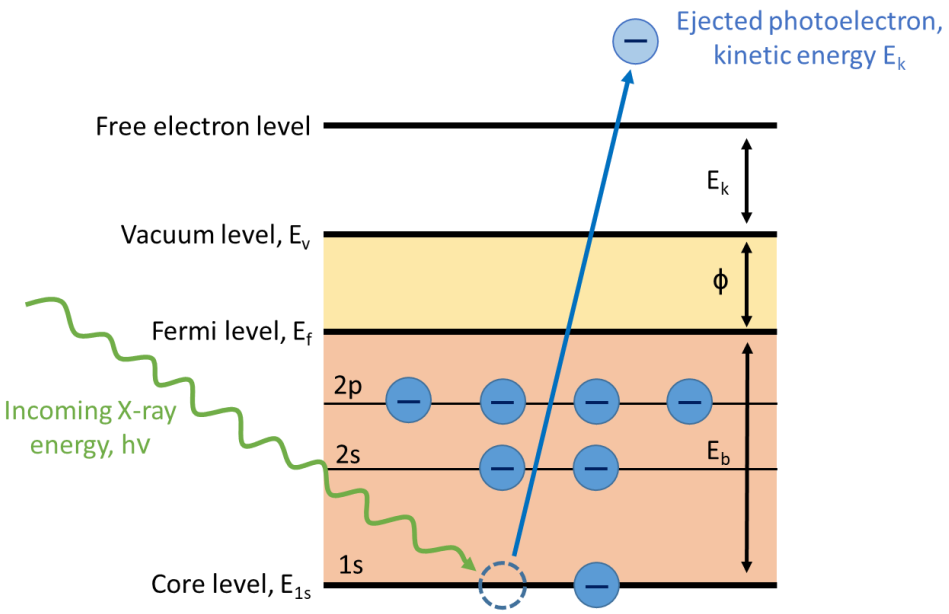


Figure 2.6. Principles of XPS (inspired by Yaghoubi, 2015 [10]).

The energy of the x-ray beam (E) can be calculated from its known wavelength (ν) by following relationship,

$$E = h\,\nu \tag{2.4}$$

where h is the Planck's constant. The binding energy (E_b) of the ejected photoelectron that is specific to a certain element is related to the x-ray photon energy and the measured kinetic energy (E_k) of the ejected photoelectron by:

$$E_b = h\nu - E_k - \phi \tag{2.5}$$

where ϕ is the work function, which is specific to the spectrometer.

2.2.5. X-ray Micro-computed Tomography

X-ray micro-computed tomography (micro-CT) is a non-destructive 3D imaging technique used to scan and visualise the interior features of a 3D material down to the micrometre range using an x-ray source. Initially, 2D x-ray images, also called radiograph projections, are recorded from 2D cross-sections of a 3D sample. These x-ray slices are then reconstructed together to recreate a 3D model or tomogram of the sample.[11]

A radiograph projection is generated by transmitting an x-ray beam through a sample rotating around its own axis at small angle increments. A scintillator transforms the transmitted beam on the other side of the sample into visible light, which is then projected as an image to a detector. The detector measures the decrease in x-ray intensity after the beam has traversed the sample. This x-ray attenuation is best described by Beer-Lambert's law:

$$I = I_0 e^{-\frac{\mu}{\rho}x} \tag{2.6}$$

which states that the transmitted x-ray intensity (I) of a monochromatic x-ray beam is proportional to the incident x-ray beam intensity (I_0) and scales exponentially with the mass thickness of the 3D sample (x), which is the mass per unit area obtained by multiplying the thickness of the sample with its density, the sample's density (ρ) and its

linear attenuation coefficient (μ), which depends on the photon energy of the incident x-ray beam and the atomic mass of the sample under investigation.[12]

The variation in x-ray attenuation is represented by different grey levels in the generated x-ray CT slices. The grey levels vary depending on the amount of x-rays scattered or absorbed by the sample, which in turn is controlled by the density and composition of the sample. By assembling all the CT slices with their characteristic grey levels together, a virtual 3D model of the sample can be reconstructed and enables the visualisation of microstructural features otherwise hidden within the sample.

2.2.6. Solid-State Nuclear Magnetic Resonance

Solid-state nuclear magnetic resonance (NMR) is a powerful and non-invasive technique used in battery research to analyse chemical changes occurring within battery materials, whether these are in electrodes, electrolyte materials or even full battery cells.

An atom is NMR active if its nucleus possesses a nuclear spin of $I \neq 0$ (has an odd number of protons and/or neutrons) that generates a nuclear magnetic moment in the presence of an external magnetic field, B_0. When B_0 is applied, the nuclear spins align with B_0 and form a local electromagnetic field that resonates at a specific frequency, also known as the Larmor frequency ω_0, in the radio frequency (RF) range.[13] This frequency is related to the difference in energy between the spin states (I = + ½ or - ½) and changes depending on the strength of B_0 by following relationship:

$$\omega_0 = -\gamma B_0 \tag{2.7}$$

where γ is the gyromagnetic ratio. Applying RF pulses perpendicular to B_0 adds perturbation to the nuclear spin's magnetic moment, generating a transverse magnetisation in the x-y plane, which, when passed through a detection coil produces a

certain voltage. The measured voltage decays with time and is also known as the 'free induction decay' (FID).[13] Applying a Fourier transform to the voltage-time signal produces the familiar NMR signal of intensity as a function of frequency. Figure 2.7 shows a schematic representation of the process.

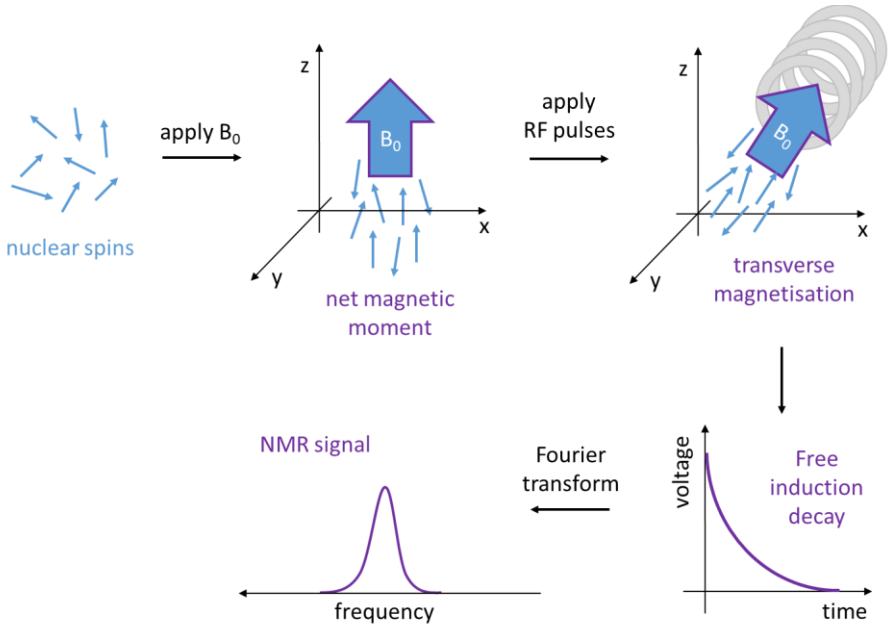


Figure 2.7. Principles of solid-state nuclear magnetic resonance (adapted from Pecher, 2016 [14]).

Every species that is in a different local chemical environment will interact differently with the magnetic field and hence will have its own NMR signal associated with it. The intensity of the signal depends on the abundance of that specific isotope or species under investigation, the number of chemical species in the sample, the temperature, the strength of B_0, etc.[14] The line shape and frequency at which the signal appears depend on the internal interactions of the atom with B_0.[14] Each different internal interaction induces a small magnetic field that alters the local magnetic field, which leads to a specific shift from the Larmor frequency. Internal interactions relevant to the solid-state NMR of battery materials include shift interactions (nuclear-electron spin) such as the chemical

shift, the Knight shift and the Fermi contact shift, dipolar coupling (nuclear-nuclear spin) and quadrupole coupling (quadrupole moment-electric field gradient).[14] While the chemical shift is caused by the interaction of valence electrons with the nucleus, the Knight shift[15] is a measure of the interaction of the conduction electrons with the nucleus, which significantly affects the NMR signals of metals and other conductive materials. For instance, the ^{7}Li NMR signal of Li metal is shifted to + 245 ppm compared to the ^{7}Li NMR of Li in the electrolyte of a cell.[16] The Fermi contact shift[17] that arises through the hyperfine coupling of unpaired electrons between neighbouring nuclear spins in paramagnetic compounds is another important interaction that drastically affects the NMR signal of battery materials. All of these interactions are anisotropic and will, depending on the sample orientation with respect to the magnetic field, cause further characteristic changes in lineshape such as chemical shift anisotropy (CSA) or Knight shift anisotropy (KSA), to name a few.[14] Magic-angle spinning NMR (MAS NMR), which is a technique that rotates the sample at an angle of 54.7º from the orientation of the external magnetic field, is one way to reduce the anisotropic internal interactions and sharpen the NMR signals of interest.[18] Furthermore, the presence of various components in a battery cell with different magnetic susceptibilities due to their metallic, paramagnetic, diamagnetic or insulating properties gives rise to additional bulk magnetic susceptibility (BMS) effects.[19,20] While these can again be mitigated by the specific alignment of the sample with respect to the magic angle and B_0, BMS effects can also give useful information on the different types of Li morphologies present in a cell, such as the differentiation between metallic ^{7}Li and dendritic ^{7}Li.[16] Hence, both the Knight shift and the BMS effects are valuable properties in the analysis of ^{7}Li NMR signals of battery materials as is summarised in Figure 2.8.

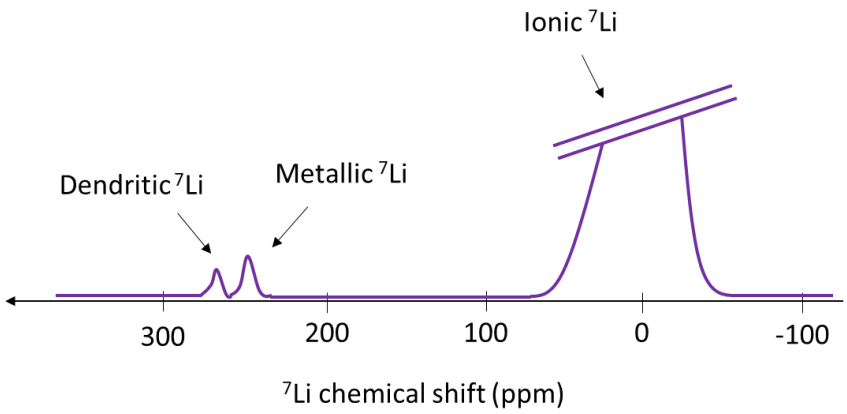


Figure 2.8. Schematic of a ^{7}Li NMR spectrum with the location of the three most typical chemical shift environments found for ^{7}Li in an all-solid-state lithium battery.

2.2.7. Magnetic Resonance ^{7}Li Chemical Shift Imaging

Magnetic resonance imaging (MRI) complements NMR spectroscopy by providing spatial information of the chemical species under investigation in all three dimensions. In this work, a specific type of MRI technique called magnetic resonance ^{7}Li chemical shift imaging (CSI) was employed, which correlates the chemical shift information from conventional NMR with an MRI image collected in either one, two or three dimensions.[21] Due to spectrometer time restraints, the results shown in this work only show MRI data collected in one dimension. Applying a magnetic field gradient (sequentially phase-encoded pulses) along a specific axis following initial RF excitation pulses, alters the resulting transverse magnetisation as a function of position. This gives rise to an MRI image with spatial information along the gradient axis and can be combined with the chemical shift information from ^{7}Li NMR to generate a ^{7}Li CSI image as illustrated in Figure 2.9 below.

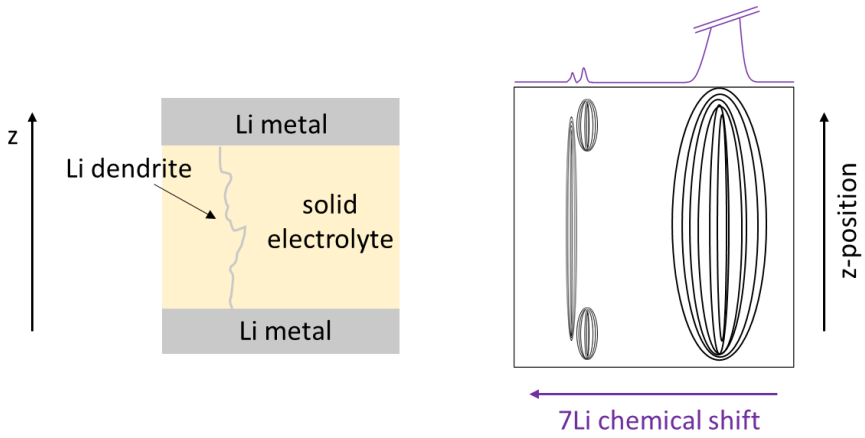


Figure 2.9. Schematic representation of a plausible ^{7}Li CSI image (right) of a solid electrolyte cell with symmetrical Li metal electrodes that has been short-circuited by a Li dendrite upon cycling (left).

2.3. Electrochemical Techniques

2.3.1. Alternating Current Electrochemical Impedance Spectroscopy

Alternating current (AC) electrochemical impedance spectroscopy (EIS) is a technique used to measure the resistance, capacitance and ultimately ionic conductivity of an ionically conductive material, such as a solid electrolyte.

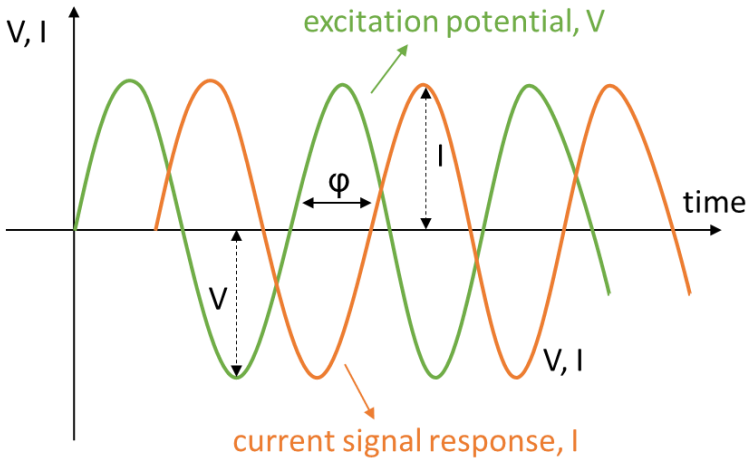


Figure 2.10. Sinusoidal excitation potential and corresponding current response in electrochemical impedance spectroscopy (adapted from Gamry, Application Note [22]).

The solid electrolyte is coated with non-ionically conductive blocking electrodes (Au, copper (Cu) or stainless-steel electrodes) on either side. An excitation AC potential is applied and passed through the electrochemical cell. This generates an AC current signal response with the same frequency as the excitation signal. Both excitation and response signals are sinusoidal and only differentiate by a phase shift (φ), as shown in Figure 2.10. Both signals can be described by following functions:[22]

$$V_t = V_0 \sin(\omega t) \tag{2.8}$$

$$I_t = I_0 \sin(\omega t + \varphi) \tag{2.9}$$

$$(\omega = 2\pi f)$$

where V_t and V_0 are the AC potentials at time t and time zero, I_t and I_0 are the AC currents at time t and time zero, ω is the angular frequency, f is the frequency in Hertz and t is the time. Both excitation and response signals are complex functions. Hence, using Ohm's law:

$$R = \frac{V}{I} \tag{2.10}$$

where R is the resistance, V is the voltage and I is the current, the impedance Z of a system can be derived as follow:

$$Z = \frac{V_t}{I_t} = \frac{V_0 \sin(\omega t)}{I_0 \sin(\omega t + \varphi)} = Z_0 \frac{\sin(\omega t)}{\sin(\omega t + \varphi)} \tag{2.11}$$

From Euler's relationship:

$$\exp(j\varphi) = \cos(\varphi) + \mathrm{j}\sin(\varphi) \tag{2.12}$$

$$(j = \sqrt{-1})$$

where j is an imaginary number, the impedance Z can also be represented as a complex number:

$$Z(\omega) = \frac{V}{I} = Z_0 exp(j\varphi) = Z_0(\cos(\varphi) + \mathrm{j}\sin(\varphi)) \qquad (2.13)$$

where cos(φ) is the real part and jsin(ω) is the imaginary part of the complex number. From both excitation and response signals, a Nyquist plot is generated, which represents the impedance Z of the system as a function of frequency, as derived from Equation 2.11 to Equation 2.13 (Figure 2.11).

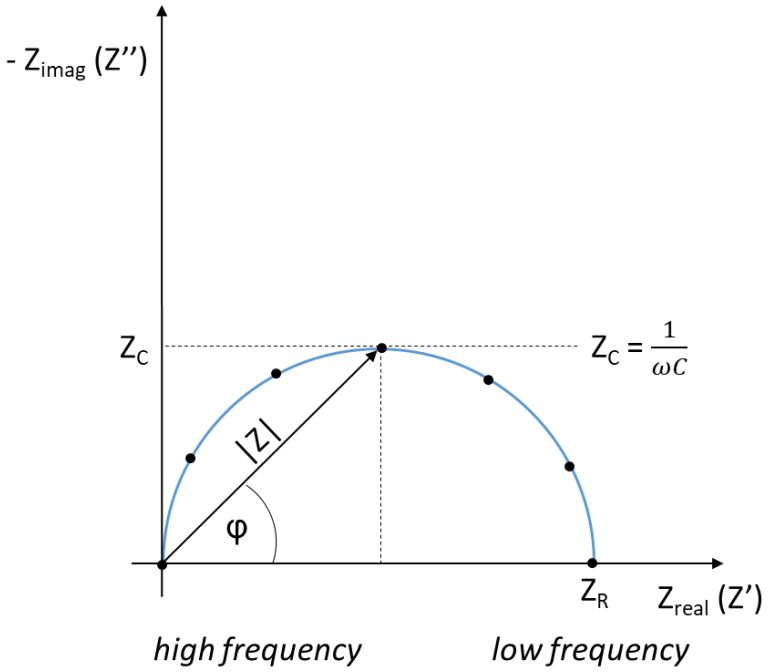
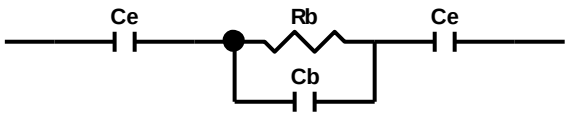


Figure 2.11.Nyquist plot showing a representation of the complex quantity Z (adapted from Gamry, Application Note [22]*).*

At each point of the characteristic semicircle of a Nyquist plot an impedance value at a specific frequency is generated. The impedance is represented either as a vector |Z| with a magnitude and phase angle (arg Z) or as a complex quantity where:

$$Z_{total} = Z_{real} + Z_{imag} \qquad (2.14)$$

When an AC potential is applied to a symmetrical cell with blocking electrodes, the non-ionically conductive electrodes alternate between being positively and negatively charged. The cations in the solid electrolyte migrate to the negative electrode and the solid electrolyte becomes polarised. The migration of ions in a bulk electrolyte is represented by a resistor R_b. The polarisation of the electrolyte and electrodes is represented by capacitors C_b and C_e, respectively. Overall, these processes can be illustrated by the following equivalent circuit:



A resistor (R) measures the resistance in a system in units of Ohms (Ω), whereas a capacitor (C) measures the capacitance or the charge stored in a system in units of Farad (F). The electrochemical impedance (Z) in units of Ωcm^2 is a measurement of the frequency dependent resistance in a system and correlates the voltage to the current density in a circuit. The resistance and capacitance relate to the impedance Z by following equations:

$$|Z| = R \tag{2.15}$$

$$|Z| = \frac{1}{Cj\omega} \tag{2.16}$$

As the resistor and capacitor of the bulk electrolyte are in parallel, the impedance for this part of the equivalent circuit can be written as:

$$\frac{1}{Z_b} = \frac{1}{Z_R} + \frac{1}{Z_C} = \frac{1}{R_b} + C_b j\omega \tag{2.17}$$

$$Z_b = \frac{1}{\left(\frac{1}{R_b}\right) + j\omega C_b} = R_b \left[\frac{1}{1+(\omega C_b R_b)^2}\right] - jR_b \left[\frac{\omega C_b R_b}{1+(\omega C_b R_b)^2}\right] \tag{2.18}$$

As the charge cannot cross the blocking electrodes, the resistance is infinite and both electrodes are represented as capacitors in the equivalent circuit. Combining Equation 2.18 with the capacitors of the electrodes in series gives following equation:

$$Z_{total} = Z_e + Z_b + Z_e \tag{2.19}$$

$$Z_{total} = \left[R_b \frac{1}{1+(\omega R_b C_b)^2}\right] - j\left\{\left[R_b \frac{\omega R_b C_b}{1+(\omega C_b R_b)^2}\right] + \frac{1}{\omega C_e}\right\} \tag{2.20}$$

Equation 2.20 can be extended to include other impedance contributions present in the solid electrolyte that contribute to the total impedance of the cell. The equation for the total impedance in the electrochemical cell is represented as a Nyquist plot as shown in Figure 2.12, where the negative imaginary part of the impedance is plotted against the real part of the impedance.

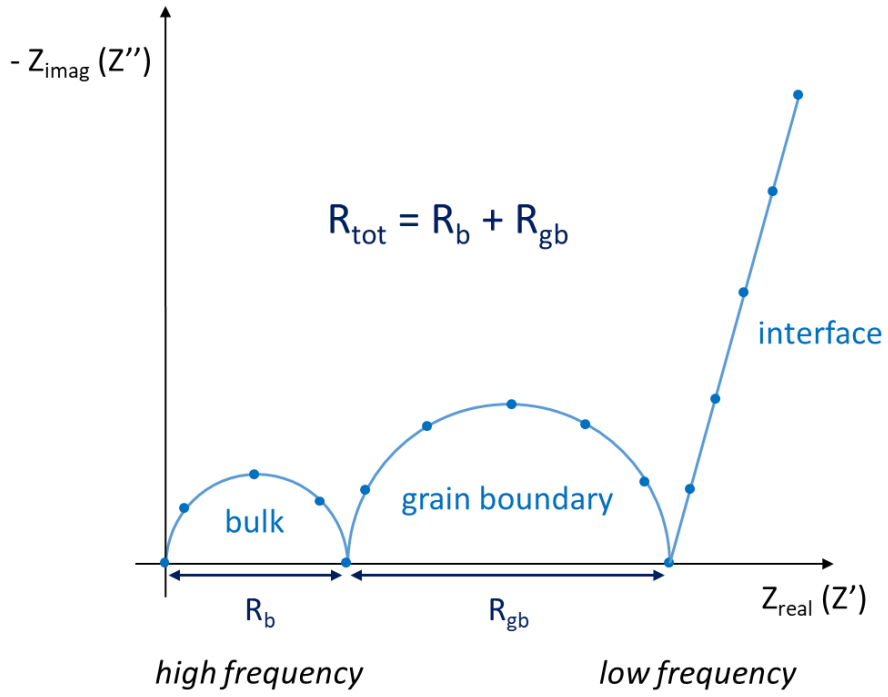


Figure 2.12. Expected Nyquist plot of a typical solid electrolyte with blocking electrodes.

The impedance of a ceramic solid electrolyte comprising of both grain and grain boundaries in their microstructure is represented by a combination of a semicircle for the

bulk and a semicircle for the grain boundary contributions at higher frequency, whereas the electrodes, being nearly identical in a symmetrical cell, combine into one distinct spike at lower frequency. The bulk resistance R_b, grain boundary resistance R_{gb} and total resistance of the solid electrolyte R_{tot} (in Ω) are all directly related to their respective ionic conductivity σ by:

$$\sigma = \frac{1}{R} \times \frac{l}{A} \ (in\ S\ cm^{-1}) \tag{2.21}$$

where l is the thickness of the electrolyte (in cm) and A is the electrode-electrolyte contact area (in cm^2). To compensate for any non-ideal behaviour of the electrochemical cell, usually visible in the Nyquist plot by a slightly suppressed semicircle, an equivalent circuit using a constant-phase element (CPE) is used instead of an ideal capacitor (C). The CPE introduces two parameters (α and Q) which account for any non-homogeneous behaviour and are incorporated into Equation 2.16 as follow:

$$Z_{CPE}(\omega) = \frac{1}{Q(j\omega)^{\alpha}} \tag{2.22}$$

From this, the effective capacitance[23] is calculated from:

$$C_{eff} = R^{\left(\frac{1-\alpha}{\alpha}\right)} Q^{\frac{1}{\alpha}} \tag{2.23}$$

where R is the resistance of the system.

The impedance of a solid electrolyte can also be measured between non-blocking electrodes such as Li metal. Compared to blocking electrodes that are only capacitors, non-blocking electrodes act as both capacitor and resistor. Hence, instead of a spike in the Nyquist plot, a semicircle at lower frequency is expected. For a crystalline solid electrolyte in a symmetrical cell with Li electrodes, a Nyquist plot as shown in Figure 2.13 is anticipated.

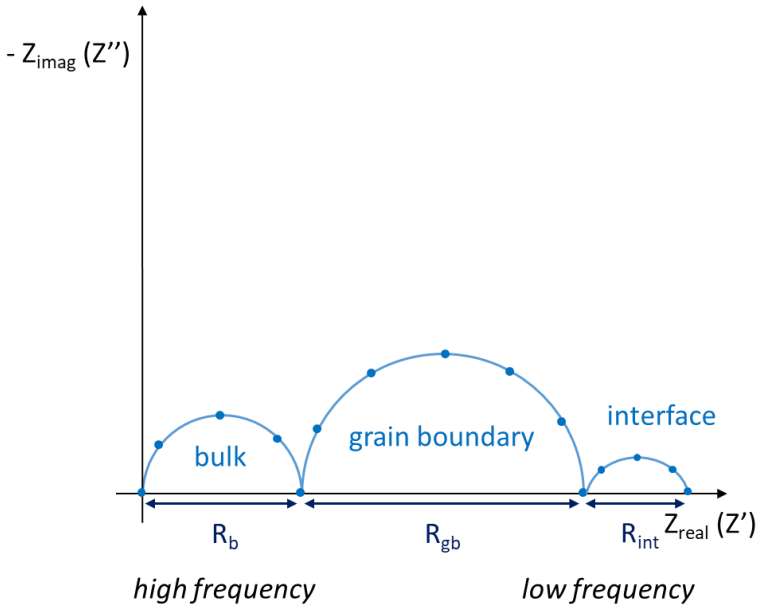
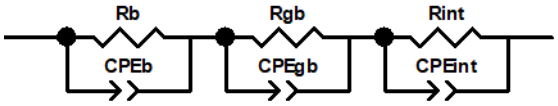


Figure 2.13. Expected Nyquist plot of a typical solid electrolyte with non-blocking electrodes.

Three semicircles corresponding to the bulk, the grain boundaries and the Li-solid electrolyte interface contributions are expected, which can be represented by following equivalent circuit:



2.3.2. Galvanostatic Cycling

Galvanostatic cycling is a typical technique used to test the performance and cycle life of battery cells. Battery cells are subjected to a series of continuous cycles of charge and discharge processes by applying a constant current and measuring the resulting cell voltage or cell potential. In this work, galvanostatic cycling was performed on symmetrical solid-state Li cells. The cells were charged and discharged at a fixed current density ($A \cdot cm^{-2}$) up to a specific capacity ($Ah \cdot cm^{-2}$) and the cell voltage over the time needed to reach that specific capacity was measured. The data is usually represented as a

plot of cell voltage as a function of capacity. EIS measurements after each charge and discharge can also be incorporated into the cycling sequence and give additional information on the effect of charge and discharge on the impedance of the solid electrolyte during cycling. The open circuit voltage (OCV) is measured for several minutes between charges and discharges as an additional cell relaxation step. Using Ohm's law,

$$V = R \times I \tag{2.24}$$

which relates the cell potential V (in Volts) to the cell current I (in Amperes, A) and cell resistance R (in Ohms, Ω), the resistance of the cell at any time during cycling can be calculated and compared to the resistance measured during EIS measurements before and after cycles.

2.4. Mechanical Testing Techniques

2.4.1. Compression testing

Compression testing is a mechanical testing technique used to measure the mechanical properties of a material, here solid electrolytes, when compressed between two parallel plates. A compressive load is applied at a constant rate and the compressive stress is measured as a function of displacement. A stress-strain curve is generated, which is unique for every material investigated. Figure 2.14 shows typical stress-strain curves for a metal, a ceramic and a polymeric material.

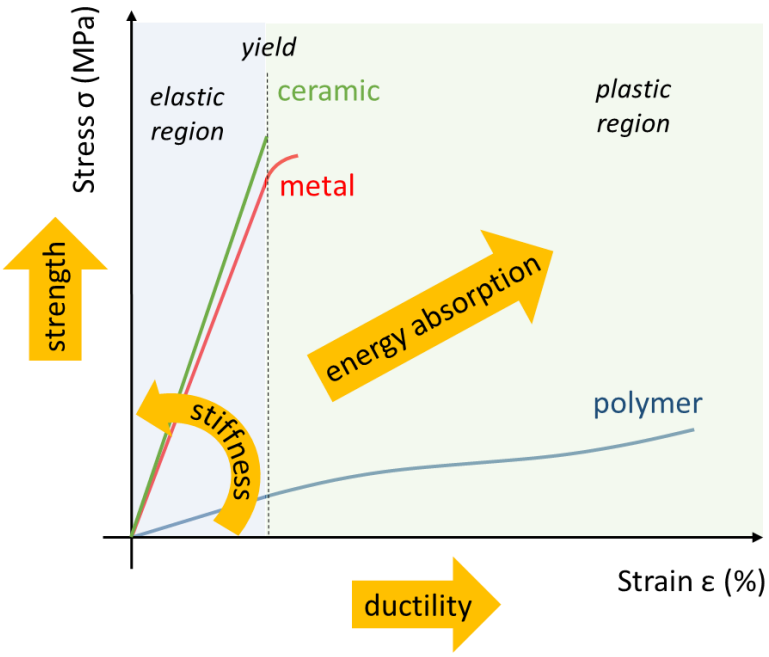


Figure 2.14. Stress-strain curve of a typical metal, ceramic and polymeric material (inspired by Callister, 2016 [24]).

The initial linear increase of stress and strain is known as the elastic region of the curve. In this region, the material is only elastically compressed and can regain its original shape upon release of the applied load. The linear relationship between stress σ and strain ε is described by Hooke's law:

$$\sigma = E \times \varepsilon \tag{2.25}$$

and allows for the elastic modulus or Young's modulus (E) for compression to be calculated from the slope of the curve. The Young's modulus (in GPa) gives indication of the material's stiffness i.e. its resistance to elastic deformation.[24] The higher E, the stiffer is the material. At a specific stress and strain threshold, the linear relationship is interrupted and permanent or plastic deformation occurs. The stress value (in MPa) that is measured once linearity is interrupted is called the yield stress or yield strength σ_y, which is a measure of the material's resistance to plastic deformation.[24] The corresponding strain value is called the yield strain ε_y. The maximum stress that can be

sustain by a material during compression testing is known as the compressive strength σ_{max}. The fracture strength is obtained in the stress-strain curve at the point just before fracture, which is observed in the stress-strain curve by a sudden drop in stress with no simultaneous increase in strain. The degree of plastic deformation that can be sustained by a material before fracture gives an indication on how ductile or brittle the material is. The more the material can deform plastically, the more ductile it is. Typically, the strain is expressed as the percentage strain i.e. the percentage displacement of the load from the original height of the material upon compression.[24]

2.4.2. Four-point bending

Four-point bending is a mechanical testing technique used to measure the flexural properties of a material. A rectangular-shaped beam of a suitable length, width and thickness is inserted between the loading span (l) and support span (S) of a four-point bending jig with four loading pins (Figure 2.15). A force (P) is applied to the top loading pins at a constant loading rate (or constant displacement rate) while the displacement (D) (or load) is measured until beam fracture. Both, load or displacement controlled measurements can be carried out. In comparison to three-point bending, four-point bending has a wider beam area between the loading points in which the bending moment is constant.[25] As shown in the diagram in Figure 2.15, shear forces and shear stresses are zero in this specific span area, which allows for the pure bending moment to be measured. This results in the flexural stress being measured within a larger sampling volume (pure bending moment), which gives a more accurate representation of the beam's properties. Hence, four-point bending is the preferred configuration for measuring fracture properties of solids.

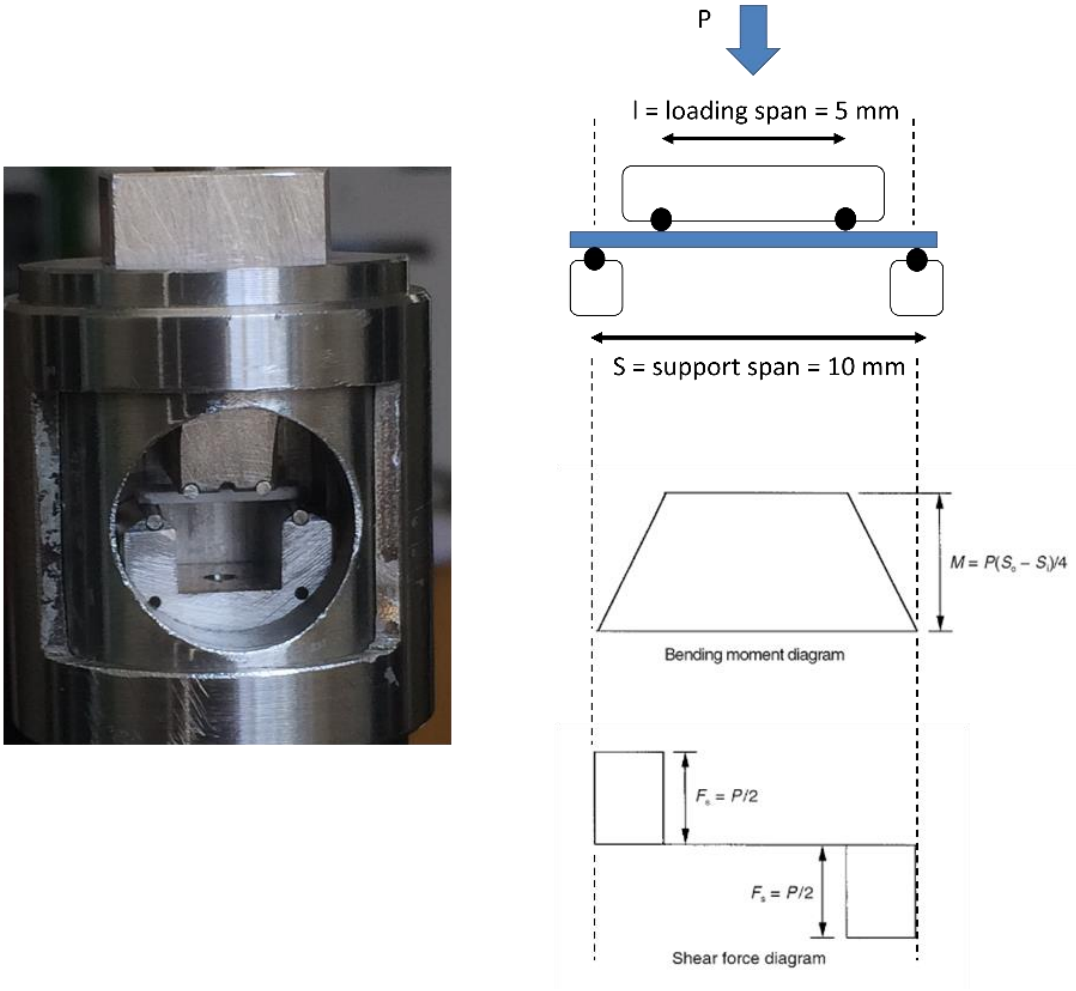


Figure 2.15. Four-point bending setup: custom-made jig with beam (left), schematic and corresponding bending moment and shear force diagrams (right).

From the recorded load and displacement data, flexural properties such as stress (σ_f), strain (ε_f), the modulus of elasticity in bending (flexural modulus E_f) and the flexural strength ($\sigma_{f,max}$) of each beam is calculated. Assuming beam theory applies,[26] following equations,[25] specific to four-point bending are valid:

$$\sigma_f = \frac{3PS}{4bh^2} \times 10^{-6} \; (in\; MPa) \tag{2.26}$$

$$\varepsilon_f = \frac{3hD}{k\left(\frac{k}{2}+\frac{3l}{2}\right)} \times 100 \; (in\; \%) \tag{2.27}$$

$$E_f = 0.17\frac{S^3\frac{\Delta\sigma_f}{\Delta\varepsilon_f}}{bh^3} \times 10^{-9}\ (in\ GPa) \tag{2.28}$$

$$\sigma_{f,max} = \frac{3P_{max}S}{4bh^2} \times 10^{-6} (in\ MPa) \tag{2.29}$$

where l is the loading span (in m), S is the support span (in m), b is the sample width (in m), h is the sample thickness (in m), P is the applied load (in N), D is the displacement (in m) and k is the difference between the support span and the loading span (in m). Stress-strain curves, similarly to the ones illustrated above for compression, can thus be generated.

2.4.3. Nanoindentation

Nanoindentation is a mechanical testing technique used to measure the mechanical properties of a material. Load-displacement curves are recorded when a diamond indenter tip with known geometry is pushed into the surface of a specimen. Figure 2.16 shows the load-displacement curve of a typical nanoindentation measurement.

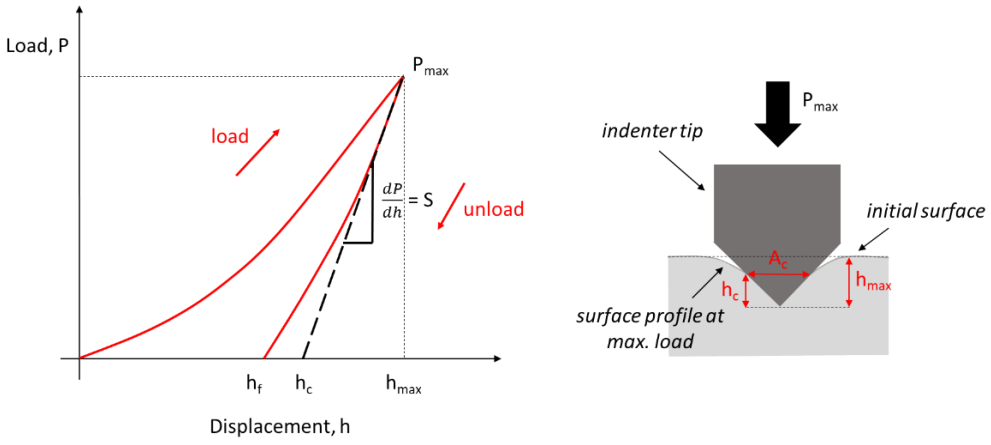


Figure 2.16. Loading and unloading curve of a typical nanoindentation measurement where P_{max} is the maximum load applied, h_{max} is the maximum surface depth reached, h_c is the depth of the contact circle, A_c is the contact area and S is the initial slope of the elastic unloading curve.

Several types of indenter tips exist, with the Berkovich (three-sided pyramid geometry) and Vickers (four-sided pyramid geometry) indenter being the most common ones used. Spherical, conical or cube corner indenter geometries can also be employed.[27] The size of the tip area function (impression area of the indenter tip with the sample), together with the applied load and indentation depth are used to calculate the mechanical properties of the material under investigation.

The indentation hardness (H), also known as the 'mean contact pressure'[27] is measured by dividing the maximum load (P_{max}) by the tip area function (A) as follow:

$$H = \frac{P_{max}}{A} \tag{2.30}$$

For a Berkovich indenter, as is employed in this work, A is given by:

$$A = 3\sqrt{3}\, h_c^2 \tan(\theta)^2 = 24.494\, h_c^2 \approx 24.5\, h_c^2 \tag{2.31}$$

using an indenter face angle of θ = 65.27 °. The tip radius is usually in the range of 50-100 nm. A so-called reduced modulus (E_r) is measured from the initial slope of the elastic unloading curve (S) by following relationship:

$$E_r = \frac{\sqrt{\pi}}{2\beta} \frac{S}{\sqrt{A(h_{max})}} \tag{2.32}$$

where A is the projected contact area at the contact depth h_{max} and β is a constant which depends on the shape of the indenter.[28] The reduced modulus includes the elastic properties of the specimen and the indenter. These can be separated by taking into account the elastic modulus of the indenter (E_i) and the Poisson ratio for the specimen (ν) and the indenter (ν_i) by following equation.[28]

$$E = \frac{1-\nu^2}{\frac{1}{E_r} - \frac{1-\nu_i^2}{E_i}} \tag{2.33}$$

From the load-displacement curve above, the values for hardness and elastic modulus can also be represented as a function of indentation depth as shown below (Figure 2.17). Depending on the surface roughness of the specimen, stabilisation of both values for the material is achieved either earlier or later on as the indentation depth is increased. Note that a reliable hardness or elastic modulus value can also be obtained without the effects of surface roughness and nucleation or dislocations during initial contact.

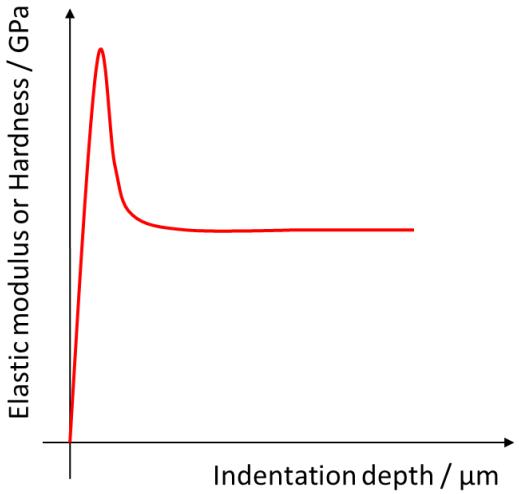


Figure 2.17. Hardness / elastic modulus as a function of indentation depth.

2.5. References

1. Gibson, I., Rosen, D. & Stucker, B. *Additive Manufacturing Technologies: 3D Printing, Rapid Prototyping, and Direct Digital Manufacturing*. (Springer New York, 2014).
2. Baldacchini, T. *Three-Dimensional Microfabrication Using Two-Photon Polymerization: Fundamentals, Technology, and Applications*. (Elsevier Science, 2015).
3. NanoScribe GmbH. *Photonic Professional (GT): User Manual*. (2014).
4. Sakka, S. *Handbook of Sol-Gel Science and Technology: Processing, Characterization and Applications*. (Kluwer Academic Publishers, 2005).
5. West, A. R. *Solid State Chemistry and its Applications*. (Wiley, 2014).
6. Waseda, Y., Matsubara, E. & Shinoda, K. *X-Ray Diffraction Crystallography: Introduction, Examples and Solved Problems*. (Springer Berlin Heidelberg, 2011).

7. Woolfson, M. M. & Woolfson, M. M. *An Introduction to X-ray Crystallography*. (Cambridge University Press, 1997).

8. Hitachi High-Tech. *Introduction to SEM (Application Note)*. (2008).

9. Hubbard, A. T. *The Handbook of Surface Imaging and Visualization*. (Taylor & Francis, 1995).

10. Yaghoubi, H. Bio-Photoelectrochemical Solar Cells Incorporating Reaction Center and Reaction Center Plus Light Harvesting Complexes. *Graduate Theses and Dissertatons* (2015).

11. Micro Photonics Inc. How does a micro-CT scanner work? (2015). Available at: https://www.microphotonics.com/how-does-a-microct-scanner-work/.

12. Ketcham, R. X-ray Computed Tomography (CT). *Geochemical Instrumentation and Analysis* Available at: https://serc.carleton.edu/research_education/geochemsheets/techniques/CT.html.

13. Levitt, M. H. *Spin Dynamics - Basics of Nuclear Magnetic Resonance*. *System* (2000).

14. Pecher, O., Carretero-González, J., Griffith, K. J. & Grey, C. P. Materials' Methods: NMR in Battery Research. *Chem. Mater.* **29,** 213–242 (2017).

15. Knight, W. D. Nuclear Magnetic Resonance Shift in Metals. *Phys. Rev.* **76,** 1259–1260 (1949).

16. Chang, H. J. *et al.* Correlating Microstructural Lithium Metal Growth with Electrolyte Salt Depletion in Lithium Batteries Using 7Li MRI. *J. Am. Chem. Soc.* **137,** 15209–15216 (2015).

17. Grey, C. P. & Dupré, N. NMR Studies of Cathode Materials for Lithium-Ion Rechargeable Batteries. *Chem. Rev.* **104,** 4493–4512 (2004).

18. Hennel, J. W. & Klinowski, J. Magic-Angle Spinning: a Historical Perspective. in *New Techniques in Solid-State NMR* (ed. Klinowski, J.) 1–14 (Springer Berlin Heidelberg, 2005). doi:10.1007/b98646

19. Trease, N. M., Zhou, L., Chang, H. J., Zhu, B. Y. & Grey, C. P. In situ NMR of lithium ion batteries: Bulk susceptibility effects and practical considerations. *Solid State Nucl. Magn. Reson.* **42,** 62–70 (2012).

20. Zhou, L., Leskes, M., Ilott, A. J., Trease, N. M. & Grey, C. P. Paramagnetic electrodes and bulk magnetic susceptibility effects in the in situ NMR studies of batteries: Application to Li1.08Mn1.92O4 spinels. *J. Magn. Reson.* **234,** 44–57 (2013).

21. Brink, H. F., Buschmann, M. D. & Rosen, B. R. NMR Chemical Shift Imaging. *Comput. Med. Imaging Graph.* **13,** 93–104 (1989).

22. Gamry. The Basics of Electrochemical Impedance Spectroscopy (Application Note). Available at: https://www.gamry.com/application-notes/EIS/basics-of-electrochemical-impedance-spectroscopy/.

23. Hirschorn, B. *et al.* Determination of effective capacitance and film thickness from constant-phase-element parameters. *Electrochim. Acta* **55,** 6218–6227

(2010).

24. Callister, W. D. & Rethwisch, D. G. *Fundamentals of Materials Science and Engineering: An Integrated Approach*. (Wiley, 2016).

25. Hammant, B. The use of 4-point loading tests to determine mechanical properties. *Composites* 246–249 (1971).

26. Timoshenko, S. *Strength of Materials - Part 1 Elementary Theory and Problems*. (D. van Nostrand Co Inc, 1940).

27. Fischer-Cripps, A. C. *Nanoindentation*. (Springer New York, 2011).

28. Ma, D., Chung Wo, O., Liu, J. & He, J. Determination of Young's modulus by nanoindentation. *Sci. China Ser. E Eng. Mater. Sci.* **47,** 398–408 (2004).

Chapter 3: Electrochemical and Mechanical Analysis of the Interfacial and Bulk Properties of $Li_{1.4}Al_{0.4}Ge_{1.6}(PO_4)_3$ as Solid Electrolyte

3.1. Aim

This Chapter aims to analyse and understand in depth the microstructural, electrochemical and mechanical properties of the phosphate-based ceramic electrolyte $Li_{1.4}Al_{0.4}Ge_{1.6}(PO_4)_3$ (LAGP). Particular attention is paid to the interfacial properties of LAGP with Li, its performance when assembled in a symmetrical cell with Li metal electrodes, the limiting factors of the cell's lifetime and reasons for its failure.

3.2. Introduction

First synthesised and reported in literature by J. Fu in 1997,[1] LAGP is a NASICON-type Li-ion conductor that is considered as a potential solid electrolyte in future battery systems. The ionic conductivity of LAGP has been reported in the range of 2.4 to 4.0 x 10^{-4} $S \cdot cm^{-1}$ at 25 ºC depending on the synthesis procedure used.[1,2,3] This is slightly lower than its Ti-equivalent $Li_{1.3}Al_{0.3}Ti_{1.7}(PO_4)_3$ (LATP), reported at 7.0 x 10^{-4} $S \cdot cm^{-1}$ at 25 ºC.[4,5] LAGP was widely synthesised as it was believed that Ge might decrease the reactivity with Li compared to LATP. Although LAGP has shown to be more stable in air and water than LATP,[4] its reactivity with Li metal could not be fully inhibited. The oxidative stability of LAGP has been reported up to 7 V vs. Li.[6] However, Cui *et al.* have shown that similarly to LATP, LAGP becomes reduced below a voltage of 0.9 V vs. Li (2.7 V vs. Li for LATP [7]).[8] As shown by Janek and co-workers,[9] a 'mixed electronic/ionic conducting interphase' (MCI) layer is formed when Li is contacted with LAGP. An in-depth EDX analysis shows that Li diffuses into the electrolyte forming new Al^{3+}

containing species, Li_2O and Li_2CO_3 species, as well as reducing Ge^{4+} nearly completely to Ge^0.[9] No further analysis of the growth of this interphase layer within an electrochemical cell upon cycling has been reported. Similarly, the cycling performance and lifetime of a cell using LAGP or LATP as the solid electrolyte has scarcely been investigated in the literature,[6,10] neither have the mechanical properties of LAGP and LATP.[11] Only recently, several research groups have reviewed and compared some of the mechanical properties of crystalline, oxide-based solid electrolytes and how these might influence the cycling performance and mechanism through which Li dendrites penetrate the material.[11,12,13]

This Chapter aims to fully analyse the electrochemical and mechanical properties of LAGP and understand the challenges that inhibit its current use as solid electrolyte in an all-solid-state battery. It is hoped that by acquiring a full understanding of the properties that influence the cycling performance of LAGP, a solution on how to improve the properties of ceramic electrolytes can be suggested.

3.3. Experimental Methods

3.3.1. Synthesis of $Li_{1.4}Al_{0.4}Ge_{1.6}(PO_4)_3$

$Li_{1.4}Al_{0.4}Ge_{1.6}(PO_4)_3$ was synthesised by a sol-gel process.[14] Citric acid monohydrate (CA) (≥99.0 %, 0.105 mol) and ethylene glycol (EG) (99.8 %, 0.105 mol) were mixed together in a 1:1 molar ratio and left to stir overnight at RT until a white viscous mixture was formed. Stochiometric amounts of Ge (IV) ethoxide (≥99.95 %, 0.0993 mol) were then added to the mix. In a separate vial, stoichiometric amounts of lithium nitrate (99.99 %, 0.087 mol), aluminium nitrate nonahydrate (≥99.99 %, 0.0248 mol) and ammonium dihydrogen diphosphate (≥99.99 %, 0.1861 mol) were added together with distilled water and left to stir until all salts were dissolved and a clear aqueous solution was obtained.

An ice bath was prepared using water and sodium chloride. Both mixtures were immersed in the ice bath until cooled. The clear solution was then slowly added to the white viscous mixture and left to stir at RT until a gel-like mixture was obtained. The LAGP precursor gel was then dried at 75 °C overnight. The solidified gel was calcined on an Au crucible at 800 °C for 5 hours at a heating rate of 2 °C per minute and a cooling rate of 10 °C per minute to form the final product. The calcined powder (0.5 g) was ball-milled (Retsch Emax high energy ball mill equipped with two 50 mL zirconia grinding jars each containing 21.5 g of 5 mm diameter zirconia balls) with ethanol (0.5 mL) at 600 rpm for 10 minutes. The dried ball-milled LAGP powder was pressed into 5 mm diameter pellets with a thickness of 1 mm using a uniaxial hydraulic press (Specac) at a load of 1 tons. The pellets were then sintered on an Au crucible at 900 °C for 5 hours at a heating rate of 2 °C per minute and a cooling rate of 10 °C per minute.

3.3.2. Microstructural analysis

3.3.2.1. SEM and EDX

LAGP powders, the surface and cross-section of LAGP pellets and cross-sectioned Li | LAGP | Li cells (the preparation of which is described in Chapter 3 Section 3.3.3.2) were placed on a stub with Cu adhesive tape and analysed using a Zeiss Merlin SEM at an acceleration voltage of 3 kV and a probe current of 100 µA. SE images were recorded at several magnifications. To avoid charging effects during the imaging process, samples were coated with a 30 nm layer of Au using a manual sputter coater (Agar Scientific). For cross-sectional SEM analysis of the samples, an ultrasonic cutter (Sonotec) was used to cut samples into two equal halves using a tungsten carbide blade. EDX was performed within the Zeiss Merlin instrument using a built-in Oxford Instruments X-Max 150 Silicon drift detector. To achieve smooth surfaces on pellets, samples were first polished

with a silicon carbide (SiC) waterproof abrasive disc (Kemet, Grade 400 to 2500) followed by Ar beam etching using a Precision Etching Coating System (PECS) for 1 hour at an etching angle of 4 ° and a beam voltage of 3 kV. SE images were acquired up to 10 kV. The Aztec software package was used to analyse the collected data.

3.3.2.2. PXRD

PXRD was performed on the synthesised LAGP powders using a Rigaku SmartLab x-ray diffractometer with Cu $K_{\alpha 1}$ radiation and a 3 kW rotating anode x-ray generator. Ground LAGP powders were placed onto a Si low background sample holder and flattened to achieve a smooth and even surface. Patterns were collected from 10 ° to 80 ° in $\theta/2\theta$ with a step size of 0.01 at RT.

3.3.2.3. XPS

XPS was performed on differently polished LAGP pellet surfaces in collaboration with the Oxford Materials Characterisation Service using an ion pumped ultra-high vacuum (UHV) chamber fitted with a VG nine channel CLAM4 electron energy analyser. The samples were placed on a Cu adhesive tape and transferred into the XPS analyser using an air-tight transfer holder.

3.3.3. Electrochemical analysis

3.3.3.1. EIS

EIS measurements were performed on LAGP pellets using a ModuLab XM® (Solartron Analytical). A SiC waterproof abrasive disc (Kemet, grade 1200) was used to polish the surfaces of the pellets in contact with the electrodes. The samples were then sonicated in cyclohexane for 10 minutes and dried in air at 70 °C for 20 minutes. A sputter coater (Manual Sputter Coater, Agar Scientific) was used to coat both sides of the polished surfaces with a 30 nm layer of Au. The coated samples were then placed between two

stainless steel plates and the impedance of the LAGP was recorded in a frequency range of 1MHz and 0.1 Hz at an applied voltage of 10 mV. EIS measurements were carried out between -30 °C and 75 °C using a temperature circulator (Model F32-MA, Julabo). Temperatures lower than -20 °C were achieved using a liquid nitrogen vessel. The data was analysed using the ZView software.

3.3.3.2. Galvanostatic cycling

Galvanostatic cycling of Li | LAGP | Li cells was performed using Gamry Interface-1000 devices. LAGP pellets were polished with a SiC waterproof abrasive disc (Kemet, grade 1200) using water as a solvent. The pellets were then dried at drying at 70 °C in air for 20 minutes followed by sonication in dried cyclohexane for 10 minutes and additional drying at 70 °C in air for 20 minutes before being introduced inside a glovebox. In an Ar-filled glovebox (O_2 and H_2O levels below 0.1 ppm), a Li metal foil was scratched to remove any oxidised species and cut into a 5 mm diameter disc. The disc was pressed up to 10 tons using a manual hydraulic press (Specac) to reach a thickness of about 40 µm. This procedure was performed to limit the expansion of Li during cell assembly and cycling. A 2.2 mm diameter disc of pressed Li metal was placed in the centre on either side of the polished pellet. The average size of an LAGP pellet was 4.4 mm in diameter and 1 mm in thickness. The assembled cell was placed between two Cu current collectors inside a pouch cell sealed under vacuum. The pouch cell was positioned between two plastic plates and clamps, which together apply an external pressure of about 8 MPa during measurements. Galvanostatic cycling was performed at different constant current densities ranging from 0.05 $mA \cdot cm^{-2}$ to 2 $mA \cdot cm^{-2}$ for 0.5 hours per charge and discharge at RT. A rest time of 5 minutes was recorded between each current direction. Additional EIS measurements were taken after each charge or discharge step.

3.3.4. Mechanical characterisation

3.3.4.1. Compression testing

Compression tests were performed on polished rectangular cross-sectioned LAGP samples of 1 mm x 1 mm x 2 mm in width, length and height, respectively using a strain rate controlled universal testing equipment (Shimadzu AGS-X, 50 kN load cell). The samples were prepared by cross-sectioning a synthesised LAGP pellet before sintering as described in Chapter 3 Section 3.3.1 to the required size, after which the sectioned part was sintered in the same way as described for LAGP in Chapter 3 Section 3.3.1. Surfaces of the samples were polished using a diamond lapping film with an abrasive size of 9, 6, 3 and 1 µm. To ensure parallel surfaces are achieved, samples were placed between two rheometer plates (Anton Paar). A diamond lapping film was attached to the plates of the rotating rheometer whilst a force of 2 N was applied. Surfaces of the samples were polished down to 10 µm in height differences over a length of 1 mm. This was confirmed by optical depth profiling (Alicona) for which results are shown in Appendix 1. First, a preload of 50 N was applied after which the samples were compressed at a constant displacement rate of 1 $\mu m \cdot min^{-1}$ until failure. Compliance of the instrument was accounted for during testing.

3.3.4.2. Four-point bending

LAGP samples were prepared and polished by the same method as described above for compression testing. An Instron 3360 Series Dual Column table top testing system using a custom-made four-point bending jig was used to bend rectangular-cross-sectioned beams of approximately 12 mm x 3 mm x 0.5 mm in length, width and height, respectively. For the preparation of the LAGP beams, a die set of 13 mm diameter instead of 5 mm diameter as described in Chapter Section 3.3.1 was used. After an initial preload

of 0.05 N, the samples were bent at a constant displacement rate of 5 µm·min^{-1} until fracture.

3.3.4.3. Nanoindentation

Nanoindentation measurements were performed on LAGP pellets at RT using an Agilent G200 nanoindenter and a Berkovich indenter tip. The pellets were polished by the same method as described for the compression testing above. Arrays of 16-25 indents were made with a distance of 50 µm apart. The pellets were indented at a displacement rate of 10 nm·s^{-1} up to a depth of 2 µm. The elastic modulus and hardness was extracted from the load-displacement curve of each indentation measurement and plotted against the indenter displacement. Calibration of the nanoindenter was performed prior measurement using a fused-silica reference sample to account for the influence of tip geometry and frame stiffness on the measured data.

3.4. Results and Discussion

3.4.1. Synthesis and characterisation of LAGP

The synthesised LAGP powder was analysed using various characterisation techniques. Figure 3.1 shows SEM images of the LAGP powder at different stages of the synthesis. After calcination at 800 °C for 5 hours, LAGP grains have formed but are not yet compacted together. Ball milling of the LAGP grains with ethanol reduces the particle size of the grains and ensures a homogeneous particle size distribution throughout the material. After sintering the LAGP pellet at 900 °C for 5 hours, distinct LAGP grains of similar size are formed. These square-shaped grains are well sintered together, forming a dense ceramic pellet with an average density of 2.9-3.1 g·cm^{-3}. This equates to 80-86 %

of the theoretical density of $LiGe_2(PO_4)_3$ (3.5872 $g \cdot cm^{-3}$), the undoped LAGP phase reported in literature.[15]

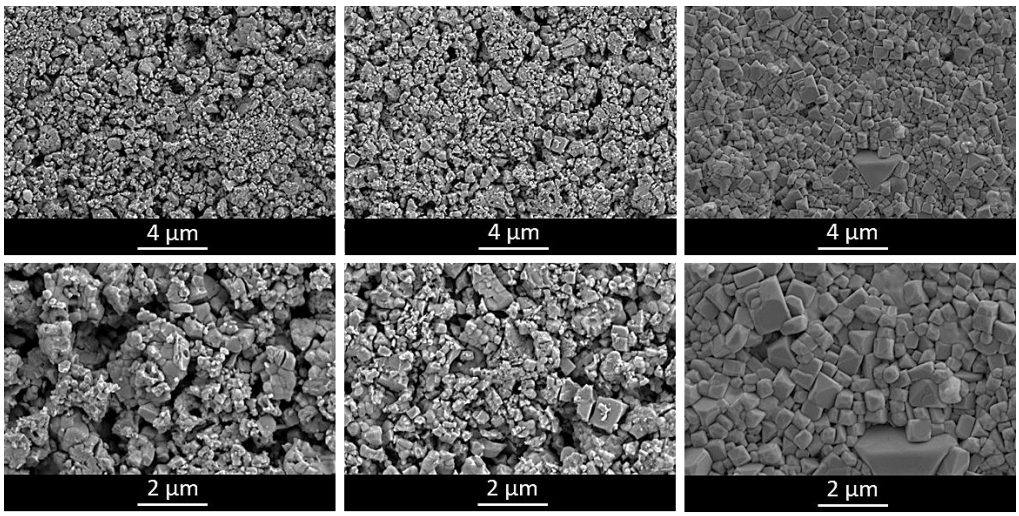


Figure 3.1. SEM images of the synthesised LAGP grains after calcination at 800 °C for 5 hours (left), after ball milling with ethanol (centre) and after sintering at 900 °C for 5 hours (right).

PXRD patterns were recorded after each synthesis step and compared to its undoped equivalent phase $LiGe_2(PO_4)_3$ reported in literature (PDF-01-080-1922).[16] Figure 3.2 shows that the correct LAGP phase was achieved from the calcination onwards. The phase was not altered by ball milling with ethanol or during sintering. No crystalline impurity phases were detected with PXRD.

The polished and etched LAGP pellet surface was additionally analysed by EDX (Figure 3.3). The smooth surface revealed three different types of grey levels. Next to the recognisable LAGP grains, a darker and a lighter grey phase were detected. From EDX mapping, these could be assigned to Ge-oxide species, such as GeO_2 and GeO, and $AlPO_4$, respectively, which are known amorphous secondary phases for LAGP.[17] Both phases can be minimised by tuning the composition and sintering conditions.[3,4] The synthesis parameters used in this work have been tuned to obtain a LAGP pellet with the highest ionic conductivity and highest level of phase purity and density.

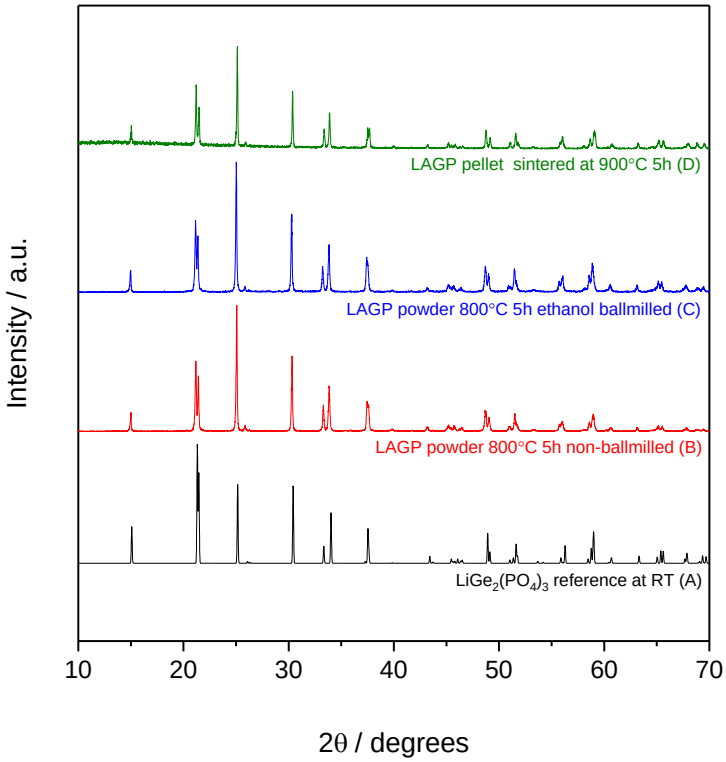


Figure 3.2. PXRD patterns of the $LiGe_2(PO_4)_3$ reference pattern (A)[16] and the synthesised LAGP powder after calcination at 800 °C for 5 hours and non-ball milled (B), after ball milling with ethanol (C) and after sintering at 900 °C for 5 hours (D).

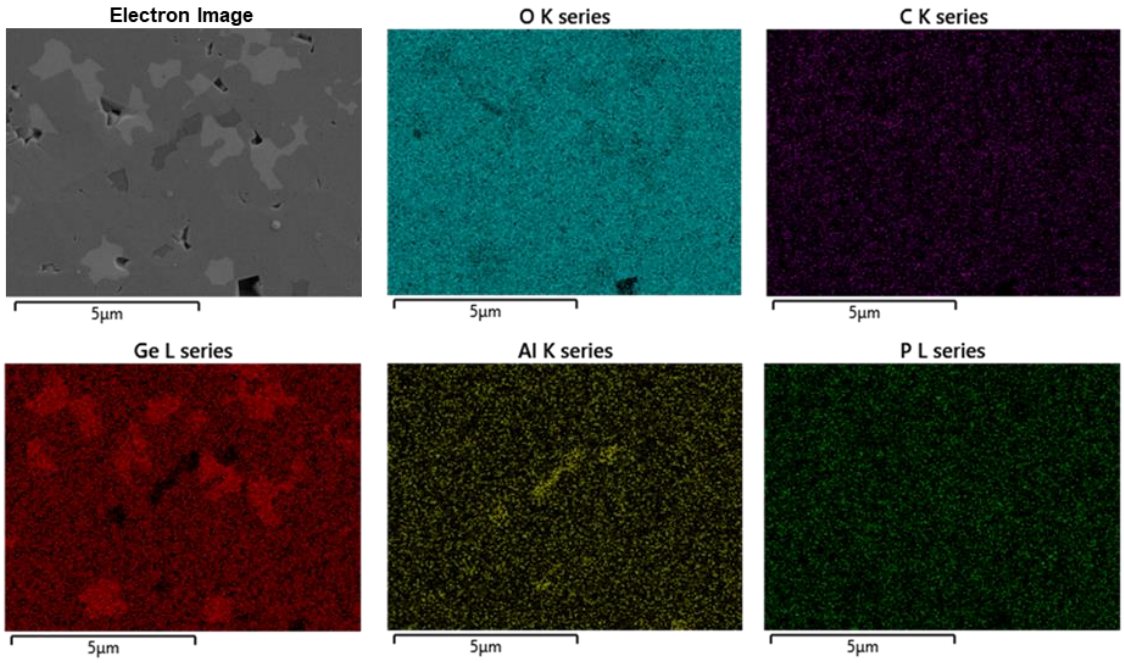


Figure 3.3. EDX mapping of an etched LAGP pellet surface.

3.4.2. Impedance measurements with Au blocking electrodes

EIS measurements were carried out on the synthesised LAGP pellets using symmetrical Au blocking electrodes. Figure 3.4-c illustrates the Nyquist plot obtained for a symmetrical Au | LAGP | Au cell at RT.

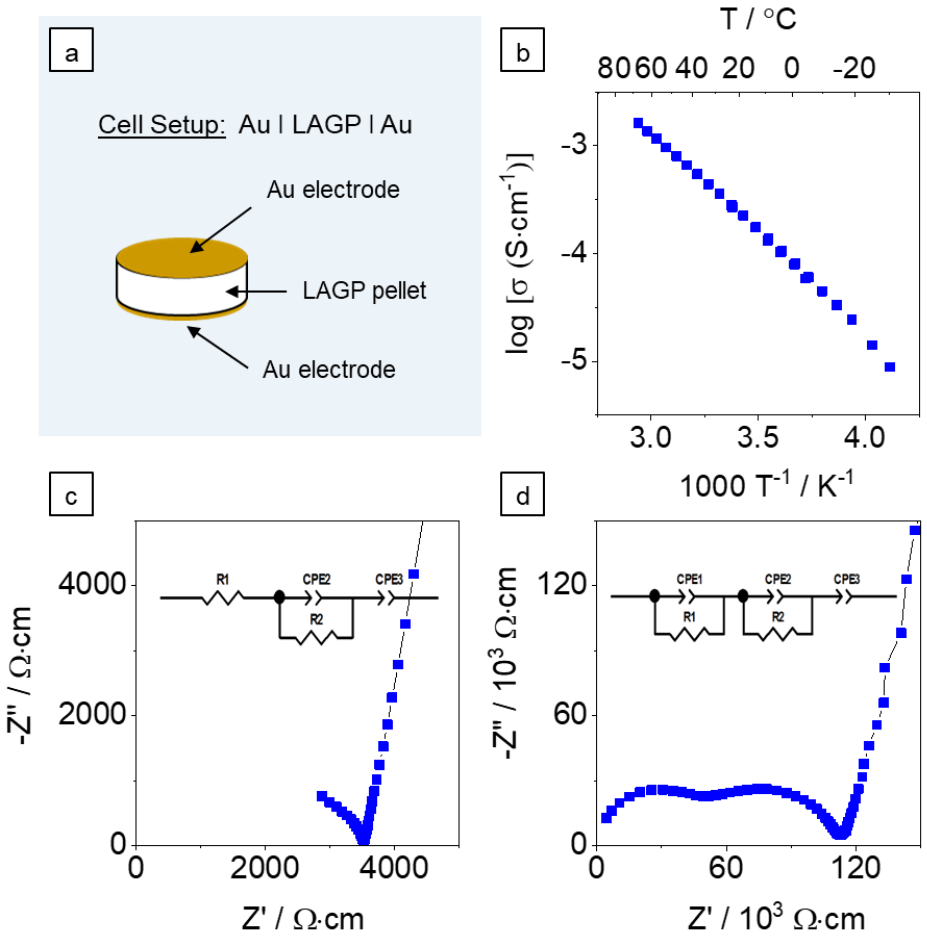


Figure 3.4. EIS analysis of a symmetrical LAGP cell using Au blocking electrodes: (a) schematic of the cell setup, (b) Arrhenius plot showing the dependence of impedance versus temperature over a temperature range of -30 °C to 70 °C, (c) and (d) the Nyquist plot and its corresponding equivalent circuit at RT and at -30 °C, respectively. Detailed fitting values are reported in Appendix 2.

The data at RT were best fitted using a resistor in series (R_1), to account for the contribution at high frequency, followed by a resistor and constant-phase element in

parallel (CPE_2 // R_2) for the partially visible semicircle, and finally a constant-phase element in series (CPE_3) for the distinct spike at lower frequency. The equivalent circuit is shown in Figure 3.4-c. The partially visible semicircle marks the resistance of the LAGP electrolyte, whereas the spike is characteristic for the presence of blocking electrodes. An ionic conductivity for the LAGP pellet at RT of 2.8 x 10^{-4} $S \cdot cm^{-1}$ was calculated. In order to visualise the possibly missing data in the higher frequency region, additional EIS measurements were performed at lower temperatures. Figure 3.4-d shows the Nyquist plot and the corresponding equivalent circuit for a symmetrical LAGP cell at -30 °C. Two overlapping semicircles fitted by a series of two resistors and constant-phase elements in parallel (CPE_1 // R_1 and CPE_2 // R_2) were obtained, followed by a spike fitted with a third constant-phase element in series (CPE_3). From the microstructure of LAGP and its ceramic properties, two distinct contributions from the grain and the grain boundaries are expected. Capacitance values for each of the semicircles in the range of 10^{-11} $F \cdot cm^{-1}$ and 10^{-10} $F \cdot cm^{-1}$ were calculated, respectively. These values fit well to the expected capacitance of intragrain (bulk) and intergrain (grain boundaries) resistances found for LAGP, respectively.[3,18,19] EIS measurements from -30 °C to 70 °C confirm the stability of LAGP over a wide temperature range as shown in Figure 3.4-b. From the slope of the Arrhenius plot, an activation energy of 35.5 $kJ \cdot mol^{-1}$ was calculated, which is comparable to the activation energies found for LAGP in literature.[4]

3.4.3. Impedance measurements with Li metal electrodes

Symmetrical Li | LAGP | Li cells were assembled and their impedance at RT was measured. A Nyquist plot with a larger semicircle at higher frequency and a smaller semicircle at lower frequency was obtained (Figure 3.5). Whereas the smaller semicircle could best be fitted to a constant-phase element and a resistor in parallel (CPE_4//R_4),

several equivalent circuit combinations were tested for the larger semicircle. Similar to the impedance measurements with Au blocking electrodes, a contribution from the grain, the grain boundaries and the Li-LAGP interface is expected. However, as known from previous work in the literature,[9] LAGP reacts with Li to form an interphase layer, which can additionally contribute to the overall resistance of the system. This contribution remains initially small, but becomes more pronounced as the LAGP pellet is left in contact with Li over time, as shown later on in this Chapter. Consequently, the larger semicircle was best fitted with a series of three constant-phase elements and resistors in parallel (CPE_1 // R_1, CPE_2 // R_2 and CPE_3 // R_3) as illustrated in Figure 3.5, corresponding to three overlapping semicircles.

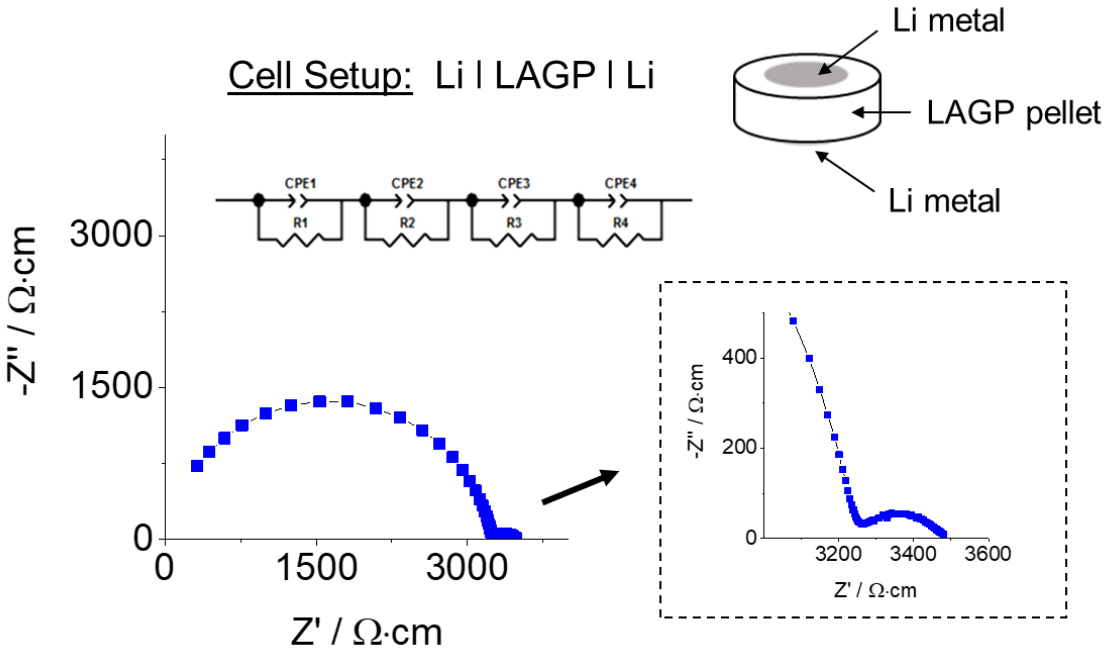


Figure 3.5. EIS measurement of a symmetrical LAGP cell using Li metal electrodes showing the schematic of the cell setup and the Nyquist plot and its corresponding equivalent circuit at RT. Detailed fitting values are reported in Appendix 3.

For the first two resistances (CPE_1 // R_1 and CPE_2 // R_2) similar capacitance values of 10^{-11} F·cm^{-1} and 10^{-10} F·cm^{-1} were obtained, corresponding again to the intragrain and

intergrain resistances, respectively. A capacitance value of 10^{-8} F·cm^{-2} was obtained for the third contribution (CPE_3 // R_3), which was not present in the EIS measurements with Au blocking electrodes. This value is characteristic in literature of a surface layer.[18] The well-resolved, smaller semicircle at lower frequencies (CPE_4 // R_4), which was also absent in the EIS measurements with Au blocking electrodes, showed a capacitance value of 10^{-3} F·cm^{-2}. Although this capacitance is slightly higher than an expected double layer capacitance at an electrode-electrolyte interface, it must represent the interfacial interaction between the solid electrolyte and the Li metal electrode. It is yet not fully understood how the reactivity of LAGP with Li might affect the capacitance at this interface. Hence, the third and fourth contributions were associated to the resistance of the interphase layer expected to form between Li and LAGP and the Li-LAGP interface resistance, respectively. Whereas the reactivity of LAGP with Li is well known, how it affects the cell impedance as a function of time and during cycling has yet not been fully analysed or reported. The subsequent sections in this Chapter aim to understand the significance of this reactivity, the characteristics of the formed interphase layer and its impact on the overall cell performance.

3.4.4. Effect of surface polishing on the impedance

Polishing the surface of the LAGP pellet has shown to affect significantly the interfacial properties between LAGP and the Li metal electrode (Figure 3.6). A non-polished LAGP pellet was assembled into a Li | LAGP | Li cell straight after sintering. Similar to the Nyquist plot discussed in the previous section (Chapter 3 Section 3.4.3), a larger semicircle and a more resolved, smaller semicircle were obtained. Again, the data were best fitted to a series of four constant-phase elements and resistors in parallel (CPE_1 // R_1, CPE_2 // R_2, CPE_3 // R_3 and CPE_4 // R_4) as shown in Figure 3.6.

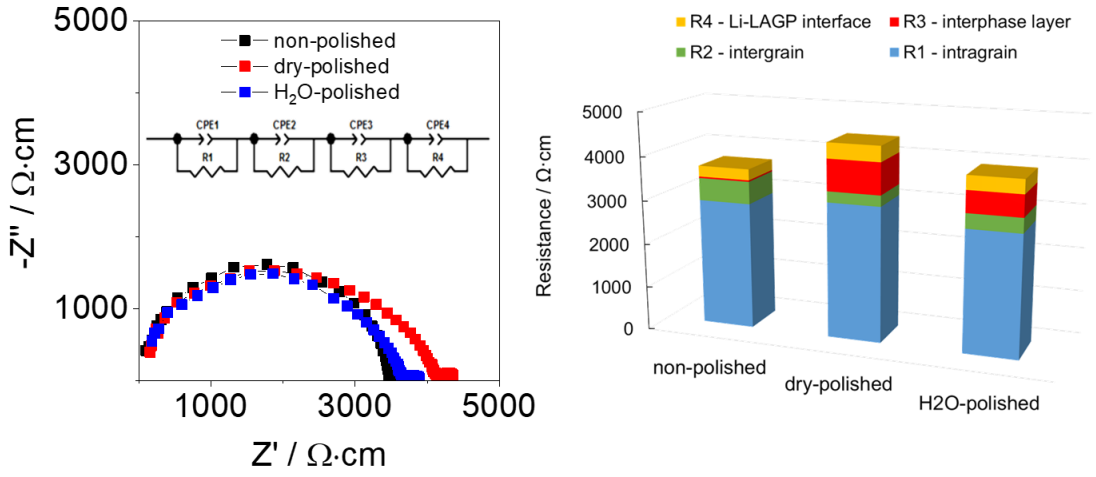


Figure 3.6. EIS measurements of non-polished, dry-polished and H_2O polished symmetrical Li | LAGP | Li cells: Nyquist plots and its equivalent circuit at RT (left) and a bar chart analysing the contributions of the resistances present for each surface polishing method (right). Detailed fitting values are reported in Appendix 4.

The extent to which each of the four resistances contribute to the overall cell impedance is shown in the adjacent bar chart (Figure 3.6). For the non-polished LAGP cell, the majority of the impedance is attributed to the intragrain resistance followed by the intergrain resistance. Only a minimal contribution from the additional interphase layer resistance is recorded. Polishing off the first few microns of this identical pellet in an Ar-filled glovebox (O_2 and H_2O levels below 0.1ppm), followed by sonicating it in dried cyclohexane and reassembling it with Li metal electrodes drastically increases the contribution of the interphase layer to the total resistance of the cell (Figure 3.6). All the other contributions remain fairly identical to the non-polished cell. Polishing the LAGP pellet with H_2O as described in Chapter 3 Section 3.3.3.2 enabled to reduce the contribution of the interphase layer back to nearly the non-polished cell state. This phenomenon was also visible in the Nyquist plot where the H_2O polished cell nearly regained the shape of the non-polished cell. During sintering, the LAGP pellet seems to

acquire a surface layer, which delays its reaction with Li. Polishing off the surface layer exposes the bulk LAGP and accelerates its reaction. Due to the difference in smoothness and roughness between the polished and non-polished cells, respectively, a change in the actual surface area of the LAGP in contact with the Li is expected. This could account for the remaining difference in resistance between both cells, as the increased surface roughness of the non-polished pellet was not taken into account in the Li electrode area calculation and could explain the artificially reduced impedance.

Figure 3.7 shows XPS measurements of the surface of the three differently polished LAGP pellets. The most significant changes in the XPS spectra were observed for the Ge and O peaks. While both non-polished and H_2O polished peaks in the Ge 3d spectra were best fitted with one line at 32.5 eV and 32.9 eV, respectively, the dry-polished Ge 3d peak could best be fitted with two lines at 33.0 eV and 31.6 eV. From literature, the peak at higher energy corresponds to Ge^{4+}, whereas the lower energy is associated to Ge^{2+}.[9] It is known that Ge gets easily oxidised in air to GeO_2 at high temperatures.[20] Hence, this suggests that the surface layer formed upon sintering must be rich in GeO_2 as only Ge^{4+} is detected in the Ge 3d spectrum for the non-polished pellet. When the surface layer is removed by dry-polishing, LAGP grains and their grain boundaries, containing Ge-oxide species (GeO_2 and potentially GeO) as seen by EDX mapping, are exposed and two signals in the Ge 3d spectrum for the dry-polished pellet surface are recorded. It is known that GeO disproportionates easily to Ge and GeO_2.[21] Hence, exposing the more reactive LAGP surface to H_2O can oxidise less stable Ge^{2+} species back to the more stable Ge^{4+} to partially recreate a similar layer to the non-polished pellet on the surface. The changes seen between the two lines fitted to the O 1s peaks at 532.5 eV and 531.5 eV support this concept of LAGP surface passivation by oxidation. However, as the binding energies of

O species are in a very narrow range to each other, it is difficult to interpret the O 1s peak lines more accurately.

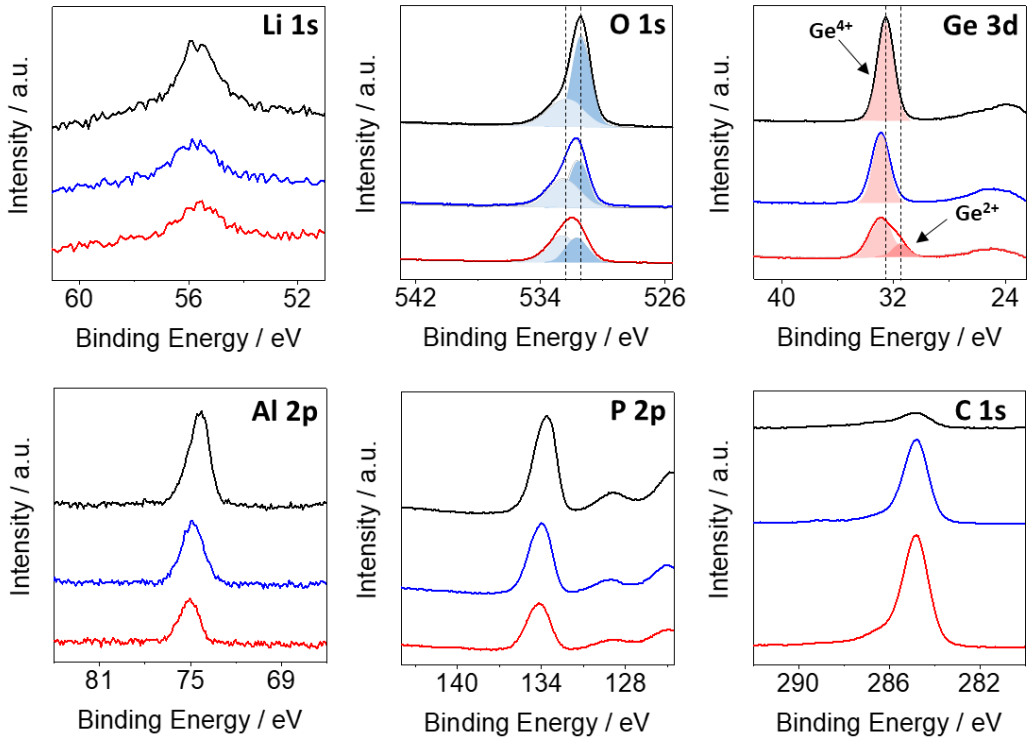


Figure 3.7. XPS spectra of non-polished (black), H_2O-polished (blue) and dry-polished (red) LAGP pellet surfaces.

3.4.5. Characterisation of the reactivity of LAGP with Li metal

From impedance, it is evident that an interphase layer forms as soon as LAGP is in contact with Li. In order to visualise and characterise the layer, a symmetrical Li | LAGP | Li cell was assembled and cross-sectioned using an ultrasonic cutter with a tungsten carbide blade after 3 days of aging at RT. The cross-sectioned cell was investigated with SEM and EDX.

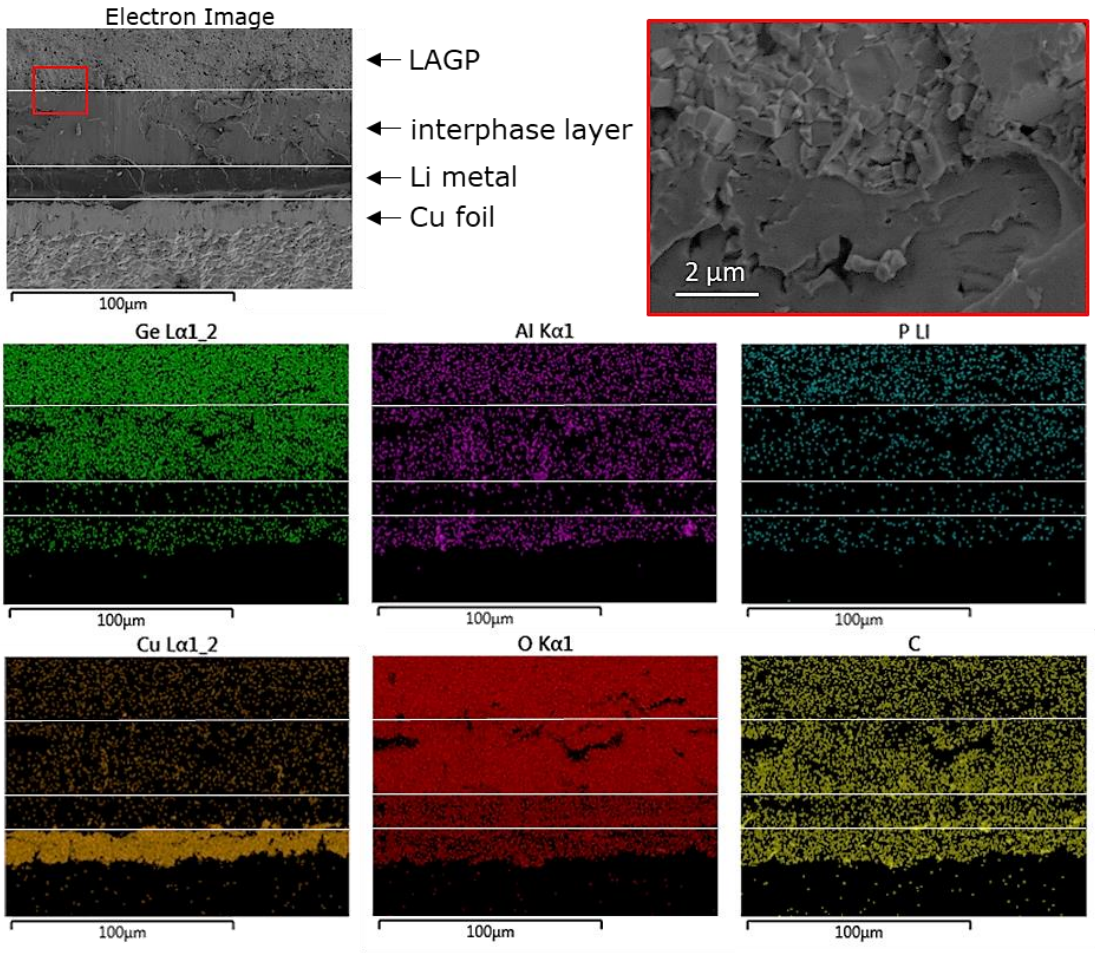


Figure 3.8. EDX mapping of the cross-section of a cycled Li /LAGP /Li cell showing the different layers present at the electrode-electrolyte interface. A magnified SEM image of the interface between the bulk LAGP and the interphase layer is also shown (red square).

As shown from the SEM images in Figure 3.8, an almost 50-µm thick interphase layer is observed between the darker Li metal and the original bulk LAGP phase. The location of the Cu foil was readily confirmed by EDX mapping of the Cu L_α signal (orange). Similarly, the bulk LAGP phase was confirmed by the presence of the elements Ge (green), Al (pink), P (cyan) and O (red). Minimal amounts of C (yellow) and O were always detected for all layers of the cross-section. Mapping of the Li metal layer did not show any elements of the LAGP phase, only traces of O and C were detected as Li is too light to be detected by EDX. As expected, the interphase layer is located between the

bulk LAGP phase and the Li metal electrode. Whereas the bulk LAGP phase is made of square-shaped grains with noticeable grain boundaries (intergrain connections), the grains in the interphase layer are more fused together and have lost their defined characteristic shape. A distinguishable change in the morphologies between the bulk LAGP phase and the smoother interphase layer is observed, as shown in the magnified SEM image in Figure 3.8. Nevertheless, EDX mapping confirms the presence of Ge, Al, P and O, which demonstrates that the same elements are still present in the interphase layer as are in the bulk LAGP phase, despite the differences in morphology.

3.4.6. Reactivity of LAGP with Li metal over time

The growth of the Li-LAGP interphase layer was monitored by regular EIS measurements of a Li | LAGP | Li cell over a period of 150 hours (Figure 3.9). A decrease in the overall ionic conductivity from 3 x 10^{-4} S·cm^{-1} to 1 x 10^{-4} S·cm^{-1} at RT was observed, which corresponds to a 70 % drop over a period of 150 hours. Analysing the different contributions of the total resistance over time shows that it is specifically the intergrain and Li-LAGP interface contributions that increase rapidly within the first 24 hours of contact with Li metal, before all four contributions increase more gradually together up to a relaxation time of 150 hours.

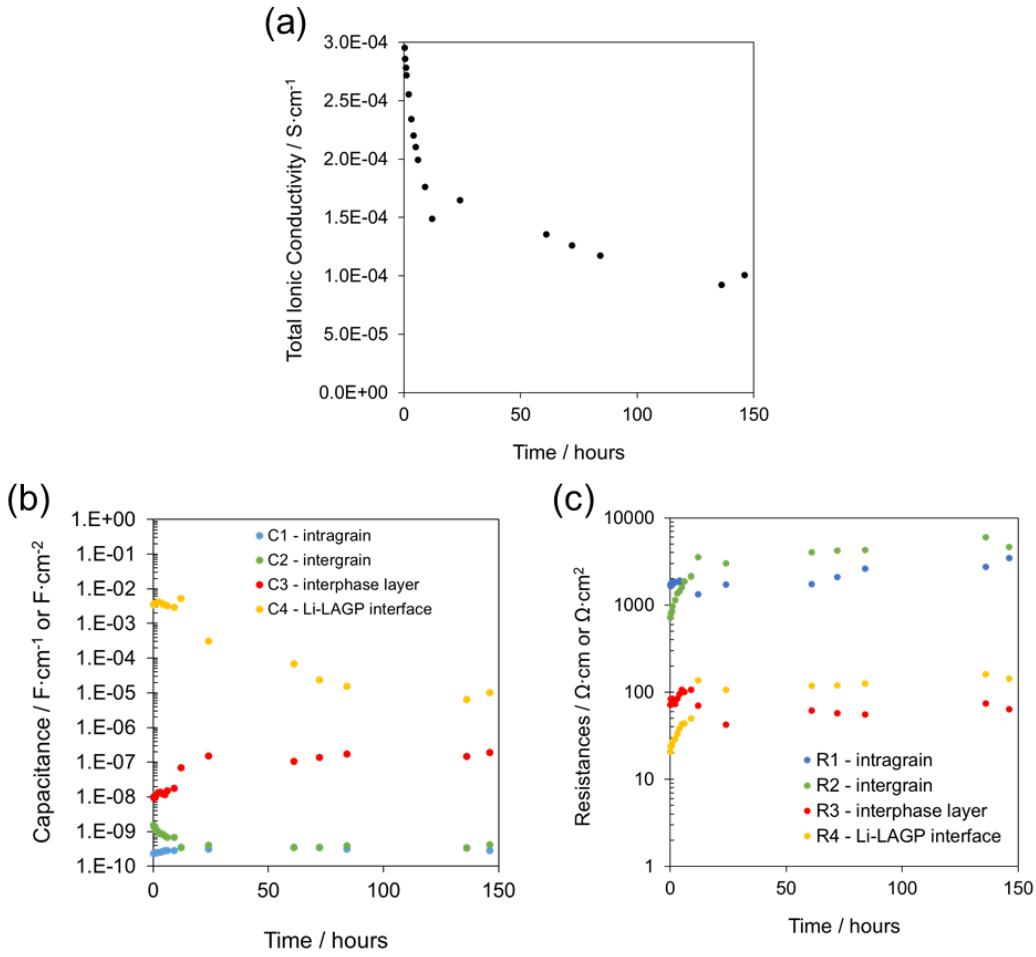
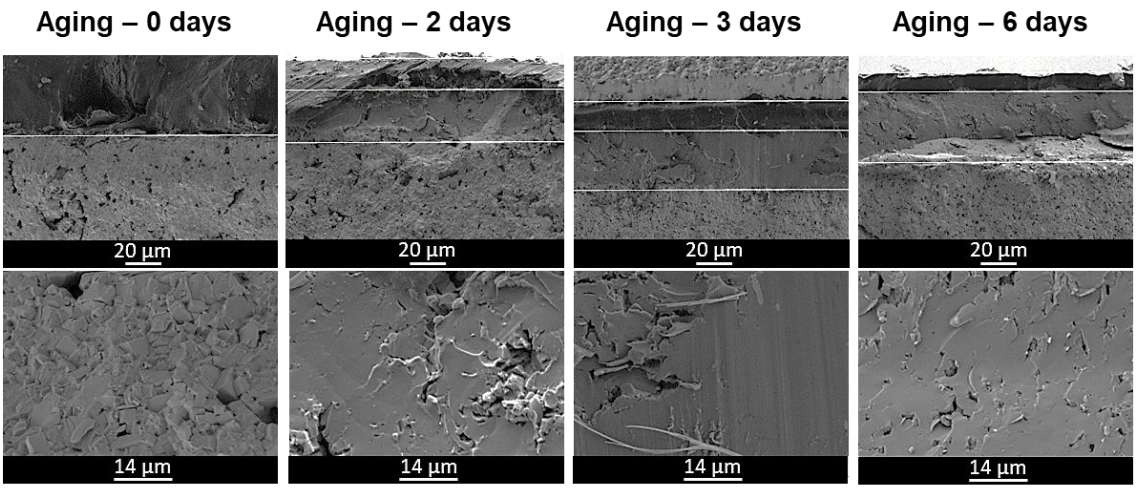


Figure 3.9. EIS analysis of a Li /LAGP/Li cell aging over 150 hours at RT: plot of total ionic conductivity (a) and capacitance (b) and resistance (c) of the four different resistances with time. Units of $F \cdot cm^{-1}$ and $\Omega \cdot cm$ are used for the intragrain and intergrain contributions, whereas units of $F \cdot cm^{-2}$ and $\Omega \cdot cm^2$ are used for the interphase layer and Li-LAGP interface contributions.

Cross-sectional SEM images of the Li and LAGP interface at different stages of the cell aging process were analysed in parallel to the EIS measurements. Figure 3.10 shows the cross-section of the interface after cell assembly and initial impedance (0 hours), after 2 days (48 hours), 3 days (72 hours) and 6 days (144 hours) of aging at RT.



Aging time / days	Li metal layer / µm	Li-LAGP mix layer / µm	Total / µm
0	50	(30)	50 (80)
2	25	15	40
3	15	25	40
6	15	35	50

Figure 3.10. Cross-sectional SEM analysis of Li /LAGP/Li cells aged for 0, 2, 3 and 6 days at RT (top row) with magnified SEM images of the LAGP phase closest to the electrolyte-electrode interface (bottom row). Qualitative thickness measurements of the Li metal layer, the reactive interphase layer and the sum of both layers are given in the table below. The solid white lines visualise the different layers present: the Li metal electrode, the interphase layer and the bulk LAGP electrolyte.

The interface after cell assembly (Aging – 0 days) shows a good interfacial contact between the LAGP electrolyte and the Li electrode. No interphase layer between the LAGP and the Li metal is yet detected. Nevertheless, the cross-section does show a slight change in grey tone of the LAGP closest to the Li metal. This change in grey tone was only visible in some areas of the Li-LAGP interface. A closer look at the grain morphology shows that distinct grains are still visible at this early stage of cell aging. As LAGP is kept in contact with Li metal for longer, an interphase layer starts to grow between the Li metal electrode and the LAGP electrolyte. After two days of aging, this

layer is yet not homogeneously present across the entire Li-LAGP interface. However, as seen from the SEM images after 3 and 6 days of aging, the layer continuously grows even after 150 hours where it ultimately covers the entire Li-LAGP interface with a uniform layer of around 35 µm. A distinct change in the grain morphology from the start to the end of the aging process is shown in the magnified SEM images in Figure 3.10.The table in Figure 3.10 qualitatively quantifies the Li metal electrode and interphase layer thicknesses with aging time. From these results, an increase in interphase layer thickness is observed, which fits very well to the observed decrease in Li metal electrode layer thickness. This suggests that the Li diffuses spontaneously from the Li electrode into the LAGP electrolyte as soon as both are in contact with each other. From both SEM and EIS results, it seems that the grain boundaries are initially the most reactive towards Li due to the observed initial increase of the intergrain resistance with time and the observed change in LAGP grain morphology from cross-sectional SEM images. This reactivity might be reinforced by the presence of GeO_2 or GeO species at the grain boundaries, as shown by EDX earlier in this Chapter (Figure 3.3). The formation of an interphase layer between the Li metal electrode and the bulk LAGP electrolyte of more than a few µm explains the drastic increase in the Li-LAGP interface resistance over time. The severe drop in total ionic conductivity also suggests that the interphase layer is electronically conductive and partially blocks Li diffusion between both electrodes during EIS measurements. The resistance of the interphase layer itself remains, after initially growing, relatively constant over time. (Figure 3.9) This supports the findings of Janek and co-workers [9] that the interphase layer is a mixed electronic/ionic conductor, where the Li reduces the Ge in the LAGP phase. Electronic conduction might dominate over the ionic conduction in this layer, keeping the resistance of it low, even though a consistent growth of this interphase layer is observed by SEM with time.

3.4.7. Galvanostatic cycling with Li metal electrodes

A rate test was first performed on a Li | LAGP | Li cell to analyse the effect of current density (also abbreviated as 'j') when cycled up to a fixed capacity of 0.1 mAh·cm^{-2} (also abbreviated as 'Q') (Figure 3.11). A stable cell voltage over 5 cycles was achieved for all current densities up to 0.2 mA·cm^{-2}. From 0.5 mA·cm^{-2} onwards the voltage profiles did show some variability as the cycle number increased. Nevertheless, for all current densities, the cell voltage increased linearly with the current density, as illustrated in Figure 3.11.

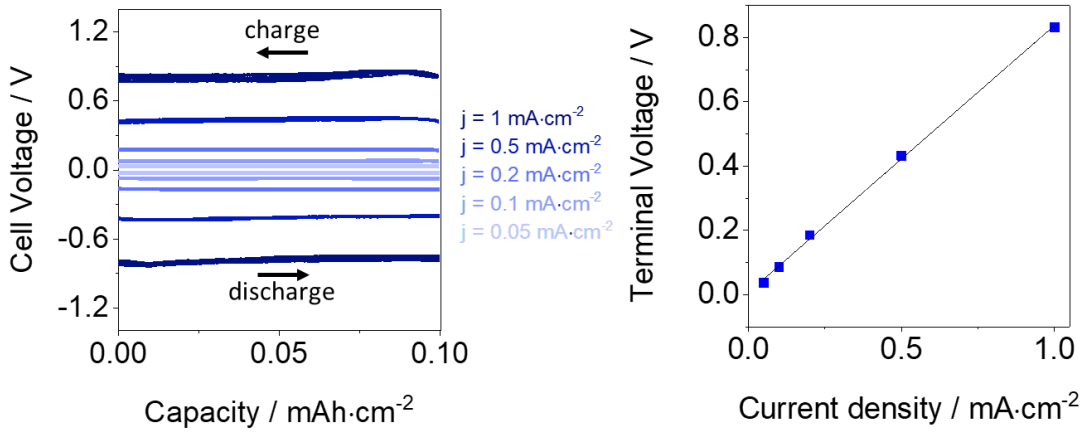


Figure 3.11. Rate test of a Li /LAGP/Li cell cycled at 0.05, 0.1, 0.2, 0.5 and 1 mA·cm^{-2} up to a capacity of 0.1 mAh·cm^{-2} with 5 cycles per current density j (left). Plot of terminal voltage after 5 cycles versus current density (right).

Subsequently, symmetrical Li | LAGP | Li cells were tested at a fixed current density of 0.2 mA·cm^{-2}, the highest and most stable current density from the rate test above, at various capacities (0.1 mAh·cm^{-2}, 0.5 mAh·cm^{-2} and 1 mAh·cm^{-2}) (Figure 3.12). For all three cells, a steady increase in cell voltage with cycle number was observed. The voltage increase per cycle number increased more drastically as the cell was cycled up to a higher capacity. Whereas more than 50 cycles were achieved for the cell cycled at a capacity of

0.1 mAh·cm^{-2}, only 10 and 5 cycles were obtained up to the same cell voltage for the cells cycled at a capacity of 0.5 mAh·cm^{-2} and 1 mAh·cm^{-2}, respectively. This shows that at low current density, the contact time and subsequent reaction time of the LAGP with Li is the limiting factor to the cell's overall lifetime and cycling performance.

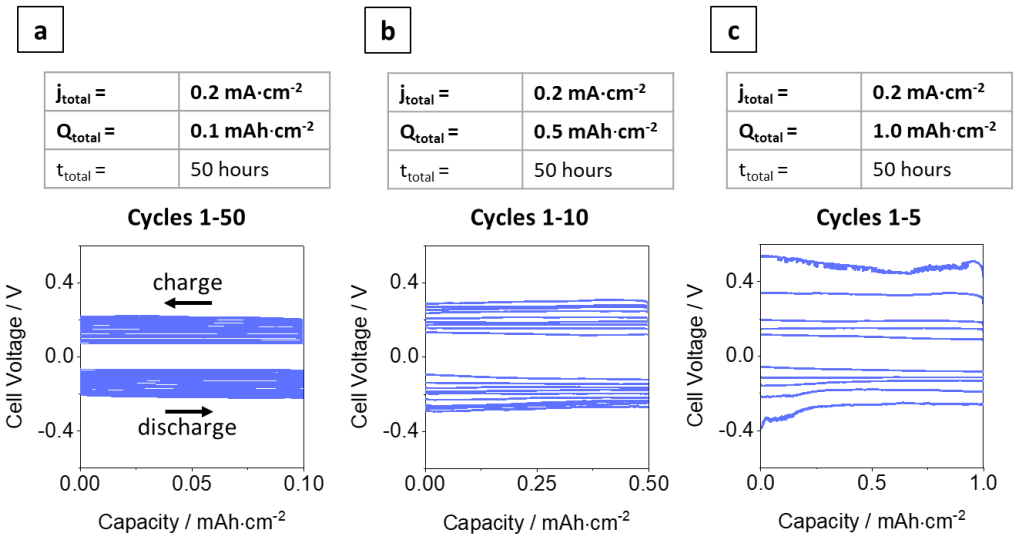


Figure 3.12. Voltage profiles of Li /LAGP/Li cells cycled at a current density of 0.2 mA·cm^{-2} up to a capacity of 0.1 mAh·cm^{-2} for 50 cycles (a), 0.5 mAh·cm^{-2} for 10 cycles (b) and 1.0 mAh·cm^{-2} for 5 cycles (c). All three cells have been cycled for a total of 50 hours at RT.

Further cycling tests at higher current densities from 0.1 mA·cm^{-2} to 2 mA·cm^{-2} up to a fixed capacity of 0.5 mAh·cm^{-2} were performed to understand if cycle time is the only factor affecting cell degradation (Figure 3.13). A drastic increase in the cell voltage per cycle number is observed as the current density is increased from 0.2 to 2.0 mA·cm^{-2}. It is evident that the increase in the cell voltage occurs despite the contact time of LAGP with Li drastically decreasing from 150 hours for the cell cycled at 0.1 mA·cm^{-2} to only 7.5 hours for the cell cycled at 2.0 mA·cm^{-2}. Hence, the cell lifetime is not only limited by the reactivity of LAGP with Li, but also greatly decreases with increasing current density. Whereas the reactivity of LAGP with Li alone is the limiting factor for the cell

aging or the low-current-density cycled cells, the loss in performance is considerably decreased when going to higher current densities.

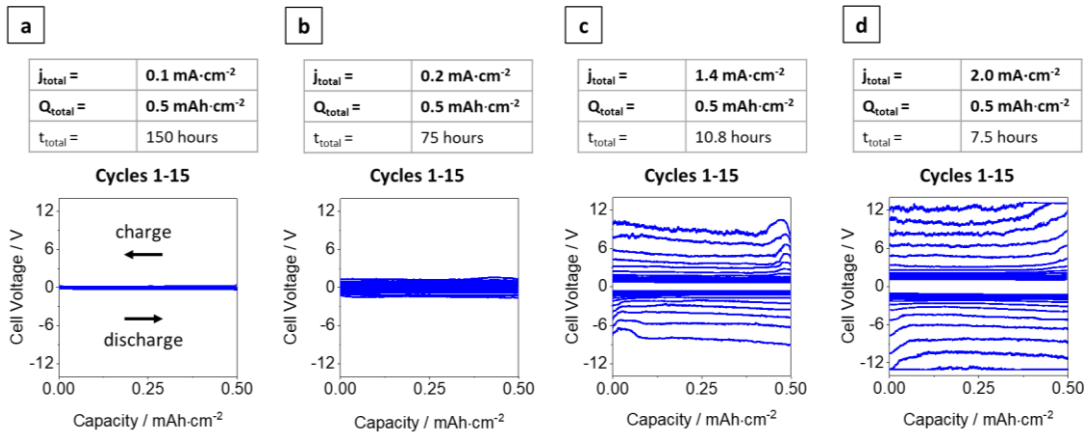


Figure 3.13. Voltage profiles of Li /LAGP/Li cells cycled at a current density of 0.1 mA·cm^{-2} (a), 0.2 mA·cm^{-2} (b), 1.4 mA·cm^{-2} (c) and 2.0 mA·cm^{-2} (d) up to a capacity of 0.5 mAh·cm^{-2} for a total of 15 cycles each at RT.

To understand how the cycling affects the growth of the interphase layer and the overall cell performance, a Li | LAGP | Li cell was cycled at 0.2 mA·cm^{-2} for 20 cycles up to a capacity of 0.5 mAh·cm^{-2} and its impedance between cycles was analysed (Figure 3.14). Over the 20 cycles, the ionic conductivity decreases from 2.6 x 10^{-4} S·cm^{-1} to 1.9 x 10^{-6} S·cm^{-1} at RT (99.3 % decay in conductivity over 100 hours of cycling), corresponding to a much more pronounced drop compared to a cell aged for an equivalent amount of time. As shown in Figure 3.14-c, all four contributions increase in resistance with cycle number. While the intragrain and interphase layer contributions increase gradually together over the 20 cycles, the Li-LAGP interface contribution increases the most within the first 5 cycles, followed by a more pronounced increase of the intergrain resistance between cycle 5 and 10. From the 15th cycle onwards it is specifically the Li-LAGP interface resistance that increases the most.

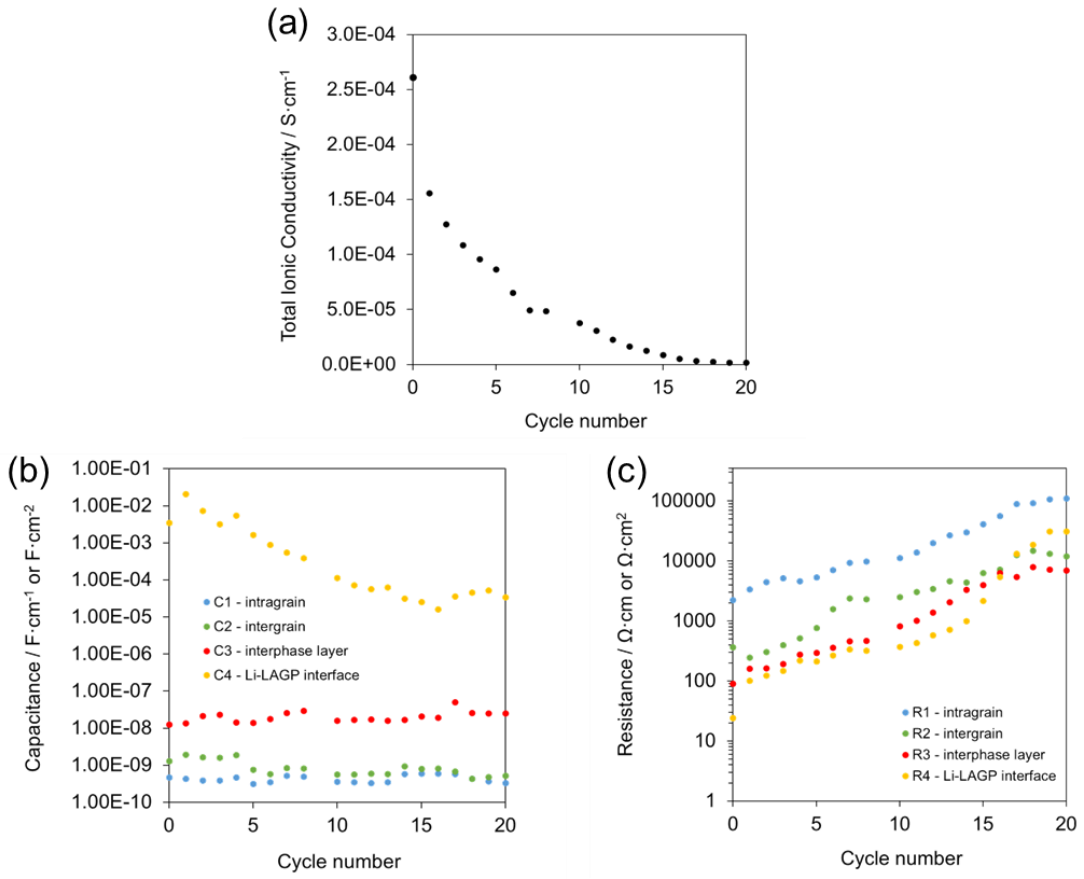


Figure 3.14. EIS analysis of a Li /LAGP/Li cell cycled at 0.2 mA·cm^{-2} up to a capacity of 0.5 mAh·cm^{-2} for 20 cycles at RT: plot of total ionic conductivity (a) and capacitance (b) and resistance (c) of the four different resistances with cycle number. Units of F·cm^{-1} and Ω·cm are used for the intragrain and intergrain contributions, whereas units of F·cm^{-2} and Ω·cm^{2} are used for the interphase layer and Li-LAGP interface contributions.

The voltage profiles after every 5 cycles were also compared along with their corresponding cross-sectional SEM images of the electrode-electrolyte interface (Figure 3.15). While the increase in the cell voltage per cycle remains low for the first 10 cycles, a significant increase of over 1 V per cycle number is observed from the 10th cycle onwards.

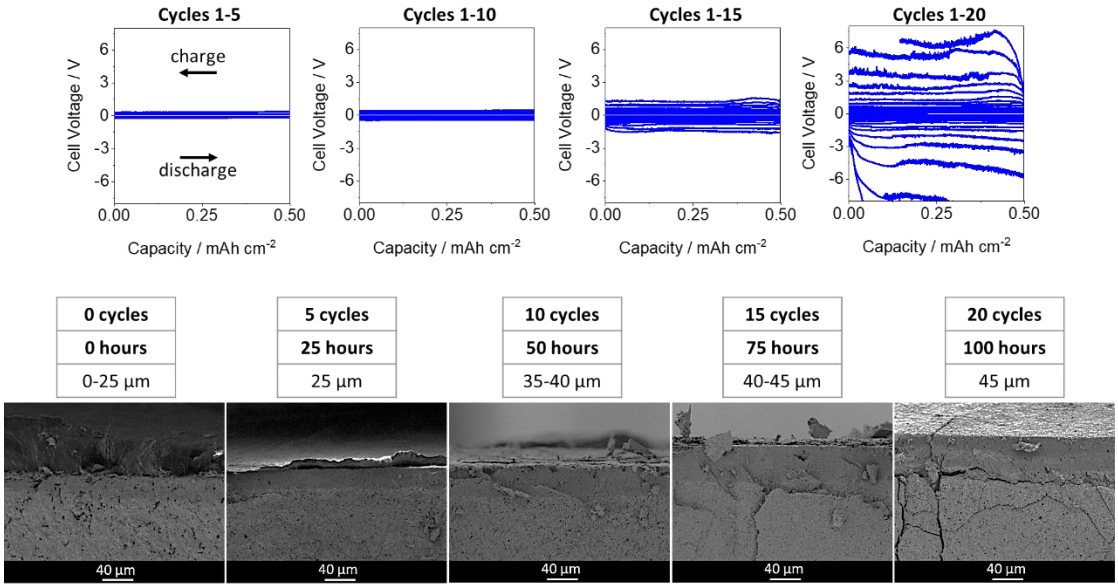


Figure 3.15. Voltage profiles and cross-sectional SEM images of Li /LAGP/Li cells cycled at a current density of 0.2 mA·cm^{-2} and capacity of 0.5 mAh·cm^{-2} for a total of 5, 10, 15 and 20 cycles at RT.

As seen by the associated SEM images in Figure 3.15, an interphase layer of 25 µm is formed along the entire Li-LAGP interface within the first 5 cycles. This is a much more rapid growth than what was observed in the aged cell. Nevertheless, after the rapid start, the growth slows down as the cycling progresses until reaching a maximum thickness of roughly 45 µm. This corresponds approximately to the available thickness of Li metal electrodes used. Hence, the Li metal electrode becomes fully consumed by the reaction with LAGP, which is accelerated by the cycling conditions the cell is exposed to. The rapid formation of the interphase layer between the Li and the LAGP and the associated change in the grain morphology can be related to the initial increase in the Li-LAGP interface followed by an increase in the intergrain resistance within the first 10 cycles. From the 15th cycle onwards, significant cracks become visible in the cross-sectional SEM images. These cracks are initiated between the interphase layer and the bulk LAGP phase, which then propagate perpendicularly into the bulk LAGP electrolyte. The

detachment, and partial loss of contact of a few microns between the interphase layer and the bulk LAGP electrolyte fits with the observed drastic rise in the Li-LAGP interface resistance and cell voltage towards the end of the 20 cycles. As shown by cross-sectional SEM images in Figure 3.16, the detachment becomes more pronounced as the current density is increased.

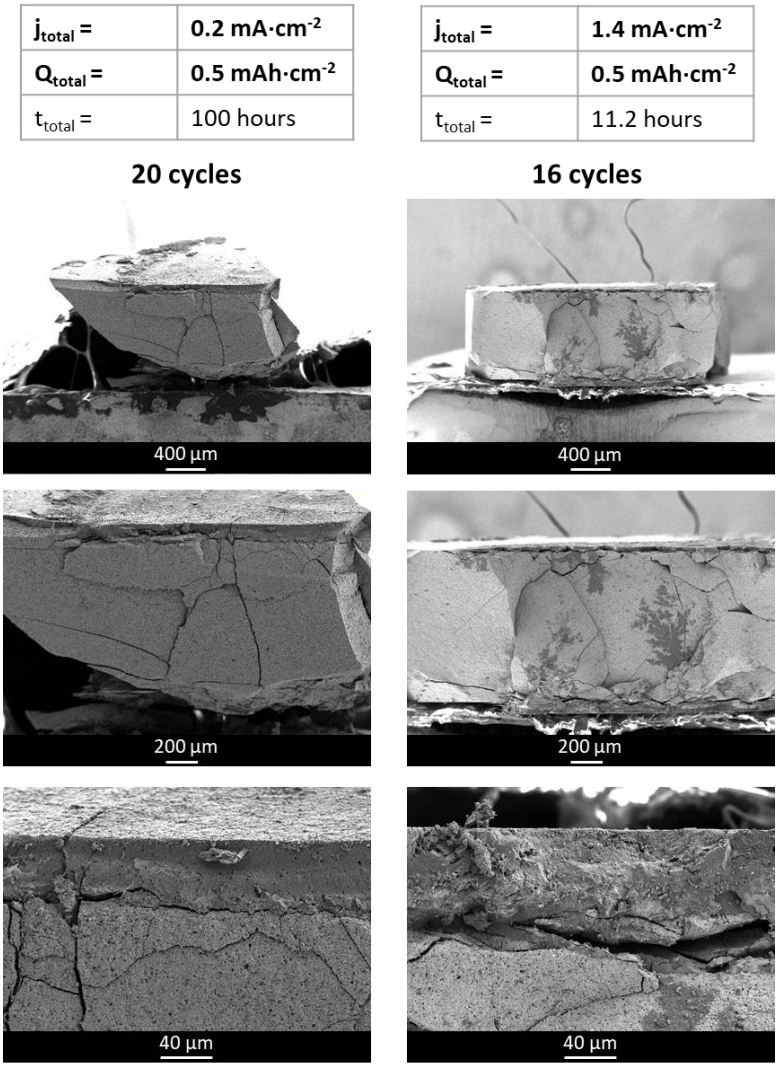


Figure 3.16. Cross-sectional SEM images of Li /LAGP/Li cells cycled at 0.2 mA·cm^{-2} up to a capacity of 0.5 mAh·cm^{-2} until failure (20 cycles, left) and 1.4 mA·cm^{-2} up to a capacity of 0.5 mAh·cm^{-2} until failure (16 cycles, right) at RT.

3.4.8. Analysis of the mechanical properties of LAGP

As shown by the cross-sectional SEM images of the cycled LAGP cells, the formation of cracks through the LAGP phase is a consequence of cycling the LAGP cell, which form and propagate from the initial detachment of the interphase layer from the bulk LAGP during cycling. LAGP is classed in literature as a brittle ceramic.[22] Its brittleness causes the propagation of cracks as seen from cycling in previous sections of this Chapter. It is important to quantify the mechanical properties of the material in order to understand the origin of cell failure and improving the battery lifetime.

For this, strain rate controlled compression tests were performed on rectangular-shaped LAGP samples, polished by a diamond lapping film to a precision of 10 µm in height over a length of 1 mm.

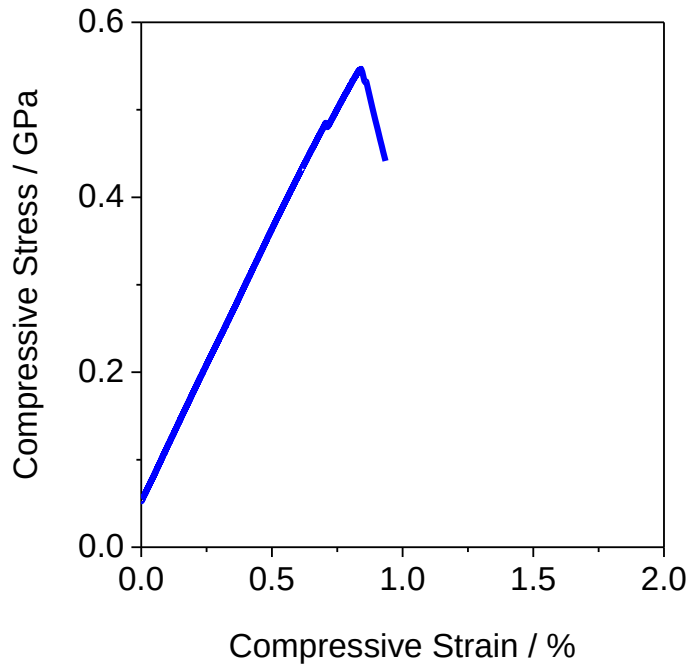


Figure 3.17. Stress-strain curve of LAGP compressed at a constant rate of 1 µm·min^{-1} until failure.

The stress-strain curve in Figure 3.17 confirms the brittle behaviour expected for LAGP, showing an initial linear stress-strain relationship up to a compressive stress of 0.55 GPa, followed by an abrupt fall in stress at a compressive strain of only 0.84 %. From the slope of the initial linear elastic region of the curve, an elastic modulus of 63 GPa was calculated, which is in the expected range of ceramics in general.[23]

An elastic modulus in a similar range was obtained from nanoindentation tests of an LAGP pellet. Here, an average modulus of 90.2 ± 10.5 GPa was calculated, together with an average hardness of 4.5 ± 0.8 GPa (Figure 3.18). The averages were taken between 1000 and 2000 nm of the indentation depth into the surface. These values fit into the modulus and hardness range of other phosphate ceramic electrolytes such as LATP,[24] especially if considering the lower density of the LAGP samples measured in this Chapter (80-86 %) compared to the ones in literature (95-99 %).

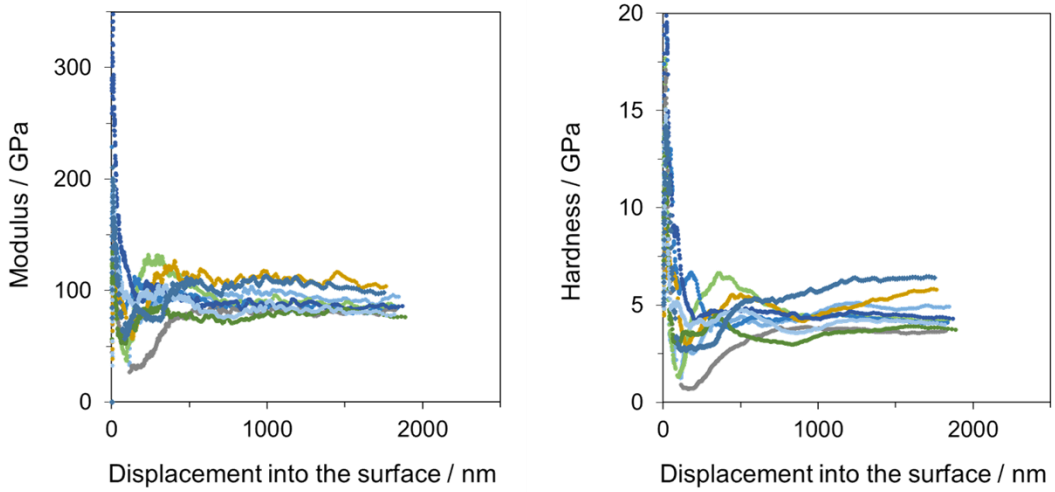


Figure 3.18. Nanoindentation of LAGP: plot of Young's modulus as a function of indenter displacement into the surface (left) and hardness as a function of indenter displacement into the surface (right).

In addition to the compression and indentation tests, a four-point bending experiment was performed on a long rectangular-shaped LAGP beam to analyse the bending properties

of the material. The stress-strain curve shows a similar brittle behaviour as observed in the other tests: an initial linear increase in stress and strain until a maximum flexure stress of 17.7 MPa was reached, followed by a sudden drop at a flexure strain of only 0.13 % corresponding again to fracture and failure of the material (Figure 3.19).

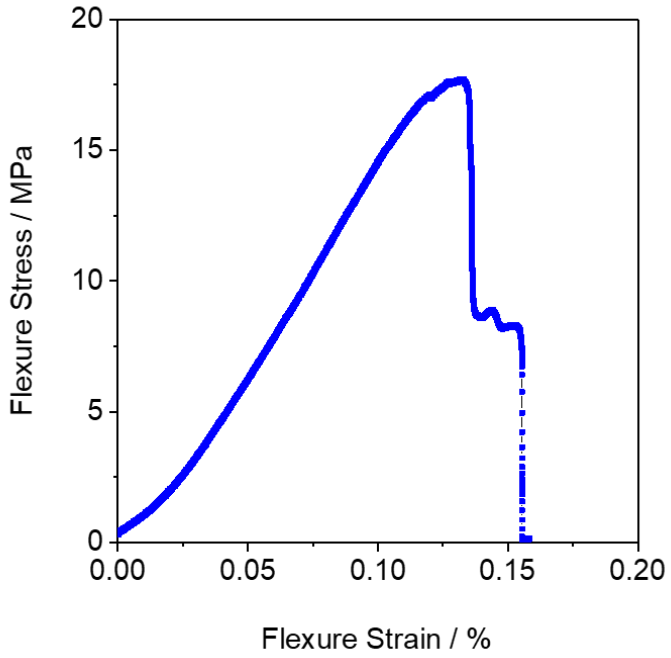


Figure 3.19. Stress-strain curve of LAGP undergoing four-point bending at a constant rate of 5 µm·min^{-1} until failure.

Overall, the mechanical analysis of the material shows that LAGP fractures readily as soon as it reaches a certain stress at only a very low strain, which is consistent with the properties of a ceramic. The mechanical characterisations confirm that LAGP is very stiff until a crack forms, which then leads to instant fracture and failure. The mechanical properties can be influenced by the microstructure such as grain size, grain boundaries, porosity and initial surface flaws. Hence, significant variations in the elastic modulus are expected not only between different experimental setups, but also between different processing procedures, samples and individual indents. The aim of the following

Chapters is to propose a solution on how to mitigate crack propagation in ceramic electrolytes upon cycling, improve their mechanical properties and increase the cell lifetime.

3.5. Conclusions

This Chapter introduced the phosphate ceramic material LAGP and its advantages and disadvantages in its functionality as solid electrolyte. In-depth analyses of its microstructural, electrochemical and mechanical properties were performed to understand the materials properties that lead to cell failure.

LAGP is an attractive material due to its high ionic conductivity of 2.8×10^{-4} $S \cdot cm^{-1}$ at 25 ºC and relatively prolonged stability in air and moisture compared to other solid electrolytes. The material was shown to be fully synthesised in air, which is a significant advantage. Unfortunately, LAGP reacts with Li upon cell assembly causing the growth of a MCI layer of 20-45 µm. The growth of the interphase layer increases with time and is additionally accelerated during cycling when a minimum current density of 0.2 $mA \cdot cm^{-2}$ is applied. The propagative Li-LAGP interphase layer is formed by Li from the Li metal electrodes being consumed and diffusing into the LAGP electrolyte. Hence, the growth of the interphase layer is limited by the amount of Li available or the original thickness of the Li metal electrodes. The difference in the morphology of the interphase layer compared to the bulk electrolyte together with the stresses induced by the applied current through the cell provokes detachment of the interphase layer from the bulk LAGP. This detachment was shown to become more pronounced as the current density is increased. Additionally, the detachment causes further crack propagation perpendicular to the interface into the cell, eventually leading to loss in interfacial contact, high resistances and cell failure. As shown by several mechanical tests performed in this

Chapter, LAGP is a very brittle ceramic, which explains the rapid propagation of cracks through the electrolyte once an initial crack from local stresses has been formed.

While the ionic conductivity of LAGP is sufficiently high, the reactivity of Li with LAGP and LAGP's susceptibility to cracking during cycling are the current major drawbacks in making LAGP a feasible solid electrolyte in future all-solid-state batteries. While the reactivity of Li with LAGP cannot be inhibited unless a change in the chemistry of the solid electrolyte is made or a protective layer between the LAGP and the Li electrode is instated, the following Chapters aim to address the possibility of tuning the mechanical properties of the electrolyte whilst retaining its suitable electrochemical properties.

3.6. References

1. Fu, J. Fast Li+ ion conducting glass-ceramics in the system Li2O–Al2O3–GeO2–P2O5. *Solid State Ionics* **104,** 191–194 (1997).
2. Kichambare, P. D., Howell, T. & Rodrigues, S. Sol-Gel-Derived Lithium Superionic Conductor Li 1.5 Al 0.5 Ge 1.5 (PO 4) 3 Electrolyte for Solid-State Lithium-Oxygen Batteries. *Energy Technol.* **2,** 391–396 (2014).
3. Mariappan, C. R., Yada, C., Rosciano, F. & Roling, B. Correlation between micro-structural properties and ionic conductivity of Li1.5Al0.5Ge1.5(PO4)3 ceramics. *J. Power Sources* **196,** 6456–6464 (2011).
4. Zhang, M. *et al.* Preparation and Electrochemical Properties of Li1+xAlxGe2-x(PO4)3 Synthesized by a Sol-Gel Method. *J. Electrochem. Soc.* **159,** A1114–A1119 (2012).
5. Aono, H., Imanaka, N. & Adachi, G. High Li+ Conducting Ceramics. *Acc. Chem. Res.* **27,** 265–270 (1994).
6. Feng, J. K., Lu, L. & Lai, M. O. Lithium storage capability of lithium ion conductor Li1.5Al 0.5Ge1.5(PO4)3. *J. Alloys Compd.* **501,** 255–258 (2010).
7. Inada, R. *et al.* Properties of aerosol deposited NASICON-type Li1.5Al0.5Ge1.5(PO4)3 solid electrolyte thin films. *Ceram. Int.* **41,** 11136–11142 (2015).
8. Cui, Y. *et al.* Ionic Conductivity and Stability of the Lithium Aluminum Germanium Phosphate. *ECS Trans.* **72,** 139–146 (2016).
9. Hartmann, P., Leichtweiss, T., Busche, M. R. & Schneider, M. Degradation of NASICON-type materials in contact with lithium metal : Formation of Mixed Conducting Interphases (MCI) on Solid Electrolytes. *J. Phys. Chem. C* **117,**

21064–21074 (2013).

10. Wu, B. *et al.* The role of the solid electrolyte interphase layer in preventing Li dendrite growth in solid-state batteries. *Energy Environ. Sci.* **11,** 1803–1810 (2018).

11. Wolfenstine, J., Allen, J. L., Sakamoto, J., Siegel, D. J. & Choe, H. Mechanical behavior of Li-ion-conducting crystalline oxide-based solid electrolytes: a brief review. *Ionics (Kiel).* **24,** 1271–1276 (2018).

12. Wolfenstine, J. *et al.* A preliminary investigation of fracture toughness of Li7La3Zr2O12 and its comparison to other solid Li-ionconductors. *Mater. Lett.* **96,** 117–120 (2013).

13. Porz, L. *et al.* Mechanism of Lithium Metal Penetration through Inorganic Solid Electrolytes. *Adv. Energy Mater.* **1701003,** 1–12 (2017).

14. Marriner-Edwards, C. The development of fibre-reinforced ceramic matrix composites of oxide ceramic electrolyte. (DPhil Thesis, University of Oxford, 2016).

15. Alami, M. *et al.* Structure and thermal expansion of LiGe2(PO4)3. *Journal of Solid State Chemistry* **90,** 185–193 (1991).

16. Alami, M. *et al.* Structure and thermal expansion of LiGe2(PO4)3. *J. Solid State Chem.* **90,** 185–193 (1991).

17. Thokchom, J. S., Gupta, N. & Kumar, B. Superionic Conductivity in a Lithium Aluminum Germanium Phosphate Glass–Ceramic. *J. Electrochem. Soc.* **155,** A915 (2008).

18. Irvine, J. T. S., Sinclair, D. C. & West, A. R. Electroceramics: characterization by impedance spectroscopy. *Adv. Mater.* **2,** 132–138 (1990).

19. Busche, M. R. *et al.* Dynamic formation of a solid-liquid electrolyte interphase and its consequences for hybrid-battery concepts. *Nat. Chem.* **8,** 426–434 (2016).

20. Housecroft, C. E. & Constable, E. C. *Chemistry: An Integrated Approach*. (Longman, 1997).

21. Atkins, P. & Overton, T. *Shriver and Atkins' Inorganic Chemistry*. (OUP Oxford, 2010).

22. Wu, X., Zong, J., Xu, H., Wang, W. & Liu, X. Effects of LAGP electrolyte on suppressing polysulfide shuttling in Li–S cells. *RSC Adv.* **6,** 57346–57356 (2016).

23. Creyke, W. E. C. Mechanical properties of ceramics for design purposes. *Int. J. Mater. Eng. Appl.* **1,** 134–142 (1979).

24. Jackman, S. D. & Cutler, R. A. Effect of microcracking on ionic conductivity in LATP. *J. Power Sources* **218,** 65–72 (2012).

Chapter 4: Synthesis and Characterisation of a 3D Ordered Hybrid Electrolyte using $Li_{1.4}Al_{0.4}Ge_{1.6}(PO_4)_3$ and an Epoxy Polymer

4.1. Aim

The aim of this Chapter is to develop a synthetic route to a solid electrolyte with tuneable mechanical properties whilst retaining a high ionic conductivity at RT. The 3D structured hybrid electrolyte presented in this Chapter is composed of bicontinuous ordered ceramic and polymer microchannels. Continuous ceramic electrolyte channels deliver high ionically conductive pathways for Li-ions, whilst the non-conductive polymer channels provide a 3D structured backbone to mitigate the ceramic's brittle properties. Its electrochemical and mechanical properties are compared to those of a pure ceramic electrolyte.

4.2. Introduction

Ceramic and glass-ceramic electrolytes have recently gained a lot of attention due to their high ionic conductivity at RT.[1–3] Nevertheless, their brittleness[4,5] and poor interfacial impedances[6] and stabilities with Li[7,8] are major drawbacks. On the contrary, polymer electrolytes show more favourable mechanical and interfacial properties due to their softness and flexibility, but unfortunately their ionic conductivity at RT is yet too low to be practically viable.

In this Chapter, a novel concept of a hybrid solid electrolyte is investigated. The idea is to combine a high ionically conductive ceramic electrolyte with a non-conductive mechanically favourable polymer to form a 3D ordered bicontinuous hybrid electrolyte. Using 3D printing, full control of the 3D microarchitecture and ceramic-to-polymer ratio

is ensured. The generation of 3D interconnecting microchannels renders the hybrid more resilient to the propagation of cracks compared to one-dimensional (1D) nanofibers and maximises alternative Li-ion conduction routes in the case of fracture. This Chapter introduces for the first time the synthesis of such a hybrid electrolyte using LAGP as the Li-ion conducting component and an epoxy polymer, a non-conducting and chemically stable polymer, as the polymeric component. The favourable Li-ion conducting properties, its chemical stability and synthesis in air make LAGP a good first candidate to be used in this work. The synthesis of the LAGP-epoxy hybrid electrolyte is in the first instance demonstrated by the use of a 3D printed template with a gyroid microarchitecture, together with a final 70 % ceramic to 30 % polymer volume ratio. The subsequent Chapter will address the effect of microarchitecture and ceramic-to-polymer ratio on the performance of the hybrid. The properties of the hybrid electrolyte are investigated by EIS, galvanostatic cycling and mechanical testing, and compared to the properties of a LAGP pellet.

4.3. Experimental Methods

4.3.1. Synthesis of the 3D structured LAGP-epoxy hybrid electrolyte

4.3.1.1. Design of the gyroid microarchitecture and template

A unit cell with a gyroid geometry is designed with Matlab R2014b (8.4.0.150421) using following input parameters for the gyroid surface:

```
a=2*π;

s=2*π/60;

[x,y,z]=meshgrid(-a:s:a,-a:s:a,-a:s:a);

cx = cos(2*x);
```

```
cy = cos(2*y);

cz = cos(2*z);

u = 50.0*(cos(x).*sin(y)+cos(y).*sin(z)+cos(z).*sin(x))-0.5*(cx.*cy+cy.*cz+cz.
*cx)-52;

[f,v]=isosurface(u,0);

vertface2obj(v,f,'thinfig%.obj')
```

The generated surface was exported as an obj. file and imported into Netfabb Professional (7.4.0). Any faults (e.g. open faces in the gyroid model) were repaired with the repair function of the software until a water-tight solid model was created. The unit cell was then multiplied to generate a print block of approximately 260 μm^3, which matches the printing field of the laser (up to 300 μm^3). The gyroid print block comprises a total of 2 x 2 x 2 gyroid unit cells. Additional print extensions were added to the print block to allow for enough overlap between the print blocks when stitched together during the template printing process. For this, the print block was imported into Netfabb Professional (7.4.0) and duplicated until the original print block was fully surrounded with no gaps in between. Using the cutting function, all surrounding print blocks were cut at exactly 10 µm distance away from the original print block. The remaining parts of the print block were removed, leaving behind only the original print block with a 10 µm extension in all three dimensions. The new print block with print extensions was merged together into one unit, made water-tight with the repair function and finally exported as a .stl file. The print block with print extensions was then imported as .stl file into DeScribe (2.3.4) and converted into a print ready .gwl file.

4.3.1.2. 3D printing of the gyroid template

A commercial stereolithography instrument (NanoScribe Photonic Professional GT System) was used to generate the 3D template with a gyroid microarchitecture. The print ready .gwl file of the gyroid template was imported into the software NanoWrite (1.8.3). The print block with print extensions was sliced into 1 µm thick layers. The hatching distance between voxel lines was set to 500 nm. A UV-sensitive photoresist (IP-S, NanoScribe) was dropped onto an indium-tin-oxide coated glass slide substrate, which was attached onto a sample holder and reversely inserted into the instrument. A 25x objective with numerical aperture of 0.8 was dipped into the photoresist. A laser with a wavelength of 780 nm was focused through the objective into the UV-curable photoresist which polymerised at the point of contact, firstly along the x- and y-direction followed by building up the structure in the z-direction. Several print blocks of 211 μm^3 in size were stitched together with an overlap of 10 µm until the desired gyroid template size was reached. After the printing process was complete, residual non-polymerised photoresist was removed by a two-step washing procedure using propylene glycol monomethyl ether acetate (>99.5 %) followed by isopropanol (99.5 %). The templates were then left at RT to dry.

4.3.1.3. Synthesis of the LAGP ceramic electrolyte

LAGP was synthesised as described in Chapter 3 Section 3.3.1. Freshly ball-milled LAGP powder was used in the following step of the hybrid electrolyte synthesis.

4.3.1.4. Synthesis of the structured LAGP scaffold

A 3D printed template was placed in a 0.75 mL glass vial and immersed in a suspension of 100 mg ball-milled LAGP powder in 0.7 mL of solvent (methanol, 99.99 %). The suspension with the template was sonicated for 5 minutes followed by centrifugation at

2000 rpm for 2 minutes, all of which was repeated twice. Clear solvent remaining above the compacted powder was removed and an additional suspension of 100 mg ball-milled LAGP powder in 0.7 mL solvent (methanol, 99.99 %) was added to the sediment. The vial was then again centrifuged at 2000 rpm for 2 minutes, sonicated for 5 minutes, and again centrifuged at 2000 rpm for 2 minutes. This procedure was repeated until the template was fully covered in sedimented LAGP powder. Excess clear solvent was removed and the filled 3D printed template was carefully extracted from the vial. Excess LAGP powder on the surface of the filled template was removed and polished on a diamond lapping film. The filled 3D templates were placed on an Au crucible and sintered at 900 °C for 5 hours with a heating rate of 2 °C·min^{-1} and a cooling rate of 10 °C·min^{-1} to generate the structured LAGP scaffold.

4.3.1.5. Epoxy polymer filling of the structured LAGP scaffold

The newly formed empty channels of the structured LAGP scaffold were impregnated with an epoxy polymer made from a 15:2 volume ratio mixture of Struers EpoFix Resin and EpoFix Hardener, respectively. The LAGP scaffold was immersed into the mixture under a dynamic vacuum for up to 2 hours at RT. The filled LAGP scaffold was removed before total solidification of the epoxy polymer was achieved. Excess polymer was manually removed, before the sample was left to dry and harden at RT overnight.

4.3.2. Microstructural analysis

4.3.2.1. SEM and EDX

LAGP and LAGP-epoxy hybrid electrolytes at different stages of their synthesis were examined by SEM and EDX as described previously in Chapter 3 Section 3.3.2.1. The same sample preparation method as described in Chapter 3 Section 3.3.2.1 was used.

4.3.2.2. PXRD

PXRD was performed on the synthesized LAGP and structured LAGP scaffolds using the preparation and parameters as previously described in Chapter 3 Section 3.3.2.2.

4.3.2.3. X-ray micro-CT

A Skyscan 1172 system (Bruker microCT, Kontich, Belgium) at the University of Edinburgh was used to generate shadow-projection images of the LAGP-epoxy hybrid electrolytes at various stages of their synthesis. The sample were rotated by 0.36° until a full 360° rotation was achieved. The Skyscan 1172 system operates using a source voltage of 70 kV (Hamamatsu 100/250), an Al + Cu filter and an image pixel size of 2.50 µm (Hamamatsu 10 Mp camera). The recorded images were reconstructed into stacks of axial slices by the NRecon software package using a beam hardening correction of 20 %, a frame averaging of 8 and no random movement. ImageJ (version Fiji) was used to reconstruct and view the data in 3D.[9] An inner 500 x 500 x 500 μm^3 volume was cut out of the data stacks and aligned with Cartesian axes by an interactive stack rotation function. The cut-out data was smoothed three times, inspected and thresholded. Ultimately, ImageJ '3D Viewer' was used to produce 3D surface renderings. Adaptations in the imaging and rendering parameters were made between different types of scanned samples to account for differences in contrast.

4.3.3. Electrochemical analysis

4.3.3.1. EIS

EIS was performed on the LAGP pellets and LAGP-epoxy hybrid electrolytes with symmetrical Au and Li electrodes as previously described in Chapter 3 Section 3.3.3.1. For the cells with Au blocking electrodes, the polishing method described in Chapter 3

Section 3.3.3.1 was followed. For cells with Li electrodes, the polishing method described in Chapter 3 Section 3.3.3.2 was followed.

4.3.3.2. Galvanostatic cycling

Galvanostatic cycling of Li | LAGP | Li and Li | gyroid LAGP-epoxy | Li cells was performed using the testing and preparation parameters as described in Chapter 3 Section 3.3.3.2. LAGP pellets of 4.4 mm in diameter and 1 mm in thickness and square-shaped gyroid LAGP-epoxy hybrid electrolytes of 2.6 mm × 2.6 mm in length and width, respectively, and 0.7 mm in thickness were measured.

4.3.4. Mechanical analysis

4.3.4.1. Compression testing

Rectangular-shaped samples of 1 mm x 1 mm x 2 mm in width, length and height, respectively, of LAGP and gyroid LAGP-epoxy hybrid electrolytes were prepared and tested as detailed in Chapter 3 Section 3.3.4.1.

4.3.4.2. Four-point bending

LAGP and gyroid LAGP-epoxy hybrid electrolyte beams of 12 mm x 3 mm x 0.5 mm in length, width and height, respectively, were prepared and tested using the method and parameters described previously in Chapter 3 Section 3.3.4.2.

4.4. Results and Discussion

4.4.1. Synthesis of the 3D LAGP-epoxy hybrid electrolyte

The synthesis of a 3D bicontinuously ordered LAGP-epoxy hybrid electrolyte was achieved by a templating/casting procedure, which converts an initial 3D polymer

template with a gyroid microarchitecture into a 3D structured LAGP scaffold with macroporous gyroid channels, which are then refilled by an epoxy polymer. An overview of the developed synthetic procedure is shown in Figure 4.1 by a schematic.

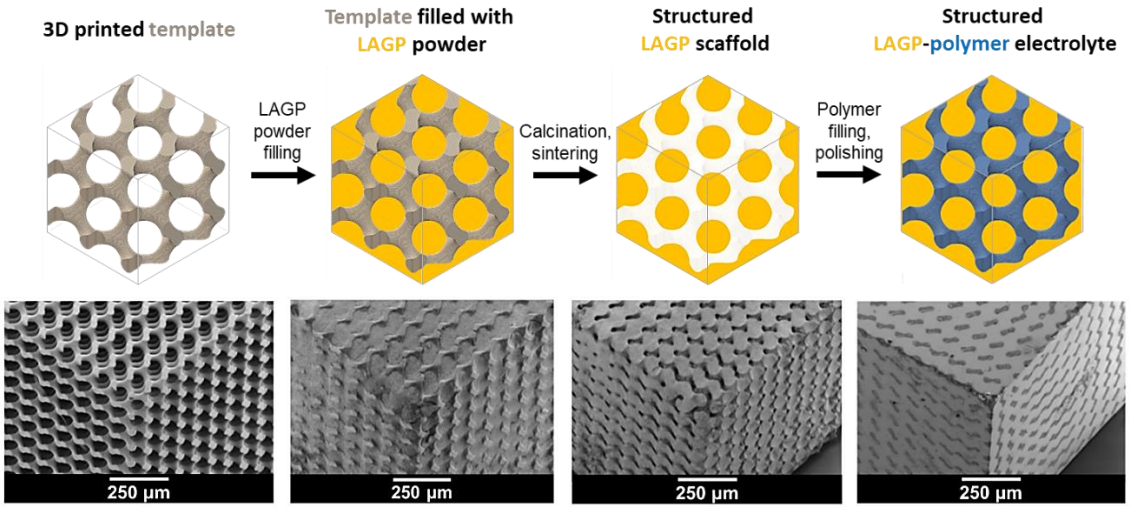


Figure 4.1. Synthesis procedure of a LAGP-epoxy hybrid electrolyte with a gyroid microarchitecture. Corresponding SEM images of each synthesis step are shown below the schematic representation.

The conversion of a 3D printed gyroid template into the final structured LAGP-epoxy hybrid electrolyte is a significant challenge as the microstructure needs to be maintained on both the micrometre and millimetre range. It is important to obtain a high degree of LAGP filling to achieve a dense ceramic electrolyte channel with the highest possible conductivity. This cannot be achieved by the use of a sol-gel precursor solution as this results only in a partial filling of the ceramic channels. Hence, a filling procedure was developed that employs a suspension composed of calcined LAGP powder with grain sizes below 5 µm and methanol as the solvent.

4.4.1.1. Design and fabrication of the 3D printed gyroid template

The design and fabrication of the 3D polymer template with a gyroid microarchitecture is achieved by a stereolithography technology based on a two-photon polymerisation process of a UV-curable photoresist by an ultra-short pulsed laser.

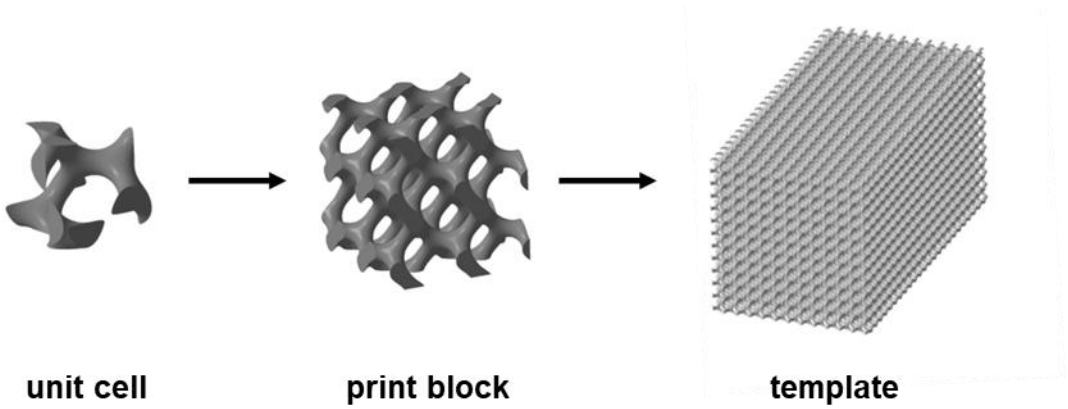


Figure 4.2. Computed models of the gyroid unit cell, print block and final template.

Firstly, a 'unit cell' (the simplest repeatable unit) of the gyroid template is designed, which is then multiplied to obtain a 'print block' of up to 300 μm^3 in size. This is the maximum size of the laser's printing field, which the laser can access before the stage itself has to be moved. The stitching of several 'print blocks' together generates the final gyroid template of any desired size. Figure 4.2 illustrates computed models of the unit cell, the print block and the final gyroid template used for the hybrid electrolyte synthesis. The building process of the 'print block' first occurs in the x- and y-direction of the printing field followed by a layer-by-layer build in the z-direction as shown in Figure 4.3-1. Each of the gyroid 'print blocks' of 211 μm^3 in size are then stitched together with an overlap of 10 µm until the desired gyroid template size is reached as illustrated in Figure 4.3-2. A template of approximately 1.2 mm x 2.4 mm x 1.2 mm in width, length and height requires 8 to 12 hours of printing time depending on the template geometry and the polymer-to-channel ratio.

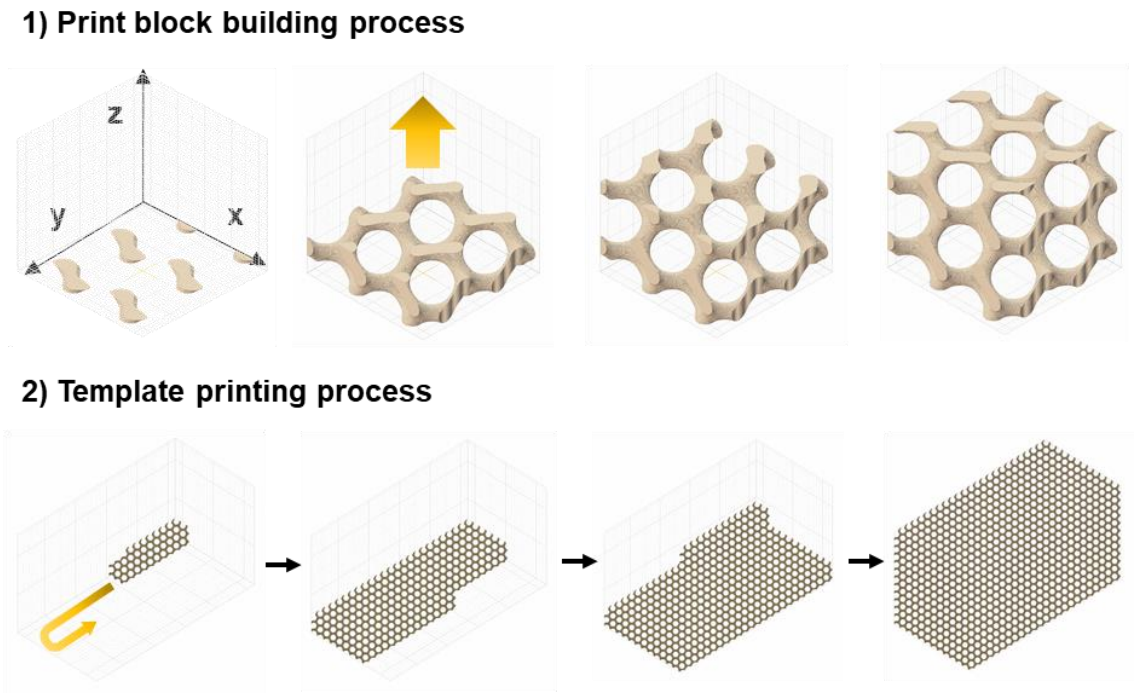


Figure 4.3. Schematic of the printing process of the gyroid print block (211.1 µm^3) and the final gyroid template (1.27 mm × 1.27 mm × 2.53 mm).

The template geometry was designed with a 85 % porosity consisting of empty gyroid channels with an average empty channel diameter of 67 µm and a 15 % solid volume fraction with an average polymer channel diameter of 20 µm. This ensures the synthesis of a hybrid electrolyte with wide enough channels and ceramic electrolyte volume fraction to achieve a good ionic conductivity within the final LAGP-epoxy hybrid electrolyte. Due to shrinkage during the printing and development stage, the 3D printed gyroid template is 5 % smaller than the original computational design.

4.4.1.2. Filling procedure of the 3D printed gyroid template

The filling procedure consists of alternating centrifugation and sonication processes of a 3D gyroid polymer template immersed in a suspension composed of calcined and ball-milled LAGP powder and methanol. Repeated centrifugation and sonication steps enable the suspension to fully penetrate inside the empty gyroid channels and fill the 3D

printed template without blocking any empty volume. While centrifugation allows fast sedimentation and compaction of the ceramic particles, sonication agitates the particles between sedimentation steps to achieve an efficient particle distribution within the template. The LAGP grain size is small enough to successfully penetrate deep into the channels and achieve a high level of filling as reported in Table 4.1. Methanol has shown to be an effective solvent that evaporates quick enough to allow for the LAGP grains to sediment and compact nicely in the channels. Sintering of the filled template at 900 °C for 5 hours in air allows for the initial polymer template to be combusted without leaving any carbon residue behind, whilst the LAGP grains sinter together to form dense LAGP channels. Whereas the template shape is well maintained, the size of the template shrinks by roughly 40 %. An average solid volume fraction of 70 % LAGP phase with a 30 % empty volume fraction was recorded. Finally, an epoxy polymer is filled into the newly created channels to generate the final gyroid LAGP-epoxy hybrid electrolyte with a ceramic-to-polymer ratio of 70 % to 30 %, respectively. Table 4.1 summarises the varying template parameters between each stage of the synthesis.

Table 4.1. Detailed parameters of the template at each stage of the gyroid LAGP-epoxy electrolyte synthesis.

Synthesis Stage	Parameter	Value
Unit cell	Cubic unit cell dimension x=y=z / µm	105.6
Print block	Unit cells per print block in x, y, z direction	2 x 2 x 2
	Cubic print block dimension x=y=z / µm	211.1
Template design	Print blocks per template design in x, y, z direction	6 x 6 x 12
	Length x, y, z / mm	1.27 x 1.27 x 2.53
	Volume / mm^3	4.07
	Solid volume fraction / %	15.6
	Average empty channel size / µm	66.4
	Average wall thickness / µm	20.4
Printed Template	Weight / mg	0.95
	Length x, y, z / mm	1.26 x 1.26 2.51
	Volume / mm^3	3.98
	Vol. shrinkage during printing / %	2
Template filled with LAGP powder	Weight / mg	7.54
	Length x, y, z / mm	1.30 x 1.33 x 2.66
	Volume / mm^3	4.60
	Filled amount of LAGP / mg	6.59
	Vol. expansion during filling / %	16
Structured LAGP scaffold	Weight / mg	6.60
	Length x, y, z / mm	1.11 x 1.12 x 2.24
	Volume / mm^3	2.78
	Density / mg mm^{-3}	2.37
	Vol. shrinkage during sintering / %	40
	Overall volume shrinkage / %	32
	Solid volume fraction / %	72.6
	Average LAGP thickness / µm	44.0
	Average empty channel size / µm	20.8
Structured LAGP-epoxy electrolyte	Weight / mg	6.36
	Length x, y, z / mm	1.06 x 1.07 x 2.13
	Volume / mm^3	2.40
	Density / mg mm^{-3}	2.65

4.4.2. Characterisation of the 3D LAGP-epoxy hybrid electrolyte

As shown by SEM images and micro-CT scans, the gyroid microarchitecture was well replicated throughout all stages of the synthesis (Figure 4.4).

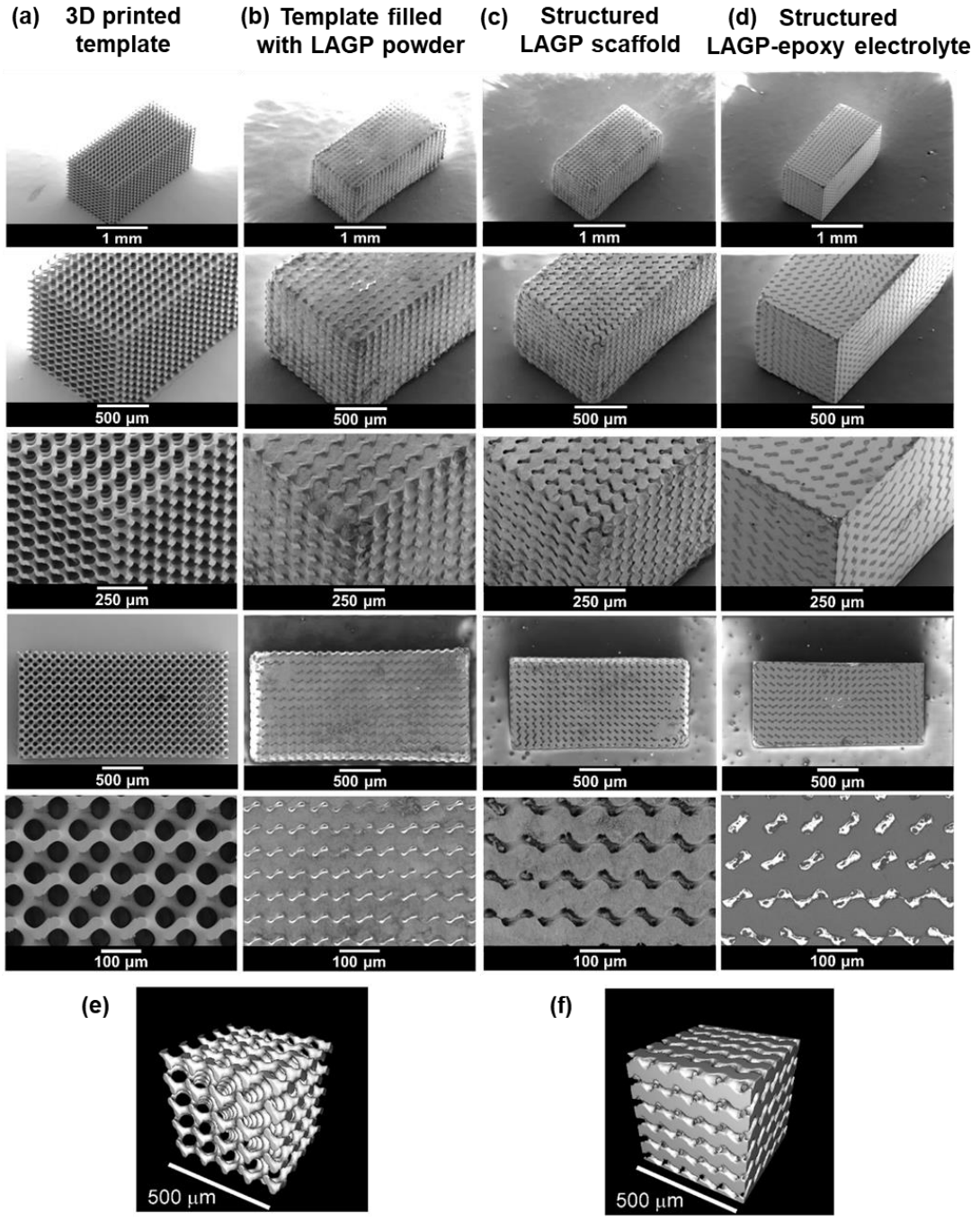


Figure 4.4. SEM images of each stage of the gyroid LAGP-epoxy electrolyte synthesis (a-d) and micro-CT scans of the 3D printed template prior filling (e) and of the structured LAGP scaffold after the sintering step (f).

PXRD patterns were compared between the LAGP phase in the structured LAGP scaffold and the LAGP phase in a pure LAGP pellet. Figure 4.5 shows that no differences in the LAGP patterns were observed between the LAGP pellet, the structured LAGP scaffold and the known undoped equivalent phase $LiGe_2(PO_4)_3$ reported in literature (PDF-01-080-1922). The LAGP phase remains unchanged even after in contact with methanol for a short period of time during the hybrid's synthesis.

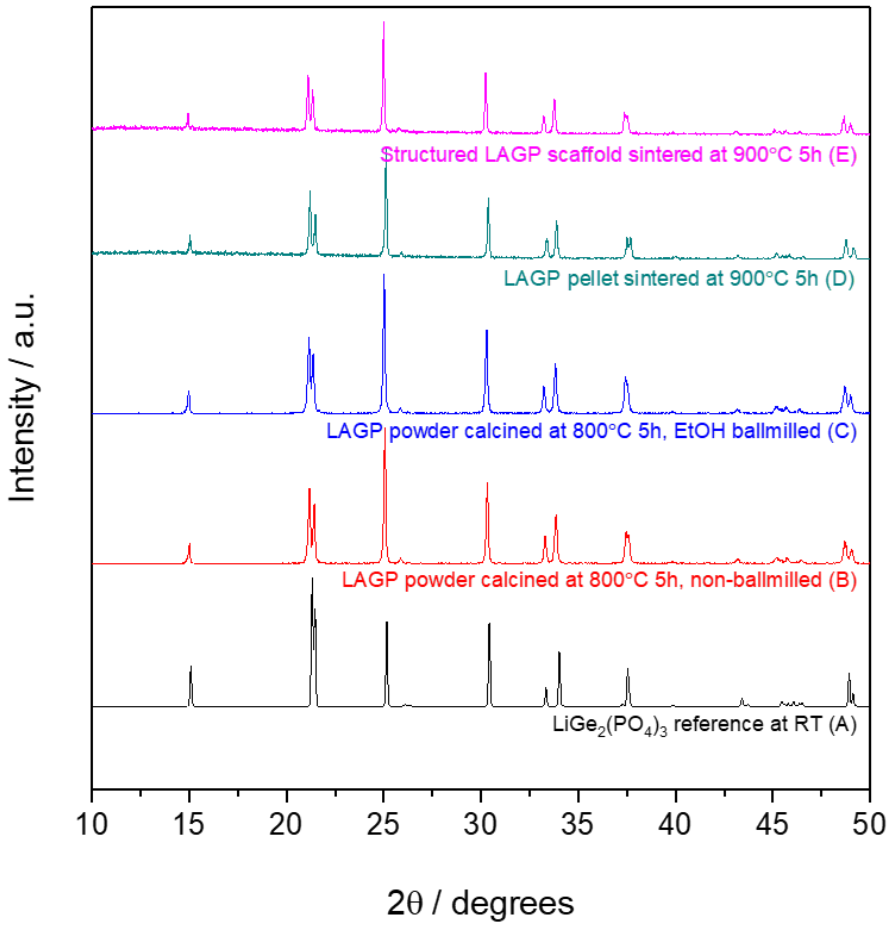


Figure 4.5. PXRD patterns of LAGP before ball milling (B), LAGP after ball milling (C), LAGP sintered as a pellet (D) and LAGP sintered within a 3D template to form the LAGP scaffold (E).

EDX mapping of the gyroid LAGP-epoxy hybrid electrolyte shows that the LAGP and the epoxy phases are well distinguished into two separate channels. A high concentration

of O, Al, P and Ge was detected in the LAGP channels, whereas only C was detected in the epoxy channels (Figure 4.6).

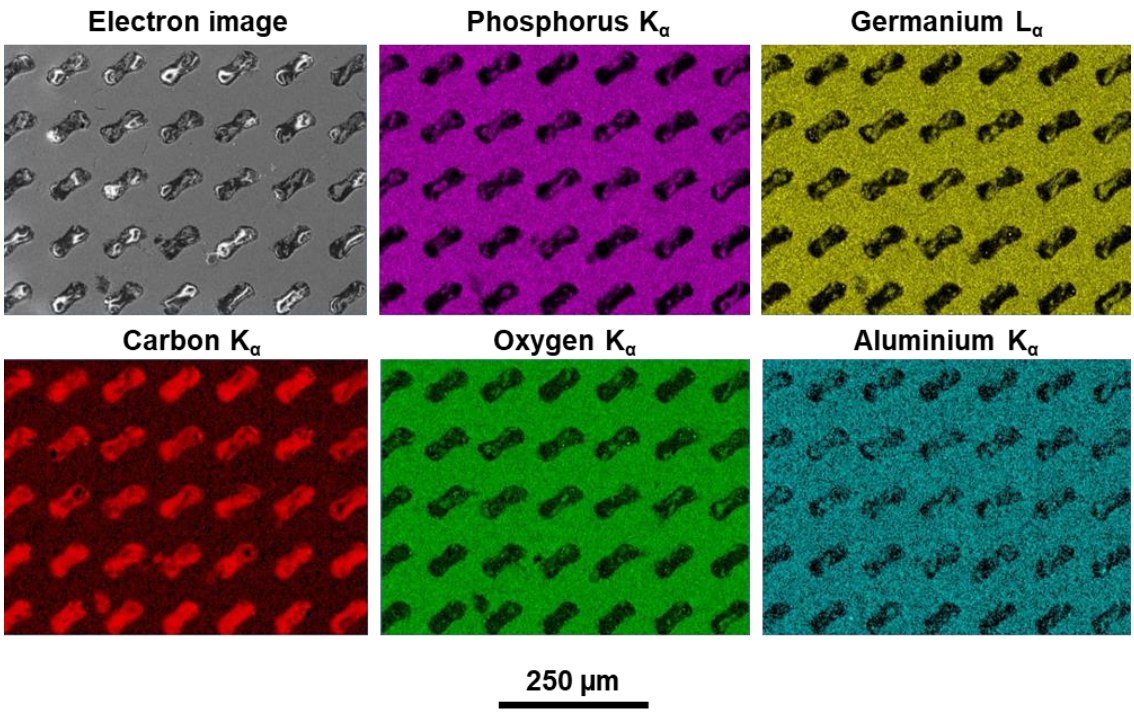


Figure 4.6. EDX mapping of the polished surface of the gyroid LAGP-epoxy electrolyte.

Additionally, similar LAGP phase densities were achieved between the gyroid LAGP-epoxy hybrid and the pellet. The LAGP density in the pellet was 3.1 $mg \cdot mm^{-3}$ (ca. 90 % of the theoretical density of LAGP). The overall density of the structured LAGP scaffold including the 30 % volume of empty channels was measured to be 2.4 $mg \cdot mm^{-3}$, which corresponds to approximately 75 % of the density of the LAGP pellet (Table 4.1). Hence, the recorded density matches well with the percentage solid volume fraction of LAGP phase in the LAGP-epoxy hybrid electrolyte and shows that an equally well densification of the LAGP grains can be achieved during the synthesis of the hybrid as in the LAGP pellet. This is a significant achievement as it shows that both ceramic phases should achieve similar ionic conductivities as the composition and densification of LAGP is unchanged in both samples. The ionic conductivity in the hybrid can therefore only be reduced by the volume fraction of insulating polymer present in the channels.

4.4.3. Impedance measurements with Au blocking electrodes

The electrochemical performance between the gyroid LAGP-epoxy hybrid electrolyte and an LAGP pellet was compared in the first instance by EIS measurements. Symmetrical cells with Au blocking electrodes were assembled and Nyquist plots were recorded for both electrolytes at RT, low temperature (-30 °C) and over a temperature range from -30 °C to 80 °C (Figure 4.7).

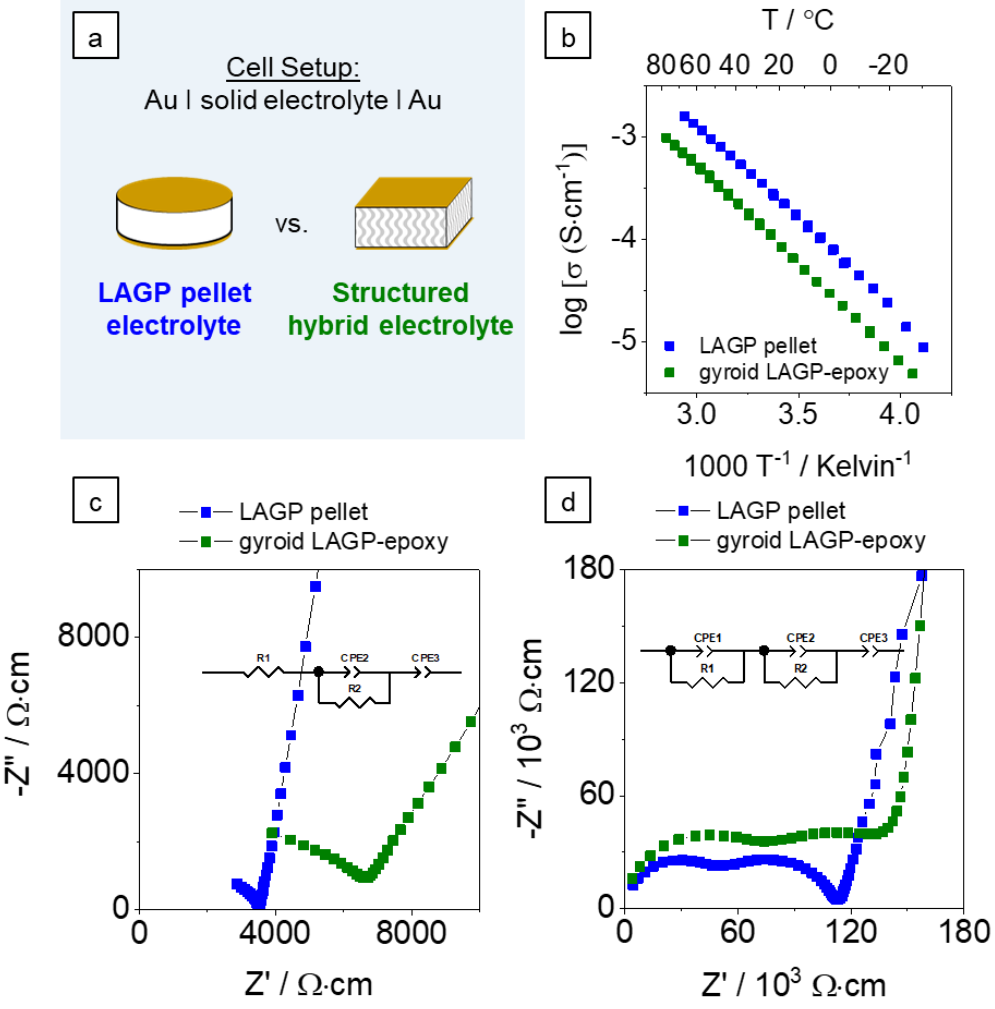


Figure 4.7. EIS analysis of symmetrical Au | LAGP | Au and Au | gyroid LAGP-epoxy | Au cells: (a) schematic of the cell setup, (b) Arrhenius plot showing the dependence of impedance over a temperature range of -30 °C to 80 °C, (c) and (d) the Nyquist plots and their corresponding equivalent circuit at RT and at -30 °C, respectively.

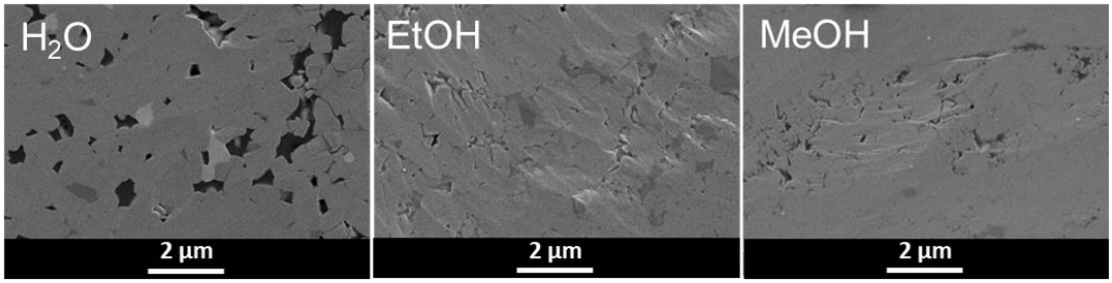
At RT, both LAGP and LAGP-epoxy electrolyte show a partially visible semicircle at high frequency corresponding to the electrolyte followed by a distinct spike at lower frequency for the blocking electrodes. The data were best fitted using a series of a resistor (R_1) for the high frequency contribution, a resistor and constant-phase element in parallel (R_2//CPE_2) for the partially visible semicircle and a constant-phase element in series (CPE_3) for the spike at lower frequency. In order to reveal more of the data in the high frequency range, the cells were cooled down to a temperature of -30 °C. For both LAGP and LAGP-epoxy hybrid electrolytes, two slightly overlapping but distinct semicircles were recorded. The data were best fitted to two parallel combinations of a resistor and a constant-phase element (R_1//CPE_1 and R_2//CPE_2) in series for the two semicircles respectively, followed by a constant-phase element (CPE_3) for the spike. As discussed in Chapter 3, the two semicircles are attributed to contributions from the LAGP electrolyte whereas the spike is indicative of symmetrical Au blocking electrodes. Capacitance values for R_1//CPE_1 and R_2//CPE_2 in the range of 10^{-11} F·cm^{-1} and 10^{-10} F·cm^{-1} for both the LAGP and the gyroid LAGP-epoxy hybrid electrolyte were calculated, respectively. The two semicircle can therefore confidently be assigned to the intragrain (bulk) and intergrain (grain boundaries) Li-ion transport in the LAGP phases. Appendix 5 summarises the resistance and capacitance values obtained for both cells at low and RT.

Overall, a total ionic conductivity of 1.6 x 10^{-4} S·cm^{-1} and 2.8 x 10^{-4} S·cm^{-1} was recorded at RT for the gyroid LAGP-epoxy and LAGP pellet, respectively. These conductivities were calculated using the entire Au area in contact with the sample and the thickness of the sample. The volume fraction of non-conductive polymer phase as well as the tortuosity present in the hybrid electrolyte, which both affect the Li-ion conduction through the material, were not taken into account. To compare the ionic conductivity of the LAGP phase of both samples more accurately, a geometry factor (also referred to as

a ‘current distribution factor’) of 0.58 was calculated by finite element modelling (Appendix 6), which takes into account the geometry of the hybrid and the 70 % LAGP volume fraction present in the sample. Consequently, the ionic conductivity of the LAGP phase in the gyroid LAGP-epoxy and LAGP pellet is 2.7×10^{-4} S·cm^{-1} and 2.8×10^{-4} S·cm^{-1} at RT, respectively. This confirms once more that the synthesis of the hybrid electrolyte achieves a high degree of LAGP filling and ultimately sinters the hybrid as well as a LAGP pellet, with nearly no increase in additional resistance. Furthermore, Arrhenius plots measured over a temperature range of -30 °C to 80 °C, confirm the stability of the gyroid LAGP-epoxy hybrid electrolyte within a wide range of temperatures. Activation energies of 36.7 kJ·mol^{-1} and 35.5 kJ·mol^{-1} for the gyroid LAGP-epoxy and LAGP pellet, respectively, were recorded. Both values are in agreement with previous reports on LAGP.[10]

4.4.4. Effect of solvent on the filling procedure

Optimisation of the hybrid electrolyte synthesis showed that the choice of solvent used in the filling procedure plays a significant role in achieving the required LAGP phase density that ultimately leads to a high ionically conductive hybrid electrolyte. Several solvents have been tested, with ethanol, water and methanol being the most promising ones. For all three solvents, the 3D printed polymer template could be replicated into a structured LAGP scaffold and backfilled with an epoxy polymer. However, for each solvent, different degrees of LAGP filling were achieved, which resulted in significant differences in the overall sample density and final ionic conductivity. SEM images of the etched LAGP phase surface of three LAGP-epoxy hybrid electrolytes using water, ethanol and methanol as filling solvents, highlight the differences in porosity obtained (Figure 4.8).



	H_2O	Ethanol	Methanol
LAGP filling range in printed template / mg	4 - 5.5	4 - 5	5.5 - 6.5
Density range in structured LAGP scaffold / mg·mm^{-3}	1 - 1.5	1.6 - 2.0	2 - 2.4
Ionic conductivity of LAGP-epoxy electrolyte at RT / S·cm^{-1}	3 x 10^{-5}	7 x 10^{-5}	1.5 x 10^{-4}

Figure 4.8. SEM images of the LAGP phase within LAGP-epoxy electrolytes using H_2O, ethanol and methanol as filling solvent. The surfaces of the LAGP phases were etched prior imaging using an Ar-ion beam. The table below summarises the key parameters for each solvent used.

The use of water as a solvent creates the most porosity between LAGP grains. Ethanol and methanol as solvents produce a considerably denser LAGP phase with only occasional closed pores. The density of the hybrid electrolyte increases with increasing degree of LAGP filling. The lowest degree of LAGP filling and density is achieved when using water as the solvent, whereas the highest degree of LAGP filling and density is obtained using methanol as the solvent. Ethanol as the solvent gives an intermediate degree of LAGP filling and density. An explanation for why methanol works best as a dispersant for producing the densest structured LAGP scaffolds is not fully understood. However, it is clear that a polar protic solvent is preferred over a non-polar or polar aprotic solvent, as solvents such as diethyl ether, cyclohexane, acetone and dimethyl sulfoxide did not give any acceptable results in filling nor structure replication. Nevertheless, the polarity itself cannot be the only factor affecting the densification process, as methanol does give better results than water as a solvent, which has the highest dielectric constant of all (80.1 for water versus 25.3 and 33.0 for ethanol and methanol,

respectively[11]). Another parameter that differentiates the three solvents is the boiling point, which is 78.2 °C, 64.6 °C and 100.0 °C for ethanol, methanol and water, respectively.[11] The lower the boiling point, the easier it is for the solvent, once the LAGP grains have been transported inside the structure, to evaporate in time and avoid any undesired side-reactions with the LAGP grains itself. Distilled water has been reported in literature to affect the properties of LAGP over time, which can also affect the hybrid's final ionic conductivity.[10]

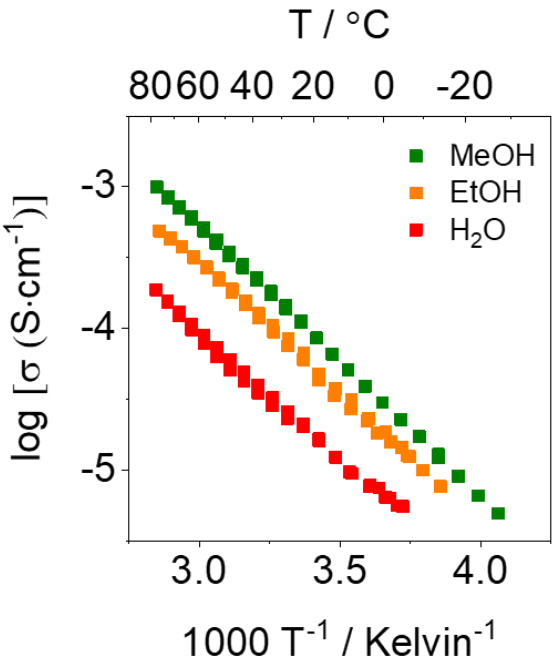


Figure 4.9. Arrhenius plots showing the dependence of impedance over a temperature range of -30 °C to 80 °C for the LAGP-epoxy hybrid electrolytes using methanol, ethanol and water as the filling solvent.

Thus, it is believed that the combination of polarity, suitable vapour pressure and solvent stability, ultimately lead to the best replicated structured LAGP scaffold with the highest LAGP density and ionic conductivity. Arrhenius plots obtained for all three solvents are illustrated in Figure 4.9, showing the efficiency of methanol over other solvents in this synthesis procedure.

4.4.5. Impedance measurements with Li metal electrodes

Next to impedance with Au blocking electrodes, EIS measurements on Li | LAGP | Li and Li | gyroid LAGP-epoxy | Li cells were recorded at RT. Figure 4.10 illustrates the cell setup, Nyquist plots and corresponding equivalent circuit used.

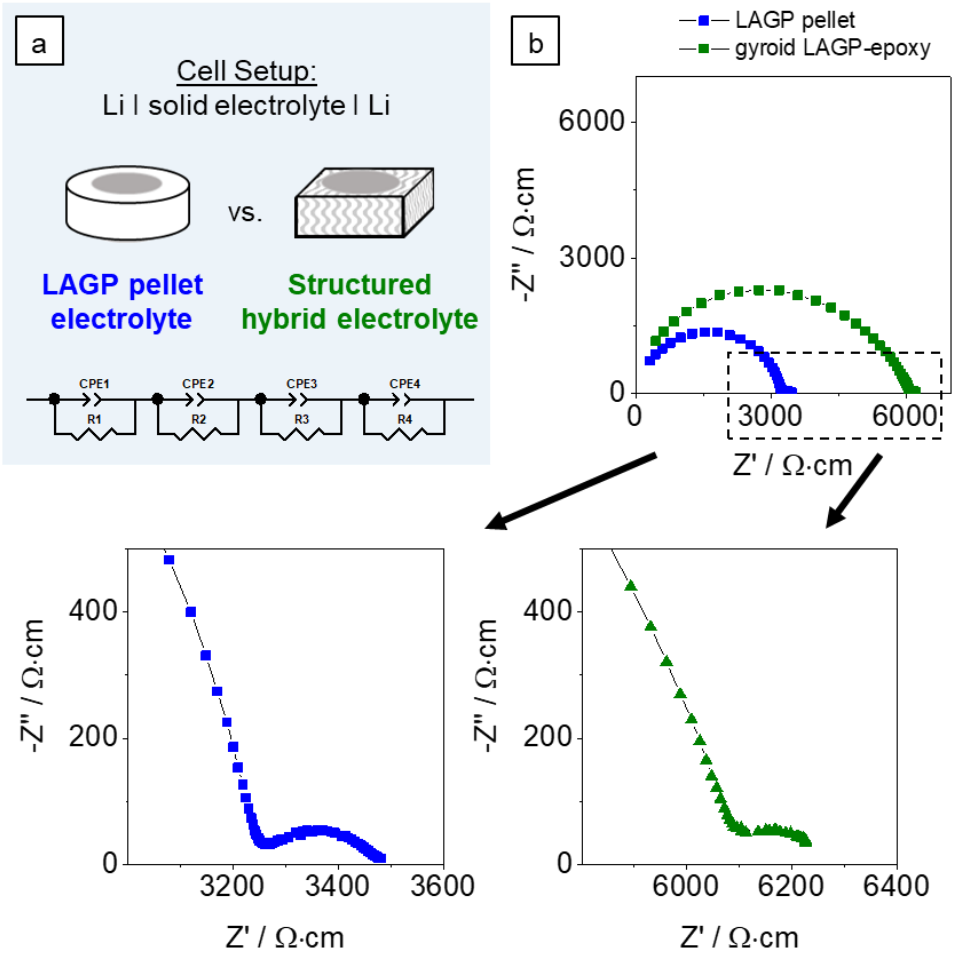


Figure 4.10. EIS analysis of a symmetrical Li | LAGP | Li and Li | gyroid LAGP-epoxy | Li cell: (a) schematic of the cell setup and equivalent circuit, (b) Nyquist plot at RT.

The Nyquist plots of both symmetric cells show very similar characteristic features: a large suppressed semicircle at higher frequency and a smaller semicircle at lower frequency. From the interfacial analysis of LAGP with Li discussed in Chapter 3, it is expected that the Nyquist plots should show the contributions of intragrain (bulk) and

intergrain (grain boundaries) resistances, as well as the contributions of the formed LAGP-Li interphase layer and the LAGP-Li interface. Although attempts were made to fit the larger suppressed semicircle to one or two overlapping semicircles, the best fitting was achieved using a total of three overlapping semicircles. Overall, an equivalent circuit with a series of four resistors and constant-phase elements (R_1//CPE_1, R_2//CPE_2, R_3//CPE_3 and R_4//CPE_4) in parallel was used. Magnified Nyquist plots of the fourth semicircles are shown in Figure 4.10. Appendix 7 summarises the resistances and capacitances calculated for both cells for all four contributions.

The first two semicircles were attributed to the intragrain (R_1//CPE_1) and grain boundary (R_2//CPE_2) resistances of LAGP due to their calculated effective capacitance values of 10^{-10} F·cm^{-1} in both cells. The third semicircle, which was not present in the impedance with Au blocking electrodes, demonstrated a capacitance value of 10^{-8} F·cm^{-2} for both cells, which can be attributed to the LAGP-Li interphase layer. As discussed in Chapter 3, this resistance can be limited with a surface polishing step. For the smaller well-resolved fourth semicircle an effective capacitance value of 10^{-3} F·cm^{-2} was calculated in both cells. This contribution was also not present in the impedance measurements with Au blocking electrodes but can be confidently attributed to the LAGP-Li interface resistance. Total ionic conductivity values of 2.9 x 10^{-4} S·cm^{-1} and 1.6 x 10^{-4} S·cm^{-1} at RT for the LAGP pellet and LAGP-epoxy hybrid cells were calculated, respectively. Using the geometry factor of 0.58 calculated by finite element modelling (Appendix 6) the ionic conductivity of the LAGP phase within the LAGP-epoxy hybrid electrolyte increases to 2.8 x 10^{-4} S·cm^{-1} at RT, which is in the same range as the ionic conductivity measured for the LAGP cell. Hence, similar impedance results were achieved between the LAGP-epoxy hybrid electrolyte and a pure LAGP electrolyte with Li electrodes.

4.4.6. Galvanostatic cycling with Li metal electrodes

Following EIS measurements, both Li | LAGP | Li and Li | gyroid LAGP-epoxy | Li cells were cycled galvanostatically at different current densities and capacities to fully understand any differences in electrochemical behaviour between both cells. Figure 4.11 shows the voltage profiles of a rate test performed on a LAGP and LAGP-epoxy hybrid cell cycled up to a capacity of 0.1 mAh·cm^{-2} at current densities of 0.05, 0.1, 0.2, 0.5 and 1 mA·cm^{-2} for 5 cycles each.

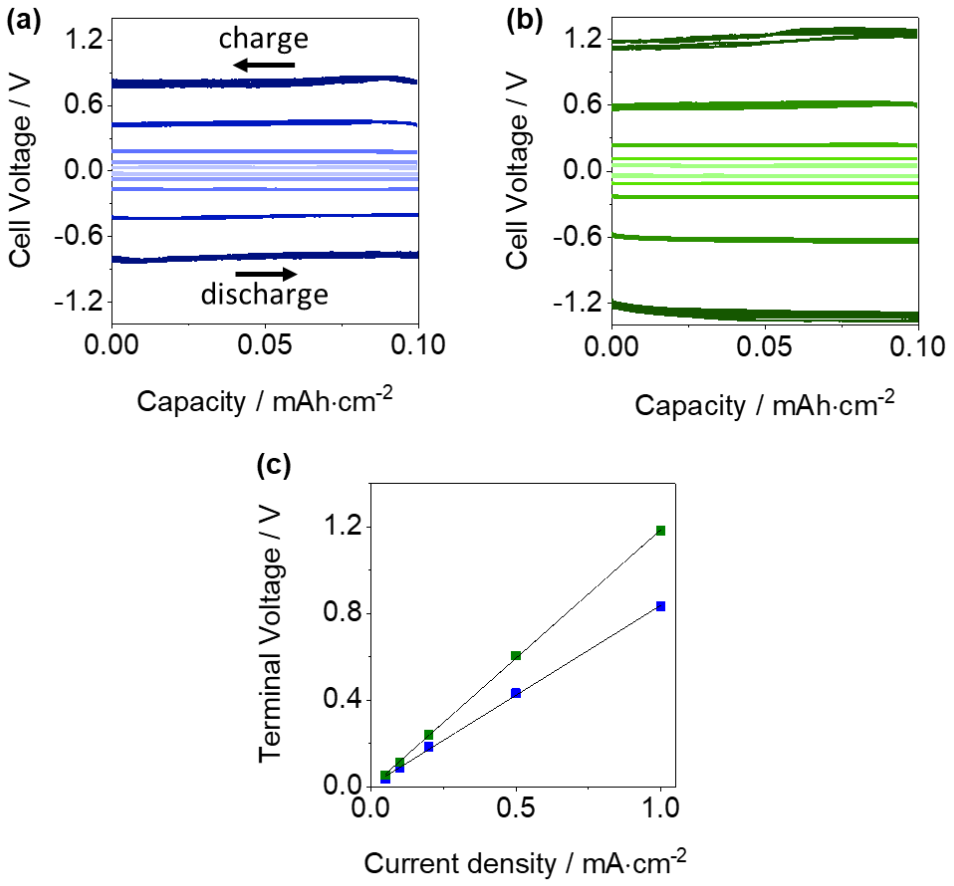


Figure 4.11. Rate test of a Li | LAGP | Li cell (a) and a Li | gyroid LAGP-epoxy | Li cell (b) cycled at 0.05, 0.1, 0.2, 0.5 and 1 mA·cm^{-2} up to a capacity of 0.1 mAh·cm^{-2} with 5 cycles per current density. (c) Plot of the terminal voltage after 5 cycles versus current density of the Li | LAGP | Li cell (blue) and the Li | gyroid LAGP-epoxy | Li cell (green).

Similar to the LAGP cell, the voltage remains stable up to a current density of 0.2 $mA \cdot cm^{-2}$, only minor variabilities are observed for the higher current densities at 0.5 and 1 $mA \cdot cm^{-2}$. While for both cells the terminal cell voltage increases linearly with current density, the increase is more significant for the LAGP-epoxy hybrid electrolyte, especially at higher current densities (Figure 4.11-c). Similar to the difference in the ionic conductivities between the LAGP and the LAGP-epoxy hybrid, a difference in cycling performance is expected between both cells. The presence of only a 70 % conductive LAGP phase in volume and surface area in the LAGP-epoxy hybrid changes the effective current density through the conductive channels compared to the current density through the 100 % ionically conductive LAGP cell. A higher effective current density through the LAGP phase of the LAGP-epoxy hybrid cell is expected. The difference in effective current density becomes particularly significant at higher current densities such as 0.5 $mA \cdot cm^{-2}$ and 1 $mA \cdot cm^{-2}$, as shown in Figure 4.11-c. Greater variabilities in cell voltages between the LAGP and LAGP-epoxy hybrid cells at these higher current densities are anticipated.

Galvanostatic cycling of both cells at low current densities and capacities are shown in Figure 4.12. At both current densities of 0.05 $mA \cdot cm^{-2}$ and 0.2 $mA \cdot cm^{-2}$ no distinct difference in performance between the LAGP and LAGP-epoxy hybrid cells is observed. The voltage polarisation increases in both cases similarly from the 1^{st} to the 50^{th} cycle at 0.05 $mA \cdot cm^{-2}$ up to a capacity of 0.025 $mA \cdot cm^{-2}$ and from the 1^{st} to the 30^{th} cycle at 0.2 $mA \cdot cm^{-2}$ up to a capacity of 0.1 $mA \cdot cm^{-2}$. A higher effective current density through the LAGP phase in the LAGP-epoxy hybrid cells for both current densities, labelled as $j_{LAGP\ phase}$ in Figure 4.12, is expected. However, the effective current densities through the LAGP phase during low current density cycling are yet not that dissimilar. Hence, differences in cycling performance between the LAGP and LAGP-epoxy hybrid cells

remain low. These ought to become more significant when cycled at higher current densities. Nevertheless, as shown previously in Chapter 3, voltage polarisation between each cycle rises noticeably as the current density is increased.

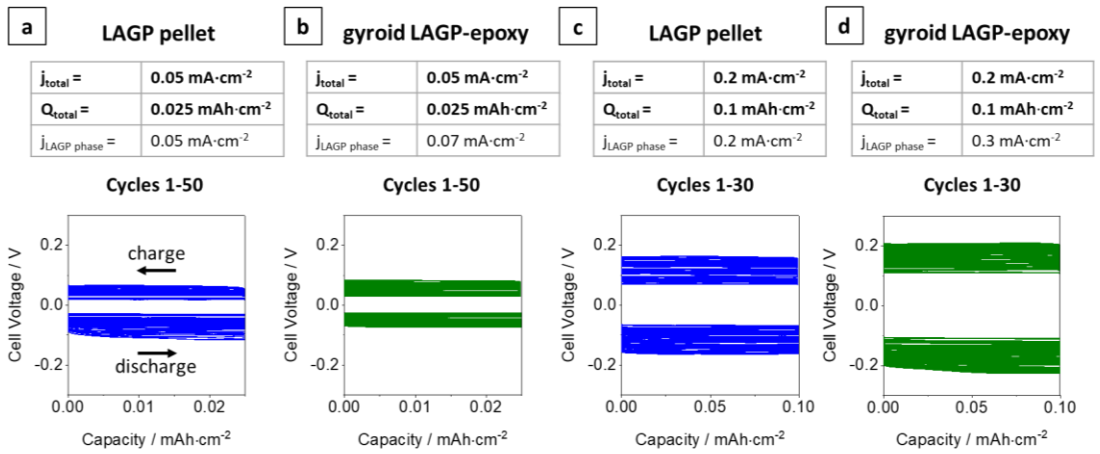


Figure 4.12. Voltage profiles of Li | LAGP | Li cells (blue) and Li | gyroid LAGP-epoxy | Li cells (green) cycled at a current density of 0.05 mA·cm^{-2} up to a capacity of 0.025 mAh·cm^{-2} for 50 cycles (a and b) and at 0.2 mA·cm^{-2} up to a capacity of 0.1 mAh·cm^{-2} for 30 cycles (c and d). All four cells have been cycled for a total of 0.5 hours per current direction.

Galvanostatic cycling at intermediate current densities of 0.7 mA·cm^{-2} and 1 mA·cm^{-2} quickly demonstrates the electrochemical performance limitation of LAGP as solid electrolyte (Figure 4.13). Compared to the cycling at low current density, a considerably lower number of cycles were achieved until cell failure. While the voltage polarisation first shows small increments between initial cycles for the LAGP cell, the cell voltage increases significantly more at both current densities on subsequent cycles (Figure 4.13-a and 4.13-c). A far more gradual increase in cell voltage between cycles is observed for the LAGP-epoxy hybrid, with the hybrid at 0.7 mA·cm^{-2} outperforming the LAGP cell and at 1 mA·cm^{-2} achieving equal number of cycles until the cells reach the limiting cell voltage of 12 V (Figure 4.13-b and 4.13-d). Comparing both cells at 0.7 mA·cm^{-2}, shows that despite the presence of a 30 % insulating polymer, the hybrid

electrolyte performs better electrochemically and extends the cycle life of the cell by 25 %. Only 20 cycles were achieved when the cells were cycled at a higher current density of 1 mA·cm^{-2} (Figure 4.13-c and 4.13-d). While again a more steady increase in voltage polarisation is observed for the gyroid LAGP-epoxy at a current density of 1 mA·cm^{-2}, the LAGP cell first increases slowly followed by more erratic increases of over 1 V per cycle from the 15th cycle onwards. A faster cell deterioration is observed at higher applied current densities for both cell systems.

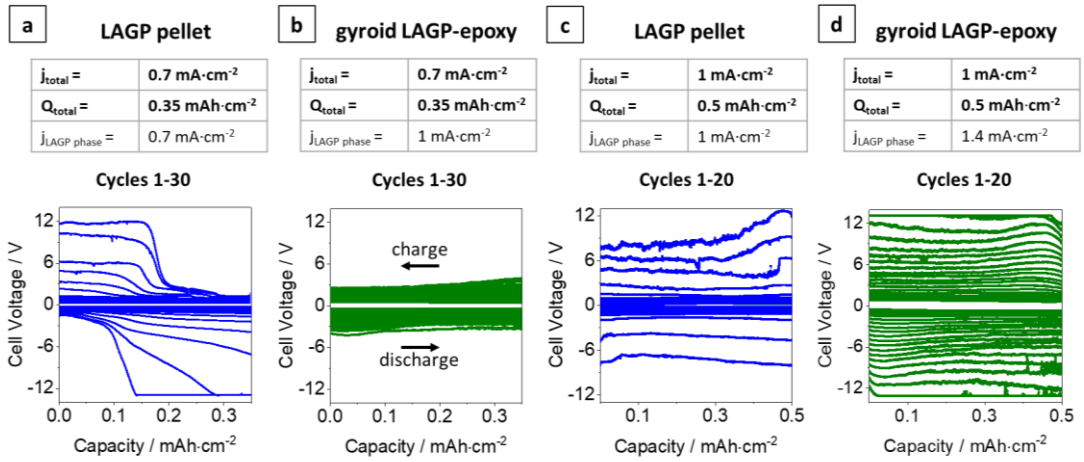


Figure 4.13. Voltage profiles of Li | LAGP | Li cells (blue) and Li | gyroid LAGP-epoxy | Li cells (green) cycled at a current density of 0.7 mA·cm^{-2} up to a capacity of 0.35 mAh·cm^{-2} for 30 cycles (a and b) and at 1 mA·cm^{-2} up to a capacity of 0.5 mAh·cm^{-2} for 20 cycles (c and d). All four cells have been cycled for a total of 0.5 hours per current direction.

Galvanostatic cycling of the cells at even higher current densities of 1.4 mA·cm^{-2} and 2 mA·cm^{-2} was performed to understand the cycling failure and upper electrochemical limit of both LAGP and LAGP-epoxy hybrid cells (Figure 4.14). A total of 12 and 4 cycles were achieved at 1.4 mA·cm^{-2} and 2 mA·cm^{-2}, respectively, which confirms the trend of cell deterioration as the current density increases. Surprisingly again, the LAGP-epoxy hybrid cell holds up well against the LAGP cell, although the effective current density through the LAGP phase between both cells is drastically increased. This

confirms that the presence of a 3D non-conductive polymer network is beneficial at extending the cycle life of LAGP as solid electrolyte.

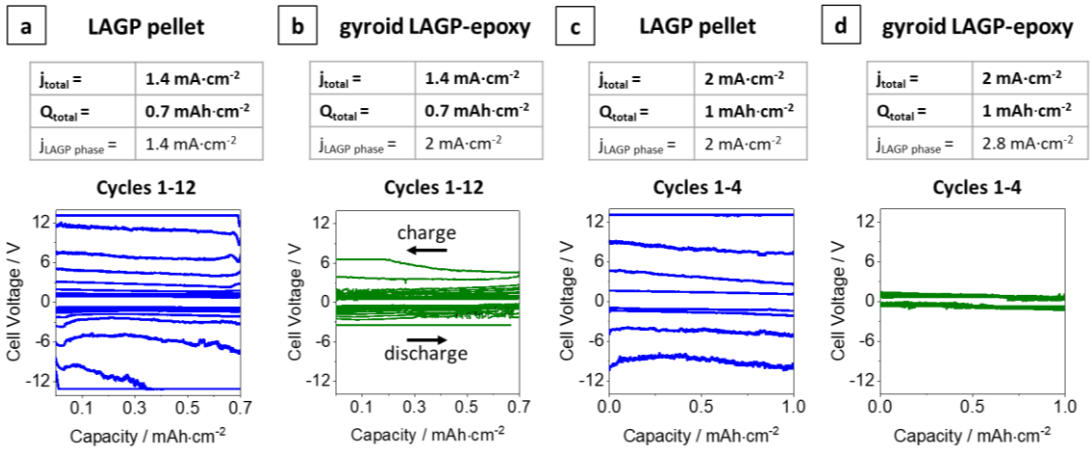


Figure 4.14. Voltage profiles of Li | LAGP | Li cells (blue) and Li | gyroid LAGP-epoxy | Li cells (green) cycled at a current density of 1.4 mA·cm^{-2} up to a capacity of 0.7 mAh·cm^{-2} for 12 cycles (a and b) and at 2 mA·cm^{-2} up to a capacity of 1 mAh·cm^{-2} for 4 cycles (c and d). All four cells have been cycled for a total of 0.5 hours per current direction.

So far, the full electrode area in contact with the electrolyte (j_{total}) was being considered for both cells in the cycling experiments above. Whereas in the LAGP cell the full Li electrode area is in contact with a conductive LAGP phase, only 70 % of the hybrid's surface area is ionically conductive due to the presence of a 30 % insulating epoxy polymer phase. Passing the same amount of current through both cells means that the LAGP phase in the hybrid cell is subjected to a roughly 40 % higher effective current density ($j_{LAGP\ phase}$) than the LAGP phase in the LAGP cell. The $j_{LAGP\ phase}$ of each of the cells is stated in Figure 4.12, 4.13 and 4.14. Comparing both cells at effective current densities through the LAGP phase of 1 mA·cm^{-2} (Figure 4.15a and 4.15b), 1.4 mA·cm^{-2} (Figure 4.15c and 4.15d) and 2 mA·cm^{-2} (Figure 4.15e and 4.15f) shows that the LAGP phase of the hybrid remains stable longer than the LAGP phase in the LAGP cells at lower and higher current densities.

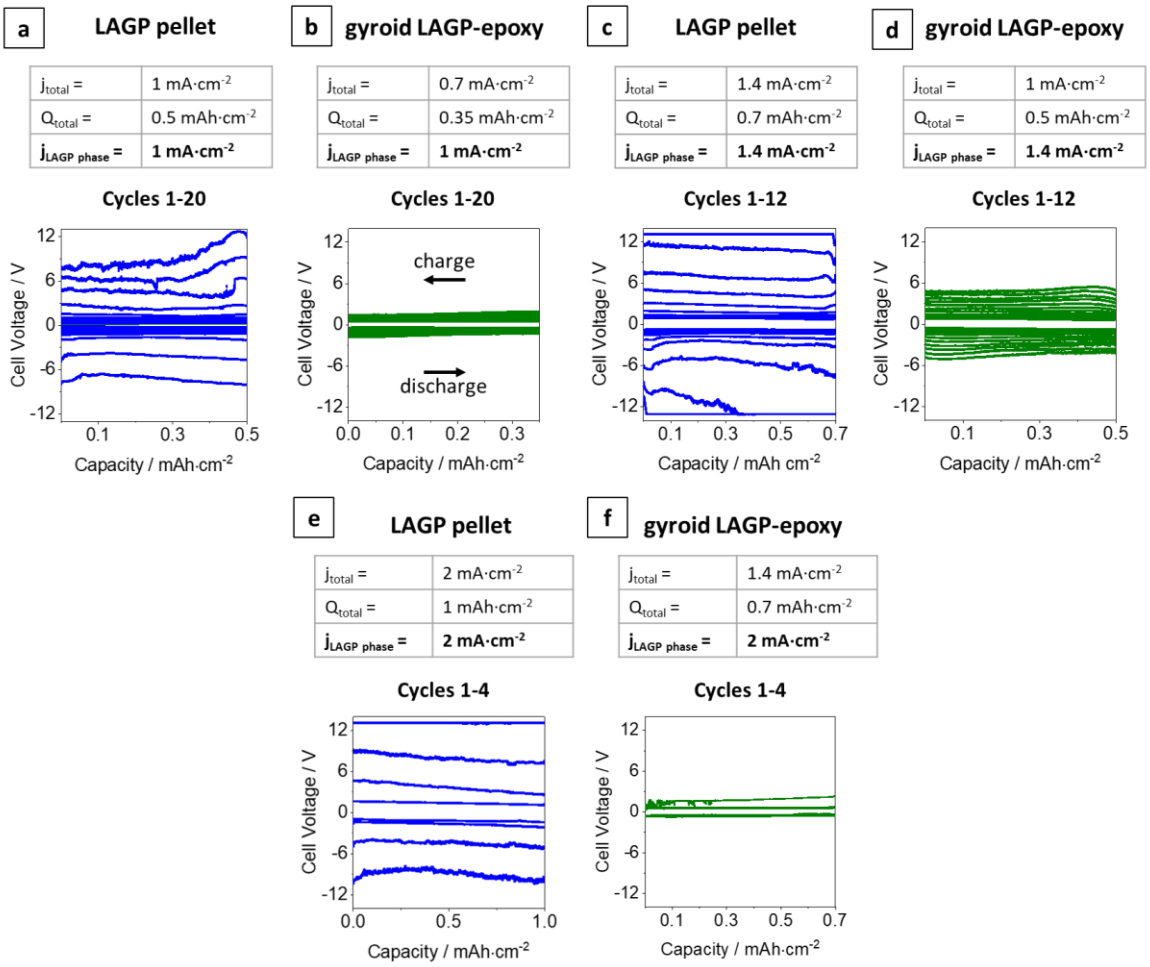


Figure 4.15. Voltage profiles of Li | LAGP | Li cells (blue) and Li | gyroid LAGP-epoxy | Li cells (green) cycled at an effective current density of 1 mA·cm^{-2} for 20 cycles (a and b), of 1.4 mA·cm^{-2} for 12 cycles (c and d) and of 2 mA·cm^{-2} for 4 cycles (e and f).

Figure 4.16 illustrates and summarises the cycle life of each of the assembled cells by comparing the terminal voltages after each cycle versus cycle number at total current densities (j_{total}) and at effective current densities through the LAGP phase ($j_{LAGP\ phase}$). At low total current densities of 0.05 mA·cm^{-2} and 0.2 mA·cm^{-2} (Figure 4.16-a and 4.16-b) the terminal voltages in both cells remain low for numerous cycles. Nevertheless, both do eventually fail after 220 and 230 cycles at 0.05 mA·cm^{-2}, and 80 and 110 cycles at 0.2 mA·cm^{-2}, for the LAGP-epoxy and the LAGP electrolytes, respectively. Due to the length scale of the cycling, it is difficult to evaluate the true performance difference

between both electrolytes. Other factors such as the reactivity of LAGP with Li, variabilities in cycling temperature and cell pressures will most likely play a role.

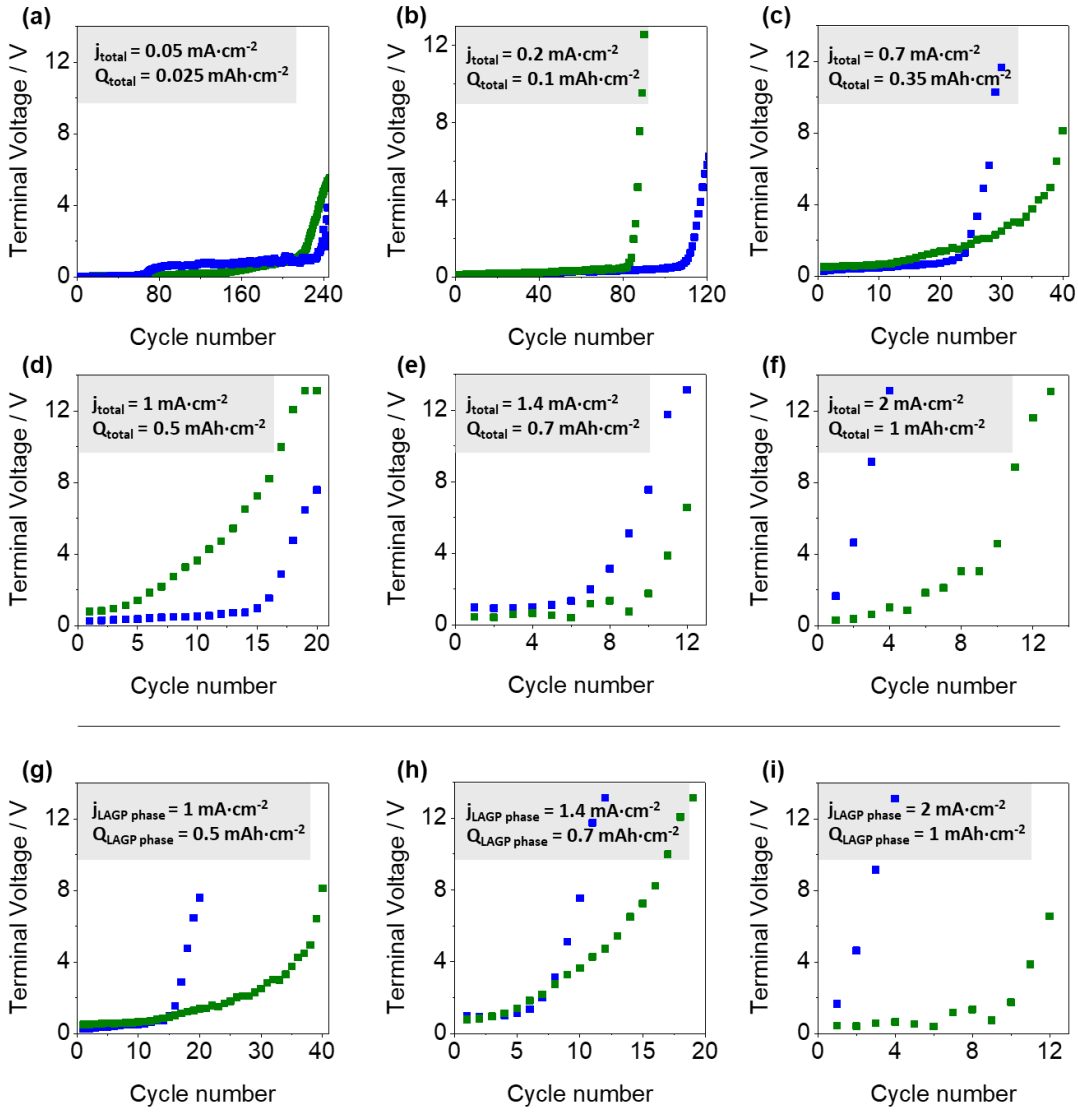


Figure 4.16. Terminal voltage after each completed cycle versus cycle number of Li | LAGP | Li cells (blue) and Li | gyroid LAGP-epoxy | Li cells (green) cycled at a total current density of 0.05 mA·cm^{-2} (a), 0.2 mA·cm^{-2} (b), 0.7 mA·cm^{-2} (c), 1 mA·cm^{-2} (d), 1.4 mA·cm^{-2} (e), 2 mA·cm^{-2} (f) and at an effective current density through the LAGP phase of 1 mA·cm^{-2} (g), 1.4 mA·cm^{-2} (h) and 2 mA·cm^{-2} (i).

At a current density of 0.7 mA·cm^{-2} (Figure 4.16-c) an improvement in the cycling performance is observed for the hybrid compared to the pellet. The voltage remains low

for both cells up to 20 cycles, followed by a rapid increase up to 30 cycles for the pellet and a more gradual increase for the hybrid up to 40 cycles. A 25 % increase in cycle life was achieved for the hybrid compared to the pellet. At a higher current density of 1 and 1.4 $mA \cdot cm^{-2}$ (Figure 4.16-d and 4.16-e), both pellet and hybrid reach their cycle life limit after 20 and 12 cycles, respectively. No significant difference in cell performances is observed. It is only at a current density of 2 $mA \cdot cm^{-2}$ that a visible difference between both cell types is observed, with the hybrid achieving three times as many cycles as the LAGP cell. This results in a 75 % increase in cycle life. While there is no distinctive trend between the cycling performance of the LAGP pellet and the LAGP-epoxy hybrid with increasing total current densities, the cycling experiments show that even with a 30 % insulating phase present in the hybrid, the hybrid is a fair competitor and can be cycled to at least the same amount of cycles as in a LAGP pellet over a wide range of current densities. Nonetheless, normalising the current density to the effective current density that is passed through the LAGP phase of the cells, shows that for all $j_{LAGP\ phase}$ from 1 $mA \cdot cm^{-2}$, 1.4 $mA \cdot cm^{-2}$ and 2 $mA \cdot cm^{-2}$ the hybrid always outperforms the pellet by 50 %, 40 % and 66 % in regards to the cycle life (Figure 4.16-g, 4.16-h and 4.16-i).

The LAGP and LAGP-epoxy cells cycled at a total current density of 0.7 $mA \cdot cm^{-2}$ and 1 $mA \cdot cm^{-2}$ from Figure 4.13 were further analysed by SEM after cycling (Figure 4.17). The photographs of the cells (Figure 4.17-I) straight after cycling show that while the hybrid cells remained in one entity and could easily be handled with a tweezer, the LAGP pellets could not be recovered in one piece. The LAGP pellets fragmented easily upon opening the cells into several pieces at both current densities. SEM cross-sectional images show that an interphase layer of 20-40 µm between the Li and the LAGP has grown in all four cells. Hence, the reaction of LAGP with Li and the growth of the interphase layer is unaffected by the presence of a 30 % insulating polymer phase.

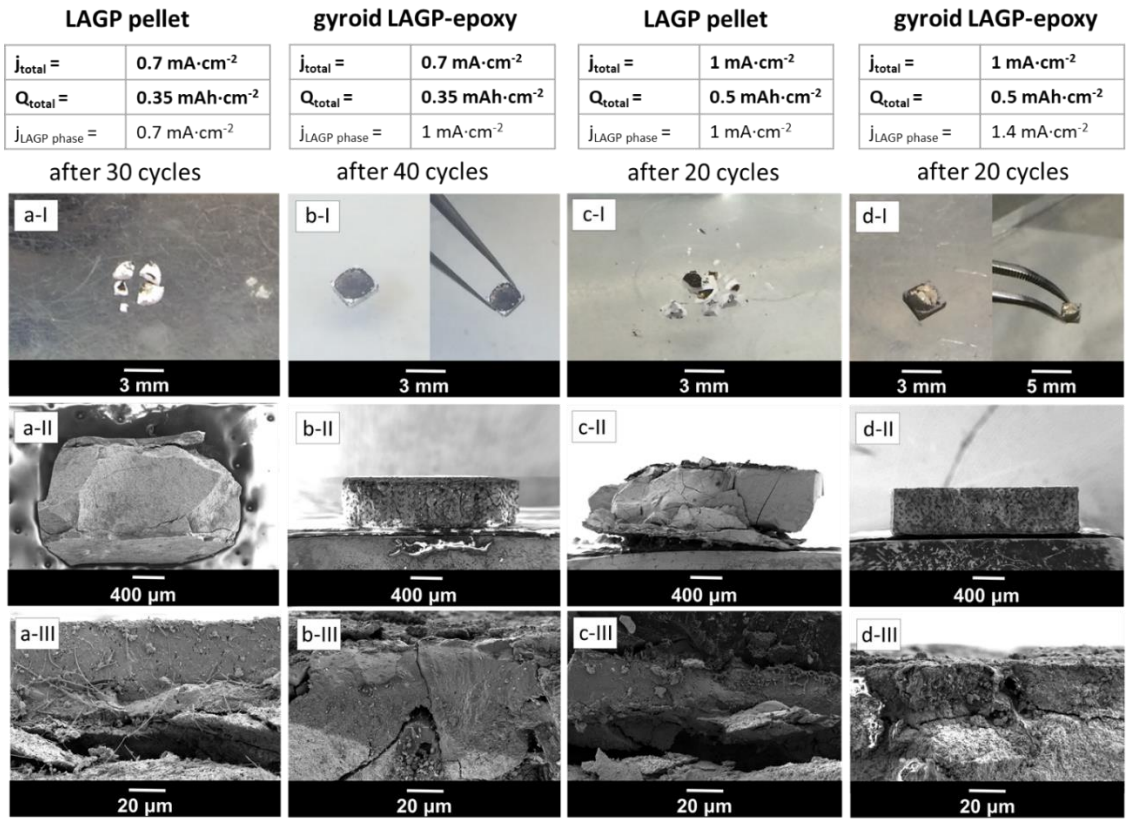


Figure 4.17. Post-cycling photographs and cross-sectional SEM images of Li | LAGP | Li cells (a and c) and Li | gyroid LAGP-epoxy | Li cells (b and d) cycled at a total current density of 0.7 mA·cm^{-2}(a and b) and 1 mA·cm^{-2}(c and d) for 0.5 hours per current direction until cell failure.

More importantly, significant detachment of roughly 20 µm of the interphase layer from the bulk LAGP phase is observed in the LAGP cells at both current densities (Figure 4.17-a-III and 4.17-c-III). A detachment of such a width could not be observed for the hybrid cells, where the interface between the interphase layer and the bulk LAGP phase revealed only a few minor and partial cracks as shown in Figure 4.17-b-III and 4.17-d-III. As previously discussed in Chapter 3, the detachment of the interphase layer from the bulk LAGP is a consequence of cycling. The LAGP reacts with the Li metal electrode forming an interphase layer with a different morphology compared to the bulk LAGP and detaches itself from the bulk upon cycling at high current densities.

To fully understand the differences observed between the LAGP pellet and the LAGP-epoxy gyroid cells after cycling, a closer look at the EIS measurements performed between cycles was taken. Figure 4.18 analyses the trends taken by all four resistances (R_1, R_2, R_3 and R_4), discussed previously in this Chapter, as a function of cycle number for all four cells discussed above.

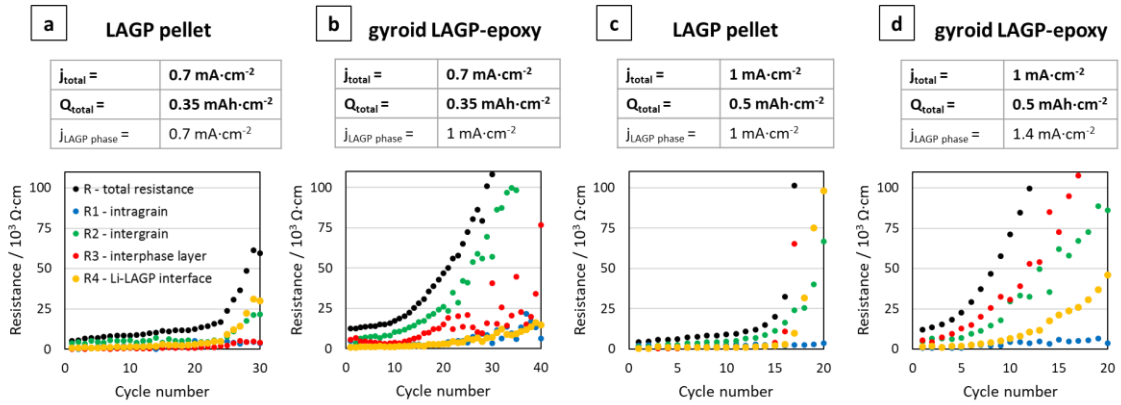


Figure 4.18. Resistances after each completed cycle versus cycle number of Li | LAGP | Li cells (blue) and Li | gyroid LAGP-epoxy | Li cells (green) cycled at an electrode areal current density of 0.7 mA·cm^{-2} (a and b) and 1 mA·cm^{-2} (c and d) until cell failure.

For all four cells an increase in total resistance with cycle number, similar to the increases in cell voltages in Figure 4.13, is observed. Looking at the four contributions involved in the total resistance separately, shows that for all four cells the intragrain resistance (R_1-blue) remains relatively constant and is not the main driver for the increase in total resistance. On the contrary, the intergrain (R_2-green) and interphase (R_3-red) resistances increase from a certain cycle number onwards in all four cells. The Li-LAGP interface resistance (R_4-yellow) increases significantly for the LAGP pellets at both current densities (Figure 4.18-a and 4.18-c), following the trend of the total resistance (R). In contrast, a much more gradual and minimal increase in R_4 is observed in the gyroid LAGP-epoxy cells, specifically at 0.7 mA·cm^{-2} (Figure 4.18-b). A slightly more

pronounced, but still lower increase than the other resistances is observed at a higher current density of 1 $mA \cdot cm^{-2}$ (Figure 4.18-d).

The increase in R_3 in all four cells is consistent with the observation of an interphase layer in all SEM cross-sectional images. The drastic increase in R_4 relates well to the severe detachment observed especially in the LAGP cells. It is likely that the detachment of the interphase layer from the bulk LAGP additionally expresses itself as an additional 'grain boundary' resistance, and increases the magnitude of R_2. The growth of the interphase layer generates most likely internal stresses, which induces the formation of cracks along the interface leading to a detachment of the interphase layer from the bulk LAGP as seen for the LAGP cells. SEM cross-sectional images of the LAGP cells show that the detachment eventually also initiates crack propagation perpendicular to the electrode-electrolyte interface (Figure 4.17-a-II and 4.17-c-II) until complete fracture of the cell (Figure 4.17-a-I and 4.17-c-I). The LAGP-epoxy gyroid cells maintain much better contact at the interfaces (Figure 4.17-b-III and 4.17-d-III), which is consistent with a slower increase of R_4 in the impedance analysis (Figure 4.18-b and 4.18-d). Some cracks parallel and perpendicular to the interfaces in the gyroid LAGP-epoxy cells after cycling were also observed. Nevertheless, the bicontinuous nature of the hybrid electrolyte with its distinct microarchitecture and polymer, maintains its structural integrity during cycling albeit the inevitable crack propagation in the LAGP phase due to its brittle properties.

4.4.7. Analysis of the mechanical properties of the hybrid

Next to comparing the LAGP-epoxy and LAGP electrolytes electrochemically, the mechanical properties of both electrolytes were also studied. For this, two types of mechanical tests were performed: compression tests and four-point bending tests. Each

of these tests measures different mechanical properties of the material and helps to understand the potential differences in mechanical properties between a ceramic-only and a ceramic-polymer hybrid electrolyte.

Stress-strain curves of strain rate controlled compression tests of LAGP-epoxy electrolyte and LAGP electrolyte samples are illustrated in Figure 4.19.

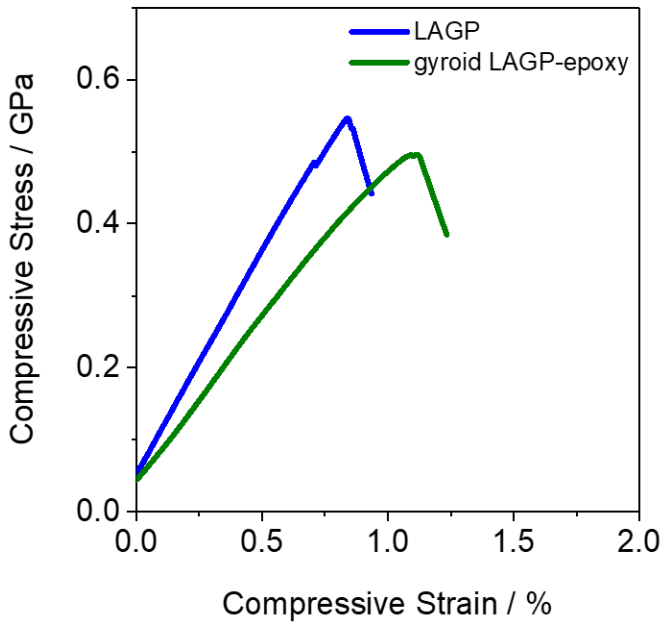


Figure 4.19. Stress-strain curves of LAGP (blue) and the gyroid LAGP-epoxy hybrid electrolyte compressed at a constant rate of 1 µm·min^{-1} until failure.

An elastic modulus of 63 GPa and 44 GPa was determined for the LAGP and LAGP-epoxy gyroid electrolyte, respectively. This is a 40 % reduction in the elastic modulus for the hybrid compared to the LAGP electrolyte. A similar reduction in fracture stress (maximum peak stress) was also obtained. Nevertheless, an increase in fracture strain (28 % more than the LAGP electrolyte) was recorded for the LAGP-epoxy gyroid electrolyte. This confirms that the epoxy has an influence on the mechanical properties of the hybrid, decreasing the stiffness of the hybrid compared to a pure LAGP electrolyte and increasing its resistance to fracture.

Similarly, both LAGP and LAGP-epoxy electrolytes and the epoxy polymer alone were tested in a strain rate controlled four-point bending setup. Figure 4.20 illustrates the obtained stress-strain curves.

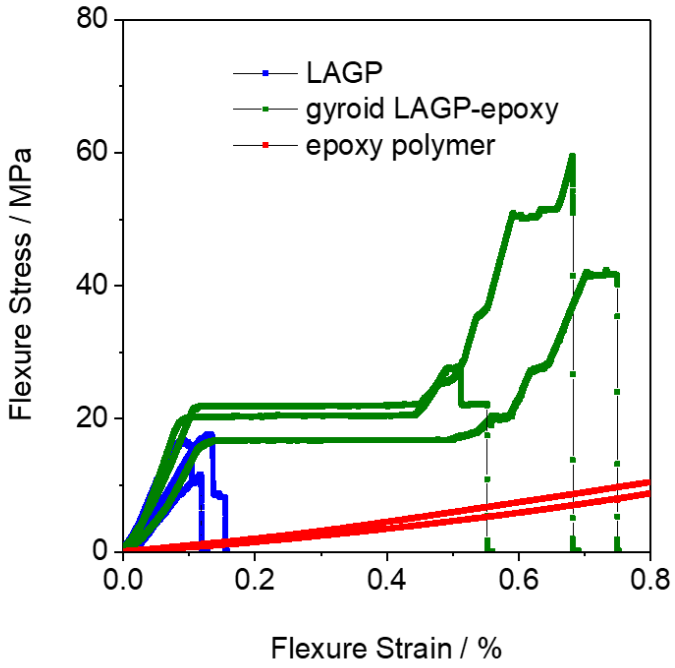


Figure 4.20. Four-point bending stress-strain curves of LAGP (3 samples, blue), epoxy polymer (2 samples, red) and gyroid LAGP-epoxy electrolyte (3 samples, green) using a loading rate of 5 µm·min^{-1} until failure.

From the first linear stage of the stress-strain curves, average flexural moduli values of 18 GPa, 0.8 GPa and 22 GPa for the LAGP, epoxy polymer, and gyroid LAGP-epoxy beams were calculated, respectively. The lower flexural modulus for the epoxy polymer fits very well with its thermosetting polymer properties of a ductile material. From literature, the modulus is expected to be in the low GPa range (<5 GPa).[12] The LAGP and LAGP-epoxy beams show a comparable modulus of bending typical of a more brittle material. It should be noted that the flexural moduli measured in these experiments for LAGP are much lower than the elastic moduli values found in literature and values

obtained from compression tests. This is mainly due to the fact that a ‘hard’ testing rig is assumed in the calculations carried out above, which is not fully the case in this setup. The displacement of the cross-head does not fully match the displacement of the loading pins down onto the beam. Hence, the flexural moduli should only be compared between the beams measured on the same four-point bending setup. The flexure strength only depends on the applied load and is therefore accurate with literature values.

The LAGP beam behaves like a typical brittle polycrystalline material, showing first a linear elastic behaviour followed by a sudden drop in stress once a specific maximum stress is reached. The beam does not undergo plastic deformation and fractures instantaneously at a fracture strength of 12-18 MPa and fracture strain of only 0.09-0.13 %. The epoxy polymer shows a much more ductile behaviour, where fracture strength values as high as 60 MPa and fracture strains of at least 5 % were recorded. Due to the slow loading rate of the epoxy polymer during the bending, the polymer beam did not fracture before reaching the limitations of the instrument. The LAGP-epoxy gyroid electrolyte beam shows a very different stress-strain curve compared to the LAGP beam. While following a similar linear stress-strain relationship to the LAGP beam in the first stage of the curve, the LAGP-epoxy beam does not undergo abrupt failure at 0.13 % strain, but develops instead into a plateau region for a period of approximately 0.35 % strain. From then, a second increase in flexure stress is observed up to a maximum fracture strength of 59 MPa, until catastrophic failure occurs at 0.5-0.75 % flexure strain. Whereas the LAGP phase of the hybrid dominates in the initial increase in flexure stress, the start of the plateau region most likely corresponds to the initiation and propagation of cracks in the ceramic phase. Instead of instant crack propagation of the LAGP phase throughout the entire thickness of the beam, it is believed that crack propagation is deflected and delayed by the presence of the epoxy channels.

Once the LAGP phase of the hybrid is fully fractured, the stress-strain curve is dominated by the epoxy phase and a second increase in stress is observed. This increase does not occur in a smooth line, but takes up a 'saw-tooth' like behaviour, which could be indicative of the 3D gyroidal arrangement of the epoxy phase within the hybrid. A failure strain of five times as high as the failure strain in LAGP was achieved, which corresponds to a significant increase in the hybrid's strength over the LAGP beam alone. Hence, the epoxy does help the hybrid to retain its overall sample integrity and mechanically strengthens the electrolyte before fracture.

4.5. Conclusions

This Chapter has described the synthesis of a hybrid solid electrolyte with 3D bicontinuous ordered ceramic and polymer microchannels using LAGP as the ceramic electrolyte and an epoxy as the non-conductive polymer.

3D printed templates of a gyroid microarchitecture were converted into a structured ceramic electrolyte scaffold by infiltration of a LAGP suspension followed by removal of the initial 3D polymer template at high temperature and refilling of the channels with an epoxy polymer. Feature sizes were chosen in the first instance to prove the concept and possibility of synthesising a structured hybrid electrolyte with bicontinuously ordered ceramic and polymer channels. Ultimately, it is hoped that the overall size of the hybrid electrolyte can be decreased to a thickness of below 10 µm which are the requirements to outperform current battery technology.

The final gyroid LAGP-epoxy hybrid electrolyte exhibited a total ionic conductivity of 1.6×10^{-4} $S \cdot cm^{-1}$ at RT. This conductivity is solely reduced from the conductivity of a dense LAGP pellet (2.8×10^{-4} $S \cdot cm^{-1}$ at RT) by the 30 % volume fraction of non-conductive polymer present and the effect of tortuosity of the gyroidal channels.

Hence, similar LAGP phase densities were achieved during the sintering process of the hybrid and a LAGP pellet. Galvanostatic cycling of the LAGP-epoxy hybrid compared to a LAGP pellet shows that the hybrid sustains a longer cycle life than the pellet at higher current densities. Additionally, the hybrid outperforms the LAGP pellet at low and high current densities if considering the same effective current density through the LAGP phase in both cell types. Next to the cycling performance, SEM cross-sectional analysis of the cells after cycling showed that the LAGP-epoxy hybrid cells maintain their structural integrity, showing less detachment at the interfaces and overall fracture after extensive cycling. The mechanical improvement of the hybrid over the LAGP pellet after cycling was confirmed by compression and four-point bending tests. The hybrid achieved a 28 % increase in compressive failure strain and a five-fold increase in flexural failure strain until fracture compared to a pure LAGP beam.

Overall, a 3D bicontinuously ordered ceramic-polymer hybrid electrolyte was synthesised that addresses the challenge of combining optimal mechanical and electrochemical properties within one solid electrolyte. The selected synthesis route allows for unlimited flexibility in terms of choice of ceramic and polymer material, microarchitecture as well as ceramic-to-polymer ratio. The effect of these parameters on the hybrid's performance will be explored and discussed in the subsequent Chapter. Despite the significant reactivity of LAGP with Li, the concept of a hybrid electrolyte and its advantages over a pure ceramic electrolyte were demonstrated.

4.6. References

1. Seino, Y., Ota, T., Takada, K., Hayashi, A. & Tatsumisago, M. A sulphide lithium super ion conductor is superior to liquid ion conductors for use in rechargeable batteries. *Energy Environ. Sci.* **7,** 627–631 (2014).
2. Hupfer, T. *et al.* Evolution of microstructure and its relation to ionic conductivity in Li1+xAlxTi2−x(PO4)3. *Solid State Ionics* **288,** 235–239 (2016).

3. Deviannapoorani, C., Dhivya, L., Ramakumar, S. & Murugan, R. Lithium ion transport properties of high conductive tellurium substituted Li7La3Zr2O12 cubic lithium garnets. *J. Power Sources* **240,** 18–25 (2013).

4. Wolfenstine, J., Allen, J. L., Sakamoto, J., Siegel, D. J. & Choe, H. Mechanical behavior of Li-ion-conducting crystalline oxide-based solid electrolytes: a brief review. *Ionics (Kiel).* **24,** 1271–1276 (2018).

5. McGrogan, F. P. *et al.* Compliant Yet Brittle Mechanical Behavior of Li2S-P2S5 Lithium-Ion-Conducting Solid Electrolyte. *Adv. Energy Mater.* **7,** 1602011 (2017).

6. Han, X. *et al.* Negating interfacial impedance in garnet-based solid-state Li metal batteries. *Nat. Mater.* **16,** (2016).

7. Wenzel, S. *et al.* Direct Observation of the Interfacial Instability of the Fast Ionic Conductor Li10GeP2S12 at the Lithium Metal Anode. *Chem. Mater.* **28,** 2400–2407 (2016).

8. Hartmann, P., Leichtweiss, T., Busche, M. R. & Schneider, M. Degradation of NASICON-type materials in contact with lithium metal : SEI formation on solid electrolytes ? (2013).

9. Schneider, C. A., Rasband, W. S. & Eliceiri, K. W. NIH Image to ImageJ: 25 years of image analysis. *Nat. Methods* **9,** 671–675 (2012).

10. Zhang, M. *et al.* Preparation and Electrochemical Properties of Li1+xAlxGe2-x(PO4)3 Synthesized by a Sol-Gel Method. *J. Electrochem. Soc.* **159,** A1114–A1119 (2012).

11. Lide, D. R. *CRC Handbook of Chemistry and Physics*. (CRC Press, 2005).

12. Yamini, S. & Young, R. J. The mechanical properties of epoxy resins. *J. Mater. Sci.* **15,** 1814–1822 (1980).

Chapter 5: Tuning the Properties of the 3D Ordered Hybrid Electrolyte

5.1. Aim

A hybrid electrolyte with 3D ordered bicontinuous ionically conductive ceramic electrolyte and non-conductive polymer microchannels has successfully been synthesised as described in the previous Chapter (Chapter 4). The aim of this Chapter is to demonstrate the flexibility of the hybrid's synthesis, in terms of the choice of the ceramic electrolyte and the polymer material, the hybrid's microarchitecture and ceramic-to-polymer ratio. How each of these parameters can be tuned ultimately to generate a hybrid electrolyte that has the necessary properties to function in an all-solid-state battery cell will be shown. Additionally, the effect of each parameter on the electrochemical and mechanical properties of the hybrid electrolyte will be analysed.

5.2. Introduction

Several tuneable parameters of the hybrid electrolyte have been investigated. Due to the superior chemical stability in air of LAGP over other ceramic electrolytes, LAGP was used as the ceramic electrolyte to analyse the effect of polymer material, microarchitecture and ceramic-to-polymer ratio on the properties of the hybrid electrolyte. Templates with four different types of microarchitecture were designed, namely with a cubic, a gyroid, a diamond and a bicontinuous interfacially-jammed emulsion gel (bijel) microarchitecture. The geometries were chosen to span a wide range of properties; from a very ordered 3D channel arrangement in the cubic structure to a randomly disordered arrangement in the bijel structure. To analyse the effect of polymer material on the hybrid's properties, two intrinsically different polymers were selected: a

thermoplastic polymer (polypropylene (PP)) and a thermosetting polymer (epoxy polymer). Using the most promising microarchitecture and type of polymer material, the effect of ceramic-to-polymer ratio on the hybrid's electrochemical and, most importantly, mechanical properties was investigated. For this purpose, three different ratios were examined using 3D printed templates with an initial ceramic-to-polymer ratio of 85 % to 15 %, 70 % to 30 % and 50 % to 50 %, respectively. Ultimately, the synthesis of the hybrid electrolyte using a garnet-type solid electrolyte (Ta-doped LLZO), which is stable against Li metal unlike LAGP, was performed. The new synthetic challenges that arise with this ceramic electrolyte material are described.

5.3. Experimental Methods

5.3.1. Synthesis of the 3D ordered hybrid electrolyte

5.3.1.1. Design and fabrication of the 3D printed templates

The design and fabrication of the 3D printed templates of different microarchitectures was achieved by the use of a commercial stereolithography instrument (NanoScribe Photonic Professional GT System) as previously described in Chapter 4 Section 4.3.1.1 and Section 4.3.1.2. Four different types of microarchitectures were considered: a cubic, a gyroid, a diamond and a bijel microarchitecture. First, a unit cell of a specific geometry and porosity was designed, which was then multiplied to generate a print block of approximately 260 μm^3 in size, which was then repeatedly printed in x-, y- and z-direction until the final size of the 3D micro-printed template was reached.

5.3.1.2. Design of the four microarchitectures

The cubic unit cell was modelled using Netfabb Professional (7.4.0). The repair function was used to fully finalise the model to a water-tight solid unit. The gyroid unit cell was

generated as previously described in Chapter 4 Section 4.3.1.1. The diamond unit cell was prepared using OpenSCAD (2015.03-1) using a shape radius of 0.33. The cubic print block is composed of 3x3x3 cubic unit cells, whereas both gyroid and diamond print blocks comprise 2x2x2 unit cells. The print block of the bijel microarchitecture was generated from a CT scan of an experimentally polymerised bijel sample. Netfabb Professional (7.4.0) was used to slice the 3D rendering of the micro-CT scan into a stack of 2D image files. These files were then imported into Avizo (9.1.1) to generate a 3D model using an auto-skeletisation process. The model was adjusted to fit to the solid volume fraction of all three other microarchitectures using Netfabb Professional (7.4.0). The synthesis of the polymerised bijel can be found in the literature.[1,2] For all four microarchitectures, additional print block extensions were added to the print blocks using Netfabb Professional (7.4.0), which then were imported as .stl files and converted into print ready .gwl files, before being printed with the NanoScribe Photonics Professional GT system, as described in Chapter 4 Section 4.3.1.2.

The design of the four microarchitectures above generates unit cells and subsequent print blocks with 85 % porosity. To generate the gyroid unit cells with 70 % and 50 % porosity, a change in the input parameter from ‘52’ in the 85 % porosity unit cell to ‘30’ and to ‘0‘ for the 70 % and 50 % porosity gyroid unit cell was performed, respectively. The input parameter in question is highlighted in bold in the code below:

```
a=2*π;

s=2*π/60;

[x,y,z]=meshgrid(-a:s:a,-a:s:a,-a:s:a);

cx = cos(2*x);

cy = cos(2*y);

cz = cos(2*z);
```

u = 50.0*(cos(x).*sin(y)+cos(y).*sin(z)+cos(z).*sin(x))-0.5*(cx.*cy+cy.*cz+cz.*cx)-**52**;

[f,v]=isosurface(u,0);

vertface2obj(v,f,'thinfig%.obj')

5.3.1.3. Synthesis of the 3D ordered LAGP-polymer electrolyte

The LAGP ceramic electrolyte was synthesised as previously described in Chapter 3 Section 3.3.1. For all four microarchitectures, 3D templates were filled with calcined and ball-milled LAGP powder using the same filling procedure and sintered using the same sintering conditions as described in Chapter 4 Section 4.3.1.4. The solid volume fraction and porosity including the channel and wall thicknesses of the 3D templates were designed to be identical in all four microarchitectures. The same synthesis procedure was also used for the 3D templates with different ceramic-to-polymer ratios. The structured LAGP scaffolds were filled with two different types of polymers: PP and an epoxy polymer. For the PP filling, PP beads (isotactic, average M_w - 12000 Da) were heated in a beaker to 190 °C until fully liquefied, after which the structured LAGP scaffold was immersed in the liquid PP melt for 2 hours under a dynamic vacuum. The filled structured LAGP scaffold was then removed and the filled PP channels were left to solidify at RT. Excess PP on the outside of the LAGP scaffold was removed by gently heating and rotating the scaffold on a hot plate at 120 °C. The filling procedure as described in Chapter 4 Section 4.3.1.5 was followed for the epoxy polymer.

5.3.1.4. Synthesis of the 3D ordered LLZTO-polymer electrolyte

The design and fabrication of a 3D printed polymer template with a gyroid microarchitecture and a solid volume fraction of 50 % was performed as previously described in this Chapter (Chapter 5 Section 5.3.1.2). Ball-milled and calcined

$Li_{6.5}La_3Zr_{1.5}Ta_{0.5}O_{12}$ (LLZTO) powder as described in Chapter 6 Section 6.3.1 was used to fill the 3D printed polymer template. The filling procedure as was described for LAGP (Chapter 4 Section 4.3.1.4) using methanol as the solvent was employed. Once filled, the templates were placed into a 5 mm diameter die set together with 100 mg of ball milled LLZTO powder and pressed into a pellet at 0.5 tons. The pellet, with one of the template surfaces facing upwards, was placed on a hand-pressed 1 mm layer of 'motherpowder' LLZTO (prepared as described in Chapter 6 Section 6.3.1) placed on an alumina crucible. The template was then sintered at 1250 °C for 10 minutes as described for the LLZTO pellets in Chapter 6 Section 6.3.1. Once the furnace was cooled down to below 300 °C the alumina crucible was removed and the structured LLZTO scaffold was gently recovered from the pellet and directly immersed into a 15:2 volume ratio mixture of Struers EpoFix resin and EpoFix hardener. The polymer filling procedure as described for the LAGP-epoxy hybrid was followed (Chapter 4 Section 4.3.1.5).

5.3.2. Microstructural analysis

5.3.2.1. SEM and EDX

SEM and EDX analysis was performed on the synthesised hybrid electrolytes using the preparation, imaging and data collection methods as previously described in Chapter 3 Section 3.3.2.1.

5.3.2.2. X-ray micro-CT

X-ray micro-CT analysis as described in Chapter 4 Section 4.3.2.3 was used to obtain a 3D reconstruction of the structured LAGP scaffold with different microarchitectures.

5.3.3. Electrochemical analysis

5.3.3.1. EIS

EIS measurements were performed on all structured ceramic-polymer hybrid electrolytes with symmetrical Li metal electrodes using Gamry Interface-1000 devices with the same impedance parameters as detailed in Chapter 3 Section 3.3.3.1. The cell assembly with Li electrodes was performed as described in Chapter 3 Section 3.3.3.2. For the hybrids with LAGP electrolyte, the polishing method detailed in Chapter 3 Section 3.3.3.2 was followed. For the hybrids with LLZTO electrolyte, the samples were dry polished in an Ar-filled glovebox (O_2 and H_2O levels below 0.1 ppm) using a SiC waterproof abrasive disc (Kemet, grade 400) prior cell assembly.

5.3.3.2. Galvanostatic cycling

The LAGP-polymer hybrid electrolytes were polished, assembled with Li metal electrodes and cycled galvanostatically as symmetrical cells as previously described in Chapter 3 Section 3.3.3.2. The size of the hybrid electrolytes was kept the same for all measurements with a length and width of 2.6 mm x 2.6 mm, respectively, an electrolyte thickness of 0.4 - 0.7 mm and a Li metal electrode diameter of 1.7 - 2.2 mm. Galvanostatic cycling was performed at a constant current density of 1 $mA \cdot cm^{-2}$ for 0.5 hours per direction of charge and discharge for 10 cycles at RT. A rest time of 5 minutes was recorded between each current direction. Additional EIS measurements were taken after each charge and discharge step.

5.3.4. Mechanical analysis

5.3.4.1. *In-situ* SEM compression testing

In-situ SEM compression testing was performed on the hybrid electrolytes and an LAGP block using a Deben microtest stage with a 660 N load cell fitted on a Zeiss EVO scanning electron microscope. Samples were clamped between two compression plates and a preload of 5 N was applied before compression was performed in steps until complete fracture. SE images of the samples after compression were recorded at an acceleration voltage of 15 kV.

5.3.4.2. Compression testing

Compression tests were performed on all LAGP-polymer hybrid electrolytes as previously described in Chapter 3 Section 3.3.4.1. Stress-strain curves were compared between hybrid electrolytes with different microarchitectures and polymers.

5.3.4.3. Four-point bending

LAGP-polymer and LLZTO-epoxy hybrid electrolyte beams with different microarchitectures and ceramic-to-polymer ratios were polished and tested on a four-point bending testing setup as previously described in Chapter 3 Section 3.3.4.2. The LAGP beams were prepared as described in Chapter 3 Section 3.3.4.2. The preparation of LLZTO beams was performed similarly to LAGP using synthesised LLZTO powder as described in Chapter 6 Section 6.3.1.

5.4. Results and Discussion

5.4.1. Choice and design of the four microarchitectures

In this work, four different microarchitectures were chosen to be investigated as potential geometries for the hybrid electrolyte: a cubic, a gyroid, a diamond and a bijel microarchitecture.

The cubic microarchitecture is the simplest 3D geometry of all due to its ordered orthogonal conduction channels. The gyroid microarchitecture has been chosen due to its unique property as a triply periodic minimal surface, a zero mean curvature geometry, firstly described by Alan Schoen in 1970.[3] The structure divides space into two phases in all three dimensions with no straight lines nor reflectional symmetries, giving rise to a distinct bicontinuous channel arrangement. The diamond microarchitecture was chosen due to the exceptional properties of the diamond crystal structure being the hardest naturally occurring material known to mankind. Additionally to these ordered microarchitectures, a bijel microarchitecture with a random channel arrangement was also studied. Bijels are experimentally synthesised by spinodal liquid-liquid demixing of a two-liquid system using neutrally-wetting colloidal particles.[2] These particles congregate at the liquid-liquid interface and separate the two partially miscible liquids via interfacial jamming. By polymerising one of the channels and removing the liquid from the other channel, the formed microarchitecture can be directly used as a 3D template.

In order to keep the ceramic-to-polymer volume ratio consistent, all four microarchitectures were conceived by stereolithography. The cubic, gyroid and diamond microarchitectures were generated computationally, whereas for the bijel microarchitecture an experimentally polymerised bijel CT scan was taken as initial

design. Figure 5.1 illustrates the unit cells and print blocks of the four microarchitectures investigated in this work.

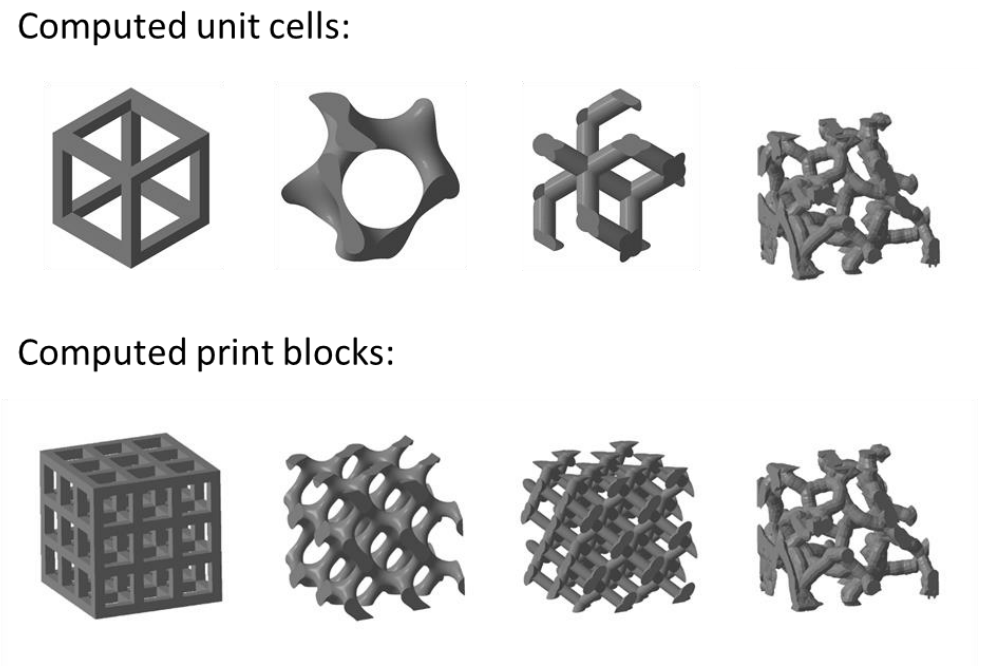


Figure 5.1. Computed unit cell and print block models of the four different microarchitectures: cubic, gyroid, diamond and bijel (left to right).

5.4.2. Synthesis of the 3D ordered LAGP-polymer electrolyte

Figure 5.2 shows the initial 3D printed polymer templates with all four microarchitectures. The dimensions of the printed templates are 1.2 mm x 1.2 mm x 2.4 mm in size, which is 5 % smaller than the original computational designs due to shrinkage during the printing and development stage. To compare all four microarchitectures with each other, all four template geometries were designed with an 85 % porosity, 15 % solid volume fraction and an average empty channel diameter and solid volume diameter of 67 µm and 20 µm, respectively as the synthesised template described in Chapter 4. The same LAGP filling procedure was used for all four microarchitectures as described in Chapter 4 Section 4.3.1.4.

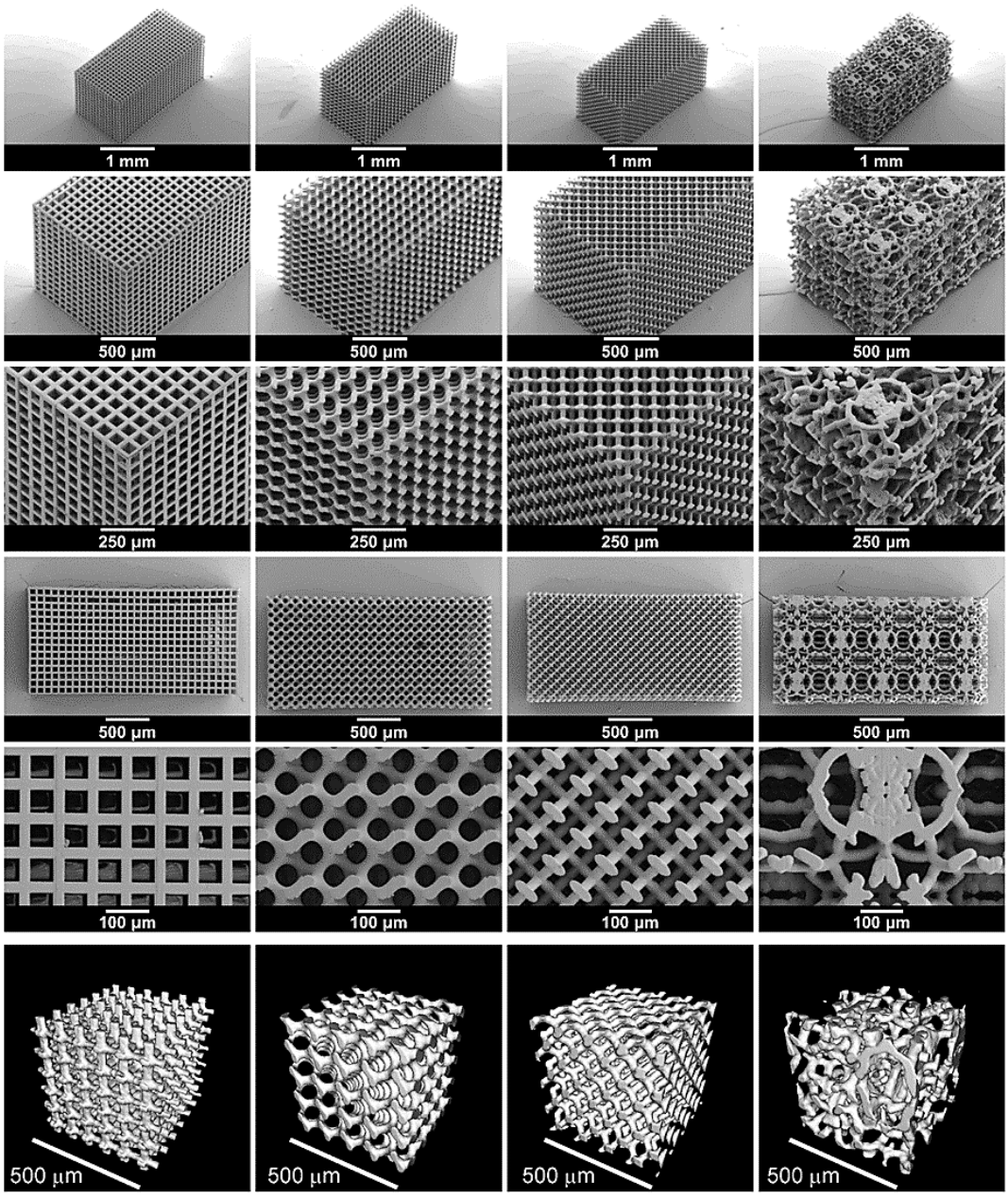


Figure 5.2. SEM images of the 3D printed polymer templates with four different microarchitectures: cubic, gyroid, diamond and bijel (left to right). Corresponding 3D renderings of micro-CT scans of the interior of the templates are also shown (bottom row).

Figure 5.3 and 5.4 show SEM images of the final LAGP-polymer hybrid electrolytes using PP and epoxy, respectively. SEM images of the filled templates and the subsequently sintered LAGP scaffolds are shown in Appendix 8.

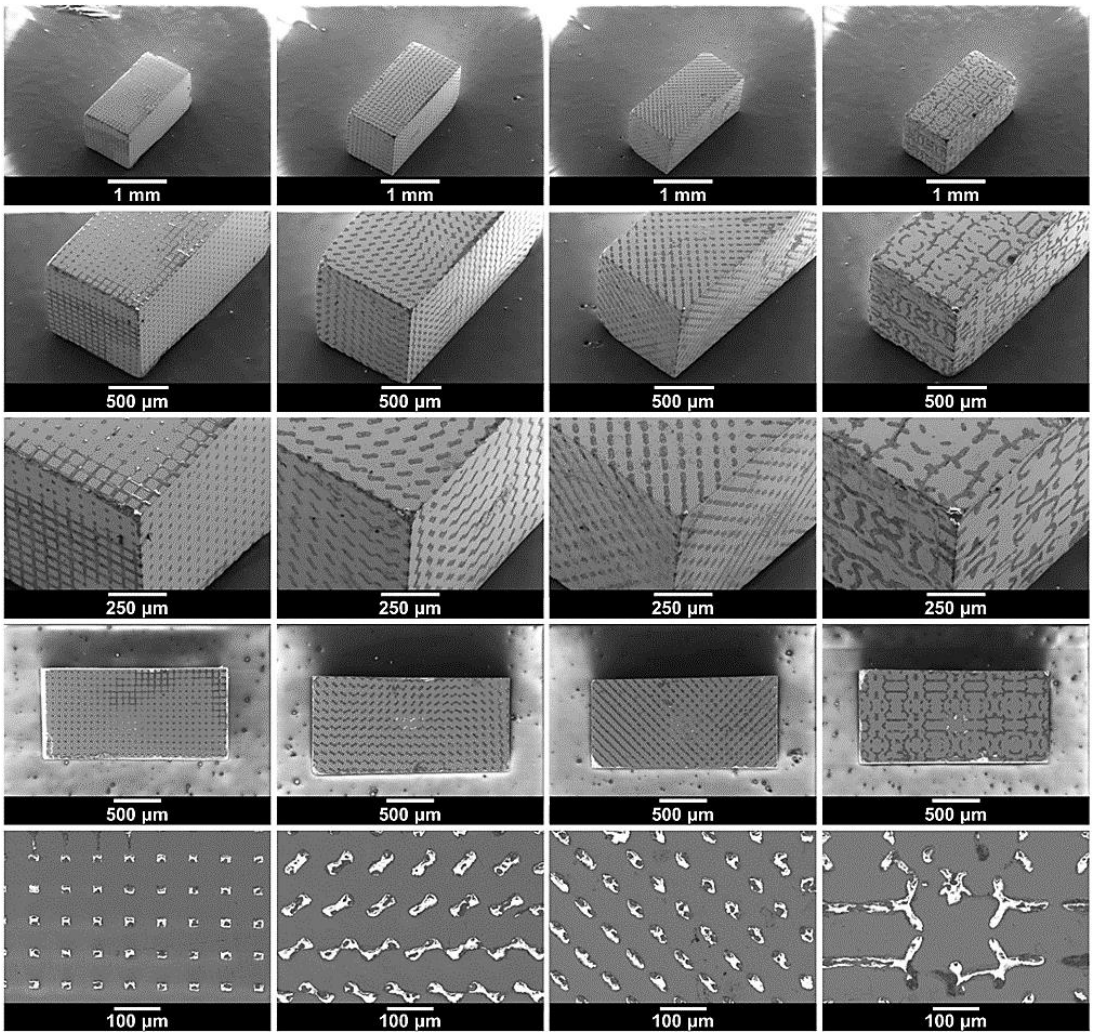


Figure 5.3. SEM images of the final LAGP-epoxy hybrid electrolytes with four different microarchitectures: cubic, gyroid, diamond and bijel (left to right).

LAGP-PP and LAGP-epoxy hybrid electrolytes with all four microarchitectures were successfully synthesised, achieving similar filling weights and densities. Yet, the gyroid microarchitecture attained the highest degree of LAGP filling out of all. Similarly to the synthesised hybrid electrolyte described in Chapter 4, all the synthesised hybrid electrolytes described in this Chapter shrank throughout the synthesis by an average of 30 %. This leads to a decrease in the ceramic-to-polymer ratio of 85 % to 15 % in the initial 3D printed polymer template to 70 % to 30 % in the final LAGP-polymer hybrid

electrolyte, respectively. Table 5.1 summarises the synthesis parameters between all four microarchitectures.

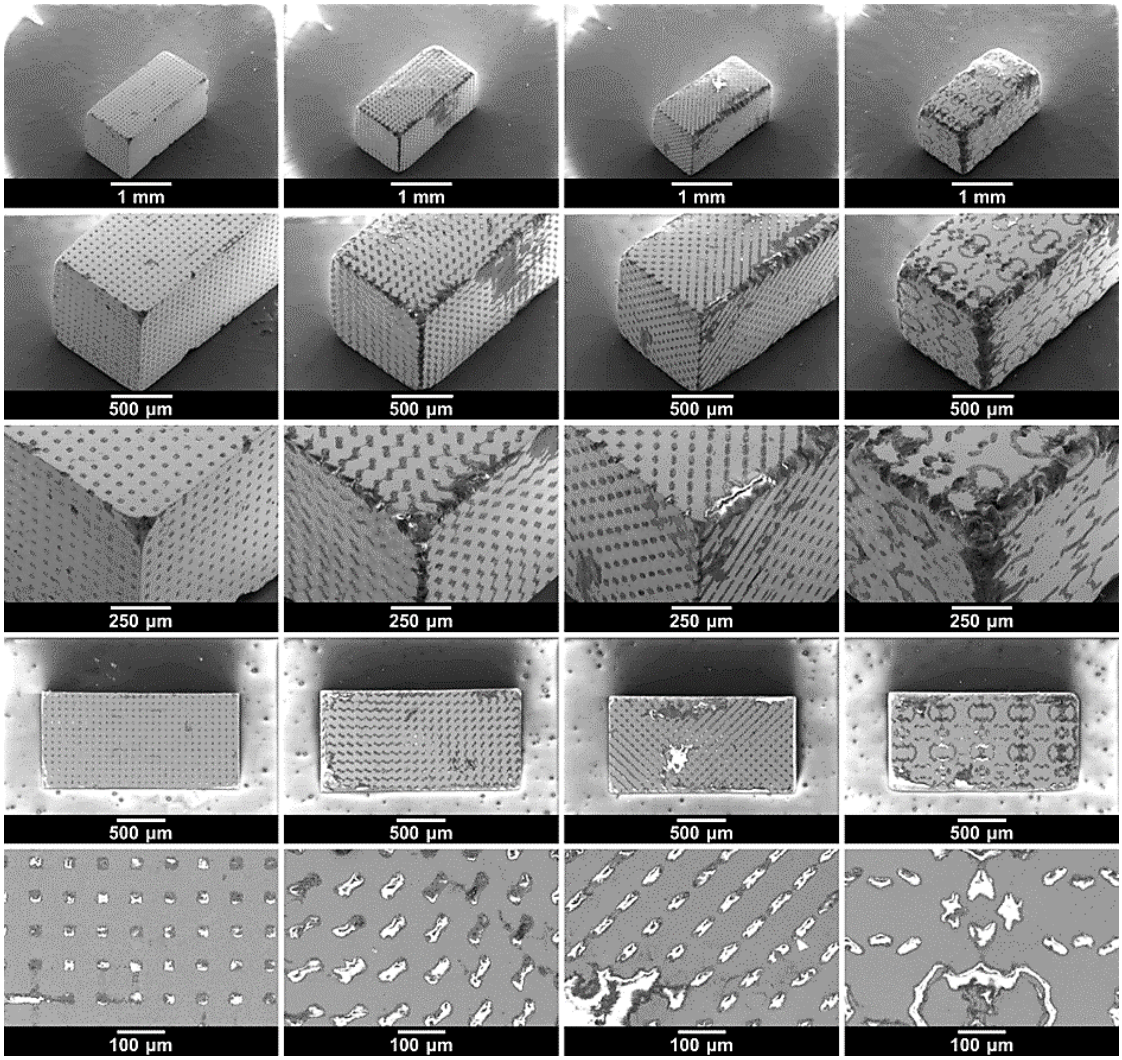


Figure 5.4. SEM images of the final LAGP-PP hybrid electrolytes with four different microarchitectures: cubic, gyroid, diamond and bijel (left to right).

Table 5.1. Parameters of the LAGP-PP and LAGP-epoxy hybrid electrolytes with four different microarchitectures at each stage of the synthesis.

Synthesis Stage	Parameter	Cubic	Gyroid	Diamond	Bijel
Unit cell	Cubic unit cell dimension x=y=z / µm	80	105.6	121.9	240
Print block	Unit cells per print block in x, y, z direction	3 x 3 x 3	2 x 2 x 2	2 x 2 x 2	1 x 1 x 1
	Cubic print block dimension x=y=z / µm	240	211.1	243.8	240
Template design	Print blocks per template design in x, y, z direction	5 x 5 x 10	6 x 6 x 12	5 x 5 x 10	5 x 5 x10
	Length x, y, z / mm	1.20 x 1.20 x 2.40	1.27 x 1.27 x 2.53	1.24 x 1.24 x 2.46	1.20 x 1.20 x2.40
	Volume / mm^3	3.46	4.07	3.77	3.46
	Solid volume fraction / %	15.6	15.6	15.4	15.6
	Average empty channel size / µm	66.1	66.4	67.8	69.0
	Average wall thickness / µm	15.1	20.4	19.9	22.5
Printed template	Weight / mg	0.94	0.95	0.88	0.79
	Length x, y, z / mm	1.20 x 1.20 x 2.40	1.26 x 1.26 2.51	1.21 x 1.21 x 2.41	1.19 x 1.19 x 2.39
	Volume / mm^3	3.46	3.98	3.53	3.38
	Vol. shrinkage during printing / %	0	2	6	2
Template filled with LAGP powder	Weight / mg	6.57	7.54	6.74	6.75
	Length x, y, z / mm	1.25 x 1.27 x 2.53	1.30 x 1.33 x 2.66	1.24 x 1.26 x 2.55	1.26 x 1.29 x 2.57
	Volume / mm^3	4.02	4.60	3.98	4.18
	Filled amount of LAGP / mg	5.63	6.59	5.86	5.96
	Vol. expansion during filling / %	16	16	13	24
Structured LAGP scaffold	Weight / mg	5.54	6.60	5.90	5.94
	Length x, y, z / mm	1.03 x 1.04 x 2.12	1.11 x 1.12 x 2.24	1.10 x 1.10 x 2.14	1.06 x 1.09 x 2.16
	Volume / mm^3	2.27	2.78	2.59	2.50
	Density / mg mm^{-3}	2.44	2.37	2.28	2.38
	Vol. shrinkage during sintering / %	44	40	35	40
	Overall volume shrinkage / %	34	32	31	28
	Solid volume fraction / %	71.4	72.6	72.5	78.2
	Average LAGP thickness / µm	44.2	44.0	42.0	59.5
	Average empty channel size / µm	20.4	20.8	18.4	22.3
Structured LAGP-epoxy electrolyte	Weight / mg	5.34	6.36	5.08	5.66
	Length x, y, z / mm	1.00 x 1.99 x 1.99	1.06 x 1.07 x 2.13	1.00 x 1.00 x 2.02	1.01 x 1.01 x 2.06
	Volume / mm^3	1.99	2.40	2.01	2.10
	Density / mg mm^{-3}	2.69	2.65	2.53	2.70
Structured LAGP-PP electrolyte	Weight / mg	5.58	6.61	5.62	5.84
	Length x, y, z / mm	1.18 x 1.04 x 2.02	1.09 x 1.07 x 2.13	1.03 x 1.05 x 1.97	1.06 x 1.06 x 2.01
	Volume / mm^3	2.47	2.48	2.15	2.25
	Density / mg mm^{-3}	2.26	2.67	2.62	2.59

EDX mapping of the surface of all four geometrically different hybrids is shown in Figure 5.5. In all four cases, the ceramic and polymer channels are well defined and clearly separated, as shown by the C K_α signal (red) representing the polymer channels and the O K_α signal (green), the Al K_α (blue), the P K_α signal (pink) and the Ge L_α signal (yellow) representing the LAGP phase.

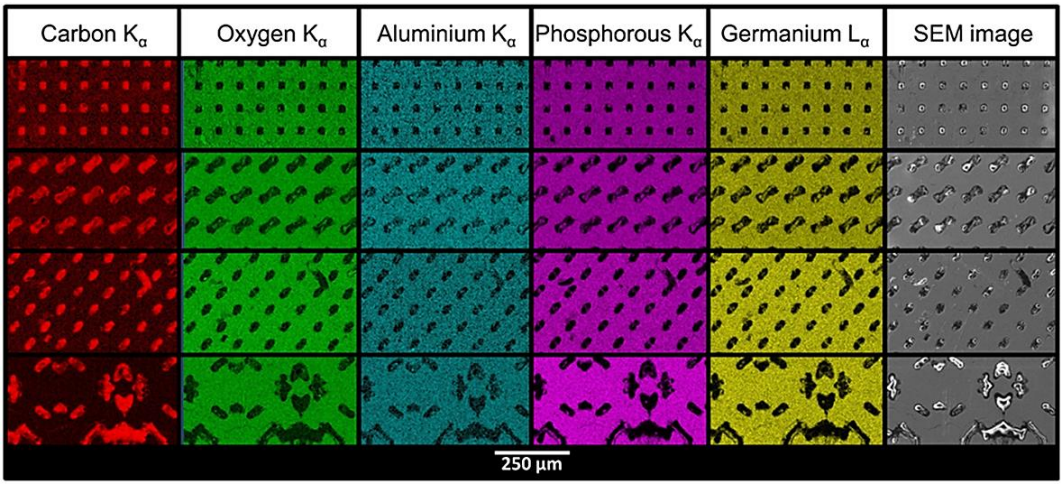


Figure 5.5. EDX mapping and corresponding SEM images of the structured LAGP-epoxy hybrid electrolytes with cubic, gyroid, diamond and bijel microarchitecture (top to bottom).

Micro-CT scans additionally confirm that the geometries are well replicated throughout the entire interior of each of the structured LAGP scaffolds as illustrated in Figure 5.6.

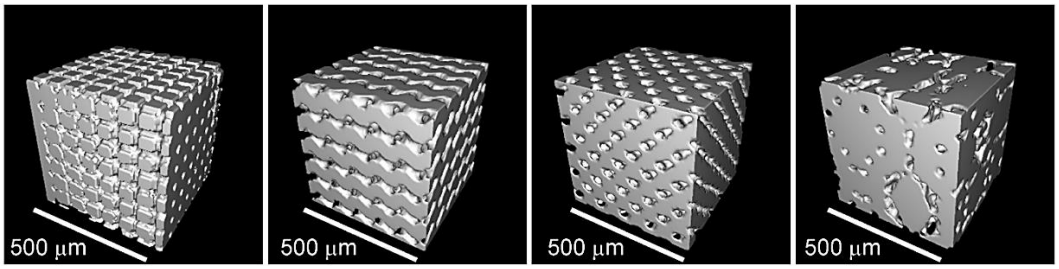


Figure 5.6. 3D renderings of the micro-CT scans of the structured LAGP scaffolds with cubic, gyroid, diamond and bijel microarchitecture (left to right).

5.4.3. Effect of microarchitecture and type of polymer on the ionic conductivity

EIS measurements were performed on the LAGP-polymer hybrid electrolytes synthesised using all four microarchitectures and both types of polymer. The Nyquist plots of the eight Li | LAGP-polymer | Li cells was recorded at RT (Figure 5.7).

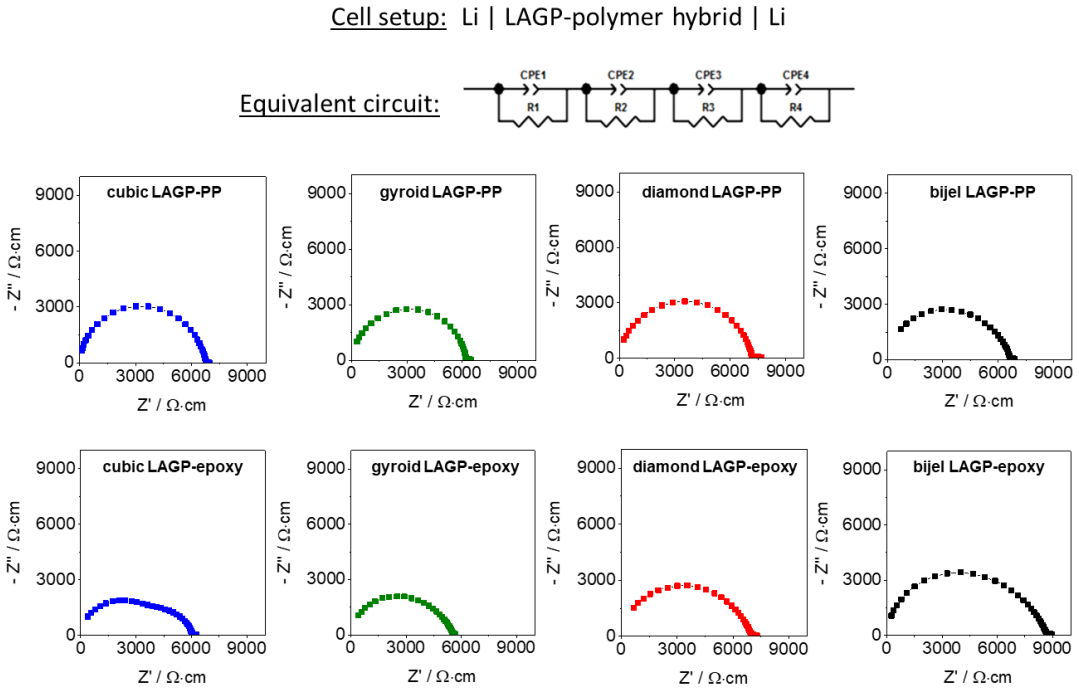


Figure 5.7. Nyquist plots of the LAGP-PP (top row) and LAGP-epoxy (bottom row) hybrid electrolytes with symmetrical Li metal electrodes at RT. The different microarchitectures are displayed in blue (cubic), green (gyroid), red (diamond) and black (bijel) from left to right. The cell setup and equivalent circuit used for fitting the data is also shown. Details of the fitting can be found in Appendix 9.

All cells are expected to exhibit the same electrical features as described in the previous Chapters for LAGP, which are the grain, the grain boundary, the interphase layer and the Li-LAGP interface contributions. The equivalent circuit that best describes the obtained impedance results is composed of four parallel resistances and constant-phase elements

in series corresponding to the grain, grain boundaries, interphase layer and Li-LAGP interface resistances of the cell, as previously discussed in Chapter 3 Section 3.4.3. As the EIS measurements were taken straight after cell assembly, the third semicircle assigned to the Li-LAGP interphase layer contribution yet remained small in all eight cells. The recorded total ionic conductivities and corresponding LAGP phase densities are summarised in Table 5.2.

Table 5.2. Key parameters of the final LAGP-PP and LAGP-epoxy hybrid electrolytes with four different microarchitectures.

	Cubic	**Gyroid**	**Diamond**	**Bijel**
Filled amount of LAGP / mg	5.6	6.6	5.9	6.0
Weight structured LAGP scaffold / mg	5.5	6.6	5.9	5.9
Density structured LAGP scaffold / mg·mm^{-3}	2.4	2.4	2.3	2.4
Ionic conductivity of **LAGP-PP** electrolyte at RT / S·cm^{-1}	1.4 x 10^{-4}	1.5 x 10^{-4}	1.3 x 10^{-4}	1.4 x 10^{-4}
Ionic conductivity of **LAGP-epoxy** electrolyte at RT / S·cm^{-1}	1.6 x 10^{-4}	1.7 x 10^{-4}	1.4 x 10^{-4}	1.1 x10^{-4}

Total ionic conductivity values in the range of 1.1 – 1.7 x 10^{-4} S·cm^{-1} at RT were achieved for all four microarchitectures, independent of the use of PP or epoxy as the polymer. The density of the LAGP phase is closely related to the measured ionic conductivity for all hybrid electrolytes. The gyroid template, which was the easiest to fill out of all four microarchitecture and gave the highest filled amount of LAGP filling in Table 5.2, achieved the highest ionic conductivities with both PP and epoxy polymer.

Although the ionic conductivities are all in a very close range to each other, the microstructure does influence the Li-ion conduction through the ceramic phase. For instance, the cubic microarchitecture is the most ordered and simplest 3D geometry of all. Nevertheless, a significant amount of volume of the ceramic phase is unused during ionic conduction. This was best shown by finite element modelling of the conduction pathways through the microarchitecture by analysing the current distribution through the

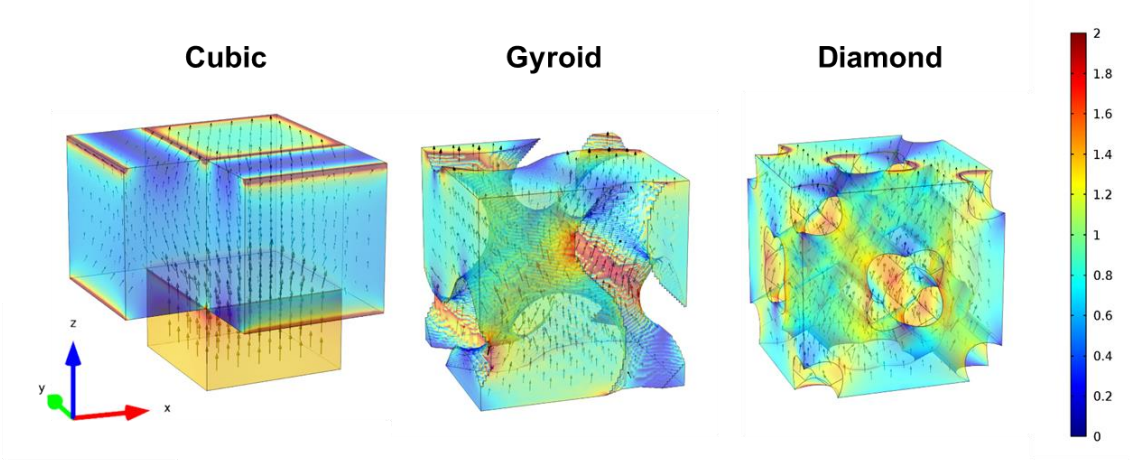
channels (Appendix 6). The efficiency of ionic conduction is mainly related to the tortuosity of the microarchitecture and the volume fraction of ionically conductive material present. All are related together by the following equation:

$$k^{apparent} = \frac{p}{\tau} \times k = f \times k$$

where $k^{apparent}$ is the measured apparent ionic conductivity of the structure, p is the volume of the ionically conductive channels, τ is the tortuosity, f is the current distribution factor (or also geometry factor) and k is the ionic conductivity of the solid electrolyte material. Figure 5.8 visualises the ionic conduction pathways within the unit cells of the cubic, gyroid and diamond microarchitectures and shows the corresponding tortuosity values calculated for a ceramic-to-polymer ratio of 70 % to 30 %, respectively.

Out of all three geometries, the cubic unit cell consists of the most non-electrochemically active volume (labelled in blue) that is not participating in the ionic conduction. Hence, the calculated tortuosity is higher than in the other two microarchitectures. From these calculations, a lower conductivity for the cubic geometry over the gyroid and the diamond geometry is expected as shown by the $k^{apparent}$ values in the table in Figure 5.8. Nevertheless, the measured conductivity for the cubic structure remains in a similar range to the other structures. The difference in tortuosity is yet too little to make a significant difference in the EIS measurements at this particular ceramic-to-polymer ratio. While the tortuosity values between the gyroid and the diamond remain very similar, the better LAGP filling achieved during the synthesis of the gyroid enables it to surpass all other hybrids in terms of ionic conductivity with both PP and epoxy polymer. Due to the random nature of the bijel microarchitecture, which in principle has no repeating channel geometry, a current distribution factor or tortuosity value could not be determined. However, it is expected that the ionic conduction pathways in the bijel will occasionally

be blocked due to the disordered nature of this experimentally synthesised microarchitecture. The ionic conductivity here is largely dependent on the orientation of the randomly ordered LAGP channels and how these are connected from one side of the electrode to the other. Hence, this explains the rather large difference in ionic conductivity observed between the bijel LAGP-PP and bijel LAGP-epoxy hybrid (Table 5.2).



	Cubic	Gyroid	Diamond
Current distribution factor f	0.540	0.577	0.576
Tortuosity τ	1.296	1.213	1.218
Ionic conductivity $k^{apparent}$ / S·cm^{-1}	1.5 x 10^{-4}	1.6 x 10^{-4}	1.6 x 10^{-4}

Figure 5.8. Current density distribution models from finite element modelling of the cubic (left), gyroid (centre) and diamond unit cell (right). The normalised current densities through the cells are represented by a colour chart from 0 (no current flow) in blue to 2 (maximum current flow) in red. The table below summarises the current distribution factor f, the tortuosity value and the apparent ionic conductivity calculated for all three geometries. An ionic conductivity of 2.8 x 10^{-4} S·cm^{-1} at RT was assumed for the ionic conductivity of the LAGP electrolyte.

5.4.4. Effect of microarchitecture and type of polymer on the cycling performance with Li metal electrodes

To understand the effect of the microarchitecture and the polymer on the cycling performance of the hybrid electrolyte, galvanostatic cycling experiments were performed on all eight symmetrical cells synthesised above using a constant current density of 1 mA·cm^{-2} for 0.5 hours per charge and discharge direction for a total of 10 cycles. It is expected that due to the reactivity of Li metal with LAGP, the cell voltages will increase by a certain degree with cycle number. However, as shown in Figure 5.9, distinct differences in cycling performances were obtained between the eight hybrid electrolytes analysed.

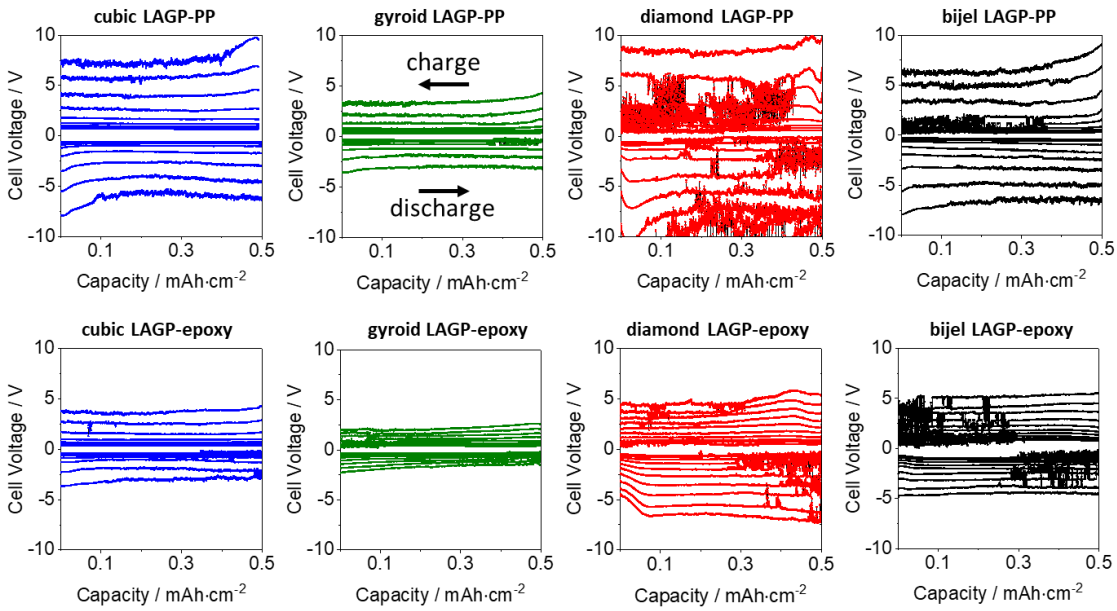


Figure 5.9. Galvanostatic cycling of symmetrical cells of structured LAGP-PP hybrid electrolytes (top row) and structured LAGP-epoxy hybrid electrolytes (bottom row) with cubic, gyroid, diamond and bijel microarchitectures (left to right), assembled with Li metal electrodes. All eight cells were cycled at a constant current density of 1 mA·cm^{-2} for 0.5 hours per charge and per discharge direction for a total of 10 cycles.

All four microarchitectures with LAGP and epoxy as the ceramic electrolyte and polymer, respectively, proved to give a better cycling performance over 10 cycles with cell voltages remaining below 5 V. On the contrary, all four geometries in the LAGP-PP hybrid electrolytes showed much higher increases in cell voltages, with final cell voltages of up to 10 V for the cubic, diamond and bijel microarchitectures. Overall, the gyroid microarchitecture outperformed all other hybrid geometries, using either PP or epoxy. The best electrochemical performance was achieved with the gyroid LAGP-epoxy hybrid electrolyte, which only attained a cell voltage of 2.6 V after 10 cycles.

The better performance of the epoxy polymer over PP could be either linked to its more favourable adhesive properties with the LAGP and the Li metal, improving the Li-solid electrolyte contact upon cycling, or to its more suitable mechanical properties as a thermosetting polymer. Thermosetting polymers are known for their chemical and heat resistance, high rigidity and dimensional stability. Their highly cross-linked polymer network, gives them a high tensile strength and a high durability compared to thermoplastic polymers such as PP. The higher strength of the epoxy polymer over PP was confirmed through four-point bending tests on both materials (Appendix 10). From the cycling performance shown in Figure 5.9 it appears that the epoxy polymer is better at retaining the sample's structural integrity and maintaining the contact between the solid electrolyte and the electrodes during cycling due to its higher fracture strength than is PP. The better cycleability of the hybrid electrolytes with the gyroid microarchitecture is considered to be related to the structural properties of the microarchitecture. The spatial distribution of stress in the gyroid architecture is believed to be the most uniform compared to the other architectures. The presence of a dense ceramic phase that is well contacted to a dense polymer phase, such as is the case for the gyroid hybrid, helps to

retain a good contact between the electrodes and the electrolyte and avoid cell polarisations during cycling.

5.4.5. Synthesis of the 3D ordered LAGP-epoxy electrolytes with different ceramic-to-polymer ratios

The effect of different ceramic-to-polymer ratios was also investigated. For this, LAGP-epoxy hybrid electrolytes with a gyroid microarchitecture with three different ceramic-to-polymer ratios were explored: 85 % to 15 %, 70 % to 30 % and 50 % to 50 %, respectively. The same synthesis as described previously in this Chapter was utilised (Chapter 5 Section 5.3.1.3). SEM images of the structured LAGP scaffolds of all three ratios are illustrated in Figure 5.10.

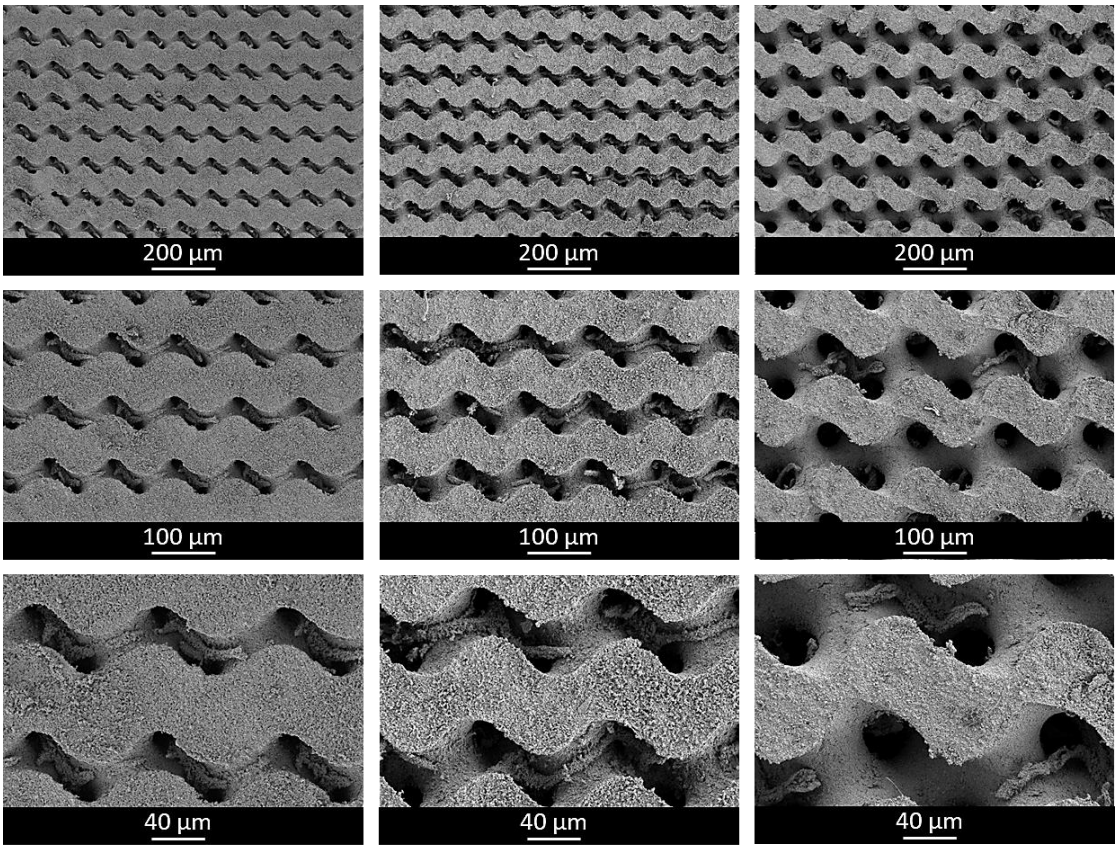


Figure 5.10. SEM images of the structured LAGP scaffolds with gyroid microarchitecture using initial 3D printed polymer templates with 85 % (left), 70 % (centre) and 50 % porosity (right).

Even though the filling procedure and sintering was more challenging for the 50 % porosity template due to the narrower channels and the greater volume of combustible polymer material, LAGP-epoxy gyroid electrolytes with all three ceramic-to-polymer ratios could be synthesised. Table 5.3 summarises the synthesis parameters for all three ratios.

Table 5.3. Parameters of the gyroid LAGP-epoxy hybrid electrolytes with three different ceramic-to-polymer ratios at each stage of the synthesis.

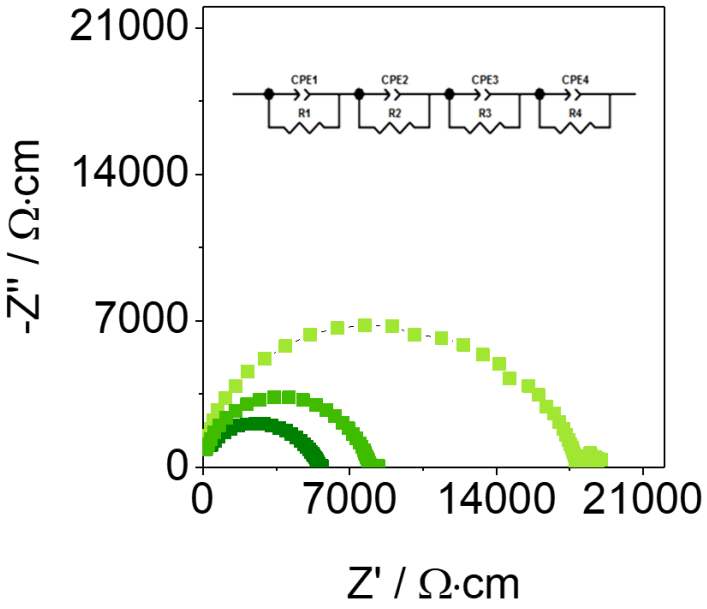
Synthesis Stage	Parameter	85 %	70 %	50 %
Unit cell	Cubic unit cell dimension x=y=z / µm	105.6	124.1	162.6
Print block	Unit cells per print block in x, y, z direction	2 x 2 x 2	2 x 2 x 2	2 x 2 x 2
	Cubic print block dimension x=y=z / µm	211.1	248.2	325.3
Template design	Print blocks per template design in x, y, z direction	14 x 14 x 5	12 x 12 x 3	9 x 9 x 2
	Length x, y, z / mm	2.98 x 2.98 x 1.08	3.00 x 3.00 x 0.76	2.95 x 2.95 x 0.67
	Volume / mm^3	9.6	6.8	5.8
	Solid volume fraction / %	15.6	30.5	49.9
Printed template	Weight / mg	2.4	2.7	3.4
	Length x, y, z / mm	2.95 x 2.96 x 1.07	3.00 x 3.00 x 0.75	2.94 x 2.93 x 0.63
	Volume / mm^3	9.3	6.8	5.4
	Vol. shrinkage during printing / %	3	0	7
Template filled with LAGP powder	Weight / mg	16.1	11.5	8.2
	Length x, y, z / mm	3.12 x 3.12 x 1.09	3.15 x 3.15 x 0.80	3.03 x 3.08 x 0.65
	Volume / mm^3	10.6	7.9	6.9
	Filled amount of LAGP / mg	13.7	8.8	4.8
	Vol. expansion during filling / %	14	29	28
Structured LAGP scaffold	Weight / mg	13.7	8.3	4.5
	Length x, y, z / mm	2.58 x 2.57 x 0.96	2.64 x 2.65 x 0.66	2.57 x 2.62 x 0.56
	Volume / mm^3	6.4	4.6	3.8
	Density / $mg \cdot mm^{-3}$	2.2	1.8	1.2
	Vol. shrinkage during sintering / %	40	42	45
	Overall volume shrinkage / %	31	32	34
	Solid volume fraction / %	69	61	45
Structured LAGP-epoxy electrolyte	Weight / mg	14.7	9.5	6.3
	Length x, y, z / mm	2.59 x 2.60 x 0.94	2.63 x 2.61 x 0.67	2.63 x 2.63 x 0.59
	Volume / mm^3	6.3	4.6	4.1
	Density / $mg \cdot mm^{-3}$	2.3	2.1	1.5

Similar to the hybrids with different microarchitectures, shrinkage also occurs during the synthesis with different ceramic-to-polymer ratios. While some minor shrinkage occurs during the printing stage, the most significant amount of shrinkage occurs during the sintering step. Although different quantities of filled ceramic material need to be sintered in each case, a similar amount of shrinkage was observed for all three ratios. An overall shrinkage from the template design to the structured LAGP scaffold of 31 %, 32 % and 34 % was measured for the 85 %, 70 % and 50 % porosity polymer templates, respectively. Due to this shrinkage, a change in the final ceramic-to-polymer ratio from the porosity of the initial template design of 85 %, 70 % and 50 % to the final LAGP volume fraction of approximately 70 %, 60 % and 45 %, is observed respectively.

5.4.6. Effect of the ceramic-to-polymer ratio on the ionic conductivity

EIS measurements were performed on the synthesised gyroid LAGP-epoxy hybrid electrolytes with LAGP phase volume fractions of 70 %, 60 % and 45 % as described in the previous section. Figure 5.11 shows the Nyquist plots of all three hybrids. As the non-conductive polymer volume fraction increases, the ionic conductivity of the gyroid hybrids decreases as shown in Figure 5.11. Finite element modelling confirms that the tortuosity of the gyroid is expected to increase and the geometry factor (or current distribution factor) to decrease as the ceramic volume fraction is decreased (Appendix 6). From these calculations, a geometry factor of 0.58, 0.46 and 0.34 for the 70 %, 60% and 45 % ceramic volume fraction hybrids was estimated. Taking this factor into account results in expected ionic conductivity values of 1.6×10^{-4} S·cm^{-1}, 1.3×10^{-4} S·cm^{-1} and 9.5×10^{-5} S·cm^{-1} at RT for the 70 %, 60 % and 45 % hybrids, respectively (Figure 5.11). While the expected and obtained ionic conductivities match well for the 70 % ceramic volume fraction LAGP-epoxy hybrid, a slightly lower conductivity of 1.1×10^{-4} S·cm^{-1} at RT and an even lower conductivity of 5.1×10^{-5} S·cm^{-1} at RT were obtained for the

60 % and 45 % LAGP-epoxy hybrid, respectively. These differences are mainly attributed to the LAGP filling and LAGP phase density achieved in these structures. The smaller the channels in the initial printed template, the more difficult it is to achieve a high degree of LAGP filling. The amount of LAGP filled into the channels is directly related to the density of the LAGP phase in the hybrid, which directly correlates to the ionic conductivity of the hybrid. Hence, a deviation in the final ionic conductivity for the 60 %, but especially for the 45 % LAGP-epoxy hybrid is expected (Figure 5.11).



	70 %	60 %	45 %
Filled amount of LAGP / mg	14.0	9.2	4.8
Weight structured LAGP scaffold / mg	13.9	9.4	4.5
Density structured LAGP scaffold / mg·mm^{-3}	2.2	1.8	1.2
Ionic conductivity of **LAGP-epoxy** electrolyte at RT / S·cm^{-1}	1.6 x 10^{-4}	1.1 x 10^{-4}	5.1 x 10^{-5}
Expected density structured LAGP scaffold / mg·mm^{-3}	2.2	1.9	1.4
Expected ionic conductivity of **LAGP-epoxy** electrolyte at RT / S·cm^{-1}	1.6 x 10^{-4}	1.3 x 10^{-4}	9.5 x 10^{-5}

Figure 5.11. Nyquist plots and synthesis parameters of the gyroid LAGP-epoxy hybrid electrolytes with 70 % (dark green), 60 % (green) and 45 % (light green) of LAGP phase volume fraction. Details of the EIS fitting are found in Appendix 11.

5.4.7. Effect of the ceramic-to-polymer ratio on the cycling performance with Li metal electrodes

The influence of the ceramic-to-polymer ratio on the cycling performance with Li metal was investigated by cycling all three cells discussed in the previous section at a constant current density of 1 mA·cm^{-2} up to a capacity of 0.5 mAh·cm^{-2} for 10 cycles. Figure 5.12 shows the differences obtained in the voltage curves between all three cells.

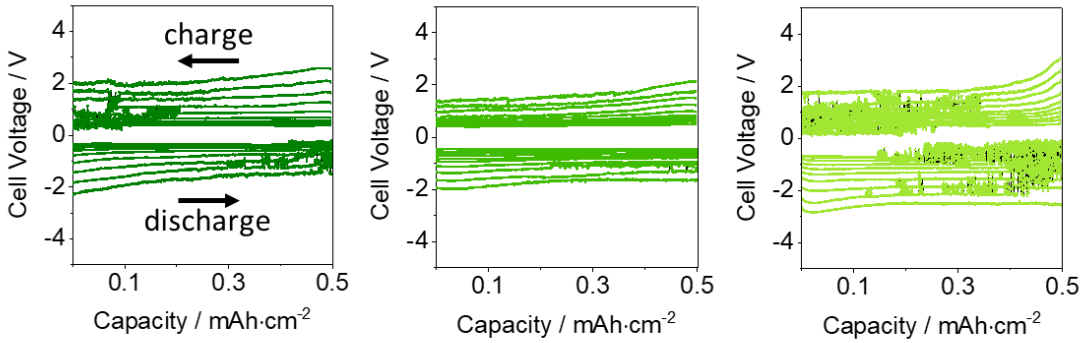


Figure 5.12. Galvanostatic cycling of the gyroid LAGP-epoxy hybrid electrolytes with 70 % (dark green), 60 % (green) and 45 % (light green) of LAGP phase volume fraction assembled with symmetrical Li metal electrodes. The cells were cycled at a constant current density of 1 mA·cm^{-2} up to a capacity of 0.5 mAh·cm^{-2} for 0.5 hours per current direction for 10 cycles.

The cell voltages remained on average below 2 V for all three cells. Although a slightly better performance was obtained for the 60 % LAGP-epoxy hybrid, no significant differences between any of the three ratios were observed. A gradual increase in the cell voltage with cycle number was observed for all three cells, which, as has been discussed in Chapter 3 and 4, is mainly related to the reactivity of LAGP with Li. This undesired reaction occurs independently of the amount of polymer or ceramic volume fraction present and seems to be the controlling factor in the cycling performance of all three cells, at least in the first 10 cycles.

5.4.8. Mechanical properties of the 3D ordered LAGP-polymer electrolytes

As seen from the two previous Chapters 3 and 4, LAGP is a brittle ceramic material. Its electrochemical performance is limited by its readiness to fracture following the formation of a reactive LAGP-Li interphase layer that leads to detachment and crack propagation from the bulk LAGP electrolyte. Chapter 4 showed that the LAGP phase in the ceramic-polymer hybrid electrolyte is still affected in the same way by its brittle properties as a LAGP pellet alone. Yet, the polymer phase supports and maintains the structural integrity of the hybrid electrolyte during cycling showing an improvement in the cell lifetime and the mechanical properties. This was demonstrated through electrochemical and mechanical tests.

Similarly to the two previous Chapters 3 and 4, mechanical tests were performed on the eight hybrid electrolytes with different microarchitectures and polymers. Initially, *in-situ* compression tests were performed on the geometrically different LAGP-PP hybrid electrolytes to qualitatively analyse the different fracture properties of each microstructure. Figure 5.13 shows that crack propagation and ultimate fracture occurs preferentially along the ordered channel pathways for the cubic and the diamond microarchitectures, whereas no preferential fracture pathway is observed for the gyroid and the bijel microarchitectures. The latter two microarchitectures split readily into several fragments upon compression. As a comparison, an LAGP block of the same shape was also compressed in the same manner. Whereas most of the hybrid electrolytes remained in the field of view after fracturing, the LAGP block split instantaneously with half of the fragmented block not remaining in the SEM viewing field.

To obtain quantitative results on the differences in mechanical properties between microarchitectures, stress-strain curves from a stand-alone Shimadzu compression testing

system were recorded at a constant displacement rate of 1 μm·min^{-1}. Figure 5.14 shows that a decrease of 20-35 % in the elastic modulus was recorded for all eight hybrid electrolytes (41-51 GPa) compared to an equivalent in size LAGP block (63 GPa). A decrease in the compressive yield stress from 0.55 GPa in the LAGP block to 0.24-0.36 GPa and 0.28-0.50 GPa in the LAGP-PP and LAGP-epoxy hybrid electrolytes was observed, respectively. A change in the percentage compressive strain until fracture from 0.84 % in the LAGP block to 0.53-0.95 % and 0.71-0.85 % for the LAGP-PP and LAGP-epoxy hybrids, respectively, was also recorded.

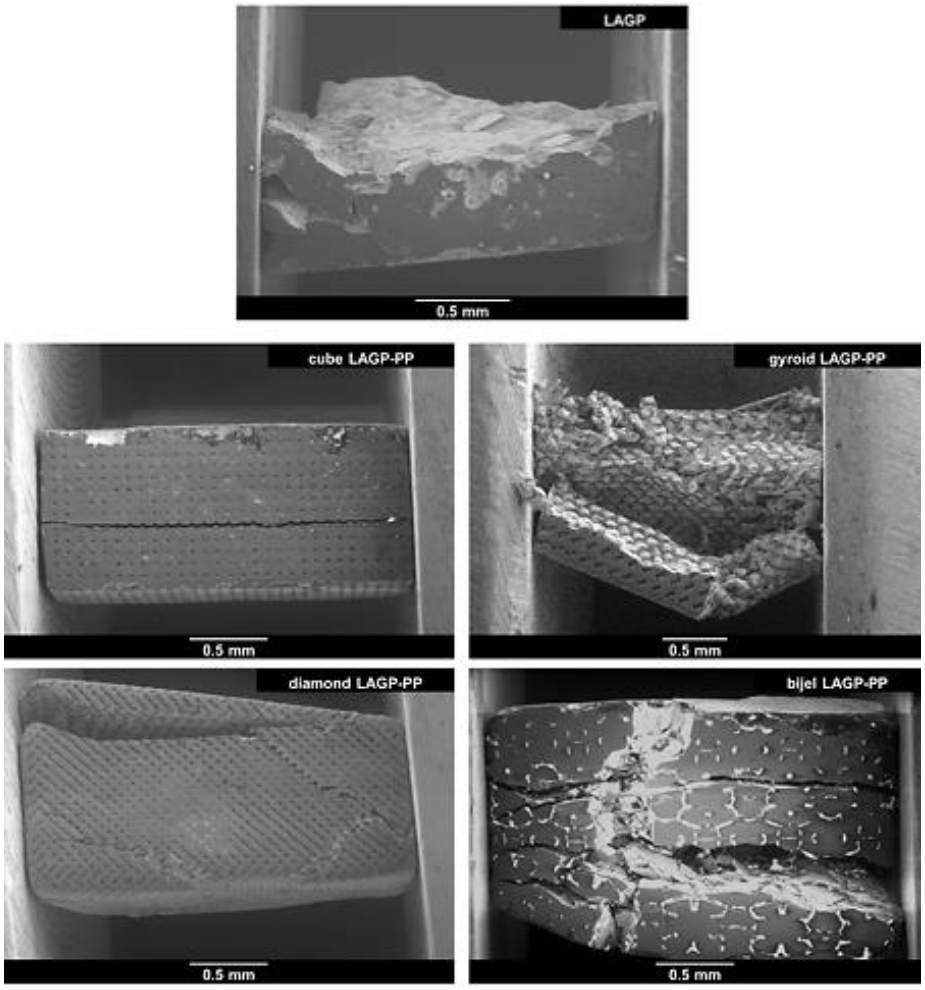


Figure 5.13. Post-in-situ compression testing SEM images of an LAGP block and structured LAGP-PP scaffolds with cubic, gyroid, diamond and bijel microarchitectures mounted between two compression plates within a scanning electron microscope.

Overall, the LAGP-epoxy hybrid electrolytes reached on average a higher compressive stress than the LAGP-PP hybrid electrolytes (0.40 GPa versus 0.29 GPa, respectively). The interaction at the interface between the LAGP and the epoxy seems to be stronger than between the LAGP and the PP. From all LAGP-epoxy hybrid electrolytes, the hybrid with the gyroid microarchitecture achieved the best results with an increase in fracture strain over the LAGP block by 28 %. It is believed that the gyroid microarchitecture has the most uniform spatial distribution of stress, compared to the other microarchitectures investigated.

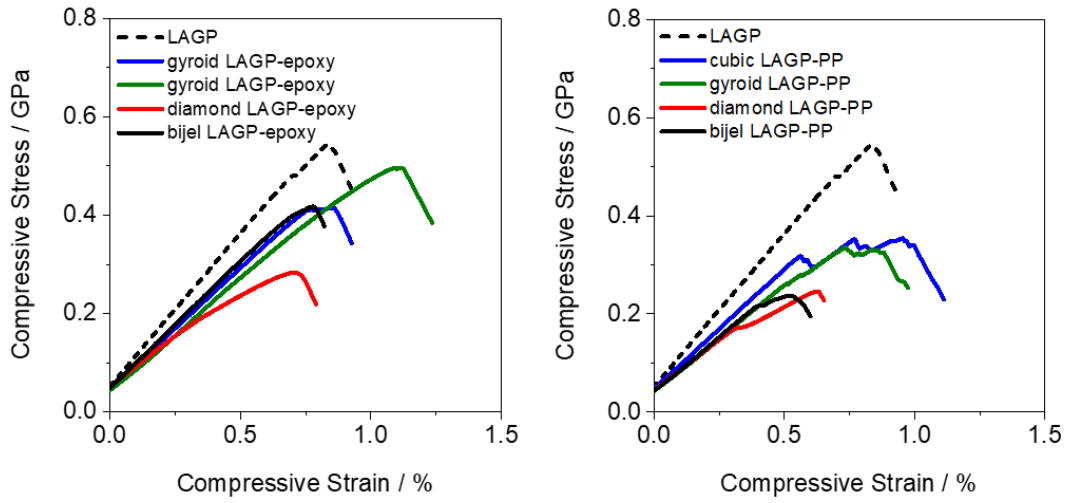


Figure 5.14. Stress-strain curves of LAGP versus LAGP-epoxy hybrid electrolytes (left) and LAGP-PP hybrid electrolytes (right) obtain from a strain rate controlled compression test.

In addition to compression tests, four-point bending measurements were also performed. Figure 5.15-a shows that the microarchitecture of the LAGP-epoxy hybrid electrolytes does not significantly affect the outcome of the stress-strain curves. The flexural moduli were measured to be in the range of 19-35 GPa for all microarchitectures, which is in a similar range to the elastic moduli measured for the gyroid hybrid electrolyte in Chapter 4 Section 4.4.7. For all four microarchitectures, a similar stress-strain behaviour to the hybrid electrolyte discussed in Chapter 4 Section 4.4.7 was observed consisting of

an initial linear increase in stress and strain, followed by a plateau region and a second 'saw-tooth' like increase in stress and strain before fracture. Even though the highest yield stress was achieved by the gyroid microarchitecture at 59 MPa, a significant variation between samples of identical microarchitectures is possible. Hence, none of the microarchitectures stood out as a specifically better microarchitecture in these measurements.

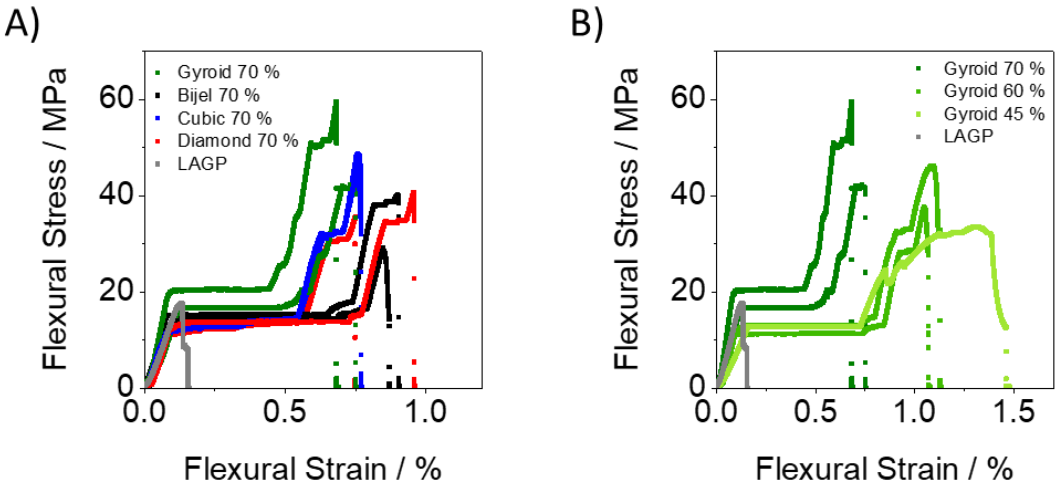


Figure 5.15. Stress-strain curves of LAGP-epoxy hybrid electrolytes with gyroid, cubic, diamond and bijel microarchitectures with a 70 % LAGP phase volume fraction (A) and of gyroid LAGP-epoxy hybrid electrolytes with a 70 %, 60 % and 45 % LAGP phase volume fraction (B). The stress-strain curve of LAGP is also shown.

The stress-strain curves of the gyroid LAGP-epoxy hybrid electrolytes with different LAGP phase volume fractions showed a more significant change in their stress-strain behaviour (Figure 5.15-b). An increase from 0.7 to 1.1 to 1.3 in percentage flexural strain was observed when reducing the LAGP phase volume fraction from 70 %, to 60 % and to 45 %, respectively. This confirms that the epoxy polymer increases the flexural properties of the hybrid, extending the hybrid's ability to resist immediate fracture. The flexural moduli for all three polymer-to-ceramic ratios were calculated to be 29 GPa,

23 GPa and 13 GPa, respectively, as the LAGP phase volume is decreased. A more pronounced decrease in the yield stress from an average of 51 MPa, to 42 MPa, to 34 MPa in the 70 %, 60 % and 45 % LAGP phase volume fraction hybrids, respectively, was also recorded. Both of these decreases can be partially due to the increasing percentage volume fraction of epoxy polymer present, but also due to the differences in the LAGP phase density and overall density of the final hybrids. As discussed previously in this Chapter (Chapter 5 Section 5.4.5), the LAGP filling of the narrower channels in the 50 % porous 3D printed templates is slightly more challenging than is the LAGP filling in the 85 % porous 3D printed templates. This leads to closed micro-sized pores that remain empty throughout the remainder of the synthesis, which can ultimately reduce the stiffness of the LAGP phase in the hybrids. Nevertheless, the increasing percentage volume fraction of epoxy polymer around the LAGP channels assists the hybrids to achieve higher fracture strains.

5.4.9. Synthesis of a 3D gyroid LLZTO-epoxy electrolyte

Garnet-type ceramic electrolytes are praised in the literature for their ability to form a chemically stable interface with Li metal. This is a significant advantage over other ceramic electrolytes such as LAGP, which, as shown in details in Chapter 3, tend to rapidly react with Li and form an MCI layer at the electrode-electrolyte interface. Similarly to LAGP, garnet-type electrolytes are extremely brittle. Hence, the synthesis of a hybrid electrolyte using a garnet ceramic electrolyte could help to tune its mechanical properties and prolong its cycle life.

As will be discussed more thoroughly in the following Chapter (Chapter 6), the synthesis of $Li_{6.5}La_3Zr_{1.5}Ta_{0.5}O_{12}$ (LLZTO) is far more challenging than the synthesis of LAGP. Whereas the filling procedure of the initial 3D printed template could be taken over

without any changes from the LAGP-polymer hybrid electrolyte synthesis, the sintering procedure had to be significantly adapted, as illustrated by a schematic in Figure 5.16.

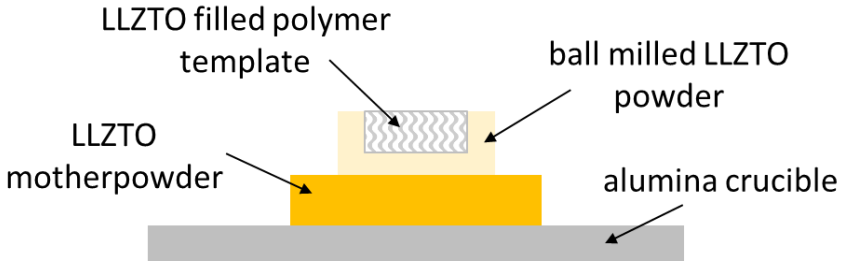


Figure 5.16. Schematic of the employed sintering configuration of a LLZTO filled 3D polymer template.

In order to retain the hybrid's microarchitecture in the best way possible during the sintering step, LLZTO-filled polymer templates were pressed into a pellet with calcined LLZTO powder and placed on a pressed layer of LLZTO 'motherpowder' composed of a mixture of calcined LLZTO powder and Li_2O. LLZTO motherpowder is used to cover LLZTO pellets to avoid the evaporation of Li and loss of the favourable cubic LLZTO phase, as will be discussed in more detail in Chapter 6. If the filled templates are covered throughout with LLZTO motherpowder, the microstructure is completely lost and the templates cannot be recovered. Compared to the sintering of LAGP, a significant increase in sintering temperature up to a temperature of 1250 °C and a significant decrease in sintering time down to only 10 minutes is required. This drastically complicates the synthesis of the hybrid. The initial 3D printed polymer template has much less time and space to burn out of the 3D structure without reacting with the LLZTO inside the hybrid or the LLZTO motherpowder surrounding the hybrid. Prolonging the sintering time leads to an increase in grain growth as will be discussed in Chapter 6, which leads to a rapid loss in the defined microarchitecture of the 3D scaffold and the disappearance of any empty polymer channels. Even when using shorter sintering times, the surrounding

LLZTO motherpowder fuses readily together with the filled template, making it difficult to remove from the excess motherpowder after sintering without polishing or losing the shape of the structured LLZTO scaffold.

Hence, a 3D polymer template with an initial porosity and polymer volume fraction of 50 % was used to facilitate the combustion of the polymer and the growth of LLZTO grains in the template during sintering. Additionally, due to its favourable electrochemical and mechanical properties as shown earlier in this Chapter, 3D polymer templates with a gyroid microarchitecture were used. Similarly, epoxy was used as the polymer material. The filling of the epoxy polymer into the newly created channels of the structured LLZTO scaffold was performed as developed for the LAGP-epoxy hybrids (Chapter 4 Section 4.3.1.5).

SEM images of the obtained LLZTO scaffold and the final freestanding LLZTO-epoxy hybrid electrolyte are shown in Figure 5.17. Compared to a 50 % 3D polymer template filled with LAGP that results into a 45 % ceramic volume fraction LAGP scaffold after sintering, a roughly 60 % ceramic volume fraction LLZTO scaffold is obtained in the case of LLZTO. Whereas the LAGP grains fuse together upon sintering to a more compact volume with minimal grain boundaries, the growth of the LLZTO grains and its corresponding grain boundary phase is much more important, which highlights again the sintering difficulties with this specific solid electrolyte.

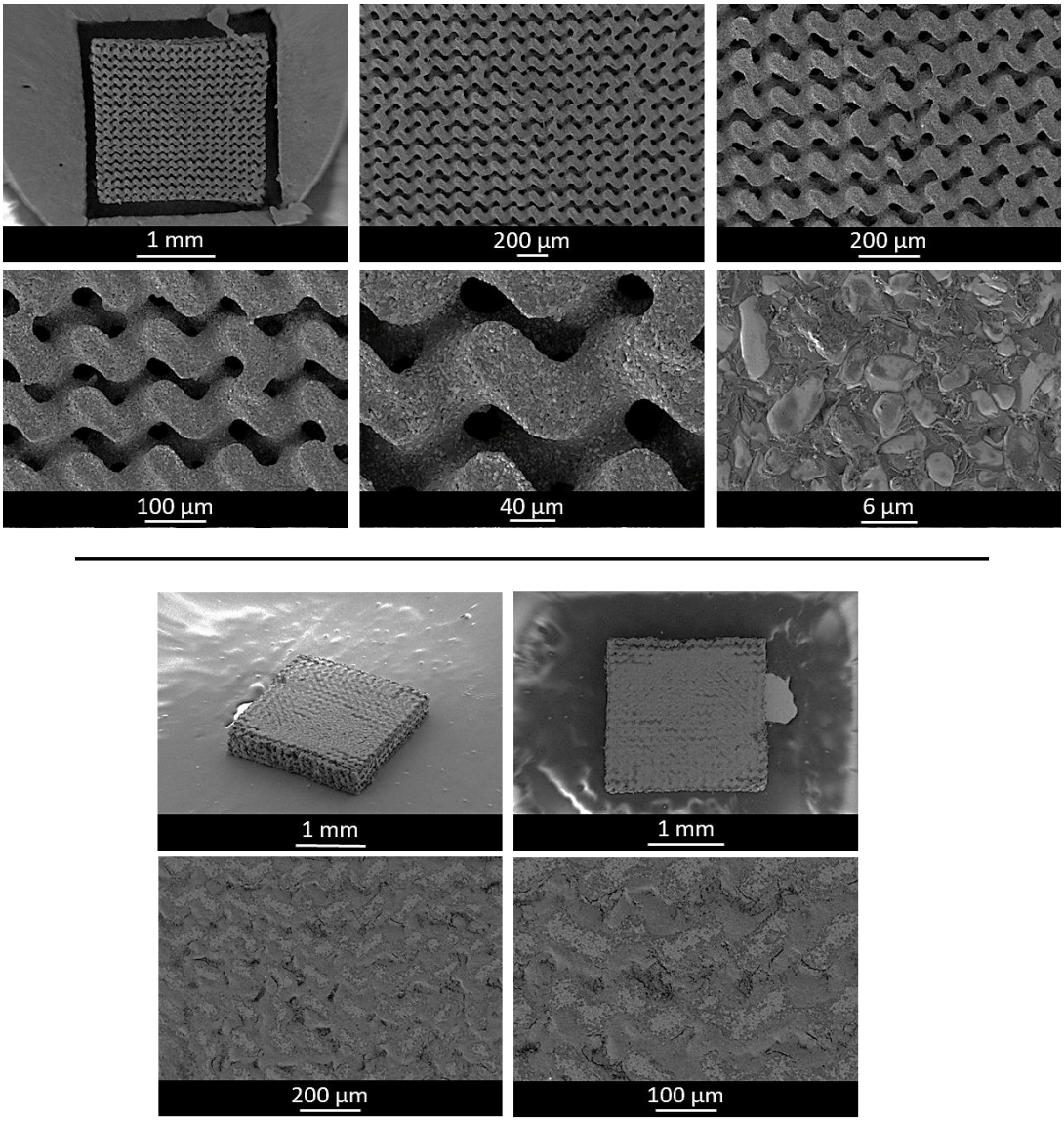


Figure 5.17. SEM images of the gyroid LLZTO scaffold after sintering (top) and final free-standing LLZTO-epoxy hybrid (bottom).

Analysing the structured LLZTO scaffold with PXRD showed all relevant peaks of the desired LLZTO cubic phase, as was also obtained for an equivalently sintered LLZTO pellet (Figure 5.18). This confirms that the scaffold retains the conductive cubic garnet phase during its synthesis. Nevertheless, two impurity peaks (labelled in red) were found, which could not be assigned to any other known crystalline phases in the literature.

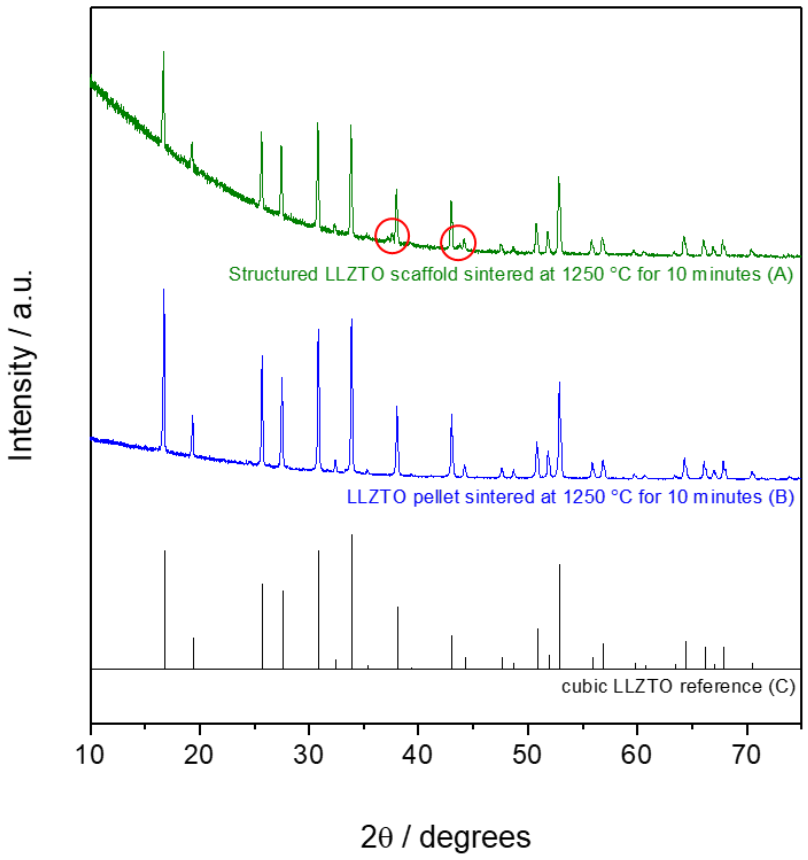


Figure 5.18. PXRD pattern of the structured LLZTO scaffold after sintering (A) compared with a sintered LLZTO pellet (B) and the cubic LLZTO reference pattern (C).[4] Detected impurities are circled in in red.

EDX analysis of the final gyroid LLZTO-epoxy hybrids shows that a separation between the ceramic and the polymer phase into two channels was achieved with C mainly found in the polymer channels and La, Zr and O found in the LLZTO channels (Figure 5.19). Ta as a dopant was more difficult to detect in the ceramic channels only. An improvement in the polishing of the surfaces could lead to a more distinct separation between ceramic and polymer channels in the EDX maps.

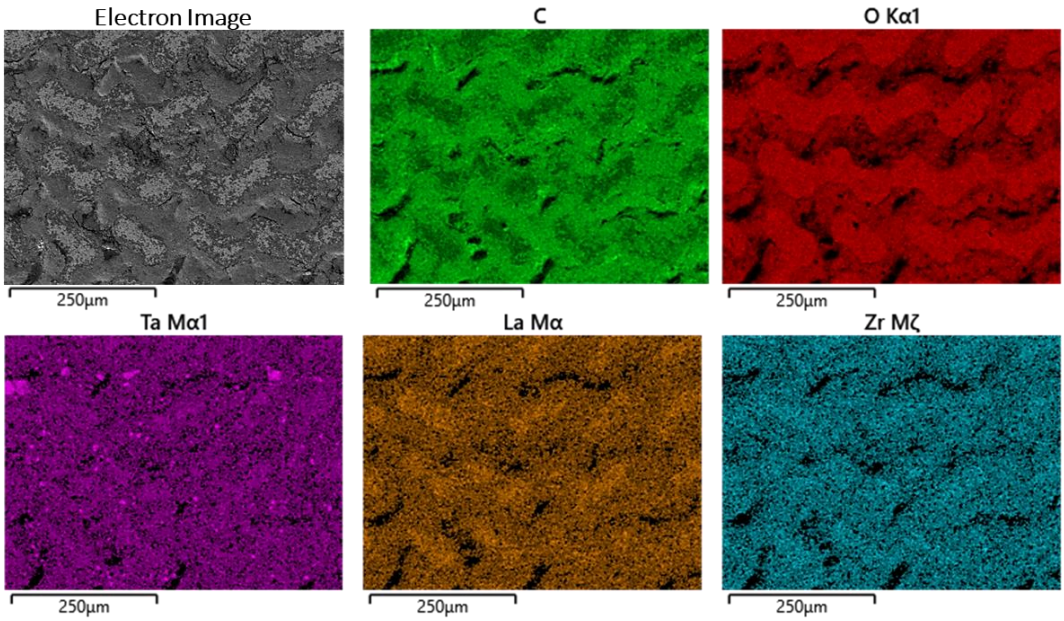


Figure 5.19. EDX mapping of the gyroid LLZTO-epoxy hybrid electrolyte showing the two distinct ceramic and polymer channels.

A closer look at the LLZTO phase reveals the presence of a secondary phase between grains (Figure 5.20). This phase could relate to the additional peaks observed in the PXRD pattern of the structured LLZTO scaffold. The use of less LLZTO motherpowder, especially when covering the templates, together with the longer exposure of the filled templates to air during the synthesis and the difficulty of the polymer to be able to freely burn out of the template can easily induce impurity phases. EDX mapping of the impurity phase reveals that it is mainly composed of C and O with some minimal amounts of Ta, suggesting that the initially 3D printed polymer might not have had the time and space to burn out of the structure, but instead fused between the LLZTO grains where it became trapped during sintering.

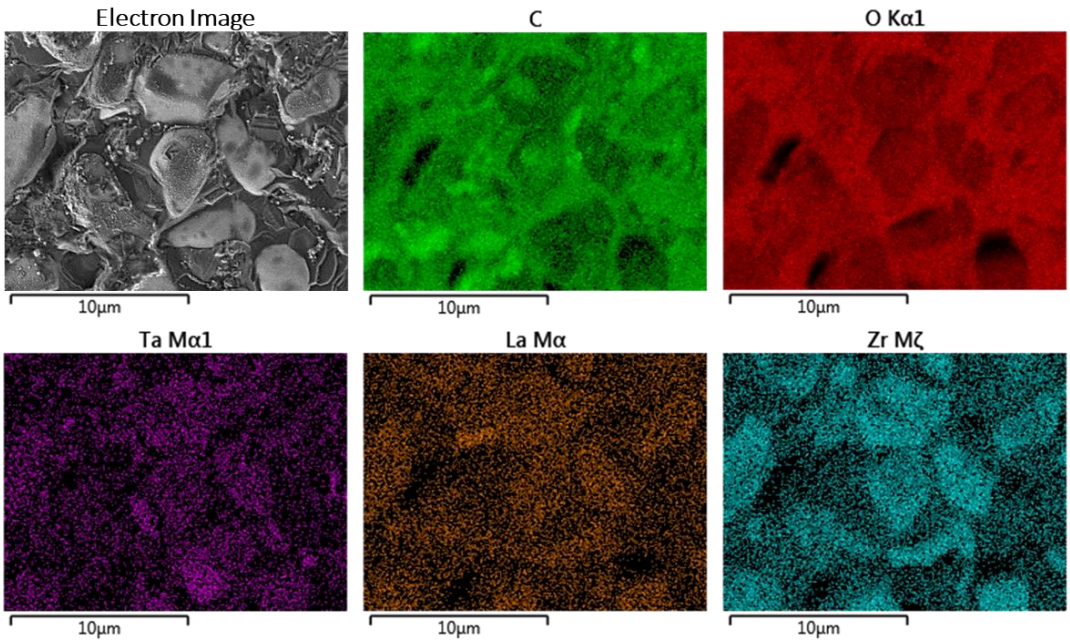


Figure 5.20. EDX mapping of the impurity phase present within the LLZTO phase of the gyroid LLZTO-epoxy hybrid electrolyte.

5.4.10. Electrochemical properties of the 3D gyroid LLZTO-epoxy electrolyte

The LLZTO-epoxy hybrid electrolyte was assembled with symmetrical Li metal electrodes and its impedance was measured at RT. Figure 5.21 shows the Nyquist plot obtained for the gyroid LLZTO-epoxy hybrid electrolyte compared to a LLZTO pellet. From finite element modelling (Appendix 6), a reduction by a factor of 0.46 in ionic conductivity is expected due to the tortuosity of the gyroid microstructure and the presence of a 40 % in volume non-conductive epoxy phase, if one assumes that a 50 % porous polymer template leads to a 40 % porous structured LLZTO scaffold. Hence, a total ionic conductivity of 2.3 x 10^{-4} S·cm^{-1} at RT is expected (considering a total ionic conductivity of a Li | LLZTO pellet | Li cell of 5.0 x 10^{-4} S·cm^{-1} at RT, as will be discussed in Chapter 6). Nevertheless, only a total ionic conductivity of 2.7 x 10^{-5} S·cm^{-1} at RT was achieved for the gyroid LLZTO-epoxy hybrid electrolyte. The not yet optimal sintering

conditions of the hybrid which induces the growth of a secondary phase between the LLZTO grains could be the reason for this decrease.

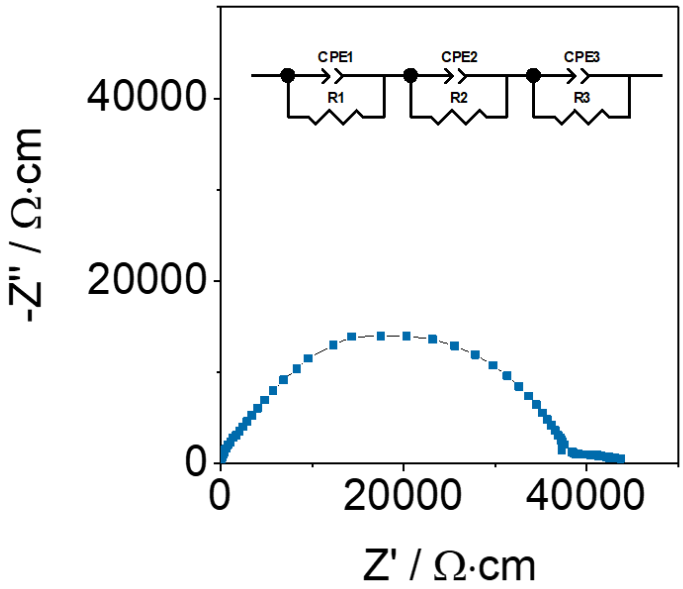


Figure 5.21. Nyquist plot of a Li | gyroid LLZTO-epoxy hybrid electrolyte | Li cell and the equivalent circuit used to fit the data. Detailed fitting values are reported in Appendix 12.

5.4.11. Mechanical properties of the 3D gyroid LLZTO-epoxy electrolyte

Stress-strain curves from four-point bending measurements carried out on a LLZTO beam and a gyroid LLZTO-epoxy hybrid beam are shown in Figure 5.22. While a nearly twice as high fracture strength of 37 MPa was obtained for the LLZTO compared to the LAGP (up to 18 MPa), the ceramic also shows very brittle behaviour fracturing instantaneously once the yield stress after only 0.35 % strain has been reached (for LAGP a maximum of 0.13 % strain was achieved). Performing the same test on a gyroid LLZTO-epoxy hybrid beam shows that the hybrid takes over the same familiar shape as the LAGP-epoxy hybrids analysed previously. The hybrid initially follows the same path as the LLZTO beam showing a linear increase in stress and strain, followed by a plateau region of about 0.8 % strain before showing a second increase in stress and strain until

fracture after having reached a yield stress of 35 MPa at 1.1 % flexural strain. The length of the plateau region and final % strain is comparable to the gyroid LAGP-epoxy with 60 % ceramic volume fraction. Hence this shows that, while the initial part of the stress-strain curve is mostly influenced by the ceramic electrolyte used in the hybrid, the subsequent and final part of the stress-strain curve is mostly dictated by the type and volume fraction of the polymer material used.

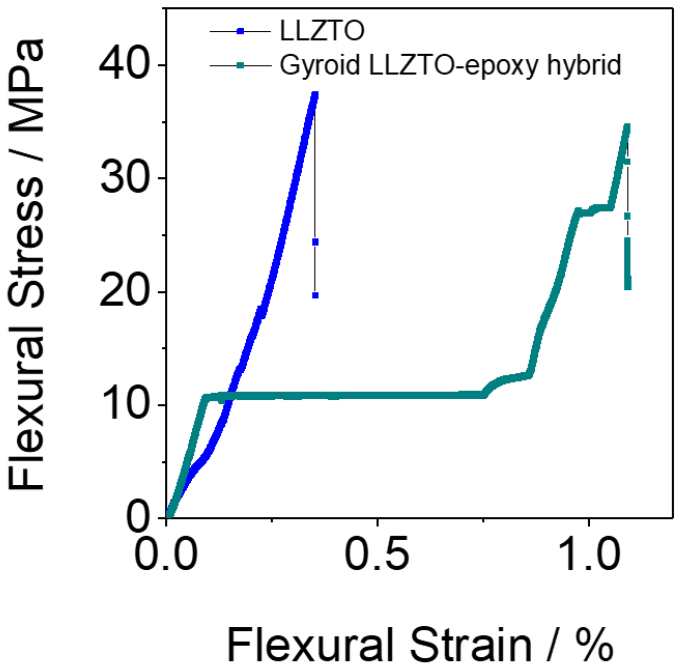


Figure 5.22. Stress-strain curves of a LLZTO beam and a gyroid LLZTO-epoxy hybrid electrolyte with a 60 % LLZTO to 40 % epoxy polymer volume fraction.

5.5. Conclusions

The ability to tune the synthesis of the hybrid electrolyte discussed in Chapter 4 and vary its parameters such as the microarchitecture, the choice of ceramic and polymer material as well as the ceramic-to-polymer ratio has been demonstrated in this Chapter. Various hybrid electrolytes with cubic, gyroid, diamond and bijel microarchitectures were successfully synthesised. Additionally, two different types of polymer materials, namely

PP and an epoxy-based polymer were tested. LAGP was used as the ceramic electrolyte material for both microarchitecture and polymer material investigations due to its advantageous synthesis and stability in air.

LAGP-PP and LAGP-epoxy hybrid electrolytes with all four microarchitectures were analysed electrochemically by EIS measurements and galvanostatic cycling. Total ionic conductivity values in the range of 1.1 - 1.7 x 10^{-4} S·cm^{-1} at RT were measured. It was demonstrated that the amount of LAGP filling during the synthesis is closely related to the ionic conductivity measured in the final LAGP-polymer hybrid. The gyroid microarchitecture stood out as the 'easiest-to-fill' geometry, leading to the highest ionic conductivity of 1.7 x 10^{-4} S·cm^{-1} at RT out of all, which was only reduced by the polymer volume fraction present and the tortuosity of the microarchitecture as analysed by finite element modelling. No changes in the ionic conductivity was observed between the PP and epoxy polymer. Galvanostatic cycling at 1 mA·cm^{-2} up to a capacity of 0.5 mAh·cm^{-2} for 10 cycles, showed that all microarchitectures with epoxy polymer performed better than its PP equivalent. The gyroid LAGP-epoxy hybrid electrolyte exceeded all, showing the lowest increase in cell voltage over 10 cycles.

Gyroid LAGP-epoxy hybrids electrolytes using 3D printed polymer templates with varied porosities of 85 %, 70 % and 50 % were also synthesised. Converting all three templates into gyroid LAGP-epoxy hybrids gave rise to three hybrids with three different ceramic-to-polymer ratios, namely 70 % to 30 %, 60 % to 40 % and 45 % to 55 %, respectively. The difference between the ratio in the initial template and the final hybrid is attributed to shrinkage during the synthesis and the challenge of filling narrower channels in the lower porosity templates compared to the wider channels in the higher porosity templates. The total ionic conductivity decreased significantly from a 70 % to a 45 % LAGP volume fraction hybrid, from 1.8 x 10^{-4} S·cm^{-1} to 5.1 x 10^{-5} S·cm^{-1} at RT,

respectively. This decrease is not only attributed to the decrease in ionic conductive phase present, but also to the LAGP phase density, which is, due to the synthetic difficulties, slightly lowered in the hybrid electrolyte with narrower LAGP channels. Nevertheless, it was shown that the cycling performance is not directly impeded by lowering the LAGP volume fraction in the gyroid LAGP-epoxy hybrids, as no significant difference in the cycling performance was recorded between all three ratios within the first 10 cycles. The reaction of Li with LAGP propagates at the same rate for all three gyroid LAGP-epoxy hybrids with different ceramic-to-polymer ratios and remains the major cause for the increase in cell voltage with cycle number.

From compressing testing, a higher compressive stress and strain was measured for all hybrid electrolytes with epoxy polymer channels compared to PP polymer channels, confirming the more favourable properties of the epoxy polymer as thermosetting polymer material. Additionally, the LAGP-epoxy hybrid electrolyte with gyroid microarchitecture outperformed all other hybrid microarchitectures reaching the highest compressive stress and strain values out of all before fracture. While four-point bending measurements did not show a significant difference between the LAGP-epoxy hybrid electrolytes with different microarchitectures, a substantial increase by over 45 % in fracture strain was observed as the ceramic-to-polymer ratio was decreased from a LAGP volume fraction of 70 % to 45 %. This confirms the role of the 3D polymer scaffold as a mechanically stabilising backbone to ensure mechanical integrity is maintained within the hybrid structure.

Ultimately, a possible synthetic route to generate the hybrid electrolyte using LLZTO as the ceramic electrolyte was presented. While the filling of the 3D template with LLZTO was achieved in the same way as with LAGP, the sintering of the filled LLZTO template posed a significant synthetic challenge. The final free-standing gyroid LLZTO-epoxy

hybrid electrolyte with a 60 % to 40 % ceramic-to-polymer ratio showed a total ionic conductivity of 2.7 x 10^{-5} S·cm^{-1} at RT, which is still one order of magnitude lower than expected for LLZTO. This was mainly attributed to the extended secondary phase formed between the LLZTO grains during the sintering stage of the synthesis. Further optimisation of the synthesis procedure could significantly alleviate this issue. Nevertheless, a three times increase in the LLZTO-epoxy hybrid's flexural strain over just LLZTO was measured, showing that similarly to LAGP, a significant increase in the mechanical properties of the LLZTO can be achieved by the incorporation of a 3D polymer backbone.

While the advantages of LLZTO over LAGP as the solid electrolyte were briefly introduced in this Chapter, the following Chapter (Chapter 6) aims to discuss in more detail the synthetic, but also the electrochemical challenges of LLZTO as solid electrolyte for next-generation lithium batteries.

5.6. References

1. Lee, M. N. & Mohraz, A. Bicontinuous Macroporous Materials from Bijel Templates. *Adv. Mater.* **22,** 4836–4841 (2010).
2. Reeves, M., Stratford, K. & Thijssen, J. H. J. Quantitative morphological characterization of bicontinuous Pickering emulsions via interfacial curvatures. *Soft Matter* **12,** 4082–4092 (2016).
3. Schoen, A. H. *Infinite Periodic Minimal Surfaces Without Self-Intersections*. (1970).
4. Thompson, T. *et al.* A Tale of Two Sites: On Defining the Carrier Concentration in Garnet-Based Ionic Conductors for Advanced Li Batteries. *Adv. Energy Mater.* **5,** 1500096 (2015).

Chapter 6: Electrochemical and Microstructural Analysis of the Interfacial and Bulk Properties of $Li_{6.5}La_3Zr_{1.5}Ta_{0.5}O_{12}$ as Solid Electrolyte

6.1. Aim

As shown in the previous three Chapters, the chemical stability of the solid electrolyte with Li metal is an imperative property to ensure that all-solid-state Li batteries become a viable option next to current Li battery technology. In this Chapter, the properties of the acclaimed stable garnet-type solid electrolyte will be analysed and discussed. The influence of the sintering parameters on the electrochemical performance will be shown. Additionally, a route to diagnose cell failure in garnet-type solid electrolyte cells with symmetrical Li metal electrodes by combining galvanostatic cycling and ^{7}Li magnetic resonance CSI will be explored.

6.2. Introduction

Since firstly reported by Thangadurai, Kaack and Weppner in 2003,[1] garnet-type solid electrolytes have been extensively studied within the battery community. This is mainly due to their favourable chemical stability with Li metal. Many doped, substituted or Li-enriched forms of the originally reported garnet-type $Li_5La_3M_2O_{12}$ (with M = Ta, Nb) crystal structure have since been explored.[2] Cubic phase garnet-type solid electrolytes with the general formula of $Li_{7-x}La_3Zr_{2-x}M_xO_{12}$ (with M = Ta, Al, Ga, tellurium (Te), tungsten (W), antimony (Sb) or yttrium (Y)) sintered at temperatures above 1000 ºC have since given the most promising ionic conductivity values of all, ranging from 5×10^{-4} S·cm^{-1} up to 1×10^{-3} S·cm^{-1} at RT.[2] Hence, the Ta-doped $Li_{6.5}La_3Zr_{1.5}Ta_{0.5}O_{12}$ (LLZTO) was chosen as the composition of choice to be investigated in this Chapter.

Despite the chemical stability of garnet-type solid electrolytes, symmetrical Li | LLZO | Li cells short-circuit rapidly at current densities of 0.3 $mA \cdot cm^{-2}$ and above.[3] This is due to the formation and growth of Li dendrites through the LLZO electrolyte, specifically along the LLZO grain boundaries and through voids when a constant current is applied.[4,5] Many efforts have focussed on understanding this phenomenon, specifically its cause and how to prevent its growth. The disagreement between the Monroe-Newman model[6] and the recently measured high elastic and shear moduli of Al-doped LLZO[7] that do not seem to be sufficient in preventing short-circuits, is puzzling. Recent work has shown that the electrode-electrolyte interfacial contact,[5,8] the solid electrolyte microstructure[4,9] and pre-existing flaws on the solid electrolyte's surface[10] might play a more significant role in facilitating the penetration of Li through all-solid-state cells. Next to understanding the cause of Li dendrite formation, the detection and characterisation of Li dendrites in cells is also challenging. Cross-sectioning cells at the right place to observe Li dendrites by SEM whilst keeping the cell unexposed to air is difficult and time consuming. Additionally, techniques that can quantitatively detect Li are limited.

This Chapter aims to optimise the synthesis of LLZTO and understand how its microstructural properties relate to its electrochemical properties within a symmetrical Li | LLZTO | Li cell. Additionally, a new approach of tracking and visualising Li dendrites in solid-state cells, combining the results of electrochemical and ^{7}Li CSI experiments, will be presented.

6.3. Experimental Methods

6.3.1. Synthesis of $Li_{6.5}La_3Zr_{1.5}Ta_{0.5}O_{12}$

LLZTO was synthesised via a sol-gel process. Stochiometric amounts of $Ta(V)Cl_5$ (99.99 %, 0.0028 mol), $ZrO(NO_3)_2$ $1.8H_2O$ (99.9 %, 0.00825 mol), $La(III)(NO_3)_3 6H_2O$

(99.999 %, 0.0165 mol) and $LiNO_3$ (99.99 %, 0.03575 mol) were weighed out in separate vials inside an Ar-filled glovebox (O_2 and H_2O levels below 0.1 ppm). A 20 % excess of $LiNO_3$ was used to account for the Li loss during the calcination and sintering process later on in the synthesis. 1.5 mL of dried ethanol was added to the Ta-precursor to dissolve the Ta^{5+} ions efficiently. All vials were brought out of the glovebox and distilled H_2O was added to all remaining precursors. A 500 mL beaker was heated on a hot plate at 60 °C. The Zr-solution, followed by the La-, Li- and Ta-solutions were added to the beaker and stirred well using a glass rod and a magnetic stirrer. In a second beaker, a 1:1 molar ratio of ethylene glycol (EG) (99.8 %, 0.05743 mol) and citric acid monohydrate (CA) (≥99.0 %, 0.05743 mol) was weighed out and enough H_2O was added to dissolve the CA completely. Once dissolved, the EG:CA mixture was added to the precursor beaker. More distilled H_2O was added to reach a total solution of 500 mL in volume. The precursor solution was then left to stir at 90-100 °C overnight. To ensure all H_2O has successfully evaporated, the beaker was placed in an oven at 100 °C for 4 hours to obtain a 'marshmallow-like' white gel. This gel was then mortared, placed inside an alumina crucible and heated up to 400 °C for 10 hours using a ramping rate of $2°C \cdot min^{-1}$ and a cooling rate of $10°C \cdot min^{-1}$ to form a black powder. The black powder was mortared again, pressed into 1.5 g pellets using a 13 mm in diameter die set and placed on an alumina crucible to be calcined at 900 °C for 12 hours at a ramping rate of $5°C \cdot min^{-1}$. The alumina crucible was taken out of the furnace at 900 °C after the 12 hours dwelling time and transferred straight into the glovebox. The now white calcined pellets were mortared back into a fine powder, corresponding to the calcined LLZTO.

To produce sintered pellets, the calcined LLZTO powder was ball-milled (Retsch Emax ball mill equipped with two 50 mL zirconia grinding jars each containing 21.5 g of 5 mm diameter zirconia balls) for 1 hour at 600 rpm using 1-2 mL of dried cyclohexane per 1 g

of calcined LLZTO. A LLZTO motherpowder was made by adding 7.5 weight % Li_2O to the calcined LLZTO powder and ball-milled using 1-2 mL of dried cyclohexane per 1g calcined LLZTO for 1 hour at 300 rpm. The ball-milled LLZTO was pressed into 5 mm diameter pellets with a thickness of 1 mm using a uniaxial hydraulic press (Specac) at a load of 1 tons. Three pellets at a time were placed on a pressed layer of LLZTO motherpowder and were covered with additional motherpowder which was pressed onto the pellets from the top. The covered LLZTO pellets were then placed onto an alumina crucible and inserted into a pre-heated furnace at 1250 °C for a total of 10 minutes. Once cooled down to 300 °C at a cooling rate of $10°C \cdot min^{-1}$, the pellets were removed from the furnace and stored inside the glovebox to avoid exposure to air. Excess motherpowder was polished off using a SiC waterproof abrasive disc (Kemet, grade 400).

6.3.2. Microstructural analysis

6.3.2.1. SEM and EDX

LLZTO pellets, powders and cross-sectioned Li | LLZTO | Li cells (prepared as described in Chapter 6 Section 6.3.3.2) were attached onto a custom-made holder with Cu adhesive tape and inserted into a Zeiss Merlin SEM using a transfer device (Gatan) to avoid any exposure to air. SEM and EDX imaging were performed using the parameters previously described in Chapter 3 Section 3.3.2.1.

6.3.2.2. PXRD

A Rigaku SmartLab X-ray diffractometer was used to analyse the synthesized LLZTO powders. Identical diffraction parameters as the ones described in Chapter 3 Section 3.3.2.2 were utilised.

6.3.2.3. ^{7}Li NMR and ^{7}Li MRI

^{7}Li NMR and ^{7}Li MRI, specifically ^{7}Li CSI, were performed on pristine and cycled Li | LLZTO | Li cells. Ball-milled LLZTO powder was pressed into 5 mm diameter pellets with a thickness of roughly 2.5 mm using a uniaxial hydraulic press (Specac) at a load of 1 tons. The pellets were sintered as previously described for the synthesis of LLZTO above (Chapter 6 Section 6.3.1). The sintered pellets were cut into two halves using an ultrasonic cutter (Sonotec) to fit the size requirements for the subsequent NMR and CSI analysis. The pellets were assembled with Li metal electrodes as described in the electrochemical characterization section below (Chapter 6 Section 6.3.3.2). Pristine and cycled Li | LLZTO | Li cells were sent to collaborators at the University of Cambridge in sealed pouches. There, a Bruker Avance III 300 spectrometer operating at 7.05 T (^{7}Li frequency = 116.59 MHz) and fitted with a Micro2.5 triple axis gradient system and a MicWB40 probe was used. A 1.0 M $LiCl_{(aq)}$ solution at 0 ppm was used as an external reference for all measured ^{7}Li chemical shifts. In an Ar-filled glovebox (O_2 and H_2O levels below 0.1 ppm), the cells were placed and sealed into an airtight J-Young NMR tube. The cells were positioned in such a way that the Li metal electrodes were perpendicular to the external magnetic field, B_0, before being centered inside the NMR coil for measurement. This maximises the resolution obtained between the Li dendrite and the Li metal electrode signals. Single pulse ^{7}Li NMR spectra were collected for each cell with a recycle delay of 1 second and a total of 2048 scans. Additionally, ^{7}Li CSI measurements were carried out with a single phase-encoded spatial dimension in the z-direction (the direction of the magnetic field). A phase-encoding gradient was applied and varied between ± 37.5 G·cm in 64 equal steps. Experiments were run for roughly 7-15 hours per sample to detect and collect high resolution signals of all ^{7}Li species present.

6.3.3. Electrochemical analysis

6.3.3.1. EIS

EIS measurements were performed on Au | LLZTO | Au cells using the parameters and the equipment as detailed in Chapter 3 Section 3.3.3.1. Prior to the measurements, LLZTO pellets were polished using a SiC waterproof abrasive disc (Kemet, grade 400) inside an Ar-filled glovebox (O_2 and H_2O levels below 0.1 ppm) and sputtered on both sides with a 30 nm layer of Au as described in Chapter 3 Section 3.3.3.1. To achieve the best contact and avoid exposure to air and moisture, Au-coated LLZTO pellets were sealed inside a pouch cell with Cu current collectors.

6.3.3.2. Galvanostatic cycling

Galvanostatic cycling of Li | LLZTO | Li cells was performed using Gamry Interface 1000 devices. The LLZTO pellet surfaces were polished with a SiC waterproof abrasive disc (Kemet, grade 400) in an Ar-filled glovebox (O_2 and H_2O levels below 0.1 ppm) and assembled with pre-pressed Li metal foils in pouch cells with Cu current collectors as previously described in Chapter 3 Section 3.3.3.2 for LAGP. Galvanostatic cycling was performed at constant current densities ranging from 0.2 $mA \cdot cm^{-2}$ to 1 $mA \cdot cm^{-2}$ at RT with a rest time of 5 minutes in between each current direction. Additional EIS measurements were performed after each completed cycle.

6.4. Results and Discussion

6.4.1. Synthesis and characterisation of LLZTO

LLZTO was synthesised using a sol-gel procedure as illustrated in the schematic in Figure 6.1. An aqueous precursor solution was firstly heated up to 100 °C to form a white

precursor gel, then to 400 °C to burn off excess organic precursors, followed by calcination at 900 °C and final sintering at 1250 °C.

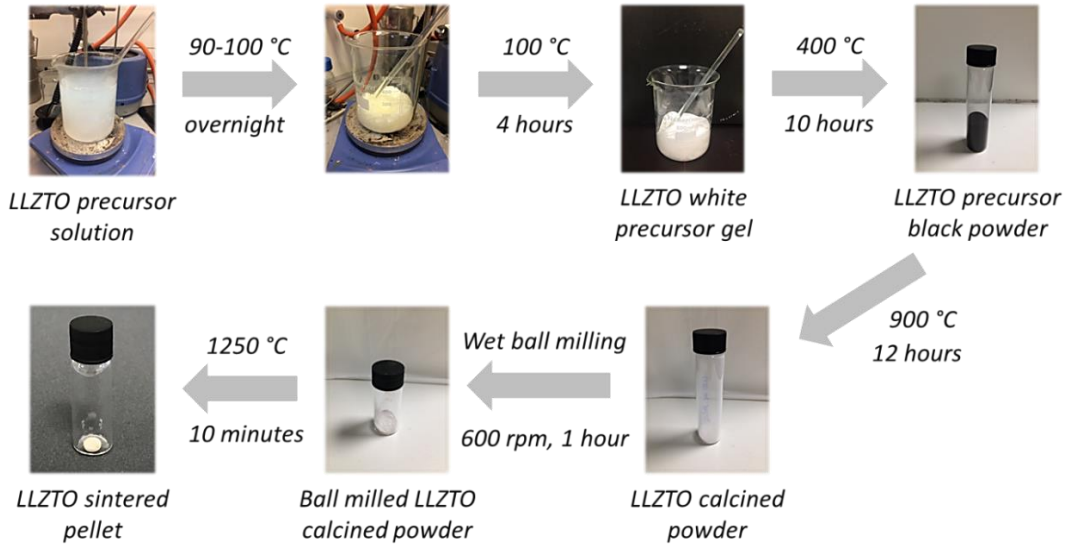


Figure 6.1. Schematic of the synthesis procedure of LLZTO.

The cubic LLZTO phase was achieved after the calcination step at 900 °C for 12 hours in the form of a white powder and confirmed by PXRD as shown in Figure 6.2. Ball milling of the LLZTO powder with cyclohexane and additional sintering of the ball-milled LLZTO pellet covered with LLZTO motherpowder densified the pellet up to 90 % of the theoretical density of LLZTO (5.31 $g \cdot cm^{-3}$) [11] whilst retaining the favourable high ionically conductive cubic phase.

SEM images of the LLZTO grains after calcination, ball milling and sintering are shown in Figure 6.3. The addition of LLZTO motherpowder, which contains an excess amount of Li from the addition of Li_2O, is vital to ensure that no Li is lost within the LLZTO pellet during the sintering stage and that the cubic LLZTO phase is maintained.

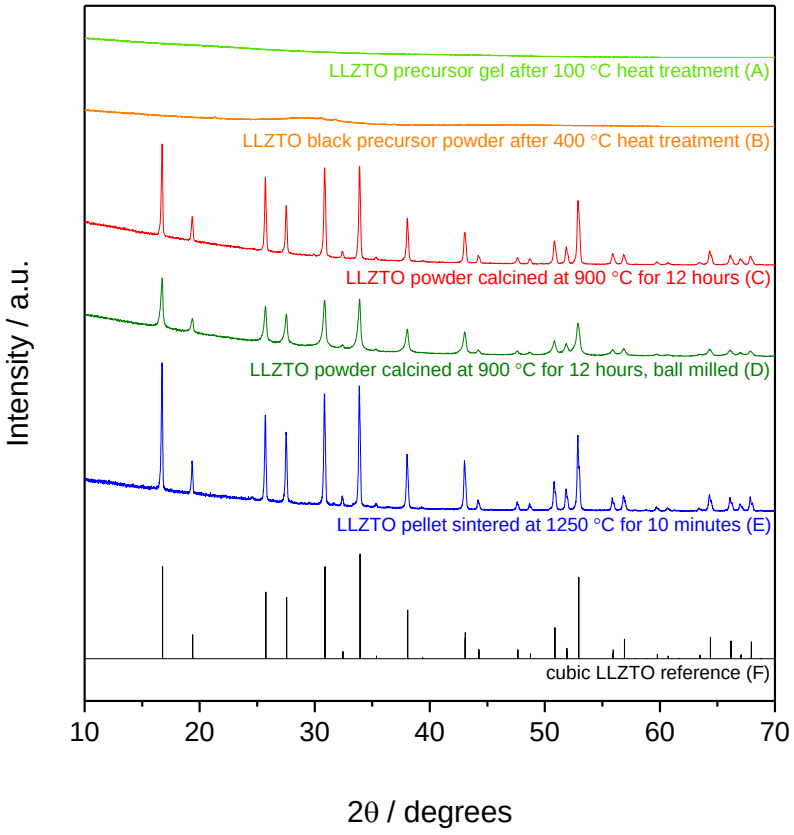


Figure 6.2. PXRD patterns of the LLZTO precursor gel (A), the LLZTO precursor powder (B), the calcined LLZTO powder (C), the calcined and ball milled LLZTO powder (D) and the powder of the LLZTO sintered pellet (E). The patterns were compared to a LLZTO reference pattern from literature (F).[12]

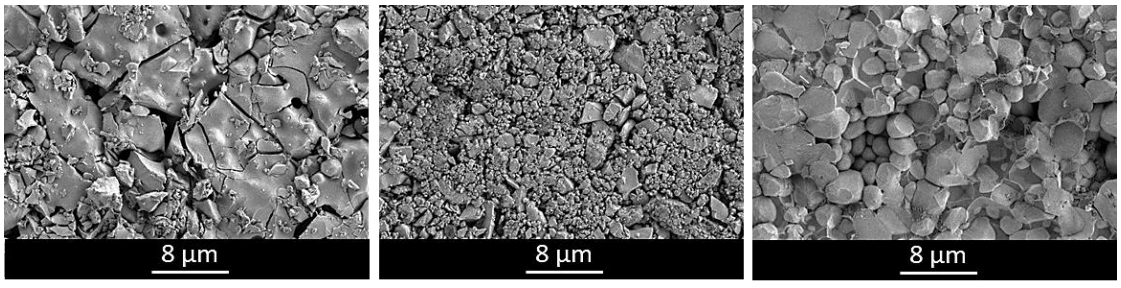


Figure 6.3. SEM images of the synthesised LLZTO grains after calcination at 900 °C for 12 hours (left), after ball milling with cyclohexane (centre) and after sintering at 1250 °C for 10 minutes (right).

Figure 6.4 shows the microstructure of a cross-sectioned LLZTO pellet after sintering together with its corresponding EDX maps. Distinct grains of less than 5 µm in size are observed with an occasional darker grey phase found at the grain boundaries. EDX confirms that the grains contain all elements of the LLZTO phase, whereas the grain boundaries mainly only contain Al and O with traces of C. From the literature, Al^{3+} is known to be found at the grain boundaries of LLZTO.[13,14] Although no Al was present in any of the precursors used during the synthesis, it is known to become easily inserted into the material from the use of alumina crucibles during the calcination and sintering stage, which cannot be avoided when using this specific sintering method.

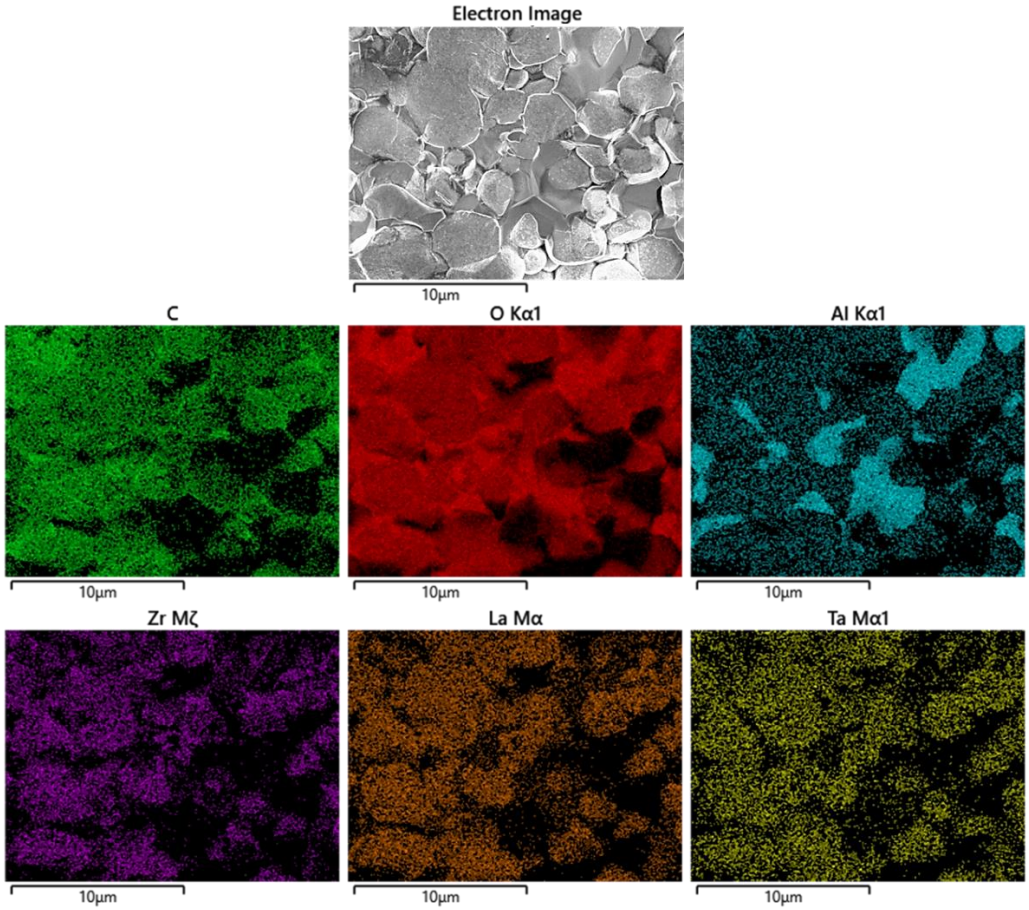


Figure 6.4. EDX mapping of a cross-sectioned LLZTO pellet after sintering.

6.4.2. Impedance measurements with Au blocking electrodes

EIS measurements were carried out on the synthesised LLZTO pellets coated on both sides with a 30 nm layer of Au blocking electrodes. Figure 6.5-c shows the Nyquist plot of a symmetrical cell obtained at RT. The data were best fitted with a resistor in series for the data at high frequency (R_1), followed by a resistor and constant-phase element in parallel (CPE_2 // R_2) for the partially visible semicircle and a constant-phase element (CPE_3) in series for the Au blocking electrodes represented in the Nyquist plot by a spike. A capacitance value of 4.5 x 10^{-10} F·cm^{-1} for the partially visible semicircle was calculated with a total ionic conductivity for the LLZTO pellet of 5.5 x 10^{-4} S·cm^{-1} at RT. This value is consistent with the ionic conductivity values obtained in literature for this specific composition.[11,12,15] The corresponding Nyquist plot obtained at -17 °C is shown in Figure 6.5-d. Similar to the EIS measurements performed for LAGP (Chapter 3 Section 3.4.2), low temperature EIS measurements of LLZTO enable visualisation of the shape of the completed semicircle at higher frequency. The data were best fitted by a series of two resistors and constant-phase elements in parallel (CPE_1 // R_1 and CPE_2 // R_2) followed by a third constant-phase element is series for the spike (CPE_3). The capacitance values obtained for both semicircles of 5.9 x 10^{-11} F·cm^{-1} and 1.4 x 10^{-9} F·cm^{-1} fit well with the expected capacitance values for the intragrain (bulk) and intergrain (grain boundaries) charge transport phenomena.[16] Additionally, an Arrhenius plot of EIS measurements over a temperature range of -25 °C to 75 °C is shown in Figure 6.5-b. An activation energy of 42.76 kJ mol^{-1} was calculated, which is comparable to the activation energies found in literature.[11,17] Details of the EIS analysis are found in Appendix 13.

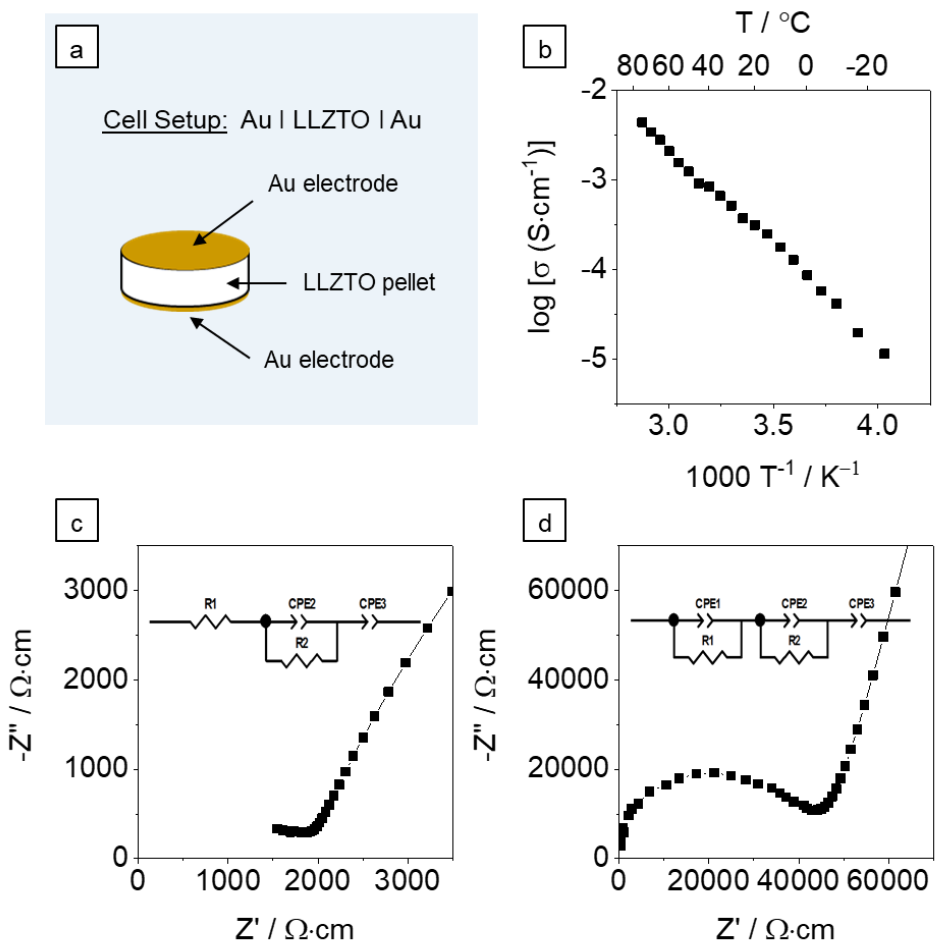


Figure 6.5. EIS analysis of an Au | LLZTO | Au cell: (a) schematic of the cell setup, (b) Arrhenius plot showing the dependence of impedance versus temperature over a temperature range of -25 °C to 75 °C, (c) and (d) the Nyquist plot and its corresponding equivalent circuit at RT and at -17 °C, respectively.

6.4.3. Effect of sintering temperature on LLZTO

The sintering parameters used for LLZTO can drastically affect the properties of the final LLZTO solid electrolyte. In the first instance, the effect of the sintering temperature was analysed. SEM cross-sectional images of three LLZTO pellets sintered at 1050 °C, 1150 °C and 1250 °C for 10 minutes each are shown in Figure 6.6. The most apparent change when increasing the sintering temperature is the increase in pellet density from only 63 % at 1050 °C to a density of 90 % at 1250 °C. From the SEM images it is obvious

that the LLZTO grains are more effectively fused together at a higher sintering temperature. The density of the LLZTO pellet directly affects the ionic conductivity of the LLZTO solid electrolyte. As shown in the Nyquist plots in Figure 6.7, the measured impedance of the LLZTO in Li | LLZTO | Li cells increases drastically as the sintering temperature is decreased and the LLZTO pellet density is lowered. Similar observations were obtained for garnet-like materials such as $Li_5La_3Nb_2O_{12}$ [18] and magnesium (Mg), calcium (Ca), strontium (Sr) and barium (Ba)-substituted $Li_5La_3Ta_2O_{12}$.[19] The highest ionic conductivity of 5 x 10^{-4} $S \cdot cm^{-1}$ at RT was achieved for a Li | LLZTO | Li cell with a LLZTO pellet sintered at 1250 °C for 10 minutes, which is a comparable value to what has been achieved in literature.[20]

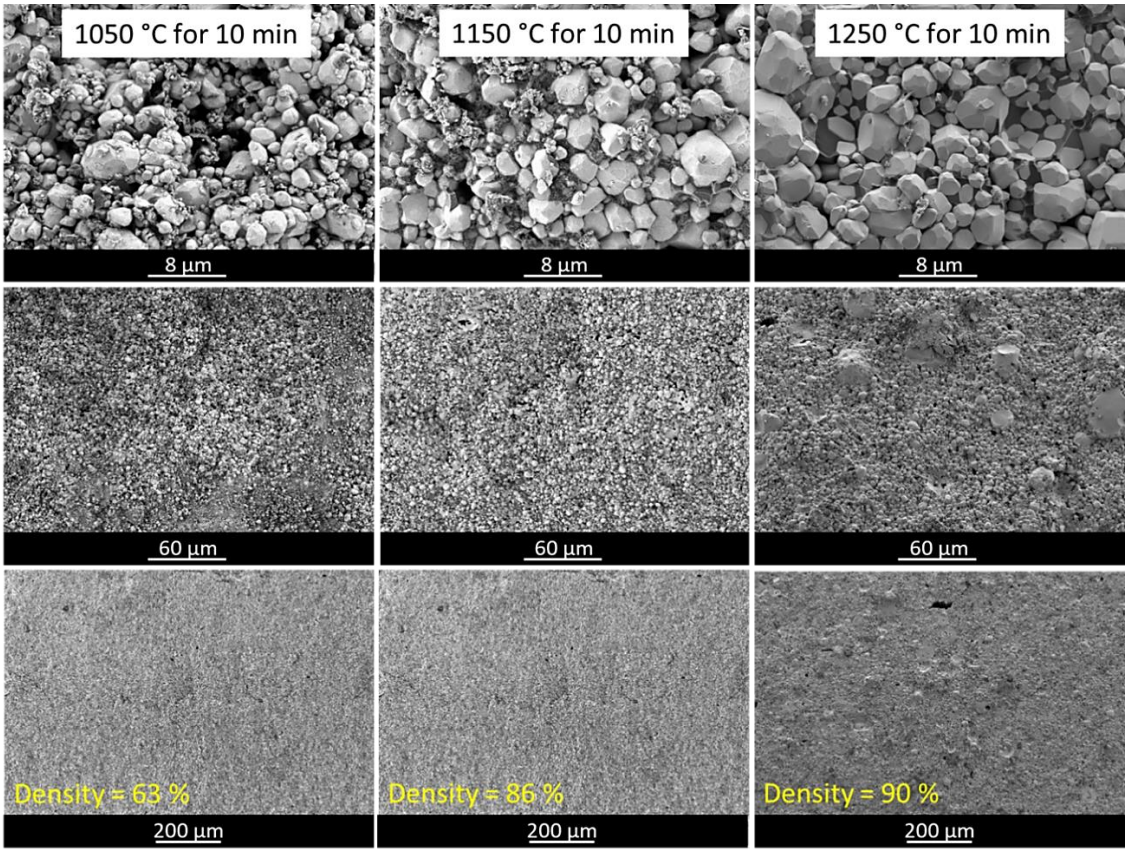


Figure 6.6. SEM images of the microstructure of cross-sectioned LLZTO pellets sintered at 1050 °C (left), 1150 °C (centre) and 1250 °C (right) for 10 minutes each. Densities of the pellets are displayed in yellow.

Analysing the intragrain and intergrain contributions showed that both do increase with decreasing sintering temperature. While the intragrain contribution doubles in resistance, the intergrain contribution triples in resistance as the temperature is decreased by 100 °C at a time. This is expected, as from the lower temperature SEM images in Figure 6.6, the LLZTO grains have yet not been fully formed and sintered together. Hence, a higher resistance at lower sintering temperature is expected for both contributions. Additionally, as anticipated, the Li-LLZTO interface contribution remains identical for all three cells as the cell assembly should not be affected by the change in sintering temperature of the solid electrolyte.

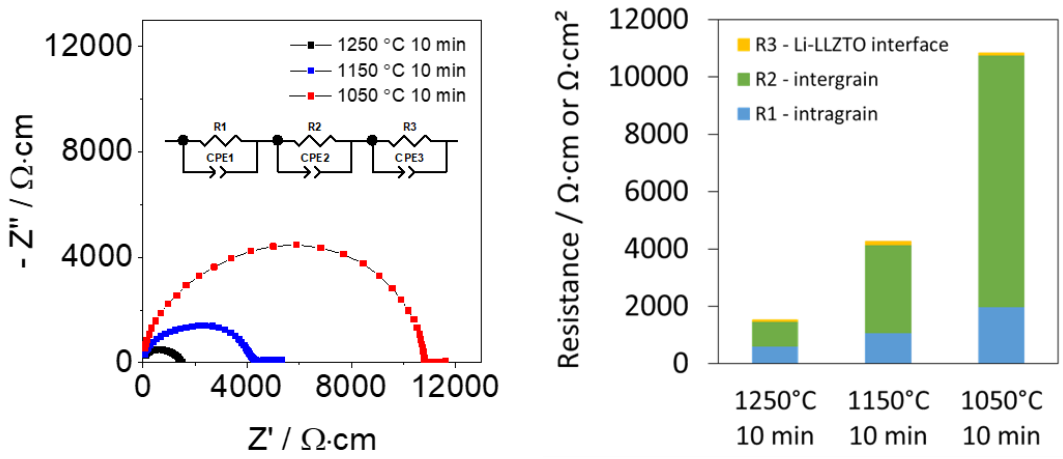


Figure 6.7. Left panel: Nyquist plots and equivalent circuit of Li | LLZTO | Li cells with LLZTO electrolyte pellets sintered at 1050 °C (red), 1150 °C (blue) and 1250 °C (black) for 10 minutes each. Right panel: Bar chart analysing the contributions of the resistances present for each Li | LLZTO | Li cell. Detailed fitting values are reported in Appendix 14.

6.4.4. Effect of sintering time on LLZTO

Next to the sintering temperature, the sintering time also severely influences the properties of the LLZTO solid electrolyte. Figure 6.8 shows SEM cross-sectional images of LLZTO pellets sintered at 1250 °C for 10 minutes, 30 minutes and 3 hours.

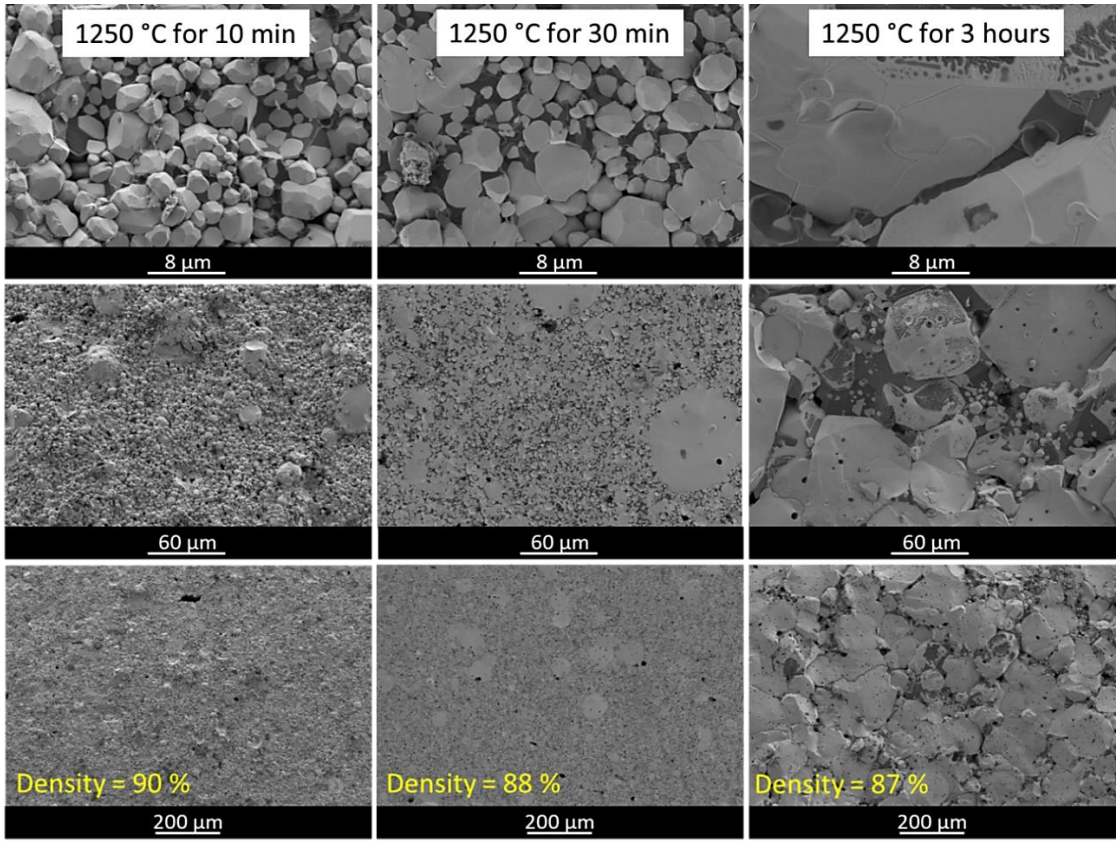


Figure 6.8. SEM images of the microstructure of cross-sectioned LLZTO pellets sintered at 1250 °C for 10 minutes (left), 30 minutes (centre) and 3 hours (right). Densities of the pellets are displayed in yellow.

Whereas the density stays consistent at around 87-90 %, the morphology of the microstructure changes significantly between all three pellets. As the sintering time is increased, the LLZTO grains increase in size from an average of 2-3 µm at a sintering time of 10 minutes to an average of 95-125 µm at a sintering time of 3 hours. With increasing time single grains fuse together more and more to form bigger grains as becomes apparent by SEM. While cross-sectional cuts were made through the grain boundaries at 1250 °C for 10 minutes, the cuts at both 30 minutes and 3 hours occurred through the grains themselves. As the grain size is smaller, the grain boundaries are more likely to be encountered by the cutting blade and offer a weak path of resistance, hence intergranular fracture is observed. For a large grain size, the cutting blade is less likely

to encounter grain boundaries, and hence transgranular failure is more frequently observed.

Analysing the different contributions that add to the overall resistance of the cell shows that varying the sintering temperature mainly affects the intergrain contribution, which increases significantly as the sintering time is prolonged (Figure 6.9). The intragrain and Li-LLZTO interface contributions remain constant in all three Li | LLZTO | Li cells. The temperature of 1250 °C is, as shown in the previous section, a suitable temperature for the complete development of the LLZTO grains and a short sintering time of only 10 minutes allows to keep the intergrain resistance to a minimum to achieve the highest possible ionic conductivity in the material.

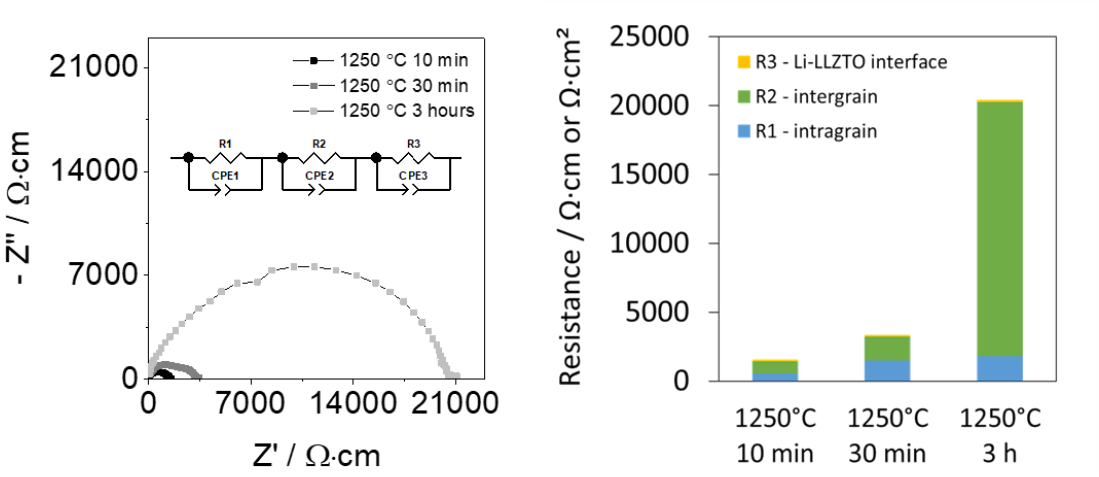


Figure 6.9. Left panel: Nyquist plots and equivalent circuit of Li | LLZTO | Li cells with LLZTO electrolyte pellets sintered at 1250 °C for 10 minutes (black), 30 minutes (dark grey) and 3 hours (light grey). Right panel: Bar chart analysing the contributions of the resistances present for each Li | LLZTO | Li cell. Detailed fitting values are reported in Appendix 15.

6.4.5. Impedance measurements with Li metal electrodes

EIS measurements were also performed on Li | LLZTO | Li cells. Figure 6.10 shows the corresponding Nyquist plot of the cell at RT.

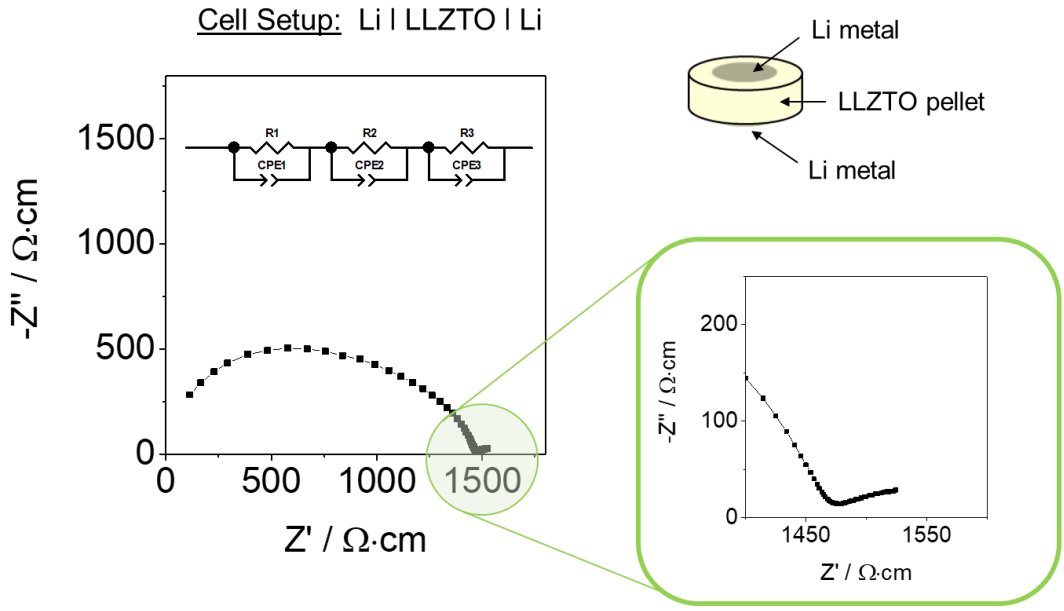


Figure 6.10. EIS analysis of a Li | LLZTO | Li cell showing the schematic of the cell setup, the Nyquist plot, its corresponding equivalent circuit at RT and a magnified view of the Li-LLZTO interface semicircle at high frequency. Detailed fitting values are reported in Appendix 16.

The data were best fitted to three parallel resistors and constant-phase elements in series (CPE_1 // R_1, CPE_2 // R_2 and CPE_3 // R_3), corresponding to three semicircles: two overlapping semicircles at higher frequency for the intragrain and intergrain contributions and a smaller semicircle for the Li-LLZTO interface. Capacitance values in the range of 10^{-10} F·cm^{-1}, 10^{-9} F·cm^{-1} and 1 F·cm^{-2} were calculated for the three semicircles. While the capacitance values for the first two semicircles fit well to the expected capacitance values for bulk and grain boundaries contributions, the capacitance value for the smaller low frequency semicircle is, similarly to the low frequency semicircle for the Li-LAGP interface, higher than expected.[16] However, despite the lack of information on the

capacitance of this smaller low frequency semicircle in literature, the three semicircles can confidently be assigned to the intragrain, intergrain and Li-LLZTO interface contributions, respectively. A total ionic conductivity of 5 x 10^{-4} S·cm^{-1} was achieved for the Li | LLZTO | Li cell at RT. Additionally, EIS measurements over a period of 130 hours were performed to confirm the stability of LLZTO with Li metal (Figure 6.11).

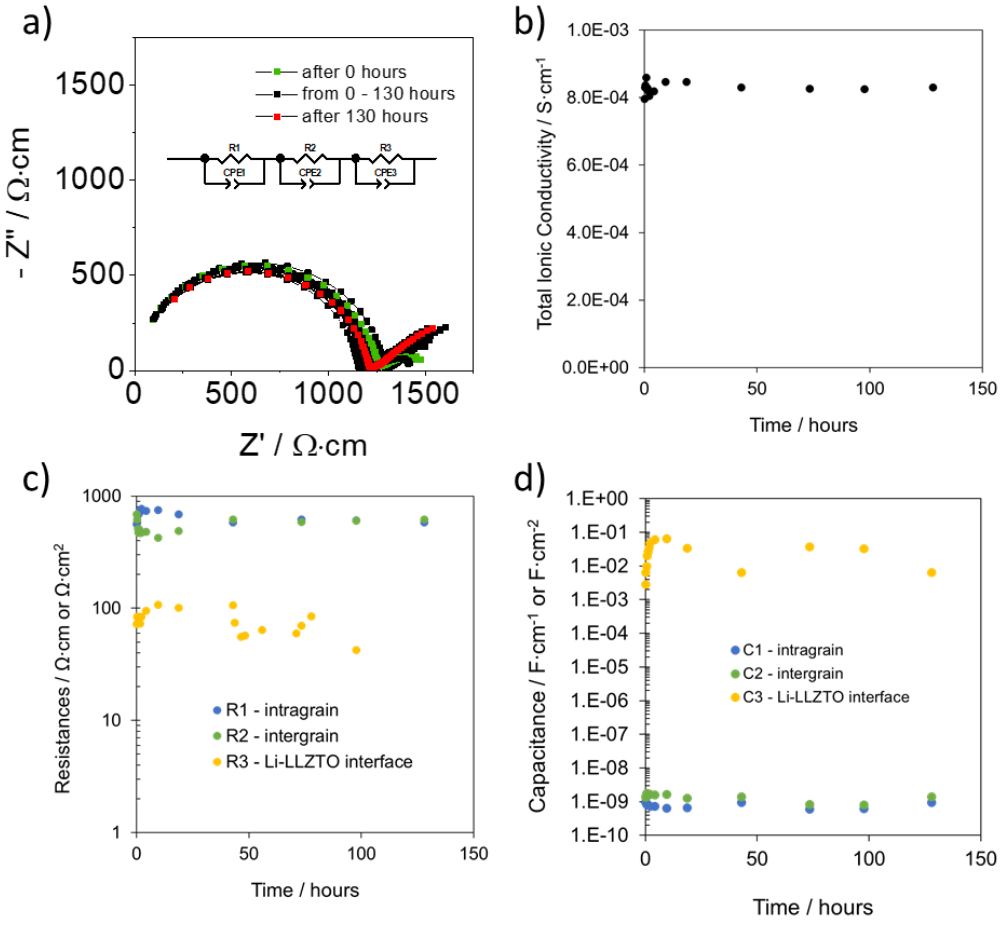


Figure 6.11. EIS analysis of a Li /LLZTO/Li cell aging over 130 hours at RT: plot of the Nyquist plots obtained at 0 hours (green), between 0 and 130 hours (black) and after 130 hours (red) (a) and the total ionic conductivity (b), and resistances (c) and capacitances (d) of the three different contributions with time. Units of F·cm^{-1} and Ω·cm were used for the intragrain and intergrain contributions, whereas units of F·cm^{-2} and Ω·cm^2 were used for the Li-LLZTO interface contribution.

As shown in Figure 6.11-a, no significant change in the shape of the Nyquist plot was observed. The ionic conductivity of the LLZTO electrolyte remained constant throughout the 130 hours. Solely, a change in the smaller Li-LLZTO interface semicircle was observed, which, as shown in Figure 6.11-c and 6.11-d, leads to slight variations in the Li-LLZTO interface's resistance and capacitance over time, which is still not fully understood and often neglected in literature. Both, intragrain and intergrain contributions remain consistent over time, both in terms of capacitance and resistance as shown in Figure 6.11-c and 6.11-d, which results in a near to no change of the total ionic conductivity of the LLZTO solid electrolyte over time. Hence, LLZTO can be regarded as stable with Li metal.

6.4.6. Galvanostatic cycling with Li metal electrodes

The cycling performance of a Li | LLZTO | Li cell was first tested by a rate test, similarly to the one performed on LAGP described in Chapter 3 Section 3.4.7. The cell was cycled up to a capacity of 0.1 $mAh \cdot cm^{-2}$ at a current density of 0.05, 0.1, 0.2, 0.5 and 1.0 $mA \cdot cm^{-2}$ for a total of 5 cycles each. Figure 6.12 shows the different voltage profiles obtained for each current density.

The cell voltages remain constant throughout cycling up to a current density of 0.2 $mA \cdot cm^{-2}$. At a current density of 0.5 $mA \cdot cm^{-2}$, irregular fluctuations in the voltage polarisation are observed. Even more significant variations in cell voltage are observed at a current density of 1 $mA \cdot cm^{-2}$ where after an initial rise in cell voltage on the first cycle, the polarisation continuously decreases on the subsequent cycles, as also illustrated in the cell voltage versus capacity plot in Figure 6.12. This cycling behaviour is different to the previously analysed LAGP ceramic electrolyte. Instead of gradual increases in cell voltage due to the reactivity of the solid electrolyte with Li, voltage fluctuations are

measured for the LLZTO electrolyte cell. The observed erratic drops in cell voltage are evident signs for the formation of Li dendrites. If cycled for a longer period of time, Li dendrites can continue to grow until they connect both Li electrodes with each other and trigger a short-circuit, which leads to immediate cell failure.

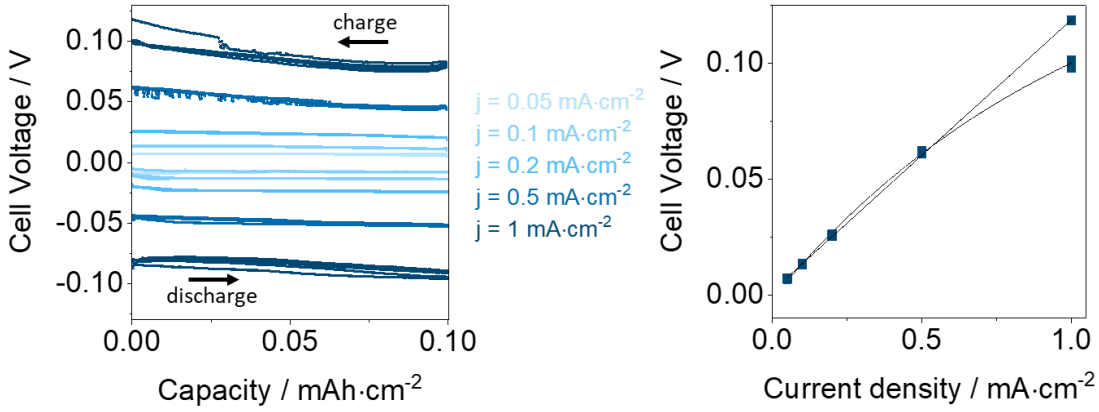


Figure 6.12. Rate test of a Li /LLZTO/Li cell cycled at current densities j of 0.05, 0.1, 0.2, 0.5 and 1 mA·cm^{-2} up to a capacity of 0.1 mAh·cm^{-2} for 5 cycles each (left). Plot of terminal voltages versus current density (right).

In order to understand if Li dendrites only form at a particular current density or also after prolonged cycling at lower current density, a Li | LLZTO | Li cell was cycled at a current density of 0.2 mA·cm^{-2} up to a capacity of 1.0 mAh·cm^{-2} for 25 cycles. Figure 6.13-a shows that a constant voltage polarisation of ± 30-40 mV was obtained in both current directions for 25 cycles. Galvanostatic cycling of a Li | LLZTO | Li cell at a higher current density of 0.5 mA·cm^{-2} up to a capacity of 1.0 mAh·cm^{-2}, as illustrated in Figure 6.13-b, shows that the lifetime of the cell is drastically reduced when the current density is increased. Within the first cycle, increases in voltage polarisations of up to 200 mV are observed in both current directions, followed by erratic drops in cell voltage towards the end of the second discharge. The cell then fully short-circuits upon the end of the second charge, reaching a cell voltage very close to 0 V. This confirms that an increase in current

density does promote a more rapid growth of Li dendrites, which eventually cause short-circuiting of the cell.

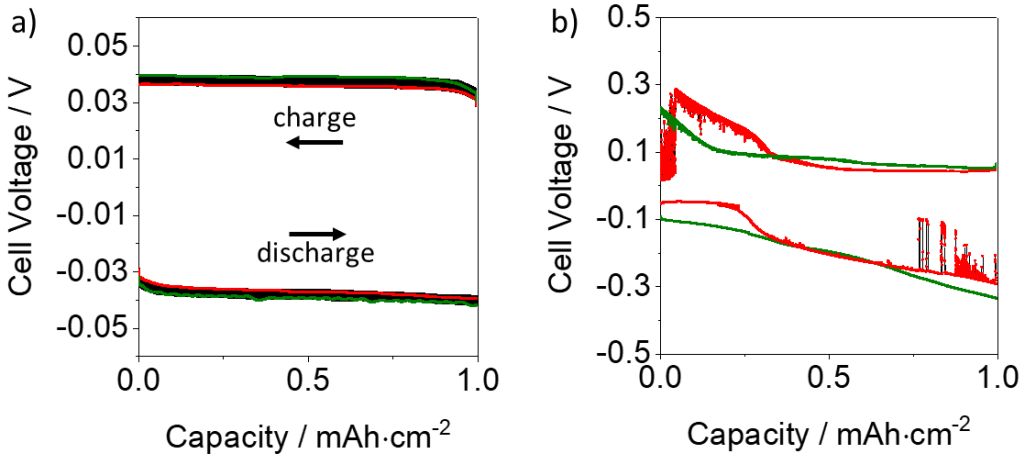


Figure 6.13. Voltage profile of a Li /LLZTO/Li cell cycled (a) at a current density of 0.2 mA·cm^{-2} up to a capacity of 1 mAh·cm^{-2} for 25 cycles for a total of 250 hours and (b) at a current density of 0.5 mA·cm^{-2} up to a capacity of 1 mAh·cm^{-2} for 2 cycles for a total of 8 hours. The first and the last cycle are labelled in green and red, respectively.

A small decrease in cell voltage for the low current density cell over 25 cycles was recorded. This could potentially be due to some microstructural Li build-up. Whether this microstructural Li would eventually grow into Li dendrites that cause short-circuits at this low current density is unknown. For extended cycling experiments of more than 250 hours, an experimental setup that controls both the surrounding temperature and applied cell pressure would be needed. Both of these parameters and potentially others can significantly affect the cell performance and quickly trigger higher local current densities at the electrode-electrolyte interfaces, which induce changes in the cell polarisation, trigger Li dendrite growth and cell failure.

To comprehend whether the growth of Li dendrite is a more gradual or rather abrupt process triggered by a certain current density, Li | LLZTO | Li cells of various LLZTO

pellet thicknesses were continuously discharged at a current density of 0.5 mA·cm^{-2} until short-circuit (Figure 6.14).

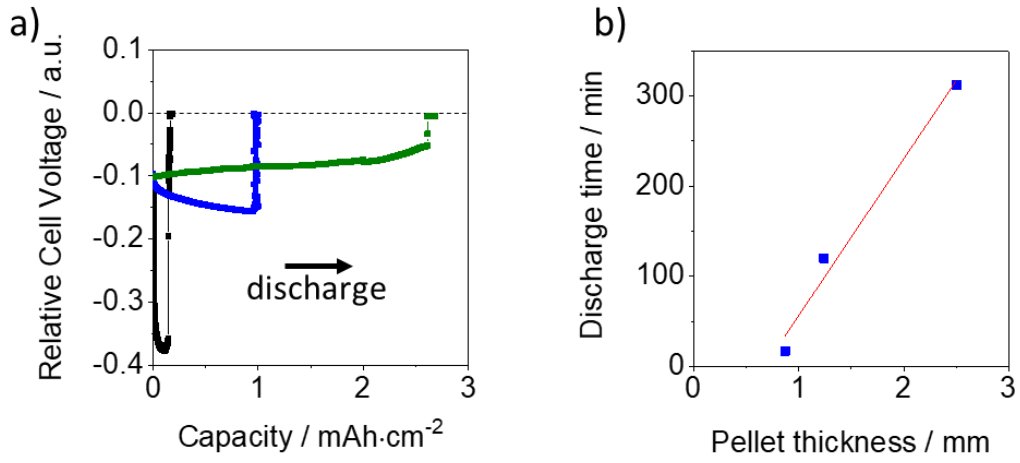


Figure 6.14. (a) Normalised voltage profiles of Li /LLZTO/Li cells with a LLZTO pellet thickness of 0.87 mm (black),1.24 mm (blue) and 2.50 mm (green) discharged at a current density of 0.5 mA·cm^{-2} until short-circuit after 17 minutes, 120 minutes and 312 minutes, respectively. (b) Plot of the relationship of LLZTO pellet thickness versus discharge time.

The results confirm that the time needed for Li dendrites to grow and reach the other electrode depends on the thickness of the LLZTO electrolyte. A linear relationship between the discharge time and the pellet thickness was established (Figure 6.14-b). Hence, from these experiments, one can regard the growth of Li dendrites as a gradual process that is ultimately triggered at the electrode-electrolyte interface when either a certain current density is applied or eventually reached within the cell due to initial surface flaws, changes in temperature, pressure and other factors that could promote uneven stripping and plating mechanisms within symmetrical Li | LLZTO | Li cell.

6.4.7. Li dendrite imaging in LLZTO by SEM and EDX

While the short-circuit behaviour in Li | LLZTO | Li cells at higher current densities is evident by the instant decrease of the voltage polarisation in the cell's voltage profile, the definitive proof that this is caused by the formation and growth of Li dendrite is more challenging. Li dendrites can range from a few nm to a few µm in size. Once exposed to air they readily react to form Li_2O or Li_2CO_3 species.[9,21] Hence, tracking the pathway taken by Li dendrites is yet extremely difficult. Figure 6.15 shows SEM images of darker regions, sometimes even visible web-like structures, of cross-sectioned short-circuited Li | LLZTO | Li cells. It should be noted that these darker features have never been observed in pristine Li | LLZTO | Li cells.

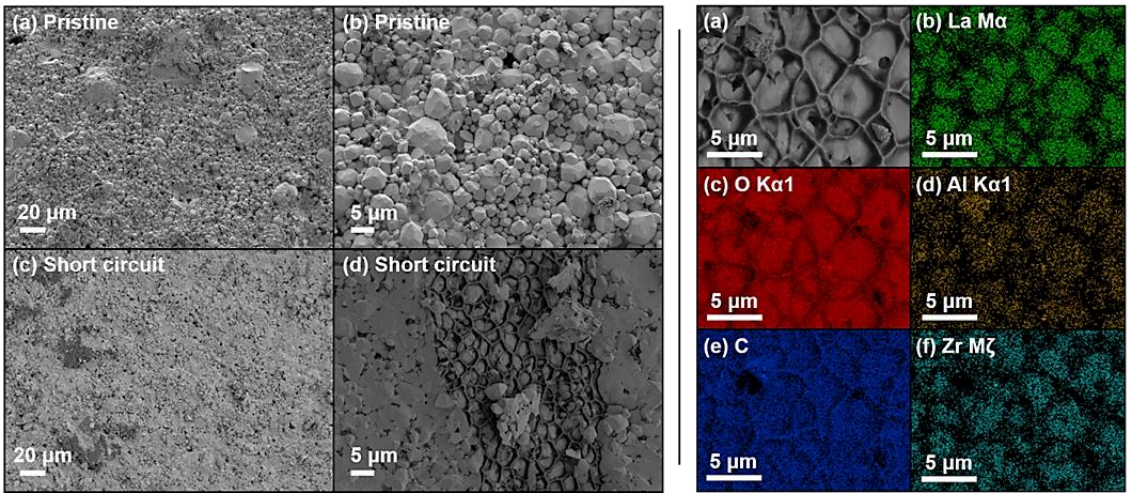


Figure 6.15. Left panel: SEM images of pristine Li /LLZTO/Li cells (a and b) and short-circuit Li/LLZTO/Li cells after cycling (c and d). The darker discolourations in (c) are the same features as the web-like structures seen in (d), which correspond to Li dendrite regions. Right panel: EDX mapping of the web-like Li dendrite structure.

EDX mapping shows that these dark areas do not contain any elements of the LLZTO phase. Unfortunately, Li cannot be detected by EDX. From the web-like structures seen in the right panel of Figure 6.15 it is evident that the detected features grow along the

grain boundaries of the LLZTO electrolyte. The dark grey colour tone of the features implies that it must contain one or more lighter elements and that it must be significantly lighter than LLZTO itself. The dark grey tone also resembles considerably the colour tone of the Li metal electrode placed on each side of the Li | LLZTO | Li cell. This provides sufficient evidence to suggest that the observed features are most likely Li dendrites penetrating through the electrolyte.

6.4.8. Li dendrite imaging in LLZTO by ^{7}Li CSI

The difficulty of cross-sectioning a symmetric Li | LLZTO | Li cell at the right place after cycling to detect, visualise and characterise Li dendrites through the solid electrolyte by SEM and EDX has led to the idea of using ^{7}Li CSI as an additional diagnostic tool to analyse cell failure in symmetric Li | LLZTO | Li cells. These measurements were performed together in a collaboration with the Prof. Clare Grey research group at the University of Cambridge.

LLZTO pellets of a thickness and diameter of around 2.5 mm and 4.5 mm, respectively, were prepared and assembled with Li metal electrodes on both sides. The preparation of Li | LLZTO | Li cells of at least twice the thickness of previously measured Li | LLZTO | Li cells is necessary to maximise the information that can be obtained from the ^{7}Li CSI experiments, as the spatial resolution is very limited (in the range of 300 µm). Hence, it is important that the distance between both Li metal electrode is as large as possible to allow to detect any Li dendrites located in between. Figure 6.16 shows the results and the cell setup of ^{7}Li CSI experiments on a pristine Li | LLZTO | Li cell and a short-circuited Li | LLZTO | Li cell. Each ^{7}Li chemical shift image displays a 1D ^{7}Li NMR spectrum on the horizontal axis and a magnetic resonance image (MRI) taken

along the z-axis, which is composed of several slices collected in the x- and y-plane along the z-axis.

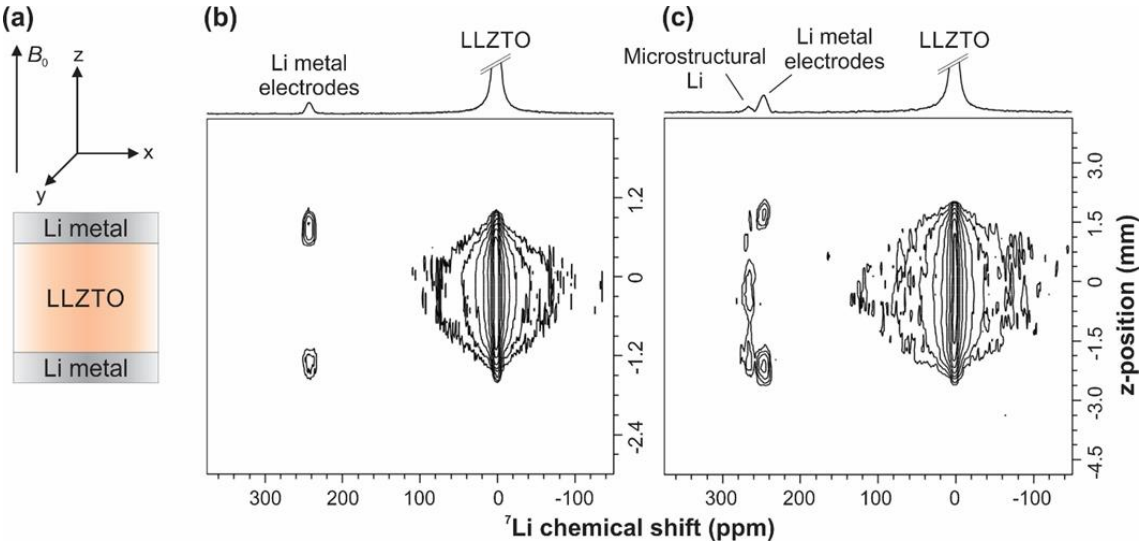


Figure 6.16. (a) Schematic of the cell setup of the Li /LLZTO/Li cell and its orientation in respect of the external magnetic field B_0 during the ^{7}Li chemical shift imaging experiment. ^{7}Li chemical shift images of (b) a pristine Li /LLZTO /Li cell and (c) a cycled Li /LLZTO /Li cell at a current density of 0.2 to 1 mA·cm^{-2} until short-circuit occurred.

Two distinct ^{7}Li chemical shifts are observed in the ^{7}Li NMR spectrum of the pristine cell: a small peak at 244 ± 6 ppm and a bigger peak at 1 ± 2 ppm), which can be associated to ^{7}Li in the Li metal and the LLZTO, respectively. The location of these two different ^{7}Li environments within the symmetric cell is clearly illustrated in the MRI. The ^{7}Li chemical shift of the Li metal electrodes appears at either side of the LLZTO pellet and is separated by the exact thickness of the LLZTO pellet, whilst the ^{7}Li chemical shift of the LLZTO spreads as expected across the entire thickness of the LLZTO pellet. Comparing the MRI of the pristine cell to the short-circuited cell, shows that the short-circuited cell has a second Li metal peak appearing at 267 ± 6 ppm that is known to correspond to microstructural Li.[22,23,24] The growth of microstructural Li (or Li dendrites) is also apparent from the MRI, showing a nearly continuous signal of the

microstructural Li peak through the LLZTO electrolyte from one Li metal electrode to another. This correlates well with the observed short-circuit in the electrochemistry of this cell (Appendix 17). Hence, combining the results of electrochemical testing with ^{7}Li CSI measurements is a valuable approach to confirm and detect Li dendrites in an all-solid-state cell in all three dimensions.

To understand the growth of Li dendrites through the LLZTO electrolyte, ^{7}Li CSI experiments were performed on Li ⏐LLZTO⏐Li cells cycled at a current density of 0.5 mA·cm^{-2} up to a capacity of 1.0 mAh·cm^{-2} and stopped at various cycle times (0-720 minutes) (Figure 6.17).

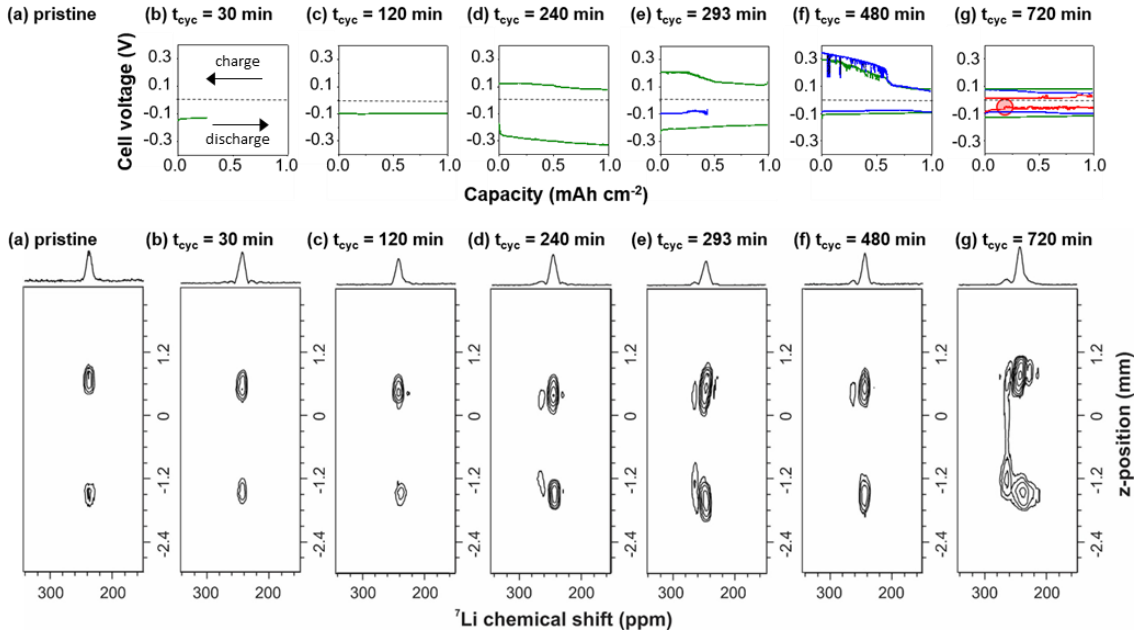


Figure 6.17. Combined electrochemical and ^{7}Li chemical shift imaging analysis of (a) a pristine Li ⏐LLZTO⏐Li cell and several Li ⏐LLZTO⏐Li cells cycled galvanostatically at a constant current density of 0.5 mA·cm^{-2} up to a capacity of 1 mAh·cm^{-2} for (b) 30 minutes, (c) 120 minutes, (d) 240 minutes, (e) 293 minutes, (f) 480 minutes and (g) 720 minutes. The first, second and third cycle are shown in green, blue and red, respectively. The short-circuit that occurred in (g) at 501 minutes is marked with a red circle in the corresponding voltage profile.

At the time points of 30 minutes and 120 minutes (Figure 6.17-b and Figure 6.17-c) of passing charge across the cell, a constant cell voltage with no significant fluctuations was observed. This is consistent with the corresponding ^{7}Li CSIs resembling the pristine cell discussed above. Hardly any microstructural Li that is yet within the detection limit of the setup has been formed. After a full cycle (Figure 6.17-d, 240 minutes), a slight increase in the voltage polarisation is observed, which correlates well with the appearance of some microstructural Li close to the Li metal electrodes in the corresponding ^{7}Li CSI and a small ^{7}Li chemical shift peak in the ^{7}Li NMR at 264 ± 4 ppm associated to microstructural Li. The microstructural Li still remains very close to the surface of the electrodes and is yet not affecting the cell performance to a significant extent.

As the cells are cycled for a longer time, the fluctuations in cell voltage become more pronounced, with the cell voltage decreasing on the second cycle in Figure 6.17-e and the appearance of soft shorts (or voltage spikes) in Figure 6.17-f, both features suggesting the penetration and growth of Li dendrites through the LLZTO electrolyte. Due to the thinner LLZTO pellet used in the cell cycled up to 480 minutes (Figure 6.17-f, 2.4 mm in thickness), the extent of microstructural Li seen in the ^{7}Li CSI due to resolution issues is less pronounced compared to the cell cycled for 293 minutes (Figure 6.17-e, 2.65 mm in thickness). After 720 minutes, a distinct short-circuit in both the voltage profile and the ^{7}Li CSI is observed (Figure 6.17-g). After a gradual decrease in polarisation upon every new cycle, the cell voltage eventually drops to close to 0 V after 501 minutes of cycling time. The penetration of Li dendrites through the full length of the solid electrolyte is confirmed by a ^{7}Li chemical shift peak at 267 ± 7 ppm, which connects both Li metal electrodes continuously with each other. A considerable amount of microstructural Li is also found near the electrode surfaces. This suggests that the action of stripping and plating must initially lead to inhomogeneities at the electrode-electrolyte

interface, which is visible by the build-up of microstructural Li at the interface. Subsequently, this leads to the penetration of metallic Li perpendicular to the electrodes into the solid electrolyte to cause short-circuit and immediate cell failure.

So far only a couple of *ex-situ* experiments using this combined electrochemical testing and ^{7}Li CSI approach have been performed and described in this Chapter. Nevertheless, the short-circuiting of Li|LLZTO|Li cells due to the formation and growth of Li dendrites through the LLZTO electrolyte could be confirmed. Yet many questions about the factors that affect Li dendrite growth, the growth mechanism and ways to inhibit its formation remain unknown. It is hoped that this newly developed diagnostic tool opens up a new avenue to monitor and understand Li dendrites in any type of all-solid-state lithium battery.

6.5. Conclusions

Overall, this Chapter has aimed to introduce a second ceramic Li-ion conductor, namely the garnet-type $Li_{6.5}La_3Zr_{1.5}Ta_{0.5}O_{12}$ solid electrolyte. The advantage that this ceramic electrolyte brings over the LAGP electrolyte discussed in the previous Chapters, is with no doubt its favourable stability in contact with Li metal. As shown by EIS measurements over 130 hours, no distinct increase in resistance was observed, confirming the chemical stability of the synthesised LLZTO with Li. This property is rarely found among other Li-ion solid electrolytes, which explains its appeal and interest to many researchers in the field.

Both sintering temperature and sintering time drastically influence the properties of the LLZTO whether this is visible through a change in the microstructure, density, ionic conductivity or cycling performance. The LLZTO pellets sintered at 1250 °C for 10 minutes gave the highest total ionic conductivity of 5 x 10^{-4} S·cm^{-1} at RT together

with the highest density of roughly 90 %. SEM images revealed homogeneously sintered grains of 2-3 μm in size across the entire cross-section of the pellet with minimal amount of visible grain boundaries phase, which as shown from EIS measurements, can add significantly to the resistance of the solid electrolyte.

Galvanostatic cycling of Li | LLZTO | Li cells revealed that, even though no chemical reaction occurred at the electrode-electrolyte interface, cell failure occured rapidly at higher current density. While continuous cycling of a Li | LLZTO | Li cell at a current density of 0.2 $mA \cdot cm^{-2}$ for 25 cycles was achievable, a Li | LLZTO | Li cell cycled at a current density of 0.5 $mA \cdot cm^{-2}$ quickly showed increases in cell polarisation, leading to either a drastic drop in cell voltage to 0 V or voltage fluctuations from very high to very low voltages in a short period of time. Both of these phenomena are signs of short-circuit and lead to immediate cell failure.

Post-mortem analysis of short-circuited cross-sectioned cells with SEM and EDX showed the presence of dark patches and occasionally even web-like features growing along the grain boundaries of LLZTO grains. These were not found in equivalent pristine cells. The detected features are believed to be Li dendrites as these could not be associated to any elements of the LLZTO phase by EDX. While EDX cannot detected Li, the colour tone of the features resembles considerably the one of fresh Li metal electrodes. To confirm the presence of Li dendrites within short-circuited Li | LLZTO | Li cells, an approach combining galvanostatic cycling with *ex-situ* ^{7}Li CSI has been developed. From ^{7}Li CSI experiments three types of ^{7}Li signals were able to be distinguished: ^{7}Li from the LLZTO phase at 1 ± 2 ppm, ^{7}Li from the Li metal electrodes at 244 ± 6 ppm and microstructural ^{7}Li (or Li dendrites) growing along the electrode-electrolyte interface and through the electrolyte thickness at 267 ± 6 ppm. A continuous path of Li dendrites connecting one

Li metal electrode with the other was observed for the short-circuited cell, while no Li dendrites were detected in the pristine cell. Analysing several Li | LLZTO | Li cells stopped at different time points during cycling by *ex-situ* ^{7}Li CSI showed that microstructural Li firstly builds up close to the electrode surface. This effect is visible in the corresponding voltage profiles by a gradual change in the cell voltage polarisation. Once these fluctuations become more pronounced, Li dendrites start to penetrate through the electrolyte material to eventually reach the Li metal electrode on the opposite side. How quickly these Li dendrites penetrate through the LLZTO depends on the thickness of the LLZTO itself. The thicker the electrolyte is, the longer it takes for the cell to eventually short-circuit. Hence, independently from the applied current density, Li dendrite growth can be regarded as a rather gradual process. Further work is needed to fully understand the mechanism behind its growth.

While LLZTO has many advantages over other existing solid electrolytes, new challenges regarding its implementation in an all-solid-state battery still have to be resolved. The formation of Li dendrites at higher current densities leading to short circuiting and cell failure is yet not fully understood. From this Chapter it is evident that the microstructure, density, electrolyte thickness and ionic conductivity all significantly affect the electrochemical performance of a Li | LLZTO | Li cell. Further tuning of any of these parameters could vastly improve the cycling performance of any LLZTO cell. Additionally, the performance of a combined electrochemical and ^{7}Li CSI analysis has shown to be an excellent diagnostic tool in understanding the formation and growth of Li dendrites through a symmetrical cell. This is only the first time such an approach has been considered. Further development of this technique from an *ex-situ* to an *in-situ* approach and improvement of its resolution could reveal further information on the cell failure mechanisms in all-solid-state batteries.

6.6. References

1. Thangadurai, V., Kaack, H. & Weppner, W. J. F. Novel Fast Lithium Ion Conduction in Garnet-Type Li5La3M2O12 (M: Nb, Ta). *ChemInform* **34,** 437–440 (2003).

2. Thangadurai, V., Narayanan, S. & Pinzaru, D. Garnet-type solid-state fast Li ion conductors for Li batteries: critical review. *Chem. Soc. Rev.* **43,** 4714 (2014).

3. Sharafi, A. *et al.* Surface Chemistry Mechanism of Ultra-Low Interfacial Resistance in the Solid-State Electrolyte Li 7 La 3 Zr 2 O 12. *Chem. Mater.* **29,** 7961–7968 (2017).

4. Hongahally Basappa, R. *et al.* Grain boundary modification to suppress lithium penetration through garnet-type solid electrolyte. *J. Power Sources* **363,** 145–152 (2017).

5. Tsai, C. L. *et al.* Li7La3Zr2O12 Interface Modification for Li Dendrite Prevention. *ACS Appl. Mater. Interfaces* **8,** 10617–10626 (2016).

6. Monroe, C. & Newman, J. The Impact of Elastic Deformation on Deposition Kinetics at Lithium/Polymer Interfaces. *J. Electrochem. Soc.* **152,** A396 (2005).

7. Ni, J. E., Case, E. D., Sakamoto, J. S., Rangasamy, E. & Wolfenstine, J. B. Room temperature elastic moduli and Vickers hardness of hot-pressed LLZO cubic garnet. *J. Mater. Sci.* **47,** 7978–7985 (2012).

8. Han, X. *et al.* Negating interfacial impedance in garnet-based solid-state Li metal batteries. *Nat. Mater.* **16,** (2016).

9. Cheng, L. *et al.* Effect of Surface Microstructure on Electrochemical Performance of Garnet Solid Electrolytes. *ACS Appl. Mater. Interfaces* **7,** 2073–2081 (2015).

10. Porz, L. *et al.* Mechanism of Lithium Metal Penetration through Inorganic Solid Electrolytes. *Adv. Energy Mater.* **1701003,** 1–12 (2017).

11. Inada, R., Kusakabe, K., Tanaka, T., Kudo, S. & Sakurai, Y. Synthesis and properties of Al-free Li7-XLa3Zr2-xTaxO12garnet related oxides. *Solid State Ionics* **262,** 568–572 (2014).

12. Thompson, T. *et al.* A Tale of Two Sites: On Defining the Carrier Concentration in Garnet-Based Ionic Conductors for Advanced Li Batteries. *Adv. Energy Mater.* **5,** 1500096 (2015).

13. Li, Y., Han, J.-T., Wang, C.-A., Xie, H. & Goodenough, J. B. Optimizing Li+ conductivity in a garnet framework. *J. Mater. Chem.* **22,** 15357 (2012).

14. Liu, K., Ma, J.-T. & Wang, C.-A. Excess lithium salt functions more than compensating for lithium loss when synthesizing Li6.5La3Ta0.5Zr1.5O12 in alumina crucible. *J. Power Sources* **260,** 109–114 (2014).

15. Li, Y., Han, J. T., Wang, C. A., Xie, H. & Goodenough, J. B. Optimizing Li+ conductivity in a garnet framework. *J. Mater. Chem.* **22,** 15357 (2012).

16. Irvine, J. T. S., Sinclair, D. C. & West, A. R. Electroceramics: characterization by impedance spectroscopy. *Adv. Mater.* **2,** 132–138 (1990).

17. Hamao, N., Kataoka, K. & Akimoto, J. Li-ion conductivity and crystal structure of garnet-type $Li_{6.5}La_3M_{1.5}Ta_{0.5}O_{12}$ (*M* = Hf, Sn) oxides. *J. Ceram. Soc. Japan* **125,** 272–275 (2017).

18. Thangadurai, V. & Weppner, W. Effect of sintering on the ionic conductivity of garnet-related structure Li5La3Nb2O12 and In- and K-doped Li5La3Nb2O12. *J. Solid State Chem.* **179,** 974–984 (2006).

19. Murugan, R., Thangadurai, V. & Weppner, W. Lattice Parameter and Sintering Temperature Dependence of Bulk and Grain-Boundary Conduction of Garnet-like Solid Li-Electrolytes. *J. Electrochem. Soc.* **155,** A90 (2008).

20. Kim, Y. *et al.* Electrochemical Stability of Li6.5La3Zr1.5M0.5O12 (M = Nb or Ta) against Metallic Lithium. *Front. Energy Res.* **4,** 1–7 (2016).

21. Larraz, G., Orera, A. & Sanjuán, M. L. Cubic phases of garnet-type Li7La3Zr2O12: the role of hydration. *J. Mater. Chem. A* **1,** 11419 (2013).

22. Trease, N. M., Zhou, L., Chang, H. J., Zhu, B. Y. & Grey, C. P. In situ NMR of lithium ion batteries: Bulk susceptibility effects and practical considerations. *Solid State Nucl. Magn. Reson.* **42,** 62–70 (2012).

23. Chandrashekar, S. *et al.* 7Li MRI of Li batteries reveals location of microstructural lithium. *Nat. Mater.* **11,** 311–315 (2012).

24. Chang, H. J. *et al.* Correlating Microstructural Lithium Metal Growth with Electrolyte Salt Depletion in Lithium Batteries Using 7Li MRI. *J. Am. Chem. Soc.* **137,** 15209–15216 (2015).

Chapter 7: Conclusions and Outlook

The aim of this work has been to characterise the microstructural, electrochemical and mechanical properties of two crystalline phosphate-type and oxide-type ceramic solid electrolytes, namely LAGP and LLZTO, for their application in future all-solid-state lithium batteries. Their intrinsically different behaviour with Li metal was analysed. The central part of this work presented a novel synthetic route to a 3D ordered hybrid electrolyte with bicontinous ceramic and polymer microchannels that can retain a high ionic conductivity whilst providing tuneable mechanical properties.

The properties of LAGP as a potential solid electrolyte were analysed in **Chapter 3**. While LAGP showed a high ionic conductivity of 2.8 x 10^{-4} $S \cdot cm^{-1}$ at RT, its reactivity in contact with Li metal and brittle mechanical properties were reported as major drawbacks. An in-depth analysis of the MCI interphase layer formed between LAGP and Li was performed. The growth of the interphase layer is progressive and can be accelerated through cycling when a constant current is applied. The difference in morphology between the LAGP and the interphase layer provokes interfacial stresses that lead to the propagation of cracks along the interface, a detachment of the interphase layer from the bulk and eventually further crack propagations perpendicular to the interface into the ceramic electrolyte until complete cell failure. The ease at which crack propagation can occur in LAGP was demonstrated through several mechanical tests. LAGP is a very brittle ceramic material, which rapidly fractures once a crack has been initiated.

In **Chapter 4**, a new approach to create a unique solid electrolyte that combines high ionic conductivity with suitable mechanical properties is presented. This was demonstrated by the development of a 3D hybrid electrolyte with bicontinuous ordered

ceramic and polymer microchannels. While the ceramic channels are filled with a high ionically conductive solid electrolyte such as LAGP, the non-conductive polymer channels filled with an epoxy polymer can tune the hybrid's mechanical properties. 3D templates with a gyroid microarchitecture and an 85 % porosity were designed and created by 3D printing. These 3D templates were then converted into structured LAGP scaffolds by the infiltration of a LAGP suspension into the 3D template channels and sintering at high temperatures. The channels of the structured LAGP scaffold were then backfilled with an epoxy polymer under vacuum to give the final LAGP-epoxy hybrid electrolyte. A total ionic conductivity, only reduced by the volume fraction of non-conductive polymer present and the tortuosity of the microarchitecture, of 1.6×10^{-4} S·cm^{-1} at RT was achieved. Hence, LAGP phase densities equivalent to an LAGP pellet were obtained. Galvanostatic cycling experiments proved that the gyroid LAGP-epoxy hybrid outperforms an LAGP pellet at current densities of 0.7 mA·cm^{-2} and above regarding cycle life. The hybrid electrolyte showed less detachment at the interface and was able to retain its structural integrity during extensive cycling. This improvement in the mechanical properties was confirmed by compression and four-point bending tests, in which the hybrid showed an increase of 28 % in its compressive failure strain and a five-fold increase of its flexural failure strain compared to LAGP alone.

The flexibility of the hybrid's synthesis in terms of varying its parameters such as the choice of ceramic and polymer material, the hybrid's microarchitecture and the hybrid's ceramic-to-polymer ratio was demonstrated in **Chapter 5**. Using LAGP as the ceramic material, four different microarchitectures, namely a cubic, a gyroid, a diamond and a bijel microarchitecture together with two different polymer materials, epoxy and PP, were investigated. Total ionic conductivity values in the range of 1.1-1.7 x 10^{-4} S·cm^{-1} at RT were obtained for all LAGP-PP and LAGP-epoxy hybrids. While the choice of polymer

did not affect the ionic conductivity, the tortuosity and 'ease-to-fill' of the microarchitecture did play a significant role. The highest amount of LAGP filling was obtained with the gyroid microarchitecture leading to the highest ionic conductivity of all. Galvanostatic cycling of all eight hybrid electrolytes at a current density of 1 $mA \cdot cm^{-2}$ showed that the epoxy was much more efficient at prolonging the hybrid's cycle life compared to the PP. Mechanical testing confirmed the improved mechanical properties of the LAGP-epoxy hybrids over the LAGP-PP hybrids and the suitability of the gyroid microarchitecture with regards to fracture. Three different ceramic-to-polymer ratios, namely 70 % to 30 %, 60 % to 40 % and 45 % to 55 %, and their effect on the hybrid's properties was also investigated. The ionic conductivity decreased from 1.8×10^{-4} $S \cdot cm^{-1}$ to 5.1×10^{-5} $S \cdot cm^{-1}$ at RT as expected with the decrease in the LAGP volume fraction from 70 % to 45 %. The difficulty in filling narrower channels such as was the case for the 45 % to 55 % ceramic-to-polymer ratio, caused an additional drop in ionic conductivity. No difference in the cycling performance between the three ratios was observed. The cell voltage increased similarly with time for all three cells, which suggests that the reactivity of LAGP with Li is the main cause of cell failure for hybrids with identical microarchitecture and polymer. Four-point bending measurements showed a significant increase of the flexural fracture strain by over 45 % from a hybrid with 70 % to 45 % LAGP volume fraction, which validates the role of the polymer channels to provide 3D mechanical stability to the hybrid. Finally, an attempt to replace LAGP with LLZTO, which is stable against Li metal, was initiated. A free-standing, gyroid LLZTO-epoxy hybrid electrolyte with a 60 % to 40 % ceramic-to-polymer ratio was successfully synthesised. Nevertheless, due to the challenging sintering conditions of the LLZTO solid electrolyte, a secondary phase between the LLZTO grains could not be avoided, lowering the conductivity of the LLZTO-epoxy hybrid down to 2.7×10^{-5} $S \cdot cm^{-1}$

at RT. Further optimisation of the synthesis could improve the conductivity of the hybrid significantly. Yet, the LLZTO-epoxy hybrid showed a three-fold increase in the flexural failure strain compared to LLZTO alone, which again corroborates the strengthening function of the polymer within the hybrid's structure.

The favourable chemical stability of LLZTO with Li has led to an investigation of its synthetic and electrochemical challenges in **Chapter 6**. Both sintering time and temperature directly alter the microstructure, density, ionic conductivity and cycling performance of the LLZTO electrolyte. While the sintering temperature affects the pellet density, the sintering time varies the grain sizes and the amount of secondary phase in the grain boundaries. The highest conductivity of 5 x 10^{-4} $S \cdot cm^{-1}$ at RT for a LLZTO pellet was achieved at sintering conditions of 1250 ºC for 10 minutes, leading to a 90 % dense pellet with 2-3 µm grains and minimal amount of grain boundaries using conventional sintering methods. While it was shown that LLZTO is stable against Li metal over time, Li | LLZTO | Li cells still led to short-circuit phenomena at a low current density of 0.5 $mA \cdot cm^{-2}$ due to the formation and growth of Li dendrites. These are hard to track with conventional imaging techniques such as SEM and EDX. Hence, an approach combining galvanostatic cycling with *ex-situ* ^{7}Li chemical shift imaging was presented. This approach enabled to identify the presence of Li dendrites in short-circuited cells in 3D space. The growth of Li dendrites was analysed by imaging Li | LLZTO | Li cells stopped at different stages of cycling and showed that the Li dendrites firstly build up very closely at the electrode's surface before gradually piercing their way perpendicular into the solid electrolyte to the opposite Li electrode. The thickness of the solid electrolyte influences the time needed by the Li dendrites to short-circuit the cell. Hence, the combination of electrochemical and imaging techniques has shown to be a promising approach in trying to diagnose cell failure in all-solid-state cells.

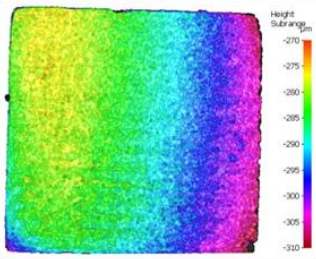
All in all, this work has shown that the high ionic conductivity alone in ceramic solid electrolytes is not enough to yet make these materials suitable candidates in future all-solid-state batteries. To find a solid electrolyte that is stable with Li metal is of upmost importance to ensure long-term cycling. However, even if the chemical stability is assured, the formation of Li dendrites at higher current densities needs to be inhibited. Hence, the mechanical properties of solid electrolytes, which can significantly change depending on the microstructure and the employed synthesis methods, should not be neglected. The concept of a 3D structured ceramic-polymer hybrid electrolyte presented in this work, which can retain the high ionic conductivity of a ceramic electrolyte but tune its mechanical properties, will hopefully contribute to further ideas that will ultimately create solutions to make the all-solid-state battery a reality.

Appendices

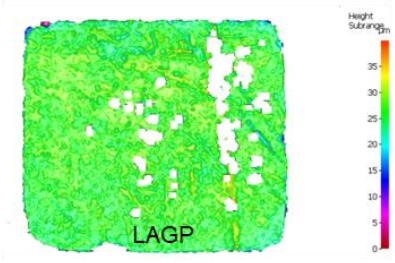
Appendix 1

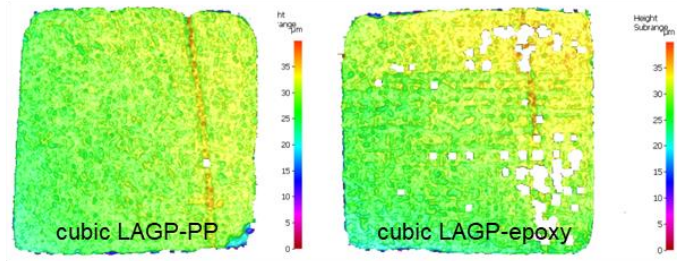
Optical depth profiling of the surfaces of LAGP and LAGP-polymer hybrid electrolytes as a polishing quality check before compression testing.

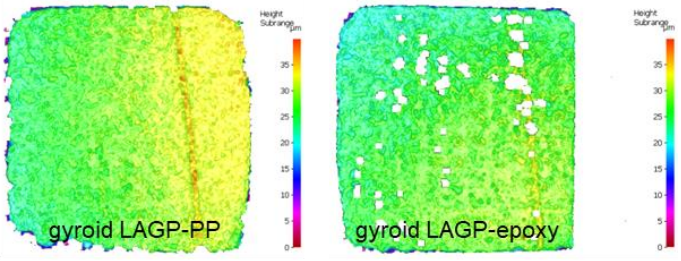
LAGP-polymer hybrid electrolytes polished by hand

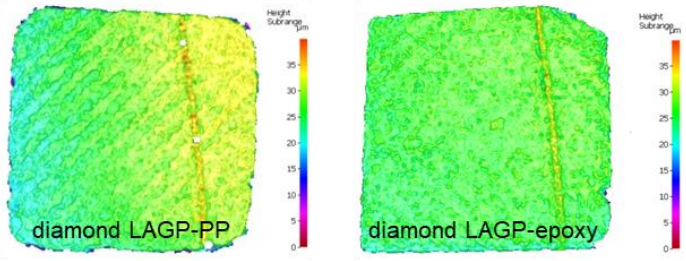


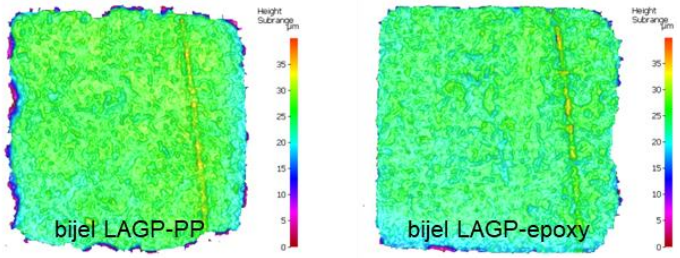
LAGP and set of LAGP-polymer hybrid electrolytes polished using a rheometer











Appendix 2

EIS analysis of a symmetrical Au | LAGP | Au cell at 25 ºC and -30 ºC.

	EIS at 25 ºC	EIS at -30 ºC
R_1 / Ω·cm	2036	44390
$Ceff_1$ / F·cm^{-1}	/	1.1 E-11
σ_1 / S·cm^{-1}	4.9 E-4	2.25 E-5
f_1 / Hz	/	3.3 E5
R_2 / Ω·cm	1484	68296
$Ceff_2$ / F·cm^{-1}	9.9 E-11	1.8 E-10
σ_2 / S·cm^{-1}	6.7 E-4	1.5 E-5
f_2 / Hz	1.1 E6	1.3 E4
σ_{tot} / S·cm^{-1}	2.8 E-4	8.9 E-6

Appendix 3

EIS analysis of a symmetrical Li | LAGP | Li cell at 25 ºC.

EIS at 25 ºC							
R_1 / Ω·cm	1495	R_2 / Ω·cm	1257	R_3 / Ω·cm^2	34	R_4 / Ω·cm^2	13
$Ceff_1$ / F·cm^{-1}	3.1 E-10	$Ceff_2$ / F·cm^{-1}	8.8 E-10	$Ceff_3$ / F·cm^{-2}	1.4 E-8	$Ceff_4$ / F·cm^{-2}	1.1 E-3
σ_1 / S·cm^{-1}	6.7 E-4	σ_2 / S·cm^{-1}	8.0 E-4	σ_3 / S·cm^{-1}	1.9 E-3	σ_4 / S·cm^{-1}	5.0 E-3
f_1 / Hz	3.4 E5	f_2 / Hz	1.4 E5	f_3 / Hz	2.3 E5	f_4 / Hz	11.4
σ_{tot} / S·cm^{-1}	2.9 E-4						

Appendix 4

EIS analysis of non-polished, dry-polished and H_2O polished symmetrical Li | LAGP | Li cells at 25 ºC.

	Non-polished	Dry-polished	H_2O-polished
R_1 / Ω·cm	2897	3090	2777
$Ceff_1$ / F·cm^{-1}	6.0 E-10	5.5 E-10	4.1 E-10
σ_1 / S·cm^{-1}	3.5 E-4	3.2 E-4	3.6 E-4
f_1 / Hz	9.2 E4	9.4 E4	1.4 E5
R_2 / Ω·cm	512	249	337
$Ceff_2$ / F·cm^{-1}	1.0 E-9	7.5 E-10	6.7 E-10
σ_2 / S·cm^{-1}	2.0 E-3	4.0 E-3	3.0 E-3
f_2 / Hz	3.0 E5	8.6 E5	7.0 E5
R_3 / Ω·cm^2	4	72	38
$Ceff_3$ / F·cm^{-2}	1.3 E-8	1.9 E-7	2.2 E-7
σ_3 / S·cm^{-1}	2.9 E-2	1.4 E-3	2.0 E-3
f_3 / Hz	3.3 E6	1.1 E4	2.0 E4
R_4 / Ω·cm^2	26	36	24
$Ceff_4$ / F·cm^{-2}	1.0 E-3	3.5 E-4	5.4 E4
σ_4 / S·cm^{-1}	4.0 E-3	2.8 E-3	3.1 E-3
f_4 / Hz	5.8	13.0	12.3
σ_{tot} / S·cm^{-1}	2.7 E-4	2.3 E-4	2.6 E-4

Appendix 5

EIS analysis of a symmetrical Au | LAGP | Au cell and Au | gyroid LAGP-epoxy | Au cell at 25 ºC and -30 ºC.

	EIS at 25 ºC		EIS at -30 ºC	
	LAGP pellet	gyroid LAGP-epoxy	LAGP pellet	gyroid LAGP-epoxy
R_1 / Ω·cm	2036	3333	44390	64797
$Ceff_1$ / F·cm^{-1}	/	/	1.1 E-11	7.40 E-12
σ_1 / S·cm^{-1}	4.9 E-4	3.0 E-4	2.25 E-5	1.5 E-5
f_1 / Hz	/	/	3.3 E5	3.3 E5
R_2 / Ω·cm	1484	2964	68296	83485
$Ceff_2$ / F·cm^{-1}	9.9 E-11	1.0 E-10	1.8 E-10	9.7 E-11
σ_2 / S·cm^{-1}	6.7 E-4	3.4 E-4	1.5 E-5	1.2 E-5
f_2 / Hz	1.1 E6	5.4 E5	1.3 E4	2.0 E4
σ_{tot} / S·cm^{-1}	2.8 E-4	1.6 E-4	8.9 E-6	6.7 E-6

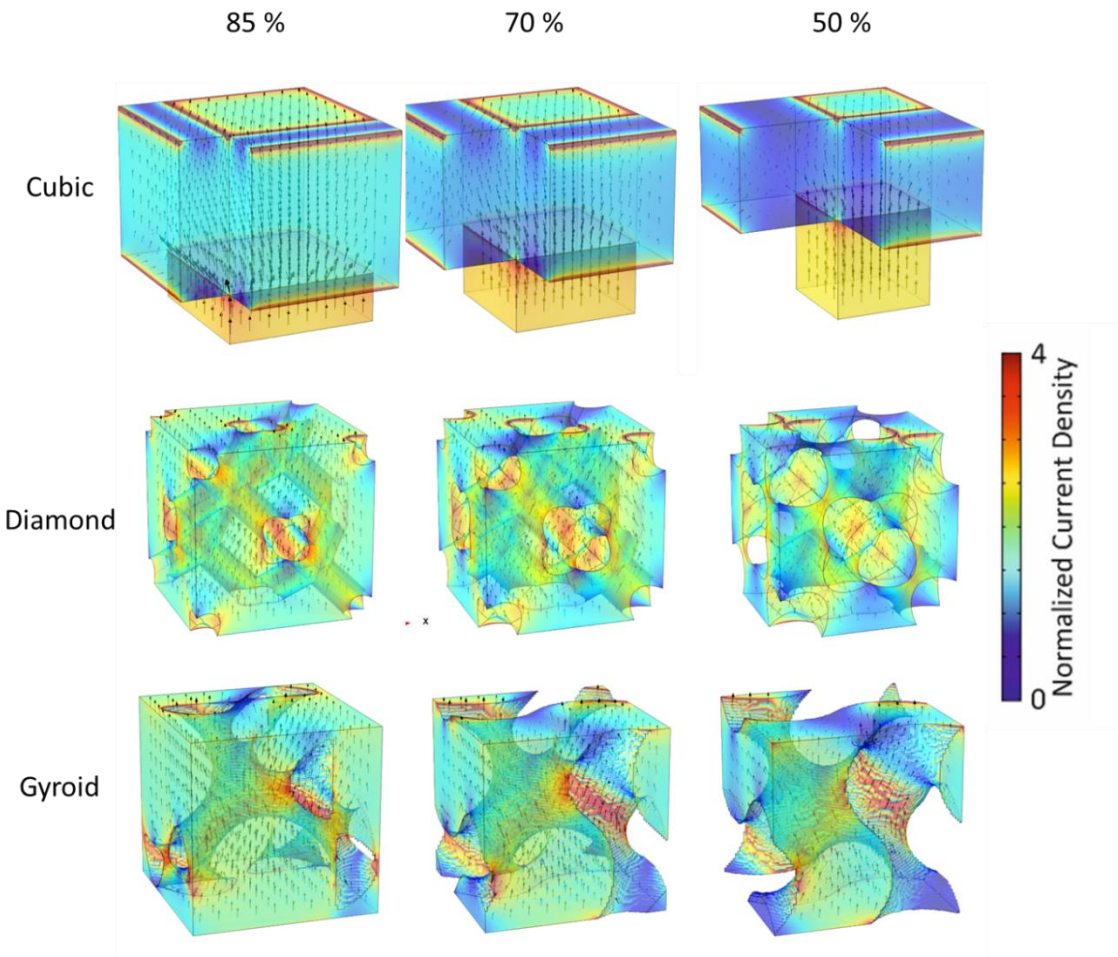
Appendix 6

Finite element modelling was performed on the three ordered microarchitectures (cubic, gyroid and diamond) using COMSOL Multiphysics 5.2 to predict their theoretical electrochemical properties. The simulations were performed on a single unit cell of each microarchitecture by using periodic boundary conditions normal to the current flux. Modelling the ionic conduction was achieved using COMSOL electric currents physics, assuming the presence of only one charge carrier and neglecting polarisability effects by the Li-ion conductor during conduction. A potential was applied to the top surface of the unit cell, while the ground was applied to the bottom surface of the unit cell. A current

flow was then simulated through the unit cell (through the channels, which corresponds to the volume fraction of Li-ion conductive material, in this case LAGP). An apparent mean conductivity ($k^{apparent}$) is obtained for each unit cell, which gives information on the tortuosity of the microarchitecture (τ) at different volume fractions of conductive material (p) by following equation:

$$\kappa^{apparent} = \frac{p}{\tau} \cdot \kappa = f \cdot \kappa$$

Where f is the current distribution factor (or geometry factor) and k is the ionic conductivity of the solid electrolyte. Calculations were performed for LAGP volume fractions of 85 %, 70 % and 50 % and compared to a 100 % LAGP phase. 3D colour maps of the current density through the unit cells are shown below.



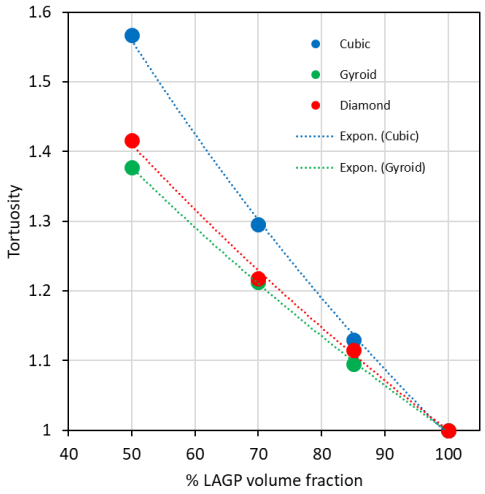
Calculated current distribution factors for all three microarchitectures at three different % LAGP volume fractions:

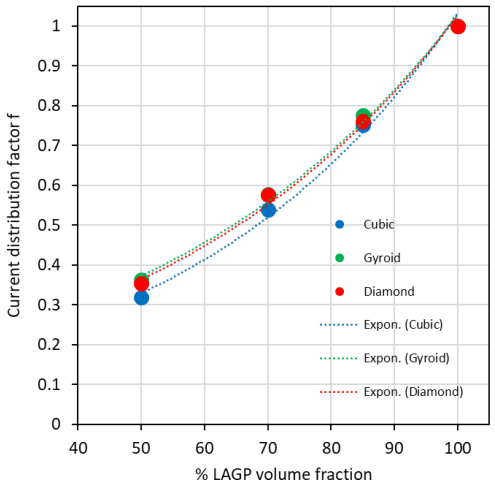
Current distribution factor (f)	85 % LAGP	70 % LAGP	50 % LAGP	100 % LAGP
Cubic	0.752	0.540	0.319	1
Diamond	0.762	0.576	0.353	1
Gyroid	0.776	0.577	0.363	1

Calculated tortuosity values for all three microarchitectures at three different % LAGP volume fractions:

Tortuosity (τ)	85 % LAGP	70 % LAGP	50 % LAGP	100 % LAGP
Cubic	1.130	1.296	1.567	1
Diamond	1.115	1.218	1.416	1
Gyroid	1.095	1.213	1.377	1

Plots of tortuosity values and current distribution factors versus % LAGP volume fraction:





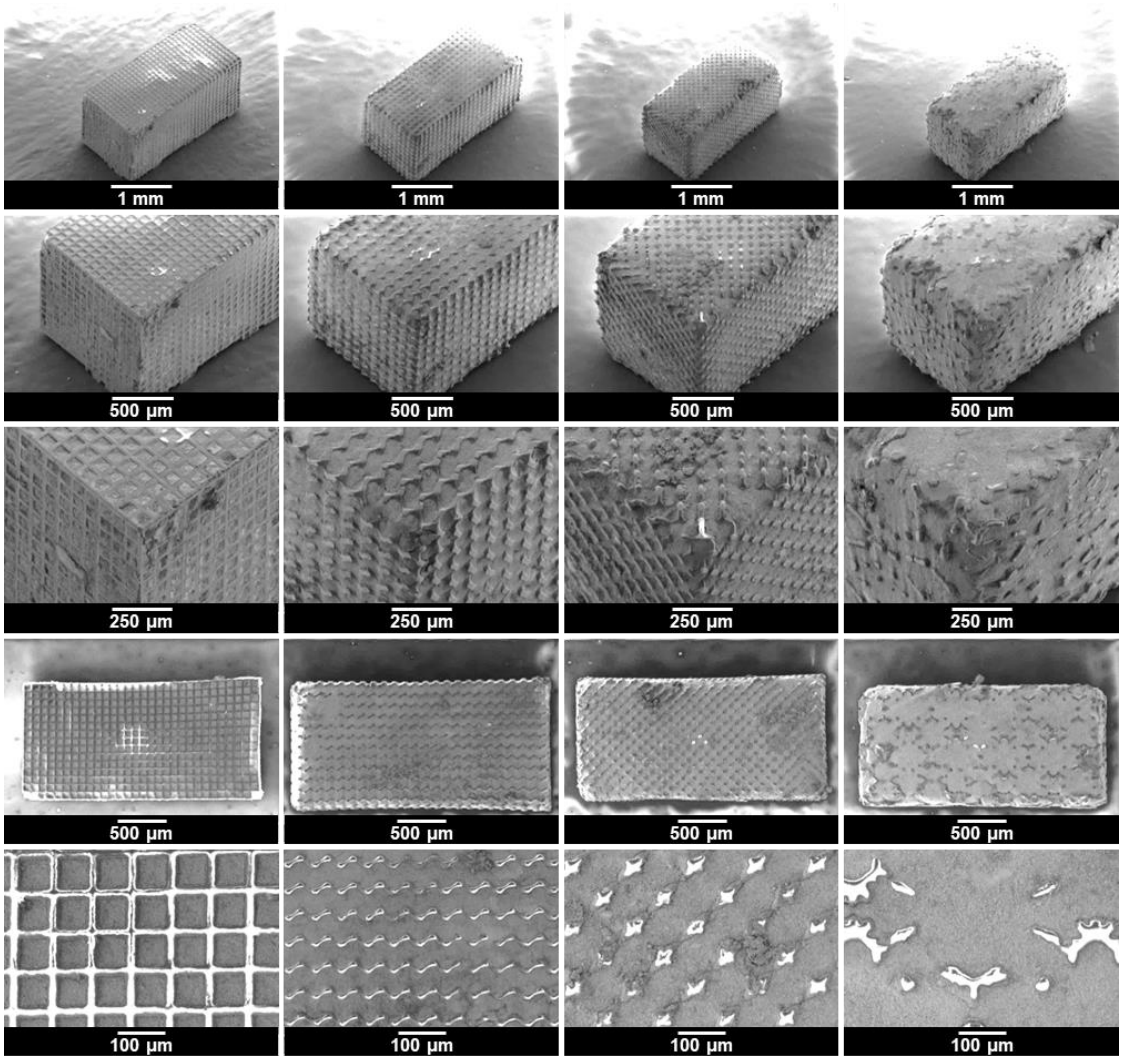
Appendix 7

EIS analysis of a symmetrical Li | LAGP | Li cell and Li | gyroid LAGP-epoxy | Li cell at 25 ºC.

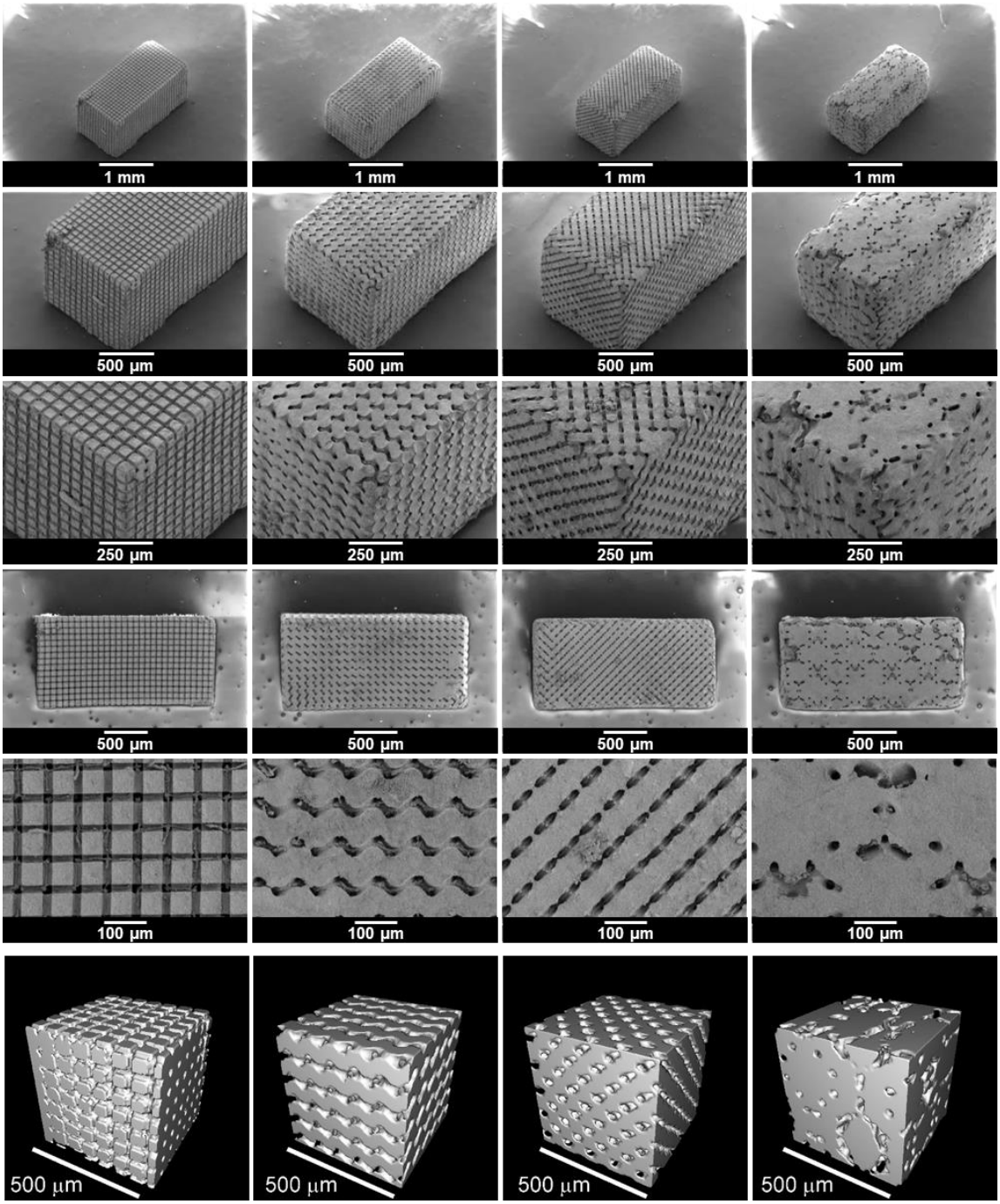
	EIS at 25 ºC	
	LAGP pellet	gyroid LAGP-epoxy
R_1 / Ω·cm	1495	2164
$Ceff_1$ / F·cm^{-1}	3.1 E-10	3.9 E-10
σ_1 / S·cm^{-1}	6.7 E-4	4.6 E-4
f_1 / Hz	3.4 E5	1.9 E5
R_2 / Ω·cm	1257	1205
$Ceff_2$ / F·cm^{-1}	8.8 E-10	3.0 E-10
σ_2 / S·cm^{-1}	8.0 E-4	8.3 E-4
f_2 / Hz	1.4 E5	4.4 E5
R_3 / Ω·cm^2	34	171
$Ceff_3$ / F·cm^{-2}	1.4 E-8	1.2 E-8
σ_3 / S·cm^{-1}	1.9 E-3	3.7 E-4
f_3 / Hz	2.3 E5	7.6 E4
R_4 / Ω·cm^2	13	15
$Ceff_4$ / F·cm^{-2}	1.1 E-3	2.4 E-3
σ_4 / S·cm^{-1}	5.0 E-3	4.3 E-3
f_4 / Hz	11.4	4.45
σ_{tot} / S·cm^{-1}	2.9 E-4	1.6 E-4

Appendix 8

SEM images of the LAGP filled templates with cubic, gyroid, diamond and bijel microarchitectures.



Sintered LAGP scaffolds with cubic, gyroid, diamond and bijel microarchitecture and micro-CT scans of the inside of the structures.



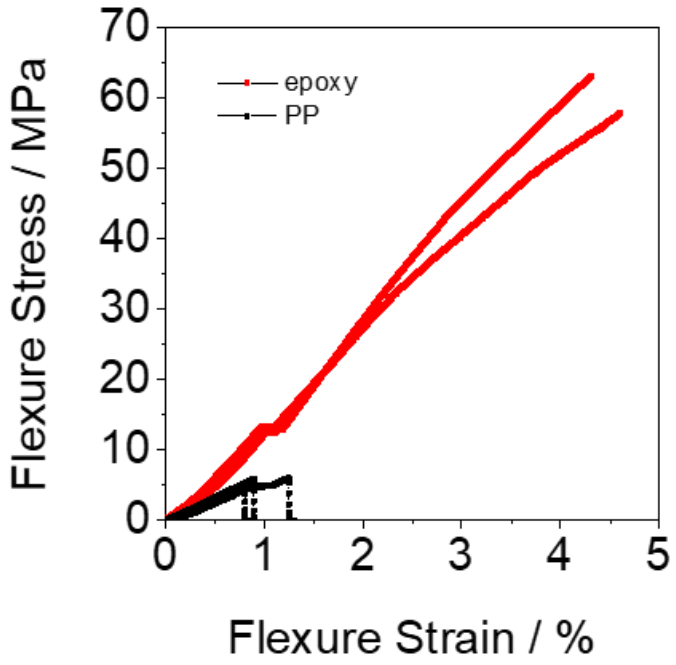
Appendix 9

EIS analysis of symmetrical Li | LAGP-polymer hybrid | Li cells at 25 ºC.

	Cubic		Gyroid		Diamond		Bijel	
	LAGP-PP	LAGP-epoxy	LAGP-PP	LAGP-epoxy	LAGP-PP	LAGP-epoxy	LAGP-PP	LAGP-epoxy
R_1 / Ω·cm	4890	2125	1807	1980	830	2824	1335	3327
$Ceff_1$ / F·cm^{-1}	3.6 E-10	2.1 E-10	6.2 E-10	4.2 E-10	4.6 E-10	2.8 E-10	3.3 E-10	5.2 E-10
σ_1 / S·cm^{-1}	2.1 E-4	4.7 E-4	5.5 E-4	5.1 E-4	1.2 E-3	3.5 E-4	7.5 E-4	3.0 E-4
f_1 / Hz	9.2 E4	3.6 E5	1.4 E5	1.9 E5	4.2 E5	2.0 E5	3.6 E5	9.2 E4
R_2 / Ω·cm	487	944	162	1100	4474	1465	1606	3284
$Ceff_2$ / F·cm^{-1}	1.5 E-9	1.4 E-9	2.2 E-9	3.3 E-10	2.7 E-10	2.1 E-10	2.8 E-10	2.2 E-10
σ_2 / S·cm^{-1}	2.1 E-3	1.1 E-3	6.2 E-3	9.1 E-4	2.2 E-4	6.8 E-4	6.2 E-4	3.1 E-4
f_2 / Hz	2.2 E5	1.2 E5	4.5 E5	4.4 E5	1.3 E5	5.3 E5	3.6 E5	2.2 E5
R_3 / Ω·cm^2	112	144	275	156	82	167	174	118
$Ceff_3$ / F·cm^{-2}	3.4 E-8	4.3 E-8	3.8 E-9	1.3 E-8	3.4 E-8	9.9 E-9	5.0 E-9	6.4 E-8
σ_3 / S·cm^{-1}	7.1 E-4	5.1 E-4	2.4 E-4	4.0 E-4	5.4 E-4	3.7 E-4	2.7 E-4	6.3 E-4
f_3 / Hz	4.2 E4	2.5 E4	1.5 E5	7.6 E4	5.8 E4	9.6 E4	1.8 E5	2.1 E4
R_4 / Ω·cm^2	12	90	19	13	25	23	14	86
$Ceff_4$ / F·cm^{-2}	3.7 E-3	1.2	3.5 E-3	2.5 E-3	2.0 E-3	2.3 E-3	2.0 E-3	8.4 E-2
σ_4 / S·cm^{-1}	6.3 E-3	8.1 E-4	3.4 E-3	4.7 E-3	1.8 E-3	2.7 E-3	3.5 E-3	8.6 E-4
f_4 / Hz	3.5	1.5 E-3	2.4	4.7	3.3	3.1	5.8	2.2 E-2
σ_{tot} / S·cm^{-1}	1.4 E-4	1.6 E-4	1.5 E-4	1.7 E-4	1.3 E-4	1.4 E-4	1.4 E-4	1.1 E-4

Appendix 10

Stress-strain curves of PP and epoxy from four-point bending measurements at a constant displacement rate of 5 µm·min^{-1} until fracture.



Appendix 11

EIS analysis of symmetrical Li | gyroid LAGP-epoxy | Li cells with different % LAGP volume fraction at 25 ºC.

	70 %	60 %	45 %
R_1 / Ω·cm	1119	4135	1530
$Ceff_1$ / F·cm^{-1}	3.3 E-10	2.3 E-10	5.2 E-10
σ_1 / S·cm^{-1}	8.9 E-4	2.4 E-4	6.5 E-4
f_1 / Hz	4.4 E5	1.6 E5	2.0 E5
R_2 / Ω·cm	1974	2875	8655
$Ceff_2$ / F·cm^{-1}	4.3 E-10	7.8 E-10	2.40 E-10
σ_2 / S·cm^{-1}	5.1 E-4	3.5 E-4	1.2 E-4
f_2 / Hz	1.90 E5	7.11 E4	7.7 E4
R_3 / Ω·cm^2	156	39	261
$Ceff_3$ / F·cm^{-2}	1.4 E-8	2.7 E-7	3.15E-8
σ_3 / S·cm^{-1}	4.0 E-4	1.40 E-3	1.3 E-4
f_3 / Hz	7.6 E4	1.5 E4	1.9 E4
R_4 / Ω·cm^2	10	61	63
$Ceff_4$ / F·cm^{-2}	1.3 E-3	4.7 E-3	5.2 E-4
σ_4 / S·cm^{-1}	6.2 E-3	8.9 E-4	5.6 E-4
f_4 / Hz	12	57	5
σ_{tot} / S·cm^{-1}	1.6 E-4	1.1 E-4	5.1 E-5

Appendix 12

EIS analysis of a symmetrical Li | gyroid LLZTO-epoxy | Li cell at 25 ºC.

EIS at 25 ºC					
R_1 / Ω·cm	1574	R_2 / Ω·cm	35533	R_3 / Ω·cm²	419
$Ceff_1$ / F·cm^{-1}	8.7 E-10	$Ceff_2$ / F·cm^{-1}	1.1 E-9	$Ceff_3$ / F·cm^{-2}	2.1 E-4
σ_1 / S·cm^{-1}	6.4 E-4	σ_2 / S·cm^{-1}	2.8 E-5	σ_3 / S·cm^{-1}	1.7 E-4
f_1 / Hz	1.2 E5	f_2 / Hz	4.2 E3	f_3 / Hz	1.8
		σ_{tot} / S·cm^{-1}	2.3 E-5		

Appendix 13

EIS analysis of a symmetrical Au | LLZTO | Au cell at 25 ºC and -17 ºC.

	EIS at 25 ºC	EIS at -17 ºC
R_1 / Ω·cm	1322	34067
$Ceff_1$ / F·cm^{-1}	/	5.9 E-11
σ_1 / S·cm^{-1}	7.6 E-4	2.9 E-5
f_1 / Hz	/	8.0 E4
R_2 / Ω·cm	502	16605
$Ceff_2$ / F·cm^{-1}	4.5 E-10	1.4 E-9
σ_2 / S·cm^{-1}	2.0 E-3	6.0 E-5
f_2 / Hz	7.1 E5	6.8 E3
σ_{tot} / S·cm^{-1}	5.5 E-4	2.0 E-5

Appendix 14

EIS analysis of symmetrical Li | LLZTO | Li cells at 25 ºC with LLZTO electrolyte pellets sintered at 1050 °C, 1150 °C and 1250 °C for 10 minutes each.

	1050 ºC	1150 ºC	1250 ºC
R_1 / Ω·cm	1981	1084	604
$Ceff_1$ / F·cm^{-1}	5.9 E-10	8.1 E-10	7.4 E-10
σ_1 / S·cm^{-1}	5.1 E-4	9.2 E-4	1.7 E-3
f_1 / Hz	1.4 E5	1.8 E5	3.6 E5
R_2 / Ω·cm	8771	3063	863
$Ceff_2$ / F·cm^{-1}	6.4 E-10	2.0 E-9	2.5 E-9
σ_2 / S·cm^{-1}	1.1 E-4	3.3 E-4	1.2 E-3
f_2 / Hz	2.9 E4	2.6 E4	7.3 E4
R_3 / Ω·cm^2	85	120	65
$Ceff_3$ / F·cm^{-2}	18.7	2.1 E-3	1.15
σ_3 / S·cm^{-1}	8.3 E-4	1.1 E-3	1.9 E-3
f_3 / Hz	1.0 E-4	6.4 E-1	2.1 E-3
σ_{tot} / S·cm^{-1}	8.4 E-5	2.0 E-4	5.0 E-4

Appendix 15

EIS analysis of symmetrical Li | LLZTO | Li cells at 25 ºC with LLZTO electrolyte pellets sintered at 1250 °C for 10 minutes, 30 minutes and 3 hours.

	10 minutes	30 minutes	3 hours
R_1 / Ω·cm	604	1518	1850
$Ceff_1$ / F·cm^{-1}	7.4 E-10	5.5 E-10	1.1 E-9
σ_1 / S·cm^{-1}	1.7 E-3	6.6 E-4	5.4 E-4
f_1 / Hz	3.6 E5	1.9 E5	7.8 E4
R_2 / Ω·cm	863	1757	18443
$Ceff_2$ / F·cm^{-1}	2.5 E-9	5.3 E-9	1.3 E-9
σ_2 / S·cm^{-1}	1.2 E-3	5.7 E-4	5.4 E-5
f_2 / Hz	7.3 E4	1.7 E4	6.7 E3
R_3 / Ω·cm^2	65	49	94
$Ceff_3$ / F·cm^{-2}	1.15	6.5 E-2	7.0 E-4
σ_3 / S·cm^{-1}	1.9 E-3	2.3 E-3	1.2 E-3
f_3 / Hz	2.1 E-3	4.9 E-2	2.4
σ_{tot} / S·cm^{-1}	5.0 E-4	2.7 E-4	4.7 E-5

Appendix 16

EIS analysis of a symmetrical Li | LLZTO | Li cell at 25 ºC.

EIS at 25 ºC					
R_1 / Ω·cm	604	R_2 / Ω·cm	863	R_3 / Ω·cm²	65
$Ceff_1$ / F·cm^{-1}	7.4 E-10	$Ceff_2$ / F·cm^{-1}	2.5 E-9	$Ceff_3$ / F·cm^{-2}	1.15
σ_1 / S·cm^{-1}	1.7 E-3	σ_2 / S·cm^{-1}	1.2 E-3	σ_3 / S·cm^{-1}	1.9 E-3
f_1 / Hz	3.6 E5	f_2 / Hz	7.3 E4	f_3 / Hz	2.1 E-3
		σ_{tot} / S·cm^{-1}	5.0 E-4		

Appendix 17

Galvanostatic cycling of a symmetrical Li | LLZTO | Li cell up to short-circuit, which was then analysed by MRI. The cell was first cycled at 0.2 mA·cm^{-2} up to a capacity of 1 mAh·cm^{-2} for 3 cycles (black), followed by 0.5 mA·cm^{-2} up to a capacity of 1 mAh·cm^{-2} for 3 cycles (blue), 1 mA·cm^{-2} up to a capacity of 1 mAh·cm^{-2} for 3 cycles (green) and finally at 0.5 mA·cm^{-2} for one discharge only until short circuit (labelled in red).

